CANADIAN THESES ON MICROFICHE

THÈSES CANADIENNES SUR MICROFICHE

National Library of Canada
Collections Development Branch

Canadian Theses on
Microfiche Service

Ottawa, Canada
K1A 0N4

Bibliothèque nationale du Canada
Direction du développement des collections

Service des thèses canadiennes
sur microfiche

NOTICE

The quality of this microfiche is heavily dependent upon the quality of the original thesis submitted for microfilming. Every effort has been made to ensure the highest quality of reproduction possible.

If pages are missing, contact the university which granted the degree.

Some pages may have indistinct print especially if the original pages were typed with a poor typewriter ribbon or if the university sent us an inferior photocopy.

Previously copyrighted materials (journal articles, published tests, etc.) are not filmed.

Reproduction in full or in part of this film is governed by the Canadian Copyright Act, R.S.C. 1970, c. C-30. Please read the authorization forms which accompany this thesis.

AVIS

La qualité de cette microfiche dépend grandement de la qualité de la thèse soumise au microfilmage. Nous avons tout fait pour assurer une qualité supérieure de reproduction.

S'il manque des pages, veuillez communiquer avec l'université qui a conféré le grade.

La qualité d'impression de certaines pages peut laisser à désirer, surtout si les pages originales ont été dactylographiées à l'aide d'un ruban usé ou si l'université nous a fait parvenir une photocopie de qualité inférieure.

Les documents qui font déjà l'objet d'un droit d'auteur (articles de revue, examens publiés, etc.) ne sont pas microfilmés.

La reproduction, même partielle, de ce microfilm est soumise à la Loi canadienne sur le droit d'auteur, SRC 1970, c. C-30. Veuillez prendre connaissance des formules d'autorisation qui accompagnent cette thèse.

THIS DISSERTATION
HAS BEEN MICROFILMED
EXACTLY AS RECEIVED

LA THÈSE A ÉTÉ
MICROFILMÉE TELLE QUE
NOUS L'AVONS REÇUE

NL 339 (r. 86/09)

Canada

0-315-19420-0

National Library
of Canada

Bibliothèque nationale
du Canada

72

Canadian Theses Division

Division des thèses canadiennes

Ottawa, Canada
K1A 0N4

67328

PERMISSION TO MICROFILM — AUTORISATION DE MICROFILMER

- Please print or type — Écrire en lettres moulées ou dactylographier

Full Name of Author — Nom complet de l'auteur
David Michael Antoniuk

Date of Birth — Date de naissance
Sept. 19, 1955

Country of Birth — Lieu de naissance
Canada

Permanent Address — Résidence fixe
10620-75 st.
Edmonton, Alberta
T6A 2Z9

Title of Thesis — Titre de la thèse
A Magnetogasdynamic Approach to Laser Discharge Stabilization

University — Université
University of Alberta

Degree for which thesis was presented — Grade pour lequel cette thèse fut présentée
Doctorate

Year this degree conferred — Année d'obtention de ce grade
1983

Name of Supervisor — Nom du directeur de thèse
Dr. H.J.J Seguin, Dr. C.E. Capjack

Permission is hereby granted to the NATIONAL LIBRARY OF CANADA to microfilm this thesis and to lend or sell copies of the film.

The author reserves other publication rights, and neither the thesis nor extensive extracts from it may be printed or otherwise reproduced without the author's written permission.

L'autorisation est, par la présente, accordée à la BIBLIOTHÈQUE NATIONALE DU CANADA de microfilmer cette thèse et de prêter ou de vendre des exemplaires du film.

L'auteur se réserve les autres droits de publication; ni la thèse ni de longs extraits de celle-ci ne doivent être imprimés ou autrement reproduits sans l'autorisation écrite de l'auteur.

Date
April 22/83

Signature
David M. Antoniuk

NL-91 (4/77)

THE UNIVERSITY OF ALBERTA

A MAGNETOGASDYNAMIC APPROACH TO LASER DISCHARGE STABILIZATION

by

(C)

David Michael Antoniuk

A THESIS
SUBMITTED TO THE FACULTY OF GRADUATE STUDIES AND RESEARCH
IN PARTIAL FULFILMENT OF THE REQUIREMENTS FOR THE DEGREE OF
DOCTOR OF PHILOSOPHY

DEPARTMENT OF ELECTRICAL ENGINEERING

EDMONTON, ALBERTA

SPRING 1983

THE UNIVERSITY OF ALBERTA

RELEASE FORM

NAME OF AUTHOR David Michael Antoniuk

TITLE OF THESIS A Magnetogasdynamic Approach to Laser Discharge Stabilization

DEGREE FOR WHICH THESIS WAS PRESENTED Doctor of Philosophy

YEAR THIS DEGREE GRANTED Spring 1983

Permission is hereby granted to THE UNIVERSITY OF ALBERTA LIBRARY to reproduce single copies of this thesis and to lend or sell such copies for private, scholarly or scientific research purposes only.

The author reserves other publication rights, and neither the thesis nor extensive extracts from it may be printed or otherwise reproduced without the author's written permission.

(Signed) David M. Antoniuk

PERMANENT ADDRESS:
10620 - 75 Street
Edmonton, Alberta T6A 2Z9

DATED March 25, 1983

THE UNIVERSITY OF ALBERTA

FACULTY OF GRADUATE STUDIES AND RESEARCH

The undersigned certify that they have read, and recommend to the Faculty of Graduate Studies and Research, for acceptance, a thesis entitled

A MAGNETOGASDYNAMIC APPROACH
TO LASER DISCHARGE STABILIZATION

submitted by David Michael Antoniuk in partial fulfilment of the requirements for the degree of Doctor of Philosophy in Electrical Engineering.

....
Supervisor

C. E. Capjack
Supervisor

....

Peter Smy

Michael Bennett
External Examiner

DATE .March 25, .1983...........

DEDICATION

To Penny, for encouraging me in my endeavors.

ABSTRACT

A new method of stabilizing laser gas discharges through the use of a specially profiled magnetic field is described. The magnetogasdynamic (MGD) stabilization technique utilizes crossed electric and magnetic fields to create and maintain a rapidly rotating plasma of large volume. This rapid recirculation creates a homogeneous normal glow discharge which suppresses the bulk thermal instabilities. In addition, large secondary flows were found to exist which serve to convect the hot neutral gas out of the active discharge volume. Significant increases in specific discharge power loadings have been achieved without the benefit of external gas convection. The gas discharge performance was found to be largely insensitive to the gas composition and pressure.

Theoretical investigations of this new technique were carried out in order to predict the complete flow pattern and the gas discharge characteristics. This analysis was based upon a one-fluid MGD model. A computer code, MAGIC, has been developed to numerically solve this system of time-dependent, nonlinear, coupled partial differential equations. The algorithm used to solve the compressible MGD equations is based upon an iterative, alternating direction implicit (ADI) temporal advancement scheme. This method avoids the limitation in time step size imposed by explicit methods thereby substantially reducing computational cost.

Numerical results from the computer code revealed a high speed rotational flow dependent upon the applied Lorentz driving force.

Furthermore, the secondary flows formed a convective cell for the neutral gas. Finally, the one-fluid MGD model indicated that the spatially nonuniform electric and magnetic fields within the gas discharge caused the plasma and neutral gas velocities to be strongly sheared within the cathode fall and positive column regions. This sheared rotation serves to minimize plasma micro-instabilities near the cathode surface. These results were confirmed by direct observation and by detailed diagnostic measurements.

ACKNOWLEDGEMENTS

This thesis is the culmination of five years of study at the Department of Electrical Engineering. In those years, the author has enjoyed the friendly atmosphere provided by the faculty members, technical staff, and fellow graduate students. To all these people the author extends his gratitude.

The author wishes to acknowledge his supervisors Dr. Herb Seguin and Dr. Clarence Capjack for initially suggesting this fascinating project. Their excellent guidance over the past five years has enabled the author to overcome a variety of experimental and computational problems. Furthermore, their comments and helpful advice were also greatly appreciated.

Special thanks are conveyed to Jim Dow and Jim Radizon for their technical assistance with various aspects of the project. Appreciation is also extended to the staff of the Electrical Engineering Machine Shop for their expertise and efforts in construction of the numerous system components. The author also wishes to thank the staff at Graphic Services and Photographic Services for their assistance in preparing the figures and photographs.

A special acknowledgement is conveyed to Dr. Farouk Soliman for his valuable assistance, comments, and friendship. In addition, the author is extremely grateful to Mrs. Soliman for her tremendous effort in the preparation and typing of this thesis.

The author's parents and grandparents have provided continuous support throughout his entire lifetime. To them, the author will be

forever indebted. Finally, this thesis is dedicated to the author's girlfiend, Penny, who through her wonderful presence has provided continued encouragement and never-ending love.

TABLE OF CONTENTS

PAGE

CHAPTER 1 INTRODUCTION 1

1.1 PROJECT MOTIVATION 1

1.2 BACKGROUND HISTORY 2

1.3 POSITIONAL STABILIZATION OF A PLASMA COLUMN 7

1.4 ROTATING PLASMAS 9

1.5 MGD STABILIZATION CONCEPT 12

1.6 THESIS PROLOGUE 13

CHAPTER 2 DISCHARGE INSTABILITY ANALYSIS 16

2.1 INTRODUCTION 16

2.2 PLASMA KINETIC PROCESSES 17

2.2.1 Effects of Detachment Processes 21
2.2.2 Ionization Instabilities 25
2.2.3 Effects of External Preionization 28

2.3 TRANSPORT PROCESSES 29

2.4 COLLISIONAL ENERGY TRANSFER PROCESSES 30

CHAPTER 3 SYSTEM DESIGN 32

3.1 INTRODUCTION 32

3.2 VACUUM SYSTEM 32

3.3 ELECTRODE MATERIALS AND DESIGN 34

3.3.1 Transverse Electrode Structure 38
3.3.2 Coaxial Electrode Structure 42
3.3.3 Multi-pin Ballasted Anode 44

PAGE

3.4 ELECTROMAGNET DESIGN 50

3.4.1 Cylindrical Magnet 50
3.4.2 Coaxial Magnet 54

3.5 TYRATRON PULSER 57

3.6 DC POWER SUPPLY 60

CHAPTER 4 MGD MODEL OF A GLOW DISCHARGE 63

4.1 INTRODUCTION 63

4.2 SINGLE FLUID MGD EQUATIONS 64

4.3 CURRENT DENSITY DISTRIBUTION 69

4.4 TRANSPORT PROPERTIES OF IONIZED GASES 75

4.4.1 Viscosity 77
4.4.2 Electrical Conductivity 79

4.5 DETERMINATION OF THE TRANSPORT COEFFICIENTS 82

4.6 ORTHOGONAL CURVILINEAR COORDINATES 87

CHAPTER 5 COMPUTATIONAL TECHNIQUES 91

5.1 INTRODUCTION 91

5.2 BASIC NUMERICAL CONCEPTS 92

5.3 COMPUTATIONAL MESH 97

5.4 SPATIAL FINITE DIFFERENCING 101

5.5 TEMPORAL FINITE DIFFERENCING 103

5.6 LINEARIZATION OF THE FINITE DIFFERENCE EQUATIONS 105

5.7 SOLUTION OF THE DIFFERENCE EQUATIONS 109

5.8 BOUNDARY CONDITIONS 113

5.9 ITERATIONS AND DYNAMIC TIME STEP CONTROLS 118

PAGE

CHAPTER 6 EXPERIMENTAL RESULTS AND DISCHARGE OBSERVATIONS 121

6.1 NUMERICAL RESULTS OF THE TRANSVERSE GEOMETRY 121

6.1.1 Velocity Profile 121

6.1.2 Radial Pressure Profile 129

6.2 ANALYTICAL MODEL AND RESULTS OF THE COAXIAL GEOMETRY 135

6.3 OBSERVED PHYSICAL PHENOMENA 142

6.3.1 Preliminary Observations 142
A Tubular Anode Geometry 143
B Coaxial Electrode Geometry 147
C Multi-Pin Ballasted Anode Geometry 150

6.3.2 High Speed Photographic Interpretation 152

6.3.3 Afterglow Effect 156

6.3.4 Standing Wave Striations 158

6.3.5 Dark Space Width 162

6.4 GAS DISCHARGE DIAGNOSTIC TECHNIQUES 163

6.4.1 Photodiode Measurements 163

6.4.2 Pitot Tube Measurements 172

6.5 VI CHARACTERISTICS OF A MAGNETIZED GLOW DISCHARGE 178

6.5.1 Glow-to-Arc Transition 178

6.5.2 Behavior as a Normal Glow 180

6.5.3 Voltage-Current Curves 183

6.5.4 Variation of the VI Characteristics with Magnetic Field 191

CHAPTER 7 DYNAMICS OF A MAGNETIZED GAS DISCHARGE 198

7.1 INTRODUCTION 198

7.2 DISCHARGE STABILIZATION MECHANISM 199

PAGE

7.3 ELECTRON DISTRIBUTION FUNCTION IN A MAGNETIC FIELD 202

7.4 DRIFT VELOCITY IN A MAGNETIC FIELD 207

7.5 IONIZATION AND COLLISIONAL RATE COEFFICIENTS IN A MAGNETIC FIELD 209

7.6 GAIN CHARACTERISTICS OF A MAGNETIZED GAS DISCHARGE 213

7.6.1 Temperature and Absorption Effects 213

7.6.2 Excitation Processes in a Magnetic Field 220

CHAPTER 8 CONCLUDING REMARKS 224

8.1 SUMMARY OF DISCHARGE STABILIZATION PROCESSES 224

8.2 SUMMARY OF COMPUTATIONAL WORK 226

8.3 FUTURE CONSIDERATIONS 227

REFERENCES 229

APPENDIX A 235

VITA 238

LIST OF TABLES

TABLE PAGE

2.1 Gas Discharge Instability Processes and their Characteristic Times. 19

2.2 Important Chemical Reactions in CO_2-N_2-He Discharges and their Rate Coefficients. 22

3.1 Work Functions of Tested Electrode Materials. 37

4.1 Electron Impact Cross Sections for Elastic and Inelastic Processes when $<\xi> = 1.5$ eV. 84

LIST OF FIGURES

FIGURE		PAGE
2.1	Effect of Electron Temperature on the Rate Coefficients in a CO_2 Laser Gas Mixture	23
2.2	Sequence of Events Following an Initial Disturbance in Electron Density	26
3.1	Experimental MGD Laser Discharge Stabilization Design	33
3.2	Magnetically Stabilized Transverse Discharge Geometry	40
3.3	Flow Through Tubular Anode Structure	41
3.4	Magnetically Stabilized Coaxial Discharge Geometry	43
3.5	Fluid Ballasted Multi-Element Flow Through Anode Structure	45
3.6	VI Characteristics of the Electrolyte Ballast Solution	47
3.7	Magnetic Flux Density of a Re-entrant Electromagnet	51
3.8	Magnetic Field Intensity Contours of a Re-entrant Electromagnet	52
3.9	Magnetic Flux Density of a Solenoid Electromagnet	55
3.10	Magnetic Field Intensity Contours of a Solenoid Electromagnet	56
3.11	Hydrogen Thyratron Pulse Generating Circuit	59

FIGURE PAGE

3.12 Schematic of the DC Sustainer Circuit 61

4.1 Gaussian Shaped Current Density Distribution 76

5.1 Two-Dimensional Mesh Point Orientation for Several Finite Difference Techniques 94

5.2 Schematic of the Finite Difference Computational Mesh 99

5.3 Illustration of the Mesh Points Involved in a Mixed Derivative Calculation 99

5.4 Arrangement of Ghost Point Boundaries on the Finite Difference Mesh 115

6.1 Rotational Velocity Distribution for the Transverse Geometry Neglecting Secondary Flow 122

6.2 Rotational Velocity Distribution for the Transverse Geometry Including Secondary Flow 125

6.3 Secondary Flow Pattern for the Transverse Geometry 127

6.4 Absolute Value of the Radial Pressure Gradient Distribution for the Charged Particle Fluid 133

6.5 Current Density Distribution Model for the Coaxial Geometry 137

6.6 Rotational Velocity Distribution for the Coaxial Geometry Neglecting Secondary Flow 139

6.7 Comparison of the Peak Rotational Velocity Profile Between a 1D and 2D Model, Neglecting Secondary Flow 140

FIGURE PAGE

6.8 Distortion of the Electric Field by a Rotating Discharge Column 146

6.9 Gas Discharge Diagnostic Apparatus 164

6.10 Oscilloscope Recording of Photodiode Voltage Measurements 166

6.11 Dependence of Plasma Column Rotational Velocity on Applied Discharge Current 168

6.12 Variation in Plasma Column Width 170

6.13 Effect of Applied Discharge Current on the Radial Gas Velocity Profile 175

6.14 Dependence of Radial Gas Velocity on Magnetic Field 176

6.15 Comparison of VI Characteristics for a Magnetized and Non-magnetized Glow Discharge 179

6.16 VI Characteristics of a Magnetically Stabilized Coaxial Discharge 186

6.17 VI Characteristics of a Magnetically Stabilized Coaxial Discharge 187

6.18 VI Characteristics of a Magnetically Stabilized Coaxial Discharge 189

6.19 VI Characteristics of a Magnetically Stabilized Fluid Ballasted Discharge 190

6.20 Variation of Discharge Voltage with Magnetic Field 194

6.21 Variation of Discharge Current with Magnetic Field 196

6.22 Variation of Plasma Impedance with Magnetic Field 197

7.1 Lorentz Forces Acting Upon a Glow Discharge in a Transverse Electrode Geometry 200

FIGURE PAGE

7.2 Absorption Measurement Apparatus 214

7.3 Radial Gas Temperature Profile 217

7.4 Variation of Discharge Temperature with Magnetic Field 218

7.5 Improved Convective Flow Design for a Magnetically Stabilized Gas Discharge 221

A.1 Transformation of Coordinate System Basis Vectors 236

LIST OF PHOTOGRAPHS

PLATE PAGE

1. High Speed Rotating Discharge in a Tubular Anode Geometry 144
2. High Speed Rotating Coaxial Discharge 149
3. High Speed Photographs of a Discharge in a Multi-Pin Ballasted Anode Geometry 151
4. High Speed Rotating Discharge Sequence in a Tubular Anode Geometry 154
5. Standing Wave Striations Observed in the Coaxial Geometry 159

LIST OF SYMBOLS

A	surface area
A,B	gas discharge ionization coefficients
$\vec{B}$	magnetic flux density vector
c	thermal molecular speed
c_s	adiabatic sound speed
c_P, c_V	specific heat constants/unit mass for constant pressure and volume respectively
$\vec{c}_s$	random thermal velocity of the s species
C	capacitance
CFL	Courant-Friedrichs-Lewy
CW	continuous wave
d	diameter
D	distance
D_{rs}	mutual diffusion coefficient between the r and s particles
DC	direct current
e	electronic charge
$\vec{e}_i$	unit basis vector for the x_i coordinate
eV	electron volt
E	electric field
E^*, E_{eff}	total and effective electric field respectively
$E_{11}, E_{\perp}$	parallel and perpendicular components of the electric field vector
E_d	electrochemical decomposition potential

E_t	terminal voltage between busbar and sub-electrode pins
EM	electromagnetic
f_i	fractional percentage of the ith gas
f_r	pulse repetition frequency
f_s	velocity distribution function of the s species
f_0, f_1	isotropic and directed component of the Maxwellian distribution function respectively
$\vec{F}_s$	force acting upon the s species
g	determinant of the metrix tensor
g_J	degeneracy factor of the Jth rotational level
$g(\nu)$	lineshapping function
h	Planck's constant
h_i	scale factor for the x_i coordinate
H_a	Hartmann number
I_0	initial laser intensity
I_T	total discharge current
$\hat{I}$	unit tensor
J	current density
$\hat{J}$	Jacobian tensor
k	Boltzmann's constant
k_j	collisional rate coefficient
k_p	gas permeation constant
ℓ	iteration index
L	inductance
L	scale length

m, m_e, m_i	neutral, electron, and ion mass respectively
m_{mix}	average molecular mass of a gas mixture
M	Mach number
M_i	Molecular weight
n, n_e, n_i	neutral, electron, and ion particle density respectively
n_n, n_p	negative and positive ion particle density respectively
N_A	Avogadro's number
N_i	number of degrees of freedom of the ith gas
N_J	population density of the Jth level
p, p_e, p_i	neutral, electron, and ion kinetic pressure respectively
P_C, P_D	power of a convection and diffusion cooled laser respectively
P_s, P_0	static and stagnation gas pressure respectively
PVC	polyvinyl chloride
Q	gas throughput
Q_{rs}	collisional cross section between the r and s gas species
r	radius
r_L	Larmor radius
R	universal gas constant
R_p	plasma impedance
R_m	magnetic Reynold's number
RF	radio frequency

S	pumping speed
S_j	ionization source term of the jth process
S_0, S_1	collision integrals
t	time
t_{spont}	spontaneous transition time
T, T_e, T_i	neutral, electron, and ion temperature respectively
TEA	transversely excited atmospheric
u	mobility
$\vec{u}$	solution state vector
uv	ultra-violet
v_A	Alfvén speed
$\vec{v}_s$	mass average velocity of the s species
V	voltage or volume
VI	voltage-current
$\vec{V}_e, \vec{V}_n, \vec{V}_p$	electron, negative-ion, and positive-ion drift velocity.
$\vec{w}$	particle velocity vector
X_i	excitation probability of ith state
z	axial direction coordinate
Z_s	ionization number for the s species
α	first Townsend ionization coefficient
α	absorption coefficient
β_e, β_i	electron and ion Hall parameters
γ	ratio of specific heat capacities

$\gamma(\nu)$	optical gain coefficient
Γ	particle flux density
δ_s	energy loss factor for the s species
δ_{ij}	Kronecker delta function
Δ	incremental change
ε	convergence criterion
ε_0	free space permittivity
ε_{ijk}	Levi-Civita permutation symbol
ζ	bulk viscosity coefficient
θ	azimuthal direction cordinate
Θ_s	conservative molecular property of the s species
κ_T	thermal conductivity
λ	characteristic wavelength
λ_m	mean free path
λ_D	Debye length
μ_i, μ_n	shear viscosity coefficients for charged and neutral fluids respectively
ν	frequency of radiation
ν_u	electron-electron energy exchange collision frequency
ν^{*}_{rs}	average collision frequency for momentum exchange between r and s particles
ξ	electron energy
$\xi(T)$	relaxation energy
$\hat{\Pi}_s$	partial pressure tensor of the s species
ρ, ρ_e, ρ_i	neutral, electron, and ion mass density respectively

σ_w	electrolyte fluid condictivity
$\hat{\sigma}$	electrical conductivity tensor
$\sigma_{\parallel}, \sigma_{\perp}, \sigma_T$	parallel, perpendicular, and transverse components of the electrical conductivity tensor with respect to the magnetic field
τ_C	characteristic convective gas cooling time
τ_D	characteristic diffusion time
τ_j	characteristic time for the jth instability process
τ_{rot}	discharge rotation time
$\hat{\tau}$	viscous stress tensor
ϕ	angle of rotation between coordinate systems
ω_{pe}	plasma frequency
ω_{ce}, ω_{ci}	electron and ion cyclotron frequencies respectively
$\vec{\omega}$	vorticity vector
$\hat{\Omega}$	collision frequency tensor
$\perp$	perpendicular
$\parallel$	parallel
T	transverse
∞	infinity
$\vec{\nabla}$	gradient vector
$\hat{}$	denotes a tensor quantity
$< >$	denotes an averaged quantity

CHAPTER 1

INTRODUCTION

1.1 PROJECT MOTIVATION

The study of naturally occurring and laboratory created plasmas presents an enormous challenge to our fundamental knowledge of this fourth state of matter. Various successful investigations have led to the modern day development of high voltage thyratron switching devices, magnetohydrodynamic (MHD) power generating systems, and many other discharge devices. In addition, the analysis of ionized gases has prepared a background for theoretical fusion studies.

In recent years, gas discharges have also provided an efficient pumping mechanism for a new generation of high powered gas lasers. Experience has shown that the performance of these electric discharge lasers is highly dependent upon the quality of the glow produced within the laser. The demand for larger volumes, higher pressures and complex gas mixtures has placed severe limitations on present day gas discharge technology. Specifically, an initially uniformly distributed discharge is observed to undergo a glow-to-arc transition whenever the input power density exceeds a certain instability threshold level. Numerous other plasma instabilities can also produce local current constriction which in turn results in a very nonuniform excitation and excessive local gas heating. Due to these circumstances, the scaling of larger devices to higher energy densities has become increasingly difficult.

In order to circumvent these laser discharge stability problems, various new stabilization techniques have been developed. Most of the attention has been focused upon the basic principle of convective gas cooling and its effect upon a glow, sustained by an auxiliary ionization source. Devices employing both these techniques simultaneously, have proved to be most successful thus far. However, these procedures have still been unable to overcome the scaling problems associated with the development of large volume, high power lasers.

The major objective of this research endeavor is to continue the study of laser discharge instability processes. In an attempt to eliminate the effects of these undesired processes, a new magnetogasdynamic (MGD) stabilization approach has been devised.

In this chapter, a brief history of high power lasers is presented. Included are some of the fundamental physical processes which determine useful laser operation. Some initial concepts, concerning a plasma under the influence of a magnetic field, are also discussed so as to provide the necessary background material for this project.

1.2 BACKGROUND HISTORY

Early designs, of electrically excited molecular lasers, consisted of either sealed off tubes or long tubes containing slowly flowing gas mixtures [1.1]. These gas discharges were cooled by molecular diffusion and consequently, vibrational energy was lost to the tube walls. For this type of laser discharge, the energy balance or resulting power density can be approximately expressed as

$$\vec{J}\cdot\vec{E} = -\kappa_T \nabla_r^2 T \quad .$$

Here, $\vec{J}$ is the gas discharge current density vector, $\vec{E}$ is the applied axial electric field, and T is the resulting gas temperature. This equation clearly shows the thermal constraints imposed upon the gas discharge. Since He is the major constituent in CO_2 lasers, the thermal conductivity, κ_T , of the gas mixture is effectively constant. As a result, higher power densities could only be attained by maintaining very cold walls and by limiting the tube radius to about 1 cm.

In these diffusion cooled lasers, the maximum power level is determined by the rate at which waste heat is removed from the system. For a discharge column of diameter d, the characteristic diffusion time is

$$\tau_D = \frac{d^2}{\lambda_m c}$$

where λ_m is the mean free path of the CO_2 molecules and c is the thermal molecular speed. Since the achievable power is inversely proportional to the characteristic cooling time, it can be shown that

$$P_D \propto \rho \frac{\lambda_m c}{d^2}$$

where ρ is the gas density. Consequently, this axial flow design could only produce power densities of a few tenths of a Watt/cm^3; thus forcing the construction of very long discharge tubes. Any further increases in input power led to higher gas temperatures and a substantial reduction in gain [1.2, 1.3].

Recognition of the important role played by gas temperature and transport processes led to the development of a convective laser. In this design, excess heat is removed convectively by the rapid flow of the gas mixture. If the gas is flowing at a speed v, then the characteristic cooling time is given by

$$\tau_c = d/v \ .$$

The flow of fresh material into the active region provides more efficient laser pumping and reduces the thermal population of the lower laser level.

In order to describe the factors which promote higher power levels and system scaling, the translational and vibrational energy equations were examined. The resulting studies revealed an energy dependence upon gas density as well as flow velocity. In other words,

$$P_c \propto \rho \frac{v}{d} \ .$$

A comparison of achievable power levels between a diffusion cooled laser and a convectively cooled laser, with equal active volumes, was simply proportional to the ratio of their characteristic cooling times, i.e.

$$\frac{P_D}{P_c} \propto \frac{\lambda_m c}{dv} \ .$$

Since the ratio was much smaller than unity, it was obvious that convective cooling was a superior design for a laser.

Although the utilization of convective cooling increased laser discharge power density by a factor of ten, most high power molecular lasers could only operate at levels substantially below those dictated by thermal considerations. This was primarily due to the onset of plasma instabilities.

As closed-cycle lasers became commonplace, it was found that instabilities limited the discharge power to levels significantly below those characteristic of open-cycle lasers. A new technique involving the application of RF power to the DC discharge was then introduced [1.4]. It was observed that the radio frequency source improved discharge uniformity and hence stability. In addition, the enhanced uniformity kept the current density to a minimum, which in turn, minimized the local buildup of arc-like filaments. The RF supply was also thought to produce a rotation in the current density vector. This produced a damping of unstable wave modes, provided the RF supply frequency exceeded the growth rate of the unstable wave. This process increased the discharge power density to some extent. However, as the RF power increased further, the applied DC power peaked and then decreased due to thermal loading effects in the gas. Hence, this procedure has only limited capability and use.

Further improvement in gas discharge stability was obtained through the use of external control of the electron density. This led to the development of the electron beam sustained laser discharge [1.5]. In this technique, uniform preionization is created throughout the active volume by a powerful electron beam. The external ionizing agent decouples charge production in the discharge from the electric field. This decoupling reduces a primary source of instability caused by the loss of electrons due to volume recombination of electron-ion pairs. Though effective, the electron beam controlled laser has some limitations with regards to gas discharge current, pulse duration, and the frequent occurrence of foil damage by energetic electrons.

Another common technique for conditioning the discharge is the use of photoionization [1.6-1.9] in the form of uv light sources. In this configuration, the high energy electron beam is replaced by an inexpensive low energy photon preionization source. Here, the applied electric field no longer sustains the plasma, and the ratio E/n can be independently adjusted in order to optimize vibrational excitation of the upper laser levels. This method can also provide a spatially uniform background for avalanche development in the main discharge. However, if the preionization electron density is less than the equilibrium electron density produced by the avalanche discharge, the preionizer loses control after the avalanche develops. The stability of the main discharge plasma is then again restricted by the occurrence of a glow-to-arc transition.

A unique technique that has had some success deals with aerodynamic gas conditioning [1.10, 1.11]. The introduction of turbulence upstream from the gas discharge has a noticeable stabilizing effect at low pressures. Turbulence affects the plasma in two important ways. First, it can change microscopic properties such as the particle velocity, energy, and density distributions. Secondly, macroscopic features can be altered such as the overall plasma shape. Experiments have shown that a weakly ionized plasma cannot significantly alter the turbulent field of the neutral gas, although ion-neutral collisions readily transfer turbulent motions from the uncharged to the charged species [1.11]. As a result, these small-scale eddies of turbulence enhance neutral particle and plasma transport processes. Such enhanced transport properties cause the critical wavelength of most instability modes to increase. This allows more time for the gas flow to convect any current filaments out of the discharge region.

Associated with this turbulence is an increase in particle loss and a rise in electron temperature. Under certain conditions this can favourably alter the conditions for an instability occurring in the negative-ion and ionization modes. However, the observed improvements in discharge stability have been difficult to interpret because of a lack of detailed measurements and by complications created by other possible effects.

Even with the successes achieved through the use of such innovative techniques, problems still remain which prevent the development of even larger volume, higher energy lasers. In particular, maintaining a stable, uniform plasma of high optical quality with dependable long term qualities has been difficult to achieve. Consequently, the need for new dynamic, uncomplicated methods of stabilizing discharges exists.

1.3 POSITIONAL STABILIZATION OF A PLASMA COLUMN

Arc positional control and extinction techniques by means of magnetic fields have been considered for several decades [1.12, 1.13]. These typical interactions considered between arc, gas flows, and magnetic fields usually dealt with two situations: those in which the arc was moved through a gas by an externally applied magnetic field, and those in which the arc was held stationary by a balance of forces. Such balanced arcs involve a match between aerodynamic and magnetic forces. Initial experiments determined that the magnetic field strength necessary to balance the arc column was proportional to the square of the applied transverse gas velocity.

Such studies have led to a technique of magnetically stabilizing the position of a low density plasma column. In early low pressure convectively cooled axial discharge CO_2 lasers, the plasma column was strongly bowed downstream due to the influence of the transverse gas flow. For efficient laser operation; the discharge has to be straightened and aligned with the optical axis of the laser resonator. The work done by Buczek et. al. [1.14], involved the use of a tapered transverse magnetic field mutually perpendicular to the axial electric field and the gas flow velocity. Positional stabilization of the discharge column was accomplished by the balance between gas flow velocity and the drift velocity of the plasma caused by the resulting Lorentz force. The interaction of the transverse magnetic field and the charged particle drift velocity v_d , created a force which counters the flow velocity force. Thus, the position of the discharge column could be accurately placed.

A tapered magnetic field was designed so that it would force the discharge to flow on the desired axis. Essentially, this created a potential well in which the discharge was held against velocity and current fluctuations. The size and depth of this well was dependent upon the shape and strength of the transverse magnetic field, and upon collisions with flowing neutral molecules. Thus, using a properly designed magnetic field, the plasma column could be confined. By aligning the potential well with the laser's optical axis, most of the electric energy deposited in the plasma column was available for laser output.

These and other studied have indicated that for low density gas discharges, the magnetic field necessary for positional stabilization varied linearly with pressure and flow velocity. These important facts allow the idea of system scaling to be considered. Thus, it should be possible to scale up the power density by increasing gas flow velocity and magnetic field proportionally, and still maintain a high operational efficiency.

Present day convective lasers utilize a transverse electrode design rather than the cross-field electrode design of Buczek. In these new laser devices, the gas discharge is transverse rather than parallel to the optic axis. Since the distance between electrodes is now much shorter in the transverse design, the problem of the discharge bowing downstream is significantly reduced.

1.4 ROTATING PLASMAS

Recent investigations of magnetized fluids have explored possible applications of rotating plasmas [1.15, 1.16]. Various studies have produced a wealth of information dealing with plasma confinement and momentum balance of such rotating plasmas. Several research laboratories are studying the strong centrifugal force created by the rotation and are exploring its possible uses. They have found that this force can be externally controlled and used to simulate the effect of a large thermal pressure. It also seems likely that special rotating plasma devices could be built to predict various transport coefficients in a magnetic field. Rotating plasmas are also important in fusion research since the centrifugal confinement should help reduce the end losses in magnetic mirror devices.

Ionized particles, within a gas discharge, begin to gyrate under the influence of an electrodynamic force $\vec{J} \times \vec{B}$, produced when an electric current flows through a magnetic field. This force produces a torque only when the current density and magnetic field components are mutually orthogonal. Thus, macroscopic fluid motion is created. Such motions may also arise from the interaction of time-dependent electric and magnetic fields.

The most significant aspect of a rotating plasma is the ability of the $\vec{J} \times \vec{B}$ force to produce a strong transmission of momentum in a direction orthogonal to the magnetic field, thereby creating a Lorentz force. In addition, this large force has proven to be an effective method for removing impurities from within the plasma bulk. This idea led to the development of plasma centrifuges for element and isotope separation [1.17-1.21]. In such a device, ionized particles are sent into rotation by the Lorentz force. Most devices of this type use two ring electrodes of different radii, thereby creating a radial electric field. Rotation can be observed when this radial current density is combined with an axial magnetic field. Plasma centrifuges can attain rotational velocities several orders of magnitude higher than their mechanical counterparts. Consequently, light and heavy ionic and atomic isotopes can be separated more efficiently.

These proposed plasma centrifuges can utilize one of two types of working fluids, a low density collisionless plasma or a high density collision dominated plasma. The low pressure, fully ionized plasma requires a large electrical power input to produce the high degree of ionization necessary for practical isotope separation. However, the highly ionized gas centrifuge has reduced velocity losses at its walls due to the absence of ordinary hydrodynamic boundary layers. This accounts for the extremely high rotational velocities observed.

In the high density gas centrifuge, only a small fraction of the isotopic particles need be ionized. The Lorentz force drives the ions which in turn drives the neutral particles through inter-component viscous forces. The large number of collisions and the viscous boundary layers at the containment walls interact to reduce the rotational velocity somewhat. Due to the lower input energy, the gas temperature will be substantially lower and this will have a favourable effect on isotope separation. This will also lead to a more energy efficient device.

At present these centrifuge devices are being built and theoretically analyzed. The analysis of these gas discharges are based upon magnetogasdynamic equations. Thus far, only simplified two-dimensional solutions have been attempted. With these first attempts some progress has been made to confirm the usefulness of these types of devices.

1.5 MGD STABILIZATION CONCEPT

As reported earlier, gas discharges operating in high power lasers suffer from numerous types of bulk and micro-instabilities. It was proposed that a laser gas discharge could be subjected to a Lorentz force to create a high velocity rotating plasma. This technique would then be employed to rapidly convect thermal instabilities out of the discharge volume by reducing the characteristic gas cooling time τ_c .

The viability of this concept would only prove successful provided that a proper magnetic field profile be attained. In addition to a rotational driving force, a theoretical model for a confining force was developed. With the proper configuration of magnetic field, an elaborate magnetic potential well could be constructed to confine a rapidly rotating discharge plasma. In this manner, the tendency for a glow-to-arc transition at the electrode extremities could be suppressed. Thus, the need for specially shaped or profiled electrodes would be eliminated.

It is expected that viscous forces will effectively couple the fast moving ionized particles to the slower moving neutral particles. However, at the outer edges of the potential well, the driving force terms would be weaker. This would then allow a decoupling of these particles and result in more free movement for the neutral particles in this region. The neutrals, now only under the influence of a centrifugal force, should tend to fly off tangentially. This concept would create an ideal situation in which ionized particles are captured by the magnetic field, while neutral particles would be free to travel through the containment region.

The goal of this project is to produce a highly stabilized laser discharge, utilizing the concepts of a rotating plasma within a potential well. This new dynamic stabilization system should be much simpler than any other existing approach. If the rotating gas flow velocity is sufficiently high, there should be little or no need for an external blower system. With the appropriate heat exchanger design, the gas may be allowed to circulate on its own accord.

This unique approach to gas discharge stabilization seems to satisfy the necessary requirements for producing a uniform glow discharge that should be highly immune to various types of instabilities.

1.6 THESIS PROLOGUE

The primary objective of this thesis is to define the fundamental principles for a new generation of high power gas discharge lasers based upon a MGD stabilization concept. It has long been known that magnetic fields can significantly alter the characteristics of a plasma. Furthermore, it is evident that such fields could be utilized to provide a stabilizing mechanism in which a uniform glow discharge could be maintained. It was then essential that the different types of gas discharge instability processes be analyzed to determine their significance and role. As will be explained in Chapter 2, a gas discharge contains a wide variety of instability modes that can develop with time. Each mode has its own particular driving mechanism and characteristic critical wavelength. Many of these modes are coupled to one another, thereby complicating a detailed analysis.

Some of the major components used to test the theory of MGD stabilization will be discussed in Chapter 3. Due to the harsh operating environment found within a high power laser, the physical components are forced to undergo severe thermal and structural tests. In addition, the water-cooled electrode and electromagnet assemblies are required to operate within a vacuum chamber. Using proper materials, these problems were overcome. However, to achieve a uniformly distributed glow discharge, the electrode structure underwent several design changes before a satisfactory system was developed.

In order to understand the complex processes occurring within the gas discharge, a computer code has been developed. The computer program MAGIC (MAgnetoGasdynamic Implicit Code) is designed to evaluate time varying changes in pressure and velocity. In MAGIC, a system of MGD equations was solved by the alternating direction implicit (ADI) technique on a variable Eulerian mesh. Chapter 4 developes the MGD equations necessary to form an accurate model of a partially ionized glow discharge. Furthermore, the gas transport coefficients, found in these equations are described.

The MGD equations are finite differenced in orthogonal curvilinear coordinates to allow program symmetry and to accommodate a variety of coordinate systems. The ADI method described in Chapter 5 allowed the use of longer timesteps, reduced computing costs, and improved program stability. After time and spatial differencing, the nonlinear set of MGD equations are simultaneously solved using a Newton-Raphson iterative procedure. The set of equations are iterated until a convergence criterion is satisfied.

The results of the computer similation on a transverse electrode geometry are presented in Chapter 6. These computed values are then compared with previously determined models and experimental data. In addition, the performance of the MGD stabilization technique in producing a uniformly distributed discharge is evaluated by using high speed motion pictures. To demonstrate the improvement in discharge power density, the MGD stabilization technique is compared with conventional gas discharge systems. The results are graphically illustrated for a variety of parameters.

A detailed explanation of the physical processes occurring within a gas discharge is discussed in Chapter 7. Also analyzed are the changes in the structure of the glow discharge under the influence of a magnetic field. Furthermore, an explanation of the role that the nonuniform magnetic field performs in the MGD stabilization concept is carried out.

The final chapter also summarizes the many other possible aspects that need to be explored. Moreover, it describes some problems still remaining to be resolved before the potential of this new discharge device is maximized.

CHAPTER 2

DISCHARGE INSTABILITY ANALYSIS

2.1 INTRODUCTION

The analysis and understanding of a low density, non-magnetized glow discharge is an extremely complex problem which involves a series of energy transfer and particle conservation interactions. Examination of these interactions is of special interest to those in the laser discipline who scrutinize instability processes. Their efforts have been focused upon discerning the roles played by different gas mixtures, external ionization sources, temperature and density fluctuations, and gas transport processes. This chapter will attempt to examine some of the roles and determine how they affect glow discharge behavior.

Plasma instabilities are the result of small amplitude perturbations that occur within the gas discharge. These fluctuations in temperature and/or electron density excite a number of different wave modes. These modes and their stability have been thoroughly analyzed by Haas [2.1]. Associated with the instability modes are characteristic times which collectively span the time scale 10^{-10} to 10^{-2}s. Instabilities produced in a large volume, high energy discharge plasma are strongly connected to these modes and are easily excited by a variety of mechanisms. A comprehensive list of all processes and characteristic times τ_j can be found in Table 2.1. The symbol n_j represents the particle density of the jth species. Also represented are the rate coefficients of the jth collisional process k_j. This term is defined as the normalized electron-molecule collision frequency, that is

$$k_j = \frac{\nu_{jk}}{n_j} .$$

The main processes that can occur within the discharge can be grouped into four categories: space-charge relaxation, plasma kinetic processes, transport processes, and collisional energy transfer. An analysis of the space-charge relaxation process by Haas [2.1] has determined that this mode poses no overall stability problems. The remaining groups will be briefly examined in order to investigate their relative strengths and cumulative contributions to the onset of instabilities.

2.2 PLASMA KINETIC PROCESSES

The characteristic times associated with the plasma kinetic processes measure the temporal evolution of particle production and loss processes, and are typically in the 10^{-6}-10^{-4}s range. These modes along with their individual rate coefficients are: electron impact ionization of molecules (k_i) and electrically excited species (k_i^*), electron-molecule attachment (k_a), detachment by neutral impact (k_d), electronic excitation (k_e^*), quenching of electric species (k_q), two-body electron-ion recombination (k_r^e), and positive-ion negative-ion recombination (k_r^i).

Working from the Boltzmann equation, an energy balance can be obtained for electrons within a spatially uniform gas in the presence of a steady electric field $\vec{E}$. This electron energy equation compares the rate of energy deposition from the electric field (electron Joule heating) with the rate at which electrons exchange energy through collisions with molecules. The resulting normalized electron-molecule collision frequency ν_{ej}/n_j can then be defined as [2.2]

$$k_j = \frac{\nu_{ej}}{n_j} = \left(\frac{2e}{m_e}\right)^{\frac{1}{2}} \int_0^{\infty} \xi f(\xi) Q_{ej}(\xi) d\xi \, . \tag{2.1}$$

Here, the various rate coefficients are determined by averaging the proper cross section $Q_{ej}(\xi)$ over the electron energy distribution function $f(\xi)$. The symbol ξ represents the electron energy in eV, through the definition

$$\xi = \frac{mv^2}{2e} \, .$$

Other charged particle collision frequencies or rate coefficients are determined by a similar analysis using the appropriate distribution function.

Since the electric field provides the force which accelerates the electrons, the ratio E/n becomes proportional to the electron energy. Thus, the rate coefficients described in Eqn. 2.1 are strongly dependent upon the parameter E/n.

In a subsequent chapter, the effect of a magnetic field on both the electron distribution function and the rate coefficients will be investigated.

Due to electron impact dissociation of CO_2 and N_2 , a variety of minority molecular species are created. The formation of such products as CO, O, NO and a host of positive and negative ions have little effect on electron-molecule vibrational coupling or on

Process	Characteristic time	Range of values (seconds)
I. Space-charge relaxation	$\tau_c = \varepsilon_0/\sigma \simeq \nu_m/\omega_{pe}^2$	10^{-10}-10^{-9}
II. Plasma kinetic processes		
1. direct ionization	$\tau_i = 1/nk_i$	10^{-6}-10^{-5}
2. electronic state ionization	$\tau_i^* = 1/n^*k_i^*$	10^{-6}-10^{-4}
3. attachment (dissociative)	$\tau_a = 1/nk_a$	10^{-6}-10^{-5}
4. detachment (direct and associative)	$\tau_d = 1/nk_d$	10^{-6}-10^{-5}
5. electronic excitation	$\tau^* = 1/nk^*$	10^{-6}-10^{-4}
6. electronic quenching	$\tau_q = 1/n^*k_q$	10^{-6}-10^{-4}
7. electron-ion dissociative recombination	$\tau_r^e = 1/n_pk_r^e$	10^{-6}-10^{-5}
8. ion-ion recombination	$\tau_r^i = 1/n_pk_r^i$	10^{-6}-10^{-5}
III. Transport processes		
1. sound propagation	$\tau_s = d/a$	10^{-5}-10^{-4}
2. viscous dissipation	$\tau_\mu = \rho d^2/\mu$	10^{-3}-10^{-2}

.....cont'd.

IV. Collisional energy transfer processes		
1. electron heating	$\tau_e = 3/2\nu_u$	10^{-9}-10^{-8}
2. vibrational relaxation	$\tau_{VT} = \left\{nk_{10}(1-e^{\xi kT})\right\}^{-1}$	10^{-4}-10^{-2}
3. translation-rotation heating	$\tau_T = nC_pT/(J_e^2/\sigma_e)$	10^{-3}-10^{-2}

TABLE 2.1 Gas Discharge Processes and their Characteristic Times. Typical operating conditions include $p \approx 10$-100 torr, $T \approx 300$-600 K, $T_e \approx 0.5$-2.0 eV, $n_e/n \approx 10^{-8}$-10^{-6}, $d \approx 1.0$ cm [2.1].

vibrational-translational relaxation. However, they can influence the production and loss of electrons through recombination, attachment, and detachment. These dissociative products can accumulate to significant levels, even exceeding the electron density within typical fluid residence times. Some of the more studied reactions occurring in CO_2 laser discharges are listed in Table 2.2.

Of the primary species found in most CO_2 laser mixtures, CO_2 has the largest rate coefficients for electron impact ionization and dissociative attachment. Since both these coefficients are strongly dependent on electron temperature, the electron-CO_2 kinetics dominate ionization and attachment processes in laser discharges. For comparison, several important CO_2 rate coefficients are plotted against electron temperature in Fig. 2.1. Through experimental analysis, Nighan [2.4] has determined that most discharges are dominated by detachment effects. Accordingly, the indicated discharge operating conditions were found to be quite insensitive to the electron energy distribution, fractional ionization, or positive-ion species.

2.2.1 Effects of Detachment Kinetics

A survey of the literature has revealed that detachment kinetic processes are largely responsible for determining the behavior of a self-sustained gas discharge. In particular, if the density of CO is large, then the reaction

$$O^- + CO \rightarrow CO_2 + e ,$$

Reaction type	Rate coefficient (cm^3/s)
I. Ionization, k_i	
$e + CO_2 \rightarrow CO_2^+ + 2e$	10^{-14}-2×10^{-12}
$e + N_2 \rightarrow N_2^+ + 2e$	10^{-11}-10^{-9}
II. Dissociative attachment, k_a	
$e + CO_2 \rightarrow CO + O^-$	3×10^{-13}-2×10^{-12}
III. Dissociative recombination, k_r^e	
$e + CO_2^+ \rightarrow CO + O$	$\sim 6 \times 10^{-8}$
$e + O_2^+ \rightarrow O + O$	$\sim 2 \times 10^{-8}$
$e + NO^+ \rightarrow N + O$	$\sim 7 \times 10^{-8}$
IV. Ion-ion recombination, k_r^i	
$O^- + O_2^+ \rightarrow O + O_2$	$\sim 1 \times 10^{-7}$
$O^- + NO^+ \rightarrow O + NO$	4.9×10^{-7}
$NO_2^- + NO^+ \rightarrow NO_2 + NO$	5.1×10^{-7}
V. Associative detachment, k_d	
$O^- + CO \rightarrow CO_2 + e$	7.3×10^{-10}
$O^- + O \rightarrow O_2 + e$	2×10^{-10}
$O^- + NO \rightarrow NO_2 + e$	5×10^{-10}
$O^- + CO_2 \rightarrow CO_2 + O + e$	$<4 \times 10^{-12}$
$O^- + N_2 \rightarrow N_2O + e$	$<10^{-12}$

TABLE 2.2 Important Chemical Reactions in CO_2-N_2-He Discharges and their Rate Coefficients [2.3, 2.4].

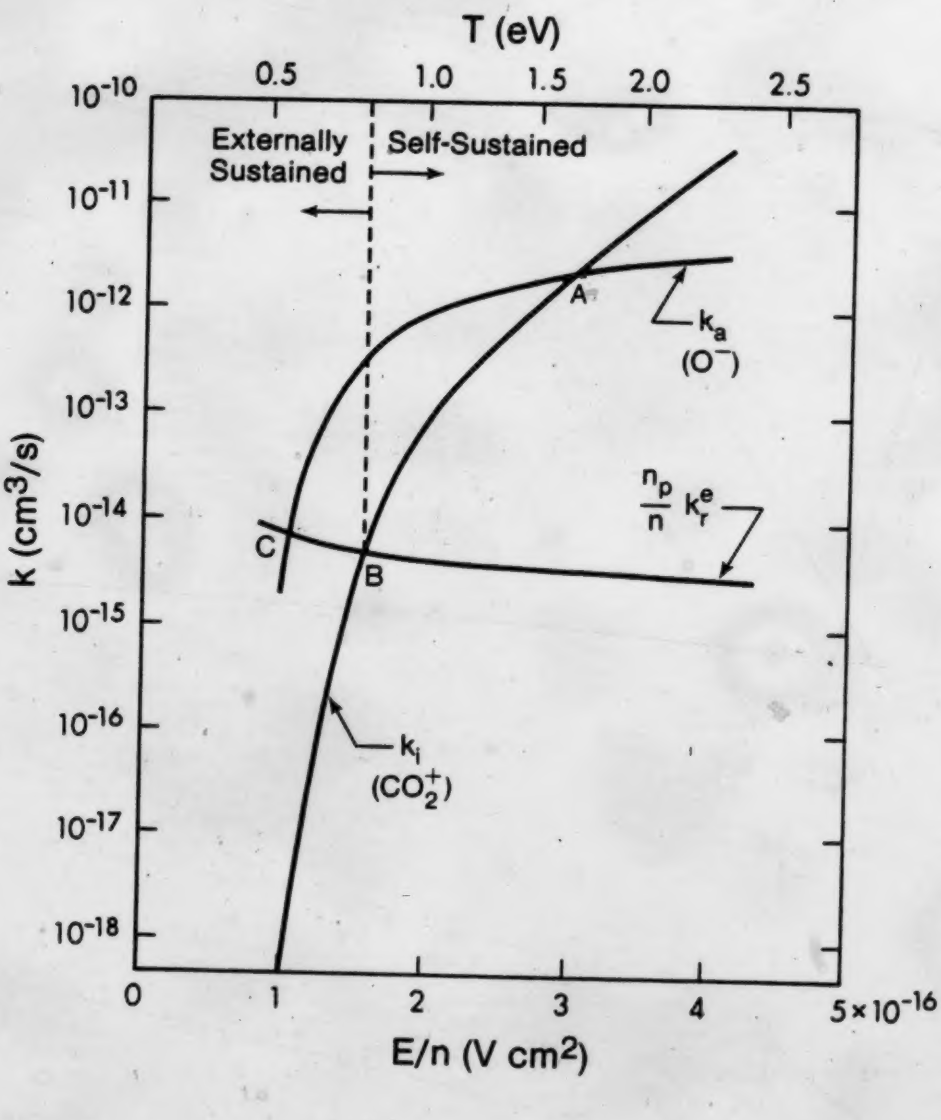

Fig. 2.1 Effect of Electron Temperature on the Rate Coefficients in a CO_2 Laser Gas Mixture.

will keep the negative-ion density small and positive-ion negative-ion recombination will be overshadowed by detachment kinetics. As a result, the characteristic time for the negative ions to respond to a disturbance is much less than the time for the electron density to respond. Hence, during an effective detachment process electrons are released from negative ions so that $n_n/n_e << 1$. Consequently, for this case, negative-ion kinetics will have little or no influence on either steady-state or transient electron production and loss processes. An examination of the electron continuity equation then reveals that ionization balances electron-positive-ion recombination, that is,

$$k_i = (n_p/n)k_r^e \ .$$

In this situation, the discharge can noramlly be sustained at a lower value of electron temperature as indicated by point B in Fig. 2.1.

Examination of the situation when detachment processes are negligible, reveals that under self-sustained operating conditions, the electron production due to ionization must balance electron loss due to attachment, that is, $k_i = k_a$. This occurs for an electron temperature of 1.7 eV (point A) for the conditions of Fig. 2.1. In this situation, the negative-ion density can become comparable to the electron density [2.4]. Such a coupling of electron and negative-ion kinetics will likely lead to an attachment induced ionization instability.

The normal region of operation for a self-sustained gas discharge, lies between points A and B of Fig. 2.1. Since CO is an effective detaching species, easily produced by dissociative recombination or attachment [2.3], the discharge operating point is significantly influenced by its fractional concentration. For the case of sealed or slow-flow discharges containing CO_2, in which CO has had sufficient time to accumulate, detachment processes are common. Thus, negative-ion processes are likely to be insignificant. However, in fast-flow convection dominated discharges, the brief gas residence time ($\lesssim 10^{-2}$s) does not allow the CO fraction to become substantial. Consequently, the negative-ion density starts to rise and thereby begins to influence plasma stability within these non-recirculating systems.

2.2.2 Ionization Instabilities

Ionization instabilities involve the production of two possible modes. The first is identifiable with the electron production and loss kinetics (ionization mode), and the second is associated with the production and loss of negative ions (negative-ion mode). Disturbances in the electron and negative-ion densities are normally controlled by electron-ion recombination and by negative-ion detachment processes. Both these effects exert a damping influence; recombination reduces the magnitude of electron density fluctuations, and detachment reduces the negative-ion concentration. However, these damping processes are not always successful in their attempts to eliminate ionization instabilities. As illustrated in Fig. 2.2, several different scenarios are possible depending upon the dominant rate process.

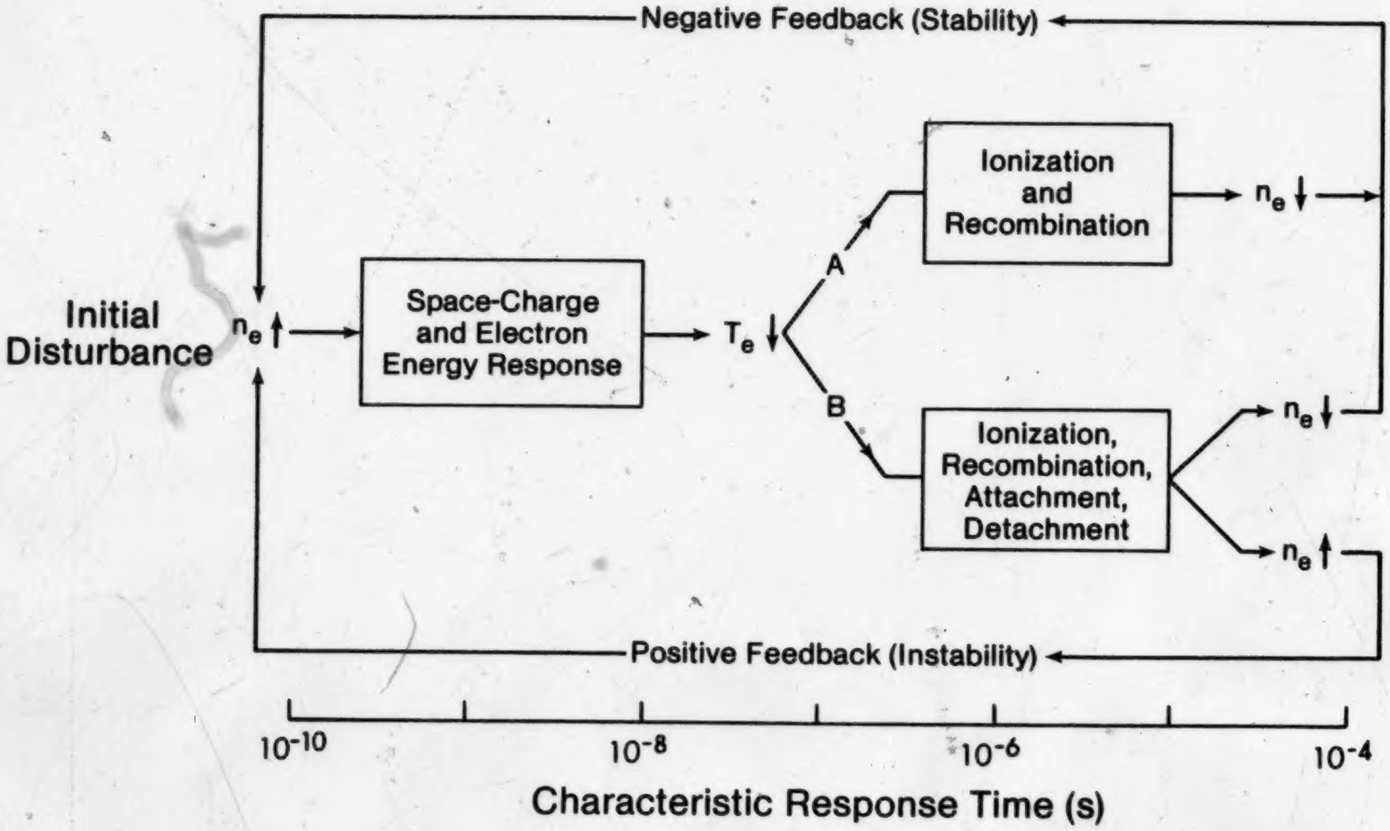
Negative Feedback (Stability)
Initial Disturbance
$n_e \uparrow$
Space-Charge and Electron Energy Response
$T_e \downarrow$
A
B
Ionization and Recombination
Ionization, Recombination, Attachment, Detachment
$n_e \downarrow$
$n_e \downarrow$
$n_e \uparrow$
Positive Feedback (Instability)
10^{-10}
10^{-8}
10^{-6}
10^{-4}
Characteristic Response Time (s)

Fig. 2.2 Sequence of Events Following an Initial Disturbance in Electron Density.

As shown in Fig. 2.2, an initial local positive disturbance in electron density is accompanied by a drop in electron temperature. This effect is the result of the electron temperature dependence on the energy exchange collision frequency ν_u , being stronger than its dependence on the momentum transfer collision frequency. Hence, electron energy transported by momentum out of a disturbance region is small compared to the electron energy loss due to collisions [2.4].

When negative ions are absent, ionization and recombination kinetics dominate electron production and loss (case A). For this particular case, Fig. 2.1 reveals that within a self-sustained plasma, $k_i << k_r^e$. Therefore, the electron density will decrease since recombination effects have a much stronger influence on electron density than due to ionization. Consequently, the electron-ion recombination process describes an effective local electron loss which exerts a stabilizing influence on the gas discharge. Subsequently, it can be concluded that the ionization mode, in the absence of negative ions, is stable.

When negative ions are present (case B), an ionization instability will occur provided that $k_a \geqq k_i$ and that the electron attachment rate increase with electron temperature [2.1]. Since the ionization and attachment times are comparable in magnitude, the negative-ion density will increase. Naturally, recombination processes will become less significant in favour of detachment. The instability occurs because the electron density and temperature fluctuations are out of phase. In this circumstance, the electron production rate due to ionization and detachment, exceeds the loss of electrons by recomination and attachment during an electron temperature decrease. As a consequence, this mechanism will produce a local electron density increase which will create a positive feedback instability process as illustrated in Fig. 2.2. Nighan [2.4] has shown that the growth rate of this instability is strongly peaked in the direction of the applied electric field. This explains the striated and/or constricted manifestations so often seen within gas discharges.

2.2.3 Effects of External Preionization

Kinetic processes which involve electron temperature dependent ionization and attachment rate coefficients, produce micro-instabilities which are independent of the discharge power density and gas pressure. One common technique to overcome this problem is to utilize an external ionization approach in the form of an electron-beam or photoionization source. With this method, charge production in the plasma is decoupled from the applied electric field. This decoupling can significantly reduce the effect of electron temperature variance on electron and negative-ion density fluctuations. In other words, the independently controlled ionization source allows the electron temperature to be adjusted to a value independent of electron production and losses. However, for this method to be successful, the contribution to the ionization rate due to direct low energy electron impact by drifting electrons, must be negligible compared with that provided by an auxiliary ionization source, that is, $S >> n_e k_i$. Thus for optimal performance, the ratio E/n is lowered such that the discharge operates in the externally sustained region as shown in Fig. 2.1.

The electron production mechanism is highly dependent upon the dominant detachment process. Since the presence of detachment processes has a stabilizing influence, less external ionization is required. Consequently, the discharge can be sustained at a higher value of electron temperature. However, if detachment processes are less significant, the electron temperature must be maintained to the left of point C in Fig. 2.1 in order to avoid excessive negative-ion formation. In this manner, the plasma will be dominated by the stabilizing influence of recombination, provided the condition $k_a \ll (n_p/n)k_r^e$ can be satisfied.

The growth times for the ionization and negative-ion modes are short compared to the characteristic times for other modes. Consequently, when they occur, the ionization and negative-ion modes dominate plasma behavior. The subsequent application of an external ionization source helps to control the plasma ionization mechanism and thereby reduces their destabilizing effects.

2.3 TRANSPORT PROCESSES

Neutral gas processes have somewhat longer characteristic times than the time associated with charged particle dynamics. Changes in gas temperature and density can cause fluctuations in neutral gas properties which can couple to the charged particle kinetics and electron energy transfer processes. The coupling that does occur primarily depends upon which rate coefficients are dominant [2.1].

The presence of negative ions can trigger adverse effects with regards to discharge stability processes. Since detachment is strongly temperature dependent, a local gas temperature increase leads to an increased electron production rate. Under these conditions, a large local increase in electron density causes additional heating of the gas by way of elastic collisions. This further stimulates the detachment process and thereby provides the positive feedback mechanism necessary for this process to be unstable. Thus, an initial disturbance in gas temperature will lead to an instability growth provided thermal conduction does not dissipate the resulting local concentration of heat.

2.4 COLLISIONAL ENERGY TRANSFER PROCESSES

Some of the other important collisional processes that occur are the thermal and the vibration relaxation modes. These modes are created by perturbations in local gas temperature and density which couple to the electronic and vibrational properties of the gas. An unstable thermal mode is developed when vibrational relaxation causes local gas heating. The rise in temperature forces the V-T relaxation time τ_{VT} to decrease. This process prevents a rapid energy release within the gas and the stabilizing influence of thermal conduction will be unable to transport this energy away from its point of origin. The net effect is a runaway condition in which the gas temperature continues to rise. The gas density will then begin to decrease and the local electrical conductivity quickly rises to create a high concentration of current flow. The time constant for the evolution of this arclike current filament is τ_T , typically 10^{-3}-10^{-2}s.

This instability mode is likely to occur for all typical high power density discharges with some degree of ionization and a large electron temperature to gas temperature ratio. This mode also has a characteristic wavelength such that if $\lambda > \lambda_{critical}$, the thermal mode is unstable. As the perturbation in temperature grows, the ability of thermal conduction to dissipate local hot spots decreases. Consequently, the critical wavelength decreases and current filaments become narrower, thus promoting the formation of an arc.

The thermal modes are insensitive to external ionization sources since they are relatively unaffected by charged particle kinetics. However, large transport processes can be used successfully if the critical wavelength is not too large. This necessitates the use of high flow velocities to provide heat removal and to convect locally unstable fluid elements from the discharge region. These effects must occur in a time less than that required for a glow-to-arc transition. The results of Nighan [2.6], have indicated that a convective laser having a power density of 10 W/cm^3 will require a gas residence time below 1 ms. Only in this manner will convective type CW gas lasers operate properly.

CHAPTER 3

SYSTEM DESIGN

3.1 INTRODUCTION

The main features of the experimental apparatus used in the MGD stabilization concept are illustrated in Fig. 3.1. It consists of five major components: a vacuum system, a thyratron pulser, an appropriately designed electrode, several types of electromagnets and a 3-phase power supply. The overall system was designed with sufficient flexibility to accommodate a wide variety of gas discharge experiments. These included the testing of various electrode and magnet designs. The apparatus was not designed to operate as a laser, but rather as an experimental device used to test new ideas and components necessary for a more advanced laser.

3.2 VACUUM SYSTEM

Using available material, the gas discharge chamber was built from a PVC pipe 40 cm in diameter, 130 cm long, with a wall thickness of 2 cm. In order to allow easy assembly, operation, and modification of the vacuum system, demountable seals were employed. The open ends of the chamber were covered with clear plexi-glass plates to allow good visual observation of the gas discharge. In order to seal the system, Viton A elastomer O-rings were installed where necessary. Additional plexi-glass access and diagnostic parts were added at a later date to allow experimental gain and temperature measurements.

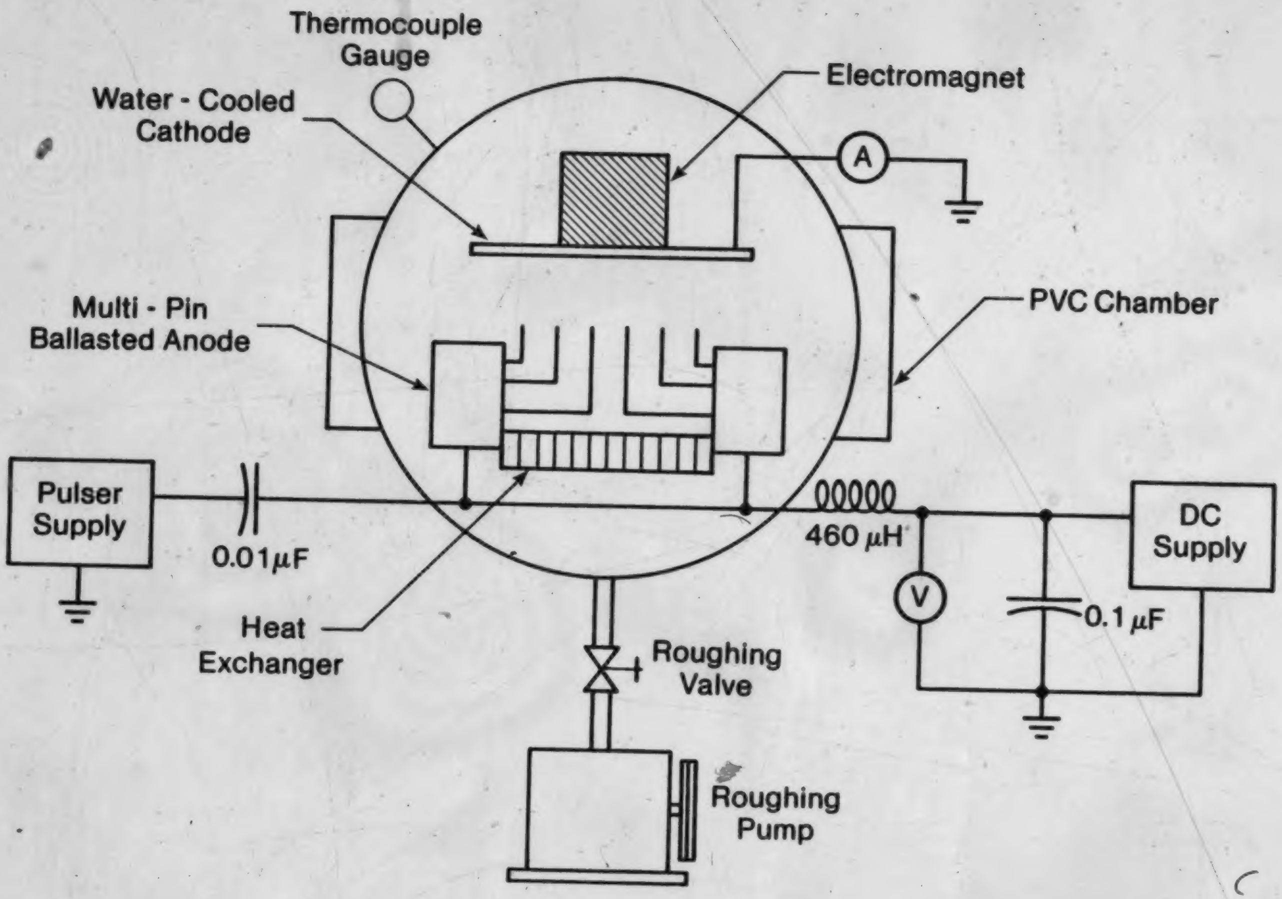
Thermocouple Gauge
Water - Cooled Cathode
Electromagnet
A
Multi - Pin Ballasted Anode
PVC Chamber
Pulser Supply
0.01μF
460 μH
DC Supply
V
0.1 μF
Heat Exchanger
Roughing Valve
Roughing Pump

Fig. 3.1 Experimental MGD Laser Discharge Stabilization Design.

To evacuate the vacuum chamber, a Welch rotary mechanical vacuum pump, with a free air displacement of 500 l/min, was attached to the system. After several hours of pumping, the lowest attainable pressure, with this roughing pump, has only been 2×10^{-3}torr. At this point, the chamber was then back-filled with the appropriate gas mixture. A mechanical diaphragm gauge was then used to measure the partial pressure of each gas species introduced into the vessel.

3.3 ELECTRODE MATERIALS AND DESIGN

To initiate an electric discharge, two metallic electrodes, each at a different potential, are required. Experience has shown that electrode materials and their configuration play an important role in determining the stability and general overall performance of an electric discharge. For a number of years, TEA lasers have relied upon the uniform electric field aspects of their Rogowski profiled electrodes. However, unlike TEA laser systems, the uniform field characteristics of a CW laser does not play a dominant role in discharge stability. Of more importance are the dynamic parameters such as; flow uniformity, boundary layer effects and gas residence time between the electrodes. Consequently, a variety of electrode shapes and materials have been evaluated for each CW laser system. It is common practice, however, that in most realistic devices care be taken to eliminate sharp edges and other prominent surface irregularities. Such imperfections can create high electric field concentrations and promote discharge instabilities.

In an attempt to arrive at an efficient device design, several different electrode materials were examined; most notably aluminum, graphite, steel and copper. In order to facilitate the choice of an optimum material, a survey of each was performed, with respect to its durability, work function (both photoelectric and thermionic) and behavior in a gas discharge.

The first electrode design was constructed from aluminum. After a relatively short period of testing, it was observed that this aluminum electrode performed quite poorly, particularly with respect to its durability when subjected to a glow-to-arc transition. More precisely, it was observed that a high current arc could easily damage the electrode surface by arc pitting. This pitted surface then promoted the formation of hot spots. With further influx of energy these hot spots became potential sites for streamers and subsequently more arcs. The occurrence of this phenomena was most likely due to the high electric fields and correspondingly excessive emission of electrons emanating from sharp edges along the pitted surface. A detailed inspection of the aluminum electrode surface revealed a myriad of tiny scratches, all running in the direction of the rotating plasma. It is most probable that these scratches are the result of a large number of streamers etching a pattern, as they rotated with the plasma. It was clearly apparent from the results of these experiments that an aluminum electrode could not withstand prolonged use in this type of electrical discharge.

A carbon or graphite electrode was then tested because of its proported durability and slightly resistive qualities. It was anticipated that a resistive electrode would assist in spreading the discharge over the electrode surface, thereby resulting in a more uniformly distributed glow. A slight spreading of the discharge was indeed observed but it was only confined to the electrode surface and consequently did little to improve the bulk plasma region.

Several other qualities make graphite favourable as an electrode. For instance, graphite has the ability to withstand very high temperatures; it is available in a variety of composite forms; and is easily machinable. With a suitably shaped graphite electrode, several experiments were performed to determine its durability in an electric discharge. Unfortunately, it was also discovered that an arc or high intensity streamer could easily damage and pit the soft graphite surface. After continued operation, the chamber apparatus became covered with a fine layer of carbon dust, due to sputtered graphite particles. It is believed that the porosity and softness of the graphite material is at fault. Choosing a graphite-metallic composite would probably alleviate this problem.

A steel electrode was then tested and observed to perform moderately well in the high current gas discharge. An examination of this metallic electrode surface revealed scratches similar to those found on the aluminum electrode, though not as deep. However, the use of a steel electrode was not advantageous since its presence could disrupt the magnetic field pattern necessary for discharge stabilization. In order to overcome this difficulty, a non-ferromagnetic stainless steel could be substituted.

Ultimately, copper was finally chosen as the material best suited for electrode fabrication. The copper electrodes were non-ferromagnetic and were less prone to arc damage than aluminum, steel, or carbon. In addition, the thermal conductivity of copper is higher than the other materials, making it ideal for transporting heat from the electrode surface. Table 3.1 lists the various work functions of the electrode materials tested. Upon examination, it is seen that copper has the lowest thermionic work function in addition to a moderate photoelectric work function. These results indicate that copper is a good source and emitter of electrons which are essential to discharge formation. An additional benefit derived from using copper is the variety of shapes and forms that are available, thus permitting the design of several types of electrode structures. In order to confirm the usefulness of MGD as a viable stabilization technique, three types of electrode structures were constructed: transverse, co-axial, and fluid ballasted.

Element	Photoelectric thermionic work function (ev)	
Al	2.98-4.43	-
C	4.81	4.39
Fe	3.91-4.7	4.04-4.77
Cu	4.07-4.8	3.85-4.38

Table 3.1 Work Functions of Tested Electrode Materials [3.2].

3.3.1 Transverse Electrode Structure

Initial experiments in the transverse geometry employed two electrodes constructed from short sections of copper tubing. The tubes were arranged in parallel and connected to water inlet and outlet headers at either end. The 6 mm diameter copper tubes, selected for the electrodes, were equally spaced 6 mm apart to provide 50% transmittivity to a flowing gas. During actual operation, cold tap water flowed through the electrode structure so as to remove excess heat generated by the gas discharge.

Observation of the rotating plasma indicated excessive turbulence at the cathode. It appeared that the copper tubes were creating a large nonuniform boundary layer which severely inhibited plasma flow. This effect was highly noticeable from the ragged appearance and jittering motion of the cathode glow layer. Furthermore, it was probable that a number of stagnant gas cells were also present. These cells eventually coalesced into numerous hot spots as more energy was fed to them. As time progressed, these spots contributed to the formation of streamer instabilities.

The tubular cathode was later replaced with a water cooled copper plate. The smooth plate eliminated turbulence and created an electrode surface over which the cathode glow layer could move unimpeded under the direction of the Lorentz force. This new cathode was constructed from a 6 mm brass plate with a machined groove, 3 mm deep, meandering across the surface. A 3 mm copper plate was then soldered onto the machined brass surface, forming a leak tight water channel. Since the initial installation, the cathode plate structure has provided reliable, trouble-free performance with a minimum of maintenance and care.

Inspection of the gas discharge near the tubular anode indicated only minor turbulence. It would seem that a major difference in behavior exists between the tubular cathode and the tubular anode. There are two probable causes, responsible for such a wide difference. First, due to a reduced Lorentz force at the anode, a much lower gas velocity is produced and, correspondingly, a lower level of turbulence exists. Of more importance though, is the absence of a highly ionized region at the anode. The space-charge layers at the cathode are highly susceptible to a disturbance, more so than one occurring within the diffuse glow near the anode. The primary reason for this is the highly organized nature of the cathode fall region and its importance in maintaining the overall structure of the glow discharge.

To further assist the maintenance of a stable glow discharge, the copper tubes of the anode were bent into a Rogowski profile. It was later discovered that this profile also assisted the recirculation of gas through the anode. To minimize any disturbance to the transverse flow, the electrodes were separated by thin, adjustable ceramic posts. These and other details of the overall assembly of the transverse electrode structure can be seen in Figs. 3.2 and 3.3.

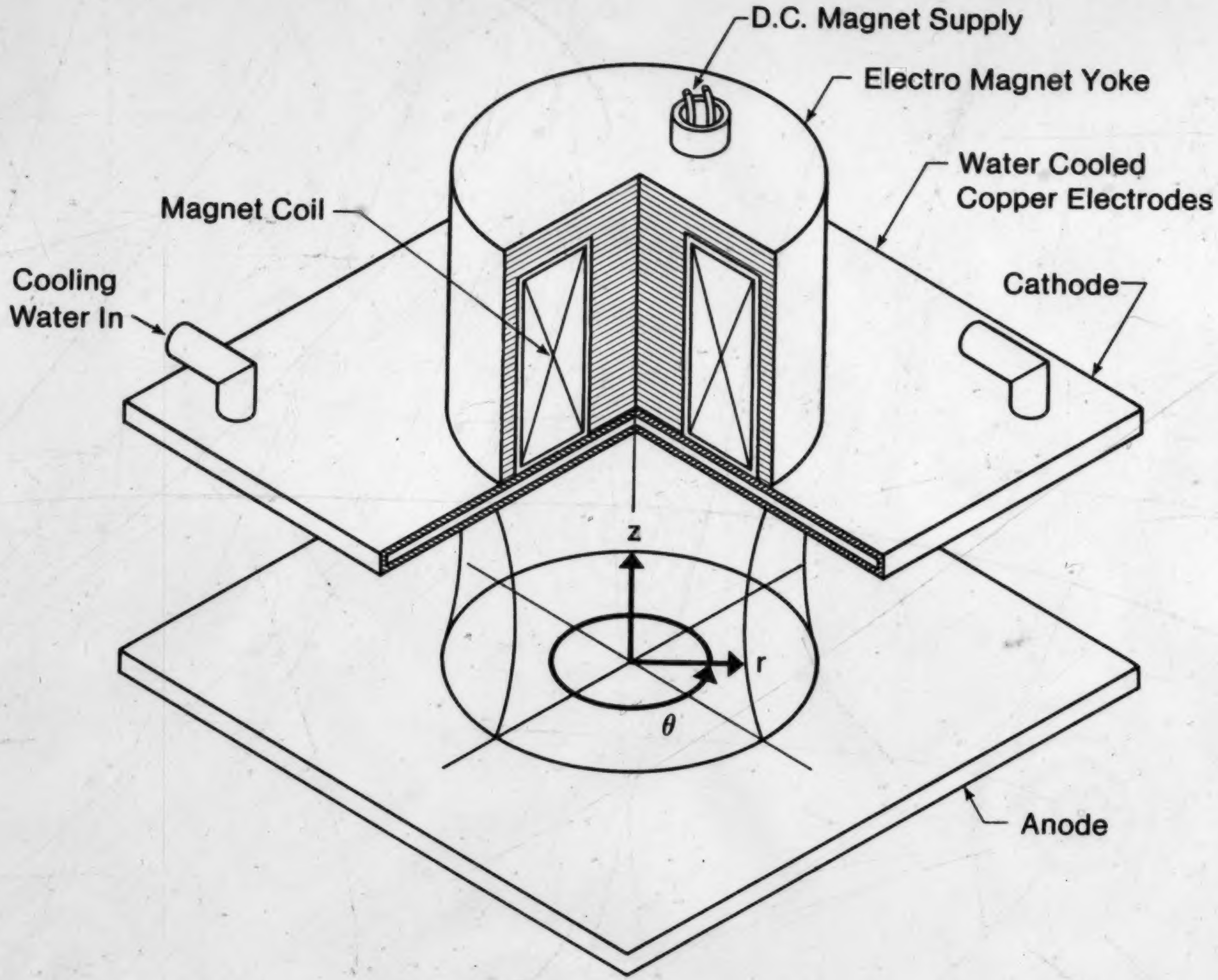
D.C. Magnet Supply
Electro Magnet Yoke
Water Cooled
Copper Electrodes
Magnet Coil
Cooling
Water In
Cathode
z
r
θ
Anode

Fig. 3.2 Magnetically Stabilized Transverse Discharge Geometry.

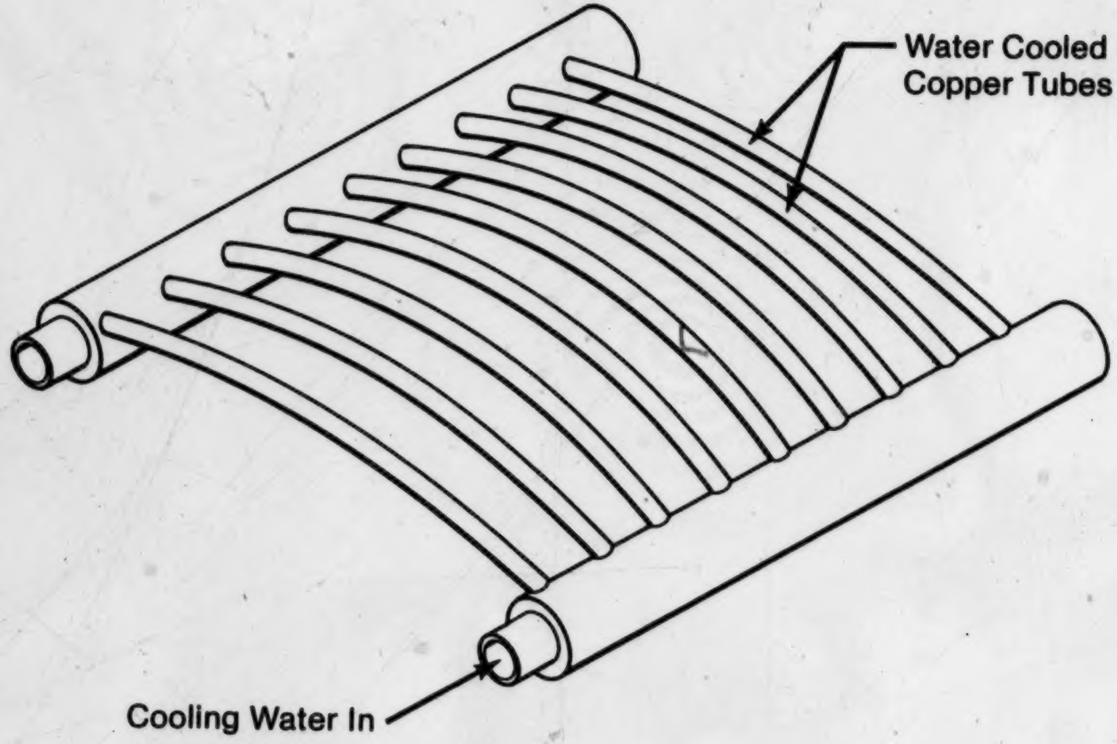
Water Cooled
Copper Tubes
Cooling Water In

Fig. 3.3 Flow Through Tubular Anode Structure.

3.3.2 Coaxial Electrode Structure

Following the successful example of the transverse electrode geometry, a coaxial structure was then investigated. As in the previous geometry, the electrodes were made of copper. The cathode consisted of a 9 cm diameter pipe with a spiral groove machined into the outer surface. Another slightly larger diameter thin-walled pipe was placed over the inner pipe, thereby leaving a spiral water channel in the middle. The ends were soldered together and provided with Swagelock fittings to supply the cooling water.

The anode was comprised simply of a 1.25 cm diameter copper pipe equipped with Swagelock fittings on either end. To vary the electrode gap, larger diameter pipes were used as the anode. Each anode was supported in the center of the cathode by an insulating frame. The complete coaxial electrode structure was then mounted inside a solenoid as illustrated in Fig. 3.4.

This electrode structure performed extremely well and had no major difficulties. Turbulence within the rapidly rotating discharge was not observed, due to the presence of smooth electrode walls. In addition, electrode edge instabilities did not present a problem, as the magnetic field kept the plasma confined to the central portion of the electrodes.

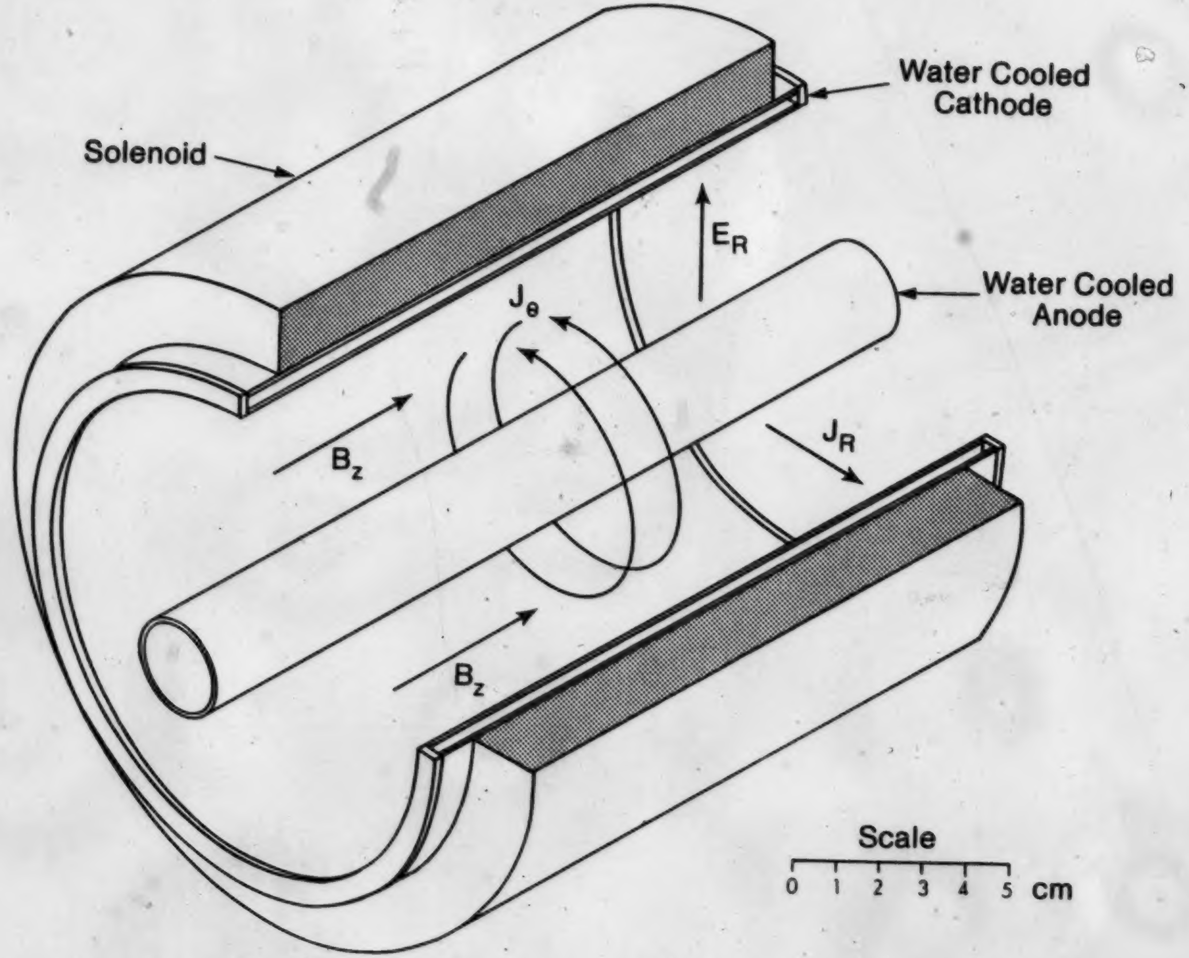
Water Cooled Cathode
Solenoid
E_R
Water Cooled Anode
J_θ
B_z
J_R
B_z
Scale
0 1 2 3 4 5 cm

Fig. 3.4 Magnetically Stabilized Coaxial Discharge Geometry.

3.3.3 Multi-pin, Ballasted Anode

The previous two electrode designs were only partially successful in their attempt to create an extended area uniform plasma distribution. It was determined, through the use of high speed photography, that only a rapidly rotating plasma column was created. The film revealed that the rotating plasma column was simply running across the continuously conducting anode surface.

As a result of the difficulty encountered with the continuous surface anode, a new electrode structure, based on the multi-pin concept [3.3], was constructed. Now, instead of a continuous plate or tubular surface, the new anode was constructed such that the overall surface was subdivided into an array of independent sub-electrodes, each with its own current limiting feature. This was accomplished by employing an internal electrolytic solution to balance the current fed to each sub-electrode pin. In this manner, a small electric discharge was created at each pin, thereby spreading the applied current over the entire pin array. Early attempts, by others, to create a uniform current distribution used discrete resistors as the ballasting components. However, these components were often prone to overheating and failure.

The initial multi-pin electode concept is displayed in Fig. 3.5. This structure employs the use of an array of bent stainless steel pins mounted such that one end was submerged into a channel containing the recirculating electrolytic fluid. The sub-electrode pins were bent at right angles to allow cool gas to flow through the anode and replace gas lost by the centrifugal pumping action of the rotating gas

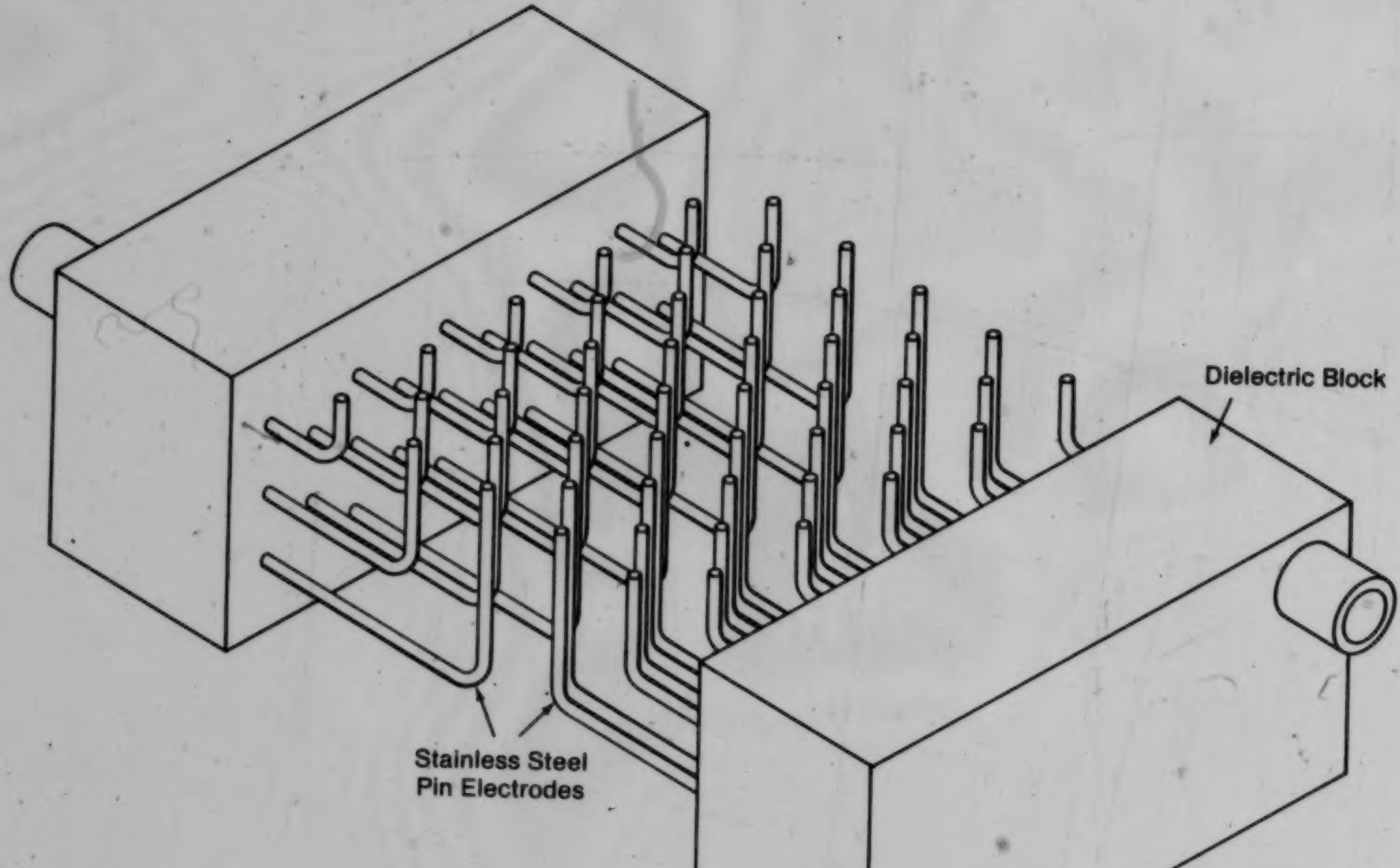
Dielectric Block
Stainless Steel
Pin Electrodes
Recirculating Electrolytic Fluid

Fig. 3.5 Fluid Ballasted Multi-Element Flow Through Anode Structure.

discharge. Furthermore, the long bent pins prevented damage to the electrode structure by the hot ionized gas.

As discussed in [3.3], the electrolytic fluid best suited for prolonged use within a current ballasted electrode consists of K_2CO_3 dissolved in distilled water. As a solvent, distilled water is free of chemical and mineral contaminants often found in ordinary tap water. Potassium carbonate was advocated as a solute because it does not produce an excessive amount of gas, nor is it strongly corrosive towards metals. In addition, the solution resistivity is easily controlled and is nearly linear when conducting a large current. With the proper solute concentration, the electrolytic solution will create a uniform current distribution without the need for external ballast. Thus, the total power lost in the system can be minimized. Optimal performance was achieved with an electrolyte concentration of 0.5 g/l. At this concentration, the VI characteristics of the electrode is shown by Fig. 3.6.

Due to the large amount of current that can be passed through the system, a significant temperature gradient can exist within the electrode structure. It has been determined that the resistivity of the electrolytic solution decreases almost linearly with increasing fluid temperature. This can be explained by the fact that the dissolved electrolyte is more readily dissociated at a higher temperature, and thus creates a higher charge carrier density. To maintain a constant temperature throughout the electrode, a high speed pump is used to recirculate the fluid through a heat exchanger. This process removes excess heat and in addition forces gas bubbles, generated by

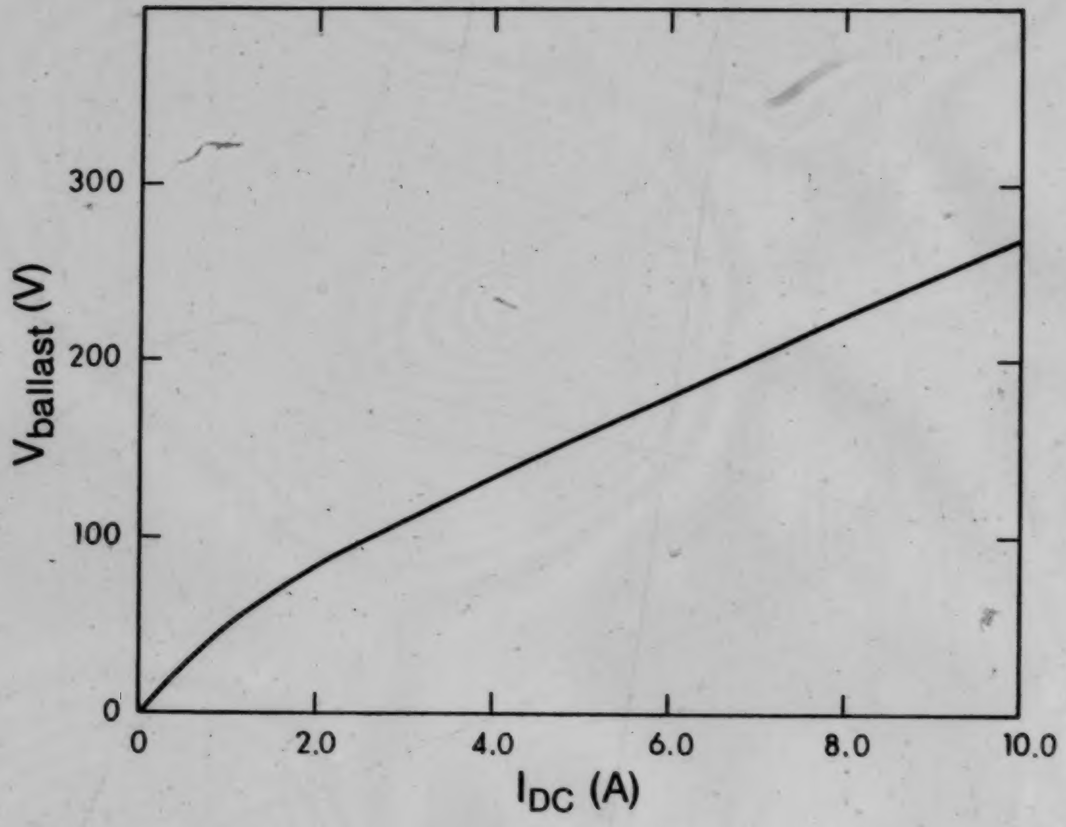

Fig. 3.6 VI Characteristics of the Electrolyte Ballast Solution.

electrolysis, out of the system. As a result of this action, the electrolytic solution provides both cooling and current distribution to each element constituting the anode.

As discussed earlier, the sub-electrode pin material was of primary importance in determining the performance of the gas discharge. Past experience with gas discharge electrodes has shown that copper and stainless steel worked best. However, with the multi-pin concept there are additional constraints to be considered. Since the pin material had to be in contact with the electrolytic solution, some corrosion was to be expected. It was discovered that corrosion by the electrolytic solution formed a prominent oxide layer on the copper pins. As the oxide layer formed, it began to inhibit the current flow to the pins. It was determined by Nam [3.3], that stainless steel pins had little or no oxide film on their surfaces exposed to the electrolyte solution. In addition, stainless steel had a very low corrosion rate. This could be determined by passing a specified current through the pin and measuring the weight lost over a period of time. These results suggested that stainless steel was ideal for a multi-pin electrode, which guaranteed good performance and a longer lifetime over other metallic pins.

The current carried, through the electrolytic solution, between the busbar and the sub-electrode pin can be expressed by Ohm's law

$$I_w = (E_t - E_d)\,\frac{A_w \sigma_w}{d_w} \tag{3.3}$$

where E_t is the terminal voltage between the busbar and the pin, E_d is the electrochemical decomposition potential of the electrolytic solution and σ_w is the fluid conductivity. From this equation, it can be concluded that the current is also controlled by the water contacting surface area of the pins, A_w,as well as the gap spacing, d_w between the busbar and the pins.

With this knowledge, the multi-pin electrode can be resistively profiled by selectively adjusting the differential gap spacing, d_w over parts of the pin array. This simple technique was used to increase the effective sub-electrode resistance near the electrode extremities. Consequently, this process was very effective in removing the tendency for a glow-to-arc transition to occur along the electrode's edges.

Perhaps the best feature of the multi-pin ballasted anode design is its ability to suppress the formation of arcs and streamers. Should one electrode pin begin to conduct more current than its surrounding neighbors, additional gas bubbles, generated by this accelerated electrolysis action, momentarily surrounds the pin. These gas bubbles reduce the effective water contacting area, causing a decrease in fluid conductivity. This naturally reduces the current density carried to the pin, the arc is suppressed and equilibrium is restored.

Another useful characteristic of this electrode design is its tendency for self-optimization. After final assembly, each pin experiences slightly different operating conditions due to non-uniformities of construction and slight differences in pin length which can alter the values of d_w and A_w. As a consequence, some pins initially conduct more current than others. This causes increased electrolysis and selectively accelerates pin corrosion. After a period of time, the individual electrode gap lengths are adjusted so that each pin carries an equal amount of current.

3.4 ELECTROMAGNET DESIGN

An integral part of MGD discharge stabilization is the design of a proper magnetic field. Such a field is essential in producing the Lorentz driving force and the magnetic bottle used for containment.

Various magnet designs were analyzed and tested by using a two dimensional iterative computer program called POTENT, which was developed at Culham laboratory [3.4]. Inputs to the POTENT program included the specific overall dimensions of the magnets, iron core permeabilities, coil current densities and boundary conditions. The use of this program enabled a detailed evaluation of magnetic field and flux density components which were illustrated and plotted. Various parameters could easily be altered and the results quickly viewed on a CRT screen.

3.4.1 Cylindrical Magnet

To satisfy the necessary field requirements in the planar electrode geometry, a cylindrical re-entrant electromagnet was chosen as the most promising design. A cross sectional view showing the magnetic core and the resulting flux lines is reproduced in Fig. 3.7. Axial symmetry has been assumed so that the magnetic flux density is independent of θ. As illustrated in Fig. 3.8, the contours of magnetic field intensity reveal a significant non-linearity in field strength. This change in intensity creates the strong shear forces that are set up between the electrodes.

The magnet core was constructed of mild steel, anodized to create an insulating layer on the surface. The magnetic field was

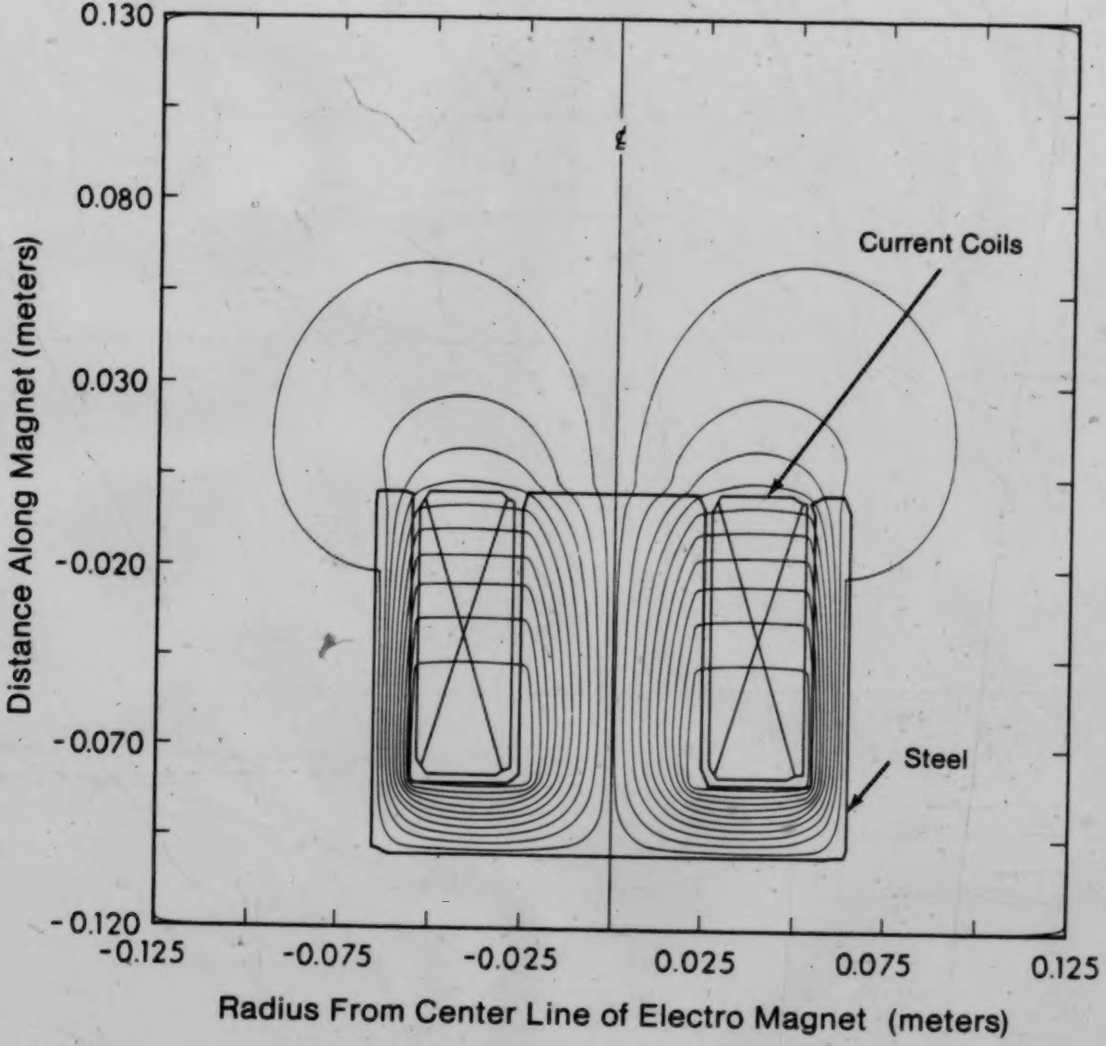

Fig. 3.7 Magnetic Flux Density of a Re-entrant Electromagnet.

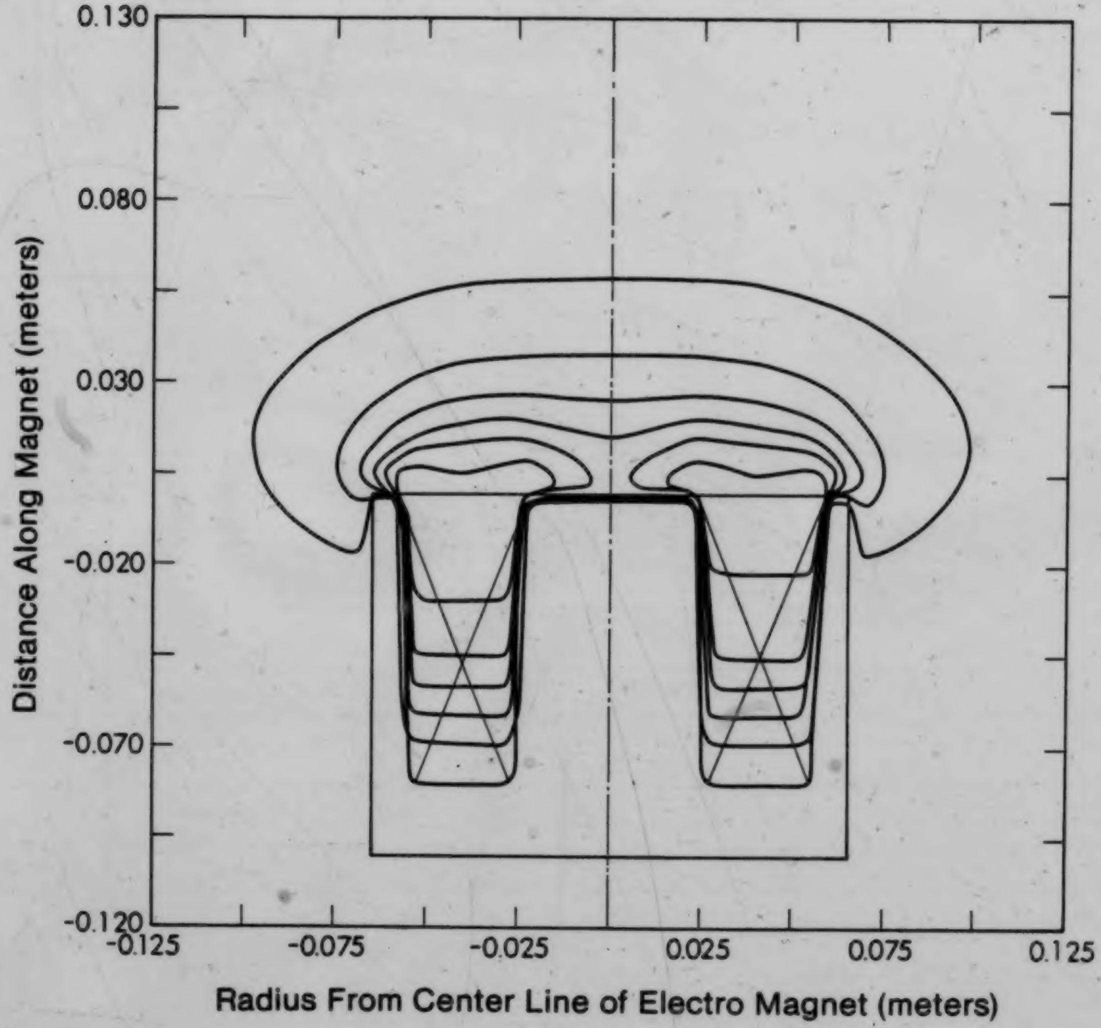

Fig. 3.8 Magnetic Field Intensity Contours of a Re-entrant Electromagnet.

created by passing a current of 10 A through 3400 turns of number 18 gauge magnet wire. However, in order to maintain this high current density within the winding, small gaps were built into the coil to facilitate the flow of water or oil. By water-cooling the magnet, the effective amp-turns could be increased and the excess heat generated could be easily removed. These considerations enabled the magnet to yield a flux density exceeding 0.2 T. The entire interior assembly was then sealed to allow the magnet to work within the discharge chamber.

The computer program POTENT can also be used to determine the magnitude of the two magnetic field components B_r and B_z . In this geometry, the current density vector points in the z-direction. The addition of a radial magnetic field B_r creates a θ-directed $\vec{J}_z \times \vec{B}_r$ force exerted on all charged particles. The axial magnetic field B_z is used in connection with the Hall current J_θ to produce a radial force wich tends to force the gas discharge into an annular region. This Lorentz force sets up a pressure potential well that acts as a confinement bottle to prevent the discharge from blowing apart. For maximum effect, the electromagnet was placed directly behind the cathode plate to allow the strongest magnetic field to permeate the most active zones of the gas discharge.

3.4.2 Coaxial Magnet

To test the radial discharge geometry, a short solenoidal magnet was chosen to provide the proper field configuration. As displayed in Fig. 3.9, the solenoid was short enough to produce both radial (B_r) and axial (B_z) field components. As expected, the contours of magnetic field intensity were symmetrical due to the imposed θ-symmetry of the computer program. The results are clearly seen in Fig. 3.10.

The coaxial magnetic field was created by passing a current of 5 A through 6500 turns of number 20 gauge magnet wire. The magnetic field within the solenoid was enhanced approximately 45% by the introduction of a 1 cm thick steel shell. The additional steel intensified the magnetic flux, in the center, by redirecting flux lines towards a path of least reluctance. The bending of these flux lines can be seen in the computer plot of the solenoidal magnetic field profile (Fig. 3.9).

In this discharge configuration, the axial magnetic field B_z in combination with the radial current J_r creates a Lorentz force $\vec{J}_r \times \vec{B}_z$, which causes plasma rotation in the negative θ direction. At the magnet edges, the radial field component is most prominent due to the presence of fringing fields. This field component B_r, interacting with the Hall current J_θ, produces a Lorentz force $\vec{J}_\theta \times \vec{B}_r$, which serves to confine the discharge axially to the central portion of the electrodes.

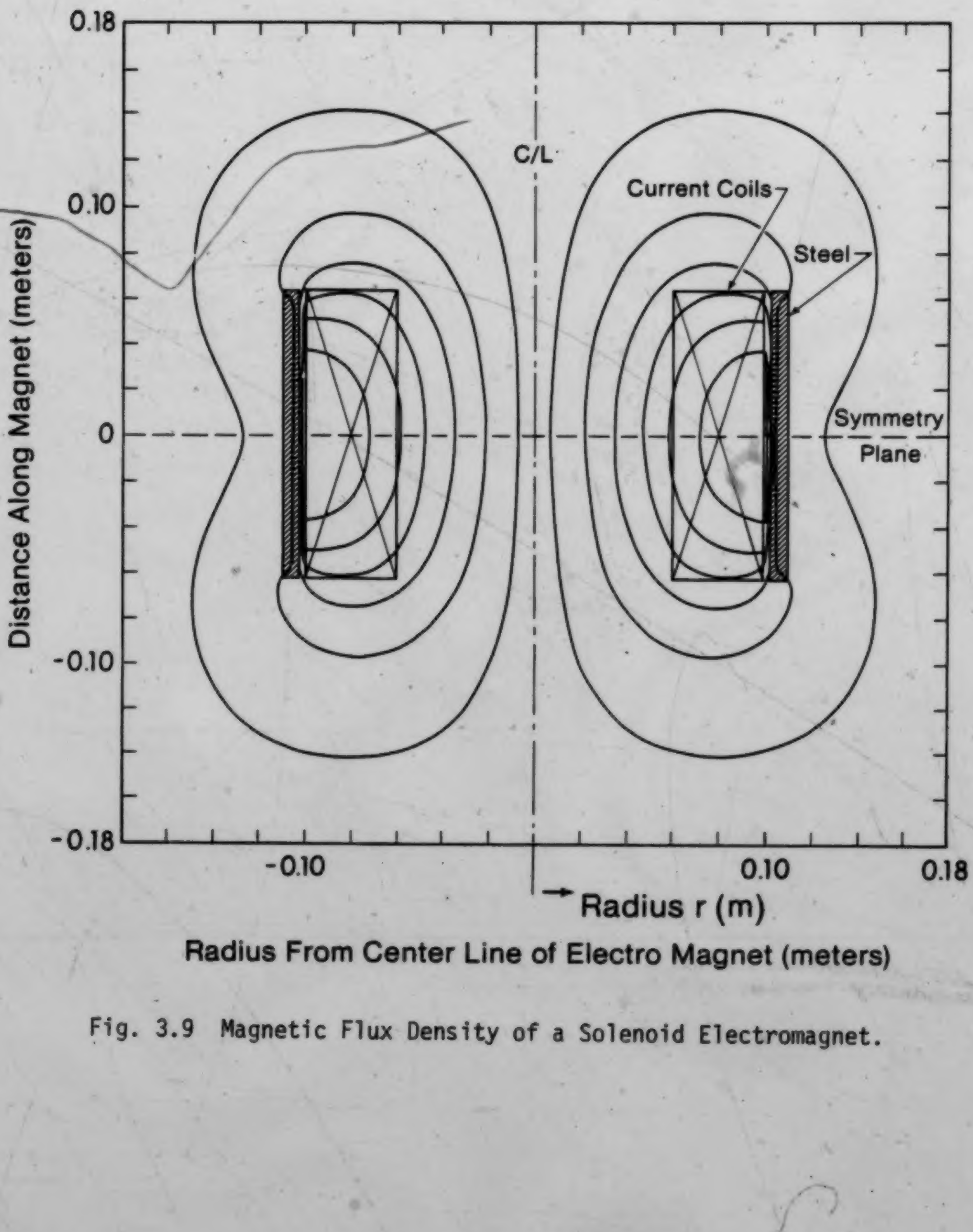

Fig. 3.9 Magnetic Flux Density of a Solenoid Electromagnet.

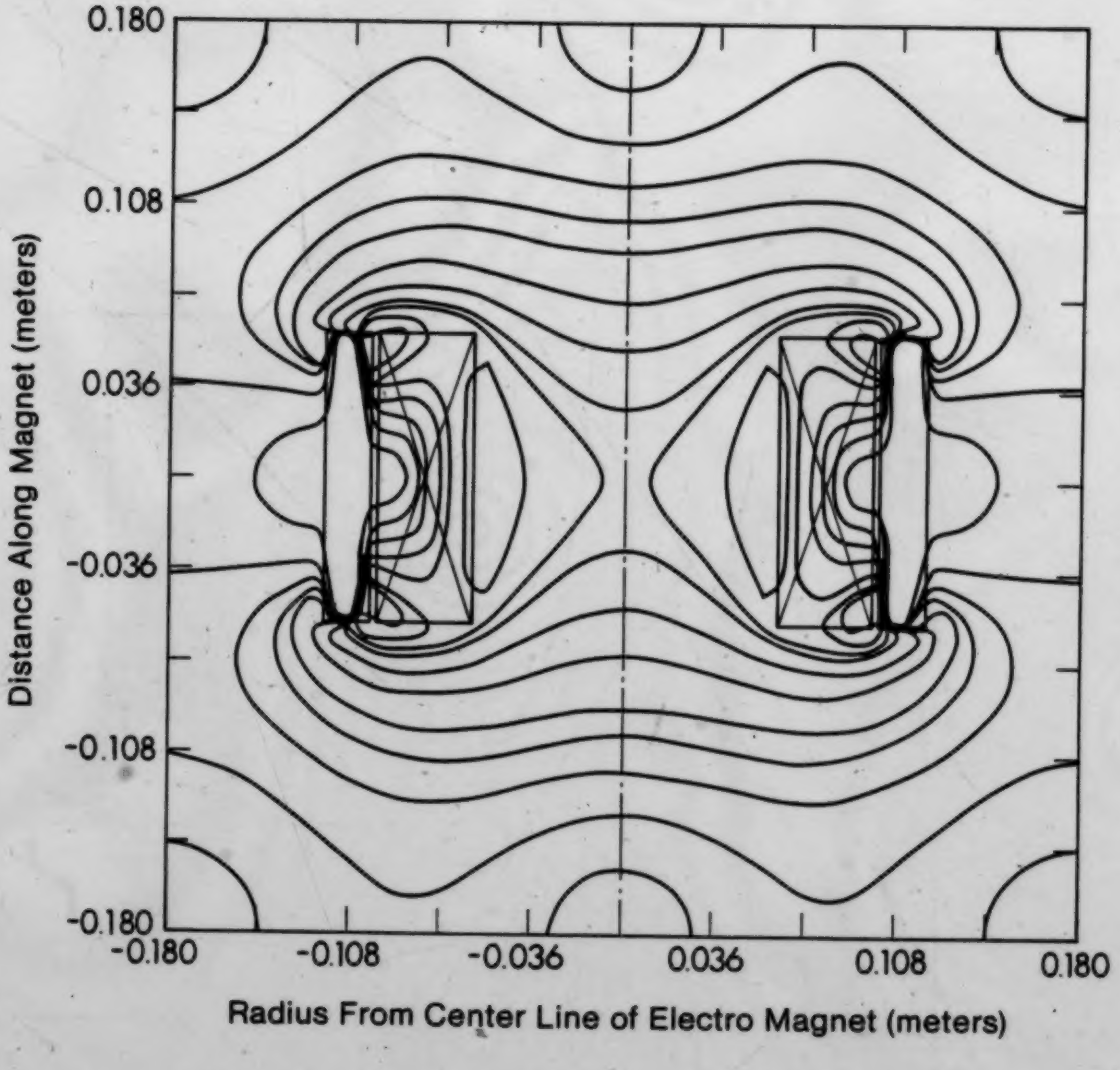

Fig. 3.10 Magnetic Field Intensity Contours of a Solenoid Electromagnet.

3.5 THYRATRON PULSER

It has been demonstrated [1.5-1.9] that gas discharge stability can be improved by any technique which externally controls the electron density. This procedure allows the ionization mechanism to be decoupled from the gas discharge current transport process. In an attempt to control and supply the electron density necessary for this experimental setup, a high power pulse generator was developed. While the pulser was in operation, a uniform preionized glow discharge was established containing an estimated electron density of 10^8 electrons/cm^3.

The primary element employed for the repetitive high voltage switching, necessary in the pulser system, was a hydrogen filled ceramic HY-1802 thyratron. A thyratron was chosen over several other devices because of its reliable high speed switching action and lower production of electrical noise. In addition, hydrogen thyratrons have a very short recovery or deionization time. In this context, t_d is the time interval from the end of the thyratron firing until the grid has regained control for the next trigger pulse. For this reason, hydrogen thyratrons are well suited for high frequency applications.

As a result of hydrogen's low molecular mass, the singly charged ion, accelerated within the thyratron, cannot gain sufficient kinetic energy to inflict significant damage to the cathode. Consequently, the hydrogen thyratron can be driven much harder and will therefore be able to handle higher voltages and currents as compared with other devices.

In order to activate the thyratron, or start conduction, it is first necessary to draw current between the grid and the cathode. This current is initiated by the application of a positive voltage trigger pulse to the grid. Following the trigger pulse, ions and electrons are produced within the grid-cathode region of the thyratron. As soon as a sufficient electron density is established, the anode field is able to produce ionization in the grid-anode region. This excessive ionization causes an avalanche breakdown to occur between the cathode and the anode. The breakdown coalesces into an arc and the thyratron is fired.

The pulse generating circuitry, as displayed in Fig. 3.11, consists of a high efficiency resonant charging curcuit. When the thyratron is non-conducting (between trigger pulses) the impulse storage capacitor C_1 is charged via the charging inductor L_1 and diode D. The holdoff diode is used to prevent any reverse current flow. After the thyratron fires, the energy stored in capacitor C_1 is transferred to the anode through the coupling capacitor C_2 .

The average current transferred to the anode by the pulser can be determined from the approximate expression given by [3.5, 3.6],

$$I \approx VC_t f_r \ .$$

In this equation, V is the capacitor charging voltage, C_t is the total circuit capacitance and f_r is the pulse repetition rate. For an applied voltage of 5 kV operating at 500 Hz, the average current is typically 50 mA.

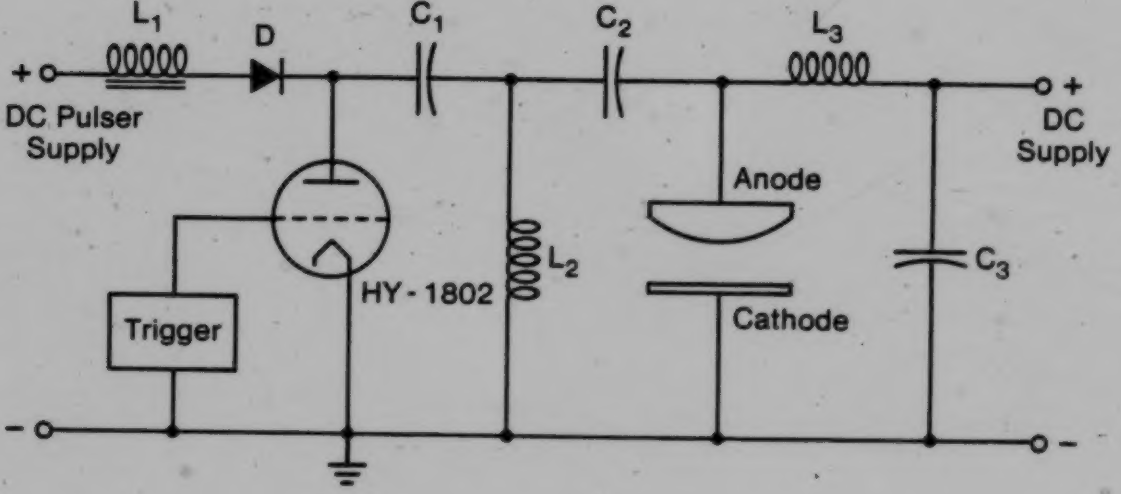

L_1
D
C_1
C_2
L_3
+
DC Pulser Supply
+
DC Supply
Anode
L_2
C_3
HY - 1802
Trigger
Cathode
-
-

HY - 1802, Hydrogen filled ceramic thyratron

L_1, Charging inductor = 13.2 H

D, Charging diode, 20 kV P.I.V.

C_1, Impulse storage capacitor = 1 nF

C_2, Coupling capacitor = 0.01 μF

L_2, Bypass recharge inductor = 375 μH

L_3, Isolation inductor = 460 μH

C_3, Isolation capacitor = 0.1 μF

Fig. 3.11 Hydrogen Thyratron Pulse Generating Circuit.

3.6 DC POWER SUPPLY

The complete power supply circuitry is shown in Fig. 3.12. From this illustration, it is seen that power was drawn from the mains and fed into a 3 phase motor controlled variac. In this manner, the stepping motor would adjust the amount of power to be sent to a 3 phase 50 kVA transformer. The 60 Hz signal was then rectified by a high current diode bridge and filtered by a 375 μF capacitor to remove the remaining AC ripple. This setup produced a maximum current of 25 A that could be fed to the gas discharge.

Since the gas discharge was well-behaved and operated in the normal glow region, less current limiting resistance was required. When operating the system, using the current ballasted anode, no external ballast resistance was necessary. As previously shown in Fig. 3.6, the total fluid resistance was only slightly more than 25 Ω. This was fortunate since more energy could be deposited into the gas discharge resulting in a more efficient device.

To isolate the pulser signal from the DC supply and voltmeter, a 460 μH inductor was placed in the main line. Any pulser signals penetrating the inductor were simply shunted to ground via a 0.1 μF high voltage capacitor placed near the experiment. High voltage coaxial cables, with the outer sheath conductor grounded, were used throughout the system. This was necessary in order to prevent the wires from radiating like antennae during the operation of the pulser.

The IV characteristics of the gas discharge were continually monitored by two analog meters. In order to maintain a solid ground connection, a high current 2.5 mΩ shunt was utilized instead of passing

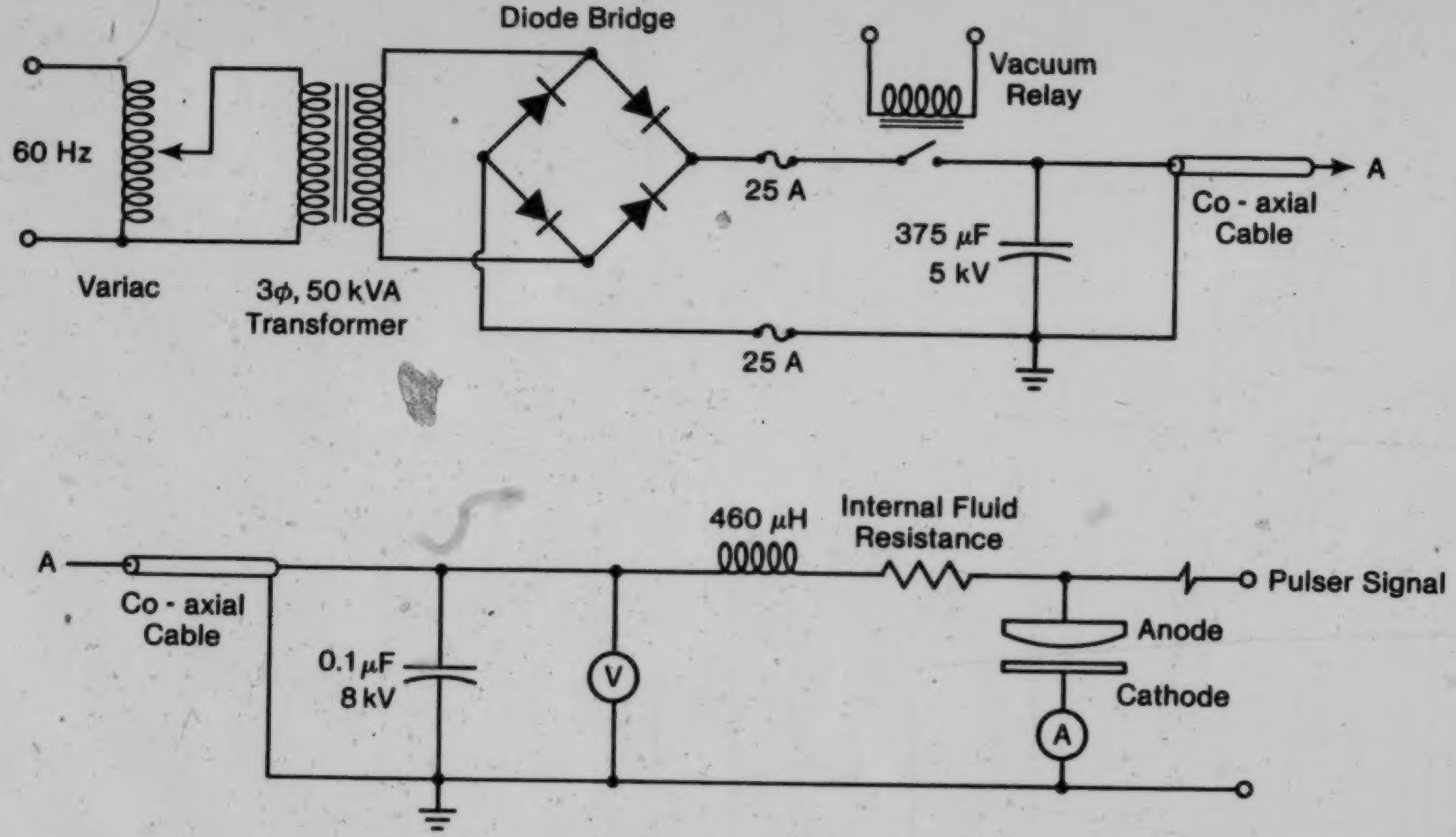
Diode Bridge
Vacuum
Relay
60 Hz
25 A
375 μF
5 kV
Co - axial
Cable
A
Variac
3φ, 50 kVA
Transformer
25 A
A
Co - axial
Cable
460 μH
Internal Fluid
Resistance
Pulser Signal
0.1 μF
8 kV
V
Anode
Cathode
A

Fig. 3.12 Schematic of the DC Sustainer Circuit.

the current directly through an ammeter. This procedure eliminated excessive line inductance which would impede the conduction of the pulser signal to ground. A voltmeter was connected directly across the incoming power line and ground. This resulted in a measurement of the voltage drop across the internal ballast fluid plus the drop across the gas discharge impedance. Thus, it was necessary to make a separate IV measurement of the fluid ballasted anode. Subtraction of these two curves yielded the true IV characteristics of the gas discharge.

An arc is characterized by a very low impedance and consequently draws a large amount of current. Thus, to provide protection for circuit components in the event of a glow-to-arc transition, a vacuum relay was installed, so that the operator could instantaneously break the DC circuit. In addition, to prevent damage to the power supply and diode bridge, several 25 A fuses were connected in series with each line. Utilizing these precautions, greatly reduced the potential damage that could be caused by an arc.

CHAPTER 4

MGD MODEL OF A GLOW DISCHARGE

4.1 INTRODUCTION

In order to properly simulate the time dependent behavior of a rotating glow discharge, it was necessary to construct a consistent set of equations. The theoretical and numerical analysis used to predict the expected flow pattern and gas discharge position was based upon the compressible MGD equations. However, a complete description of this laser discharge system must also include: an electrical conductivity which exhibits strong spatial dependence, spatially varying electric and magnetic fields, and the presence of significant radial and axial secondary flows. Furthermore, a typical glow discharge contains ionized and neutral particles, each following a complicated trajectory that is influenced by a variety of forces. To simplify the analysis of such a problem, a macroscopic fluid model is used to describe the average behavior of a collection of particles in lieu of an individual particle.

A macroscopic theory can be applied to the analysis of ordinary gases, provided the mean free path is small compared with any natural length over which the gas properties may significantly change. One further criterion required for the validity of this theory is that the mean collision time be short compared with any relevant variation in the fluid.

For a typical glow discharge, molecular collisions will prevent any molecule from straying too far from its neighbours. Thus, the finite fluid element is provided with a collective identity in terms of the specific molecules it contains. In addition, molecular collisions produce a distribution that is locally Maxwellian and can therefore be described in terms of a local thermodynamic state.

In this fluid approximation, the partially ionized gas is assumed to be composed of three interpenetrating fluids: a positively charged ion fluid, a negatively charged electron fluid, and a neutral particle fluid. The neutral fluid will only interact with the charged particles through collisions. The ion and electron fluids, however, can also interact as a result of self-generated electric and magnetic fields.

To reduce the complexity of the problem, the three separate fluids will be combined into a single fluid. The MGD equations generated from this less detailed approach will be later implemented into the computer program MAGIC.

4.2 SINGLE FLUID MGD EQUATIONS

The behavior of a flowing ionized gas can be described by a system of conservative MGD equations written for each individual gas species. These conservative equations reveal the manner in which the average properties of the flowing gas are conserved by the particles during a collision or transport process. The conservation of mass equation and the momentum conservation equation for each gas species can be obtained from the velocity moments of the Boltzmann equation. As shown in Tanenbaum [4.1], the mass conservation law may be expressed as

$$\frac{\partial \rho_s}{\partial t} + \vec{\nabla}\cdot(\rho_s\vec{v}) = \left(\frac{\partial \rho_s}{\partial t}\right)_c . \tag{4.1}$$

The global conservation of mass can be attained by summing Eqn. 4.1 over all species. The overall density becomes $\rho = \sum\limits_s \rho_s$, and the mass averaged velocity is $\rho\vec{v} = \sum\limits_s \rho_s v_s$. Thus, the global conservation of mass or equation of continuity becomes

$$\frac{\partial \rho}{\partial t} + \vec{\nabla}\cdot(\rho\vec{v}) = 0 . \tag{4.2}$$

The collision term $\sum\limits_s \left(\frac{\partial \rho_s}{\partial t}\right)_c = 0$ since mass is conserved in collisions involving chemical reactions.

The term $\rho\vec{v}$, in the continuity equation, expresses the rate of flow (mass/unit area) of the ionized gas. If the divergence of this term is positive, the gas is expanding; and if the divergence is negative, the gas is being compressed. Since a glow discharge is primarily composed of neutral particles, little change in overall mass density is expected. However, a significant change in the mass density profiles of the charged particles is anticipated.

The conservation of momentum equation for charged particles can be written as

$$\frac{\partial}{\partial t}(\rho_s\vec{v}_s) + \vec{\nabla}\cdot(\rho_s\vec{v}_s\vec{v}_s) + \vec{\nabla}\cdot\hat{\Pi}_s = \vec{P}_s + n_e e Z_s(\vec{E}+\vec{v}_s\times\vec{B}) . \tag{4.3}$$

Similarly, the conservation of momentum equation for neutral particles is given by

$$\frac{\partial}{\partial t}(\rho_n\vec{v}_n) + \vec{\nabla}\cdot(\rho_n\vec{v}_n\vec{v}_n) + \vec{\nabla}\cdot\hat{\Pi}_n = \vec{P}_n . \tag{4.4}$$

The term $\hat{\Pi}_s$ represents the partial pressure tensor of the s species. In these momentum equations, the collision term is expressed in the form

$$\vec{P}_r = \sum_s \frac{n_r m_r m_s}{m_r + m_s} \nu^*_{rs} (\vec{V}_s - \vec{V}_r) \ , \tag{4.5}$$

where $\vec{P}_r$ is the species momentum transfer between r and s particles. The variable ν^*_{rs} is known as the average collision frequency for momentum-exchange between r and s particles, and is written as

$$\nu^*_{rs} = \frac{n_s (m_r + m_s) kT}{n m_r m_s D_{rs}} \ . \tag{4.6}$$

The variable D_{rs} represents the mutual diffusion coefficient between r and s particles. Lastly, the variable $\vec{V}_s$ is defined as the diffusion or drift velocity with respect to the mass average velocity, that is,

$$\vec{V}_s = \vec{v}_s - \vec{v} \ . \tag{4.7}$$

The last term in Eqn. 4.3 represents the driving force which sets the ionized particles into motion. The expression

$$\vec{F}_s = eZ_s (\vec{E} + \vec{v}_s \times \vec{B}) \tag{4.8}$$

is more commonly referred to as the Lorentz force.

The overall momentum equation is obtained by summation over all species. The term $\sum_s \vec{P}_s = 0$, since momentum is conserved during each collision. Thus, the sum of Eqns. 4.3 and 4.4 result in the formulation

$$\frac{\partial}{\partial t} \sum_s (\rho_s \vec{v}_s) + \vec{\nabla} \cdot (\sum_s \rho_s \vec{v}_s \vec{v}_s) + \vec{\nabla} \cdot (\sum_s \hat{\Pi}_s) = \vec{E} \sum_s n_s e Z_s + \sum_s n_e e Z_s \vec{v}_s \times \vec{B} \ . \tag{4.9}$$

The first term on the right hand side contains the net charge density, given by

$$\rho_e = \sum_s n_s e Z_s \ .$$

Since a normal glow discharge is primarily composed of an electrically neutral positive column, $\rho_e = 0$. This assumption is not valid within the charged particle sheaths located in the cathode fall layer. The complete analysis of the cathode fall region requires the use of a particle code and is presently beyond the scope of this thesis.

The second term on the right hand side of Eqn. 4.9, contains the total electric current density which is written as

$$\vec{J} = \sum_s n_e e Z_s \vec{v}_s \ . \tag{4.10}$$

The total current density can be separated into a conduction current and a convection current by Eqn. 4.7. That is,

$$\vec{J} = \sum_s n_s e Z_s \vec{V}_s + \vec{v} \sum_s n_s e Z_s = \vec{j} + \vec{v}\rho_e \ . \tag{4.11}$$

As determined earlier, $\rho_e \approx 0$ within the positive column. Thus, the total current density is predominantly due to the conduction current.

Using the expression for the mass averaged velocity, Eqn. 4.9 can be simplified into the form

$$\frac{\partial}{\partial t}(\rho\vec{v}) + \vec{\nabla}\cdot(\rho\vec{v}\vec{v}) + \vec{\nabla}\cdot\hat{\Pi} = \vec{J}\times\vec{B} \ . \tag{4.12}$$

To account for the transport of momentum and energy through the gas by the diffusion of particles, the total pressure tensor $\hat{\Pi}$ is written in terms of a viscous stress tensor $\hat{\tau}$ and the hydrostatic pressure p,

$$\hat{\Pi} = \hat{\tau} + p\hat{I} \tag{4.13}$$

where $\hat{I}$ is the unit tensor. The viscous stress tensor is created as a result of internal friction produced when different fluid elements move past one another at different velocities. According to Landau and Lifshitz [4.3], $\hat{\tau}$ may be represented in subscript notation as,

$$\tau_{ij} = -\mu\left(\frac{\partial v_i}{\partial x_j} + \frac{\partial v_j}{\partial x_i}\right) + \left(\frac{2}{3}\mu - \zeta\right)\delta_{ij}\frac{\partial v_k}{\partial x_k} \tag{4.14}$$

where μ and ζ are the shear and bulk viscosity coefficients. In vector notation this equation becomes

$$\hat{\tau} = -\mu\left\{\vec{\nabla}\vec{v} + (\vec{\nabla}\vec{v})^T\right\} + \left(\frac{2}{3}\mu - \zeta\right)(\vec{\nabla}\cdot\vec{v})\hat{I} \tag{4.15}$$

where $(\vec{\nabla}\vec{v})^T$ is the transpose of the dyadic $\vec{\nabla}\vec{v}$.

To close the system of equations, the thermodynamic equation of state is applied. This equation relates the pressure p to the mass density ρ. Since a glow discharge can be treated as an ideal gas, the equation of state has the form

$$p = C\rho^{\gamma} \tag{4.16}$$

where C is a constant and γ is the ratio of the specific heats, $\gamma = C_p/C_v$.

To simplify the problem, each species within the gas discharge is assumed to have a constant temperature. In this isothermal case, $\gamma = 1$, and the overall gas pressure is simply the sum of the individual partial gas pressures. Consequently,

$$p = \sum_s n_s kT_s$$

where k is the Boltzmann constant. Since the degree of ionization is approximately 10^{-7}, $n_e \ll n_n$ and the total hydrostatic pressure is primarily due to the neutral gas molecules. As a result,

$$p = n_n k T_n \tag{4.17}$$

where T_n is the translational temperature of the neutral gas.

4.3 CURRENT DENSITY DISTRIBUTION

For a partially ionized gas, Sutton [4.2] derived an expression for the generalized Ohm's law in terms of the applied electric and magnetic fields and possible electron pressure gradients. This equation can be written as,

$$\vec{J} = \sigma_{11}\left\{\vec{E}^{\star} + \frac{\vec{\nabla}p_e}{n_e e} - \frac{\vec{J}\times\vec{B}}{n_e e} - \frac{f^2\tau_{in}^{\star}}{m_i n_e}\left[(2-\alpha)\vec{\nabla}p_e \times \vec{B} + \vec{B}\times(\vec{J}\times\vec{B})\right]\right\} \tag{4.18}$$

where

$$\sigma_{11} = \frac{n_e e^2}{m_e(\nu_{en}^{\star}+\nu_{ei}^{\star})} = \frac{n_e e^2}{m_e}\cdot\tau_e^{\star} \tag{4.19}$$

is the scalar electrical conductivity parallel to the magnetic field vector. In addition, $\tau_e^{\star}$ is the mean collision time derived by the first approximation of the Chapman-Enskog method. However, due to its complexity the more accessible Lorentz model will be used throughout this thesis. It must be noted that both these models become equivalent when the particle distribution function is Maxwellian. The variable $\vec{E}^{\star}$ is the electric field vector in a coordinate system moving with the mass average gas velocity, that is,

$$\vec{E}^* = \vec{E} + \vec{v} \times \vec{B} \ . \tag{4.20}$$

The symbol f represents the mass fraction of gas molecules which are not ionized. Mathematically, this can be stated by the expression

$$f = \frac{m_n n_n}{m_i n_i + m_n n_n} \ .$$

For a partially ionized glow discharge $n_n >> n_i$, so that $f \approx 1$. Lastly, the symbol α represents the ratio of ion to neutral particle mass. Hence, $\alpha = m_i/m_n = 1$.

The first term on the right hand side of Eqn. 4.18 is the result of an applied electric field; the second term accounts for any electron pressure gradients, the third term represents the Hall effect, and the last term accounts for ion slip.

For a partially ionized gas, influenced by a small magnetic field, the ion slip term in Eqn. 4.18 can be neglected if

$$\omega_{ce}\tau_e^* \cdot \omega_{ci}\tau_{in}^* < 1 \ .$$

In this expression, ω_{ce} and ω_{ci} are the electron and ion cyclotron frequencies, respectively. As will be shown in Section 4.5, this inequality will indeed hold true for the glow discharge under investigation. If the electron pressure gradient is also neglected, Eqn. 4.18 can be simplified to

$$\vec{J} = \sigma_{11}\left\{\vec{E}^* - \frac{\omega_{ce}\tau_e^*}{B}\vec{J} \times \vec{B}\right\} \ . \tag{4.21}$$

When the vector terms in Eqn. 4.21 are expanded into component form [4.4], the scalar electrical conductivity is transformed into the tensor $\hat{\sigma}$. This procedure produces the well known expression for Ohm's law

$$\vec{J} = \hat{\sigma} \cdot \vec{E}^{*} = \hat{\sigma} \cdot (\vec{E}+\vec{v}\times\vec{B}) \ . \tag{4.22}$$

Thus, the applied driving force is the result of the combined electric and magnetic fields acting upon the charged particles.

In the transverse geometry under investigation, the magnetic field consists of two components, namely $B_r(r,z)$ and $B_z(r,z)$. In order to obtain the electrical conductivity tensor, within the non-uniform magnetic field region, a similarity transformation, into cylindrical coordinates, must be performed. As derived in Appendix A, $\hat{\sigma}$ is transformed into the matrix expression

$$\hat{\sigma} = \begin{bmatrix} \sigma_{\perp}\sin^2\phi + \sigma_{11}\cos^2\phi & -\sigma_T\sin\phi & (\sigma_{11}-\sigma_{\perp})\sin\phi\cdot\cos\phi \\ \sigma_T\sin\phi & \sigma_{\perp} & -\sigma_T\cos\phi \\ (\sigma_{11}-\sigma_{\perp})\sin\phi\cdot\cos\phi & \sigma_T\cos\phi & \sigma_{\perp}\cos^2\phi + \sigma_{11}\sin^2\phi \end{bmatrix} , \tag{4.23}$$

where σ_{11} is the scalar electrical conductivity parallel to $\vec{B}$, while $\sigma_{\perp}$ and σ_T are the Pederson and Hall conductivities, respectively. The argument ϕ represents the angle of rotation between the localized and general coordinate systems. This angle can be expressed by the relation

$$\phi = \tan^{-1}(B_z/B_r) \ .$$

In order to obtain an exact solution for the current density within the gas discharge, it is necessary to simultaneously solve for the electric field and the rotational velocities using the expression for $\hat{\sigma}$. Such a technique was employed by Wijnakker et. al. [1.21] who used the simplifying assumptions of a constant electrical conductivity in a nonvarying magnetic field. However, for the problem under investigation, the electrical conductivity is very nonlinear, particularly in the cathode fall region. Consequently, the conservation of charge equation will be used to produce an approximate solution for the current distribution within the discharge.

Assuming a steady-state condition exists within the glow discharge, the conservation of charge equation implies that

$$\vec{\nabla} \cdot \vec{J} = \frac{1}{r}\frac{\partial}{\partial r}(rJ_r) + \frac{\partial J_z}{\partial z} = 0 \ . \tag{4.24}$$

Within a transverse electrode geometry, the electric field is primarily along the axial direction, so that $E_z \gg E_r$. Thus, it would be reasonable to expect that the axial current density J_z would dominate the radial current density J_r . Evaluation of Ohm's law (Eqn. 4.22) employing the conductivity tensor in cylindrical coordinates (Eqn. 4.23) allows a comparison to be made. As shown in [4.5], the relationship between J_r and J_z is given by

$$\frac{J_r}{J_z} = \frac{\beta_e^2 \tan^2\phi}{1 + (1+\beta_e^2)\tan^2\phi}$$

where $\beta_e = \omega_{ce}\tau_e^*$ is the Hall parameter. Examination of the magnetic field components B_r and B_z , using the computer program POTENT, has revealed that over the annular discharge region, $B_z/B_r \ll 1$. Consequently, for the geometry considered, ϕ is small. Estimates of the Hall parameter have indicated that $\beta_e \simeq 1$. Thus, under these conditions $J_r \ll J_z$ and Eqn. 4.24 simplifies to

$$\frac{\partial J_z}{\partial z} = 0 \text{ , or } J_z = \text{constant.}$$

Since the electrical conductivity is a function of the unknown, spatially dependent, electron density, it cannot be properly evaluated using the one fluid MGD approach. It is hoped that this problem can be resolved at a later date, through the use of a two fluid model.

As a first approximation, a current density distribution which matches the discharge characteristics will be selected. It has frequently been observed that the gas discharge was forced to rotate in an annular region by a combination of radial Lorentz forces. This annular region was seen to encompass the entire glow discharge including the cathode fall region. Due to this nonuniform electron emission from the cathode, a Gaussian distribution function was chosen to represent the actual current density within the gas discharge.

In order that the Gaussian distribution function accurately represent the gas discharge, it was important that this function be centered on the region of highest observed plasma intensity. Using this guideline, the distribution function can be formulated by the expression

$$J_z(r) = \frac{J_0}{b\sqrt{2\pi}} e^{-\frac{(r-r_0)^2}{2b^2}} \quad , \qquad (4.25)$$

where b^2 is the variance and J_0 is a constant. The width of the annular shaped discharge, d can be defined as the distance between the points on the distribution function curve where the current density falls to one-half its maximum value. These points are located at $r = r_0 \pm d/2$, where r_0 is the point at which the peak current density occurs. Using this standard, the variance of the curve can then be related to the annular discharge width in the following manner:

$$J_z(r_0 + \frac{d}{2}) = \frac{J_0}{2b\sqrt{2\pi}} = \frac{J_0}{b\sqrt{2\pi}} e^{-\frac{(r_0 + \frac{d}{2} - r_0)^2}{2b^2}} .$$

Simplifying this relation and taking the natural logarithm of both sides produces a simple expression in which the variance is directly proportional to the discharge width,

$$b^2 = \frac{d^2}{8 \ln 2} . \qquad (4.26)$$

The constant J_0 can now be determined by integrating the total applied current over the discharge area, that is,

$$I_T = \int J_z(r) dA = \int_0^{2\pi} \int_0^R \frac{J_0}{b\sqrt{2\pi}} e^{-\frac{(r-r_0)^2}{2b^2}} r dr d\theta . \qquad (4.27)$$

Evaluation of this integral yields the expression

$$J_0 = I_T \left\{ \sqrt{2\pi} b \left(e^{-\frac{r_0^2}{2b^2}} - e^{\frac{(R-r_0)}{2b^2}} \right) + \pi r_0 \left(erf\left(\frac{r_0}{\sqrt{2}b}\right) + erf\left(\frac{R-r_0}{\sqrt{2}b}\right) \right) \right\}^{-1} . \qquad (4.28)$$

where $erf(x)$ is the error function normally written as

$$erf(x) = \frac{2}{\sqrt{\pi}} \int_0^x e^{-t^2} dt .$$

The results of Eqns. 4.26 and 4.28 can now be substituted back into the Gaussian distribution function described by Eqn. 4.25. By using data taken from high speed still photographs, the corresponding distribution function has been calculated and plotted as illustrated in Fig. 4.1.

4.4 TRANSPORT PROPERTIES OF IONIZED GASES

The phenomena of viscosity, thermal conductivity and diffusion in nonuniform gases represent effects which tend to make the mass velocity, temperature and composition uniform through collisional processes. Transport phenomena involves the convection of these gas related properties due to a gradient or disturbance within the medium. These transport processes are vital when computing the expected macroscopic behavior of an ionized gas for a given set of boundary conditions. However, before any analysis is performed, the various transport coefficients must be identified for each gas component. Values for these transport coefficients can be estimated once a suitable model has been chosen.

In a weakly ionized gas discharge, the rigid sphere model assumes that charged particles are predominantly deflected by single collisions with neutral particles rather than by multiple scattering with other charged particles. This assumption is based upon a charged to neutral particle ratio of $n_e/n_n \simeq 10^{-7}$. With the application of an electric field, the electrons and ions now move in the direction of the field. As a result the distribution function is no longer perfectly Maxwellian, but slightly anisotropic. The ions, because of their greater mass, are assumed to move very slowly compared with the

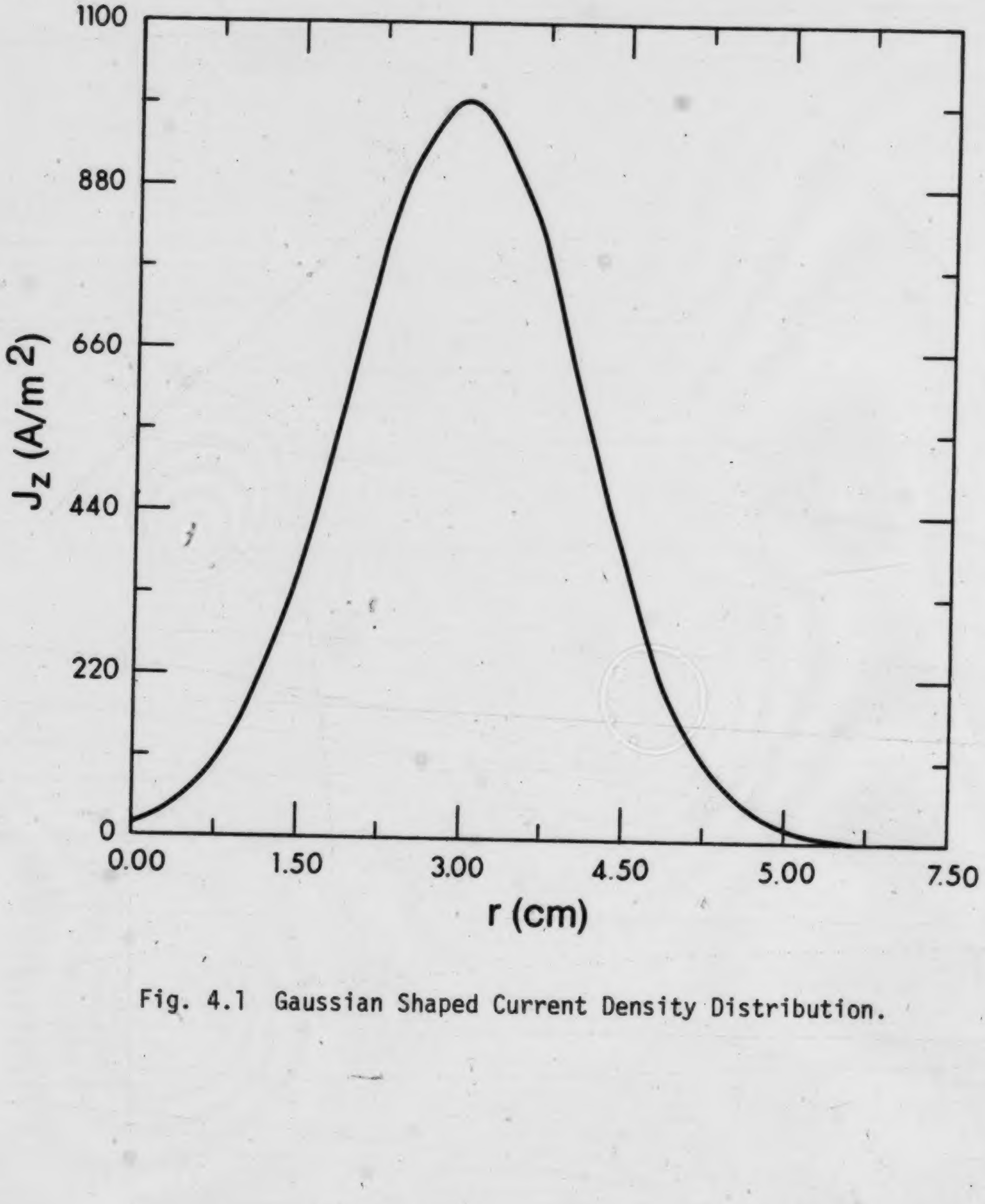

Fig. 4.1 Gaussian Shaped Current Density Distribution.

light, energetic electrons, The accelerated electrons, however, will eventually reach a finite drift velocity determined by the frequency of collisions with the neutral particles.

In general, for particles with a Maxwellian distribution function, the average collision frequency between r and s particles is given by

$$\langle \nu_{rs} \rangle = n_s Q_{rs} \left(\frac{8kT_r}{\pi m_r} + \frac{8kT_s}{\pi m_s} \right)^{\frac{1}{2}} \tag{4.29}$$

or in terms of the mean thermal speed

$$\langle \nu_{rs} \rangle = n_s Q_{rs} (\langle c_r \rangle + \langle c_s \rangle) \ .$$

In these expressions, Q_{rs} is the collision cross section between r and s particles [4.2].

4.4.1 Viscosity

Viscosity is a process involving the transport of momentum through a moving medium due to a gradient in the velocity of that medium. The resulting momentum flux creates a shear stress in the direction of the velocity gradient. The coefficient of shear viscosity can be defined as

$$p_{yz} = - \frac{1}{2} \rho \langle c \rangle \lambda \frac{\partial v_y}{\partial z} \ .$$

The coefficient of shear viscosity can then be defined as

$$\mu = \frac{1}{2} \rho \langle c \rangle \lambda \ . \tag{4.30}$$

Substituting expressions for the mean speed and the mean free path produces the result

$$\mu_r = \frac{1}{4Q_r}\left(\frac{m_r kT_r}{\pi}\right)^{\frac{1}{2}} \tag{4.31}$$

for collisions with the r species. The viscosity for a gas mixture is simply the sum of contributions from the individual gases, that is

$$\mu = \frac{5}{16}\sum_s p_s \tau_s = \sum_s \frac{n_s}{\mu_{s1}^{-1} n_1 + \mu_{s2}^{-1} n_2 + \ldots} \tag{4.32}$$

where μ_{sr} is the mutual viscosity of the sth and rth gases [4.6].

It can be readily seen that the coefficient of shear viscosity is independent of its density. Hence, the capacity of a gas for transmitting momentum is not changed when its density is altered. Consequently, an increase in pressure will not normally retard the motion of an ionized gas flowing between two electrodes. However, if the viscous gas is moving at a high velocity, ordinary laminar motion along irregular boundaries can become unstable, and turbulent motion will begin to dominate. In this instance, momentum is conducted away by turbulent eddies and not by ordinary viscosity. Therefore, the flow resistance of a high speed turbulent gas may depend upon its density.

This problem was encountered during early experimentation with a water-cooled tubular cathode. The turbulence produced when the azimuthal ionized gas passed over this electrode created hot, stagnant gas cells which led to the formation of instability streamers. This problem was subsequently solved by the substitution of a smooth cathode plate.

Another form of viscosity present in most gases is the bulk viscosity ζ. This second type of viscosity is concerned with the internal state of the gas molecules. As described by Hirschfelder et al. [4.7] the coefficient of bulk viscosity is given by

$$\zeta = \frac{n^2k^2T}{C_v^2} \sum_{\ell} C_v^{(\ell)} \tau_{\ell} \ . \tag{4.33}$$

The parameter τ_{ℓ} is the characteristic relaxation time required for the transfer of energy from the translational to the internal degree of freedom for the ℓth mode. The term $C_v^{(\ell)}$ is the contribution of the particular degree of freedom to the specific heat per molecule C_v . The heat capacity at a constant volume can be written as

$$C_v = \frac{3}{2} nk \tag{4.34}$$

for an ideal gas. For dilute monatomic gases $\zeta \simeq 0$, and for polyatomic gases, ζ is generally small and depends upon the relaxation times. These characteristic times are normally the same order of magnitude as the collision interval $\bar{\tau}_{rs}$.

4.4.2 Electrical Conductivity

For an electrically neutral glow discharge, the total current density carried by charged particles is primarily due to the conduction current. Thus, for electrons and positively charged ions, the current density is

$$\vec{J} = n_e e(\vec{V}_i - \vec{V}_e) \ . \tag{4.35}$$

However, in a glow discharge, $\vec{V}_i \ll \vec{V}_e$, and the current due to the ion drift can be neglected. The drift or diffusion velocity of the electrons can be calculated from

$$\vec{V}_e = \langle \vec{c}_e \rangle = \frac{1}{n_e} \int \vec{c}_e f_e d\vec{c}_e \tag{4.36}$$

where $\vec{c}_e$ is the random thermal velocity vector and f_e is the electron distribution function in the presence of a magnetic field. As derived by Sutton and Sherman [4.2], the current density can be written in the tensor form

$$J_{e_j} = \sum_j \sigma_{ij} E_j^\star \tag{4.37}$$

where σ_{ij} is the conductivity tensor. During evaluation of Eqn. 4.37, it may be shown that the conductivity tensor can be written as the single integral

$$\sigma_{ij} = \frac{e^2}{3k} \int \frac{\Omega_{ij} c_e^2 f_0 d\vec{c}_e}{T^*} \tag{4.38}$$

where the collision frequency tensor Ω_{ij} is defined for a magnetic field in the z direction as

$$\Omega_{ij} = \begin{bmatrix} \dfrac{\nu_{es}}{\omega_{ce}^2 + \nu_{es}^2} & -\dfrac{\omega_{ce}}{\omega_{ce}^2 + \nu_{es}^2} & 0 \\ \dfrac{\omega_{ce}}{\omega_{ce}^2 + \nu_{es}^2} & \dfrac{\nu_{es}}{\omega_{ce}^2 + \nu_{es}^2} & 0 \\ 0 & 0 & \dfrac{1}{\nu_{es}} \end{bmatrix} . \tag{4.39}$$

For a general magnetic field, Ω_{ij} must be modified by a similarity transformation as described in Appendix A.

The components of σ_{ij} can be attained by integrating Eqn. 4.38 with the approximation that ν_{es} is to be considered at some average value $\langle\nu_{es}\rangle$. Since $\langle\nu_{es}\rangle$ is independent of c_e, it may be taken outside the integral sign. Simple integration produces a first order approximation to the conductivity tensor, that is,

$$\sigma_{ij} = \frac{n_e e^2}{m_e} \Omega_{ij} \, . \tag{4.40}$$

Due to the form of the collision frequency tensor, only three distinct conductivity components remain:

$$\sigma_{11} = \frac{n_e e^2}{m_e \langle \nu_{es} \rangle} \, , \quad \sigma_{\perp} = \frac{n_e e^2 \langle \nu_{es} \rangle}{m_e \left(\omega_{ce}^2 + \langle \nu_{es} \rangle^2 \right)} \, , \quad \sigma_T = \frac{n_e e^2 \omega_{ce}}{m_e \left(\omega_{ce}^2 + \langle \nu_{es} \rangle^2 \right)} \, . \tag{4.41}$$

The curvature of an electron moving under the influence of a magnetic field, is responsible for the transverse or Hall current. Rewriting the transverse conductivity in terms of the mean collision time produces

$$\sigma_T = \sigma_{11} \cdot \frac{\omega_{ce} \tau_{es}}{(\omega_{ce} \tau_{es})^2 + 1} \, . \tag{4.42}$$

This equation can be regarded as the ratio of the Hall current to the current parallel to the electric field. The significance of this ratio is determined by the Hall parameter given as $\beta_e = \omega_{ce} \tau_{es}$. Thus for $\beta_e \simeq 1$, the Hall current can be of major importance to the operational characteristics of a glow discharge.

The Hall parameter can also be written as

$$\beta_e = \frac{\omega_{ce}}{\langle \nu_{es} \rangle} \simeq \frac{\omega_{ce}}{\langle c_e \rangle} \cdot \frac{1}{n_s Q_{es}} = \frac{\lambda_e}{r_L} \, . \tag{4.43}$$

where λ_e is the electron mean free path and r_L is the average Larmor radius. From this result, the Hall parameter can be viewed as the number of gyrations an electron makes between collisions.

4.5 DETERMINATION OF THE TRANSPORT COEFFICIENTS

In order to analytically or numerically predict the behavior of the rotating glow discharge, an accurate estimate of the transport coefficients is required. However, under the influence of a magnetic field, these coefficients become tensor variables. Thus, in order to evaluate these coefficients, the magnetic field must be known throughout the discharge volume. Magnetic field values were computed by using the computer program POTENT.

A direct calculation of the electron density is not possible through the use of a single fluid MGD treatment. For this reason, the total current density is used to estimate this parameter. For negligible ion current, the steady-state averaged electron density is given by

$$n_e = \frac{I_T}{AeV_e} \tag{4.44}$$

where I_T is the total discharge current distributed over an area A. The electron drift velocity within a composite gas mixture of $He/N_2/CO_2$ can be determined through the analysis of Elliott et. al. [4.8]. However, their calculation does not include the effects of a magnetic field. As a result of the discussion in Chapter 7, the ratio E/n must now be modified to include the presence of a magnetic field. In order to satisfy this condition, the Hall parameter $\beta_e = \omega_{ce}\tau_e$ must be known. The electron cyclotron frequency is easily determined, but the mean collision time is dependent upon the unknown electron temperature. Without a direct measurement of the glow discharge electron temperature, this evaluation cannot be performed except through an iterative procedure.

On the first step of the iteration, the ratio $E/n = 2.64 \times 10^{-16} V/cm^2$ is calculated for a 16/2/2 torr laser gas mixture with no magnetic field. Reference [4.8] then provides an estimate for the electron drift velocity and electron temperature. These values are used in turn to calculate the electron density (Eqn. 4.44) and the electron-neutral collision frequency (Eqn. 4.29). The Hall parameter is then computed so that a new E_{eff}/n ratio can be determined. After several iteration cycles are completed, $E_{eff}/n \approx 2.44 \times 10^{-16} V/cm^2$ for a magnetic flux density of 0.04 T. This translates into an overall E/n reduction of 8 percent throughout the glow discharge. Values of magnetic flux density, near the cathode, typically reach 0.1 T. In this region, the E/n ratio can be decreased by over 65 percent compared to its non-magnetized state. Consequently, a small change in magnetic field can have a substantial effect on the glow discharge.

The gas discharge typically operates at a current density of 50 mA/cm^2. Through the use of Eqn. 4.44, the average electron density is estimated to be $n_e = 1.2 \times 10^{11} cm^{-3}$ for an average drift velocity of $V_e = 2.6 \times 10^6 cm/s$. Thus, with a neutral gas density of $n_n = 4.54 \times 10^{23} cm^{-3}$, at a temperature of 425 K, the degree of ionization is $n_e/n_n = 2.64 \times 10^{-7}$. Subsequently, charged particle collisions can be neglected.

During the iteration procedure the average electron temperature was also calculated. For the above discharge conditions $<\xi>$ converged to 1.3 eV.

The average molecular mass of a gas mixture, can be determined by the expression

$$m_{mix} = \sum_i \frac{f_i M_i}{N_A} \qquad (4.45)$$

where N_A is Avogadro's number, M_i is the molecular weight, and f_i is the fractional percentage of the ith gas. For the particular gas mix under consideration, the average neutral or ion mass is $m_{mix} = 1.726 \times 10^{-26}$ kg/particle.

To determine the momentum transfer collision frequency for neutral particles, ions, and electrons, it is first necessary to know the collisional cross section of each species. The electron-neutral collision cross sections for an ionized gas mixture with an average electron energy of 1.3 eV, are displayed in Table 4.1.

	$Q_{en}(10^{-20}m^2)$	$r(\mathring{A})$
He	6.96	1.090
N_2	11.92	1.875
CO_2	5.10	2.295

Table 4.1 Electron Impact Cross Sections for Elastic and Inelastic Processes when $\langle\xi\rangle = 1.3$ eV.

As shown earlier, the collision cross section of two gas species is

$$Q_{ij} = \pi(r_i + r_j)^2 \ .$$

When considering a gas mixture, the average collision cross section for momentum transfer becomes the summation of terms

$$Q_{\substack{nn\\mix}} = \sum_{i,j} f_i f_j Q_{ij} \; . \tag{4.46}$$

By using Eqn. 4.46 and the molecular radii in Table 4.1, the average cross section for the specified gas mixture is $Q_{\substack{nn\\mix}} = 21.5 \times 10^{-20}\mathrm{m}^2$. Since ions have a low kinetic energy within the glow discharge, the collision cross sections for ion-neutral and ion-ion interactions can be assumed to be $Q_{in} \approx Q_{ii} \approx Q_{nn}$. In a similar procedure, the average electron-neutral particle collision cross section is determined by the summation

$$Q_{\substack{en\\mix}} = \sum_{j} f_j Q_{ej} \; . \tag{4.47}$$

Using the values listed in Table 4.1, $Q_{\substack{en\\mix}} = 7.264 \times 10^{-20}\mathrm{m}^2$.

The average momentum transfer collision frequency can now be determined for each species in a partially ionized gas. Summing Eqn. 4.29 over all particle species results in the equation

$$\langle \nu_r \rangle = \sum_{s} \langle \nu_{rs} \rangle \; . \tag{4.48}$$

Thus, the average collision frequency for neutral particles can be written as

$$\langle \nu_n \rangle = \langle \nu_{ni} \rangle + \langle \nu_{ne} \rangle + \langle \nu_{nn} \rangle \; . \tag{4.49}$$

However, since $n_e, n_i \ll n_n$, collision frequencies involving charged particles are significantly less than those involved with neutral particles. Hence, $\langle \nu_n \rangle \approx \langle \nu_{nn} \rangle$. With similar modifications, $\langle \nu_i \rangle \approx \langle \nu_{in} \rangle$ and $\langle \nu_e \rangle \approx \langle \nu_{en} \rangle$.

As stated earlier, the electron energy has been estimated to be $kT_e \approx 1.3$ eV. Moreover, due to the large number of collisions in the positive column, the ion temperature is relatively low. Thus, a good approximation to use is $T_i \simeq T_n$ where the measured neutral gas temperature is $T_n = 425$ K. However, the assumption does not hold in the cathode glow layer where the ions can accumulate a significant amount of directed energy as they accelerate through the cathode fall.

Now, using the calculated average molecular mass and the average collisional cross sections for the gas mixture, the species collision frequencies are evaluated by Eqn. 4.29 and 4.48. Substitution of these parameters yield

$$\begin{aligned} \langle \nu_{in} \rangle \simeq \langle \nu_{nn} \rangle &= 1.285 \times 10^{8} \mathrm{s}^{-1} \\ \langle \nu_{en} \rangle &= 2.48 \times 10^{10} \mathrm{s}^{-1} \ . \end{aligned} \tag{4.50}$$

For an average magnetic flux density of 0.04 T, the electron and ion cyclotron frequencies are $\omega_{ce} = 7.034 \times 10^{9}$ rad/s and $\omega_{ci} = 3.72 \times 10^{5}$ rad/s, respectively. Through these results, $\omega_{ce}\tau_{en} \cdot \omega_{ci}\tau_{in} \simeq 8.2 \times 10^{-4}$, which affirms the earlier assumption of neglecting ion slip.

5

4.6 ORTHOGONAL CURVILINEAR COORDINATES

To maximize the versatility of the computer model, the MGD equations are expanded in orthogonal curvilinear coordinates. This procedure would allow the program to accept different electrode geometries using different coordinate systems. In order to utilize this powerful technique, the force fields and differential operators must be expressed in terms of a generalized coordinate system. Since the differential operators are not often found in this form, they will be listed in this section for convenience.

In this particular system, a differential arc length may be described by

$$ds^2 = h_1^2 dx_1^2 + h_2^2 dx_2^2 + h_3^2 dx_3^2 \ ,$$

where the term $h_i dx_i$ respresents the differential arc length in the $\vec{e}_i$ direction. The quantity h_i is known as the scale factor for the x_i-coordinate and is generally spatially dependent. Associated with the scale factors is a transformation matrix known as the metrix tensor G. The determinant of this matrix is given by

$$g = (h_1 h_2 h_3)^2 \ .$$

In a generalized coordinate system, special notation is required when dealing with the dot and cross products of the unit vectors $\vec{e}_i$. These operations are described in the following manner:

$$\vec{e}_i \cdot \vec{e}_j = \delta_{ij} = \begin{cases} 1 \ , & \text{for } i = j \\ 0 \ , & \text{for } i \neq j \end{cases} \ . \tag{4.51}$$

where δ_{ij} is the Kronecker delta and

$$\vec{e}_i \times \vec{e}_j = \varepsilon_{ijk}\vec{e}_k \tag{4.52}$$

where ε_{ijk} is the Levi-Civita permutation symbol. This symbol has been defined as

$$\varepsilon_{ijk} = \begin{cases} +1 & \text{, for an even permutation of } (ijk) \\ -1 & \text{, for an odd permutation of } (ijk) \\ 0 & \text{, otherwise.} \end{cases}$$

It now becomes necessary to describe expressions for various operations of scalar, vector, and tensor quantities in a generalized coordinate system. In this system, the gradient operator becomes

$$\vec{\nabla} = \frac{\vec{e}_1}{h_1}\frac{\partial}{\partial x_1} + \frac{\vec{e}_2}{h_2}\frac{\partial}{\partial x_2} + \frac{\vec{e}_3}{h_3}\frac{\partial}{\partial x_3} = \sum_i \frac{\vec{e}_i}{h_i}\frac{\partial}{\partial x_i} \tag{4.53}$$

for $i = 1,2,3$. By using this result, the gradient of a scalar ϕ is

$$\vec{\nabla}\phi = \sum_i \frac{1}{h_i}\frac{\partial\phi\vec{e}_i}{\partial x_i} . \tag{4.54}$$

The divergence of a vector $\vec{v}$ can be written as

$$\vec{\nabla}\cdot\vec{v} = \sum_i \frac{1}{\sqrt{g}}\frac{\partial}{\partial x_i}\left(\sqrt{g}\,\frac{v_i}{h_i}\right) . \tag{4.55}$$

The curl of the vector $\vec{v}$ becomes the expression

$$\vec{\nabla}\times\vec{v} = \sum_i \frac{h_i\vec{e}_i}{\sqrt{g}} \sum_{\ell,m} \varepsilon_{i\ell m}\frac{\partial(h_m v_m)}{\partial x_\ell} . \tag{4.56}$$

The expression for the divergence of a tensor $\hat{T}$ is given by

$$(\vec{\nabla}\cdot\hat{T})_j = \sum_i h_j\vec{e}_i T^{ij}_{,i} \tag{4.57}$$

where $T^{ij}_{,i}$ is the covariant derivative of $\hat{T}$. By using expressions developed by Morse and Feshbach [4.9], Eqn. 4.57 is transformed into

$$(\vec{\nabla}\cdot\hat{T})_1 = \sum_i h_j \vec{e}_j \left[\frac{1}{\sqrt{g}} \frac{\partial}{\partial x_i} (\sqrt{g} T^{ij}) + \sum_k T^{ik} \begin{Bmatrix} j \\ i \; k \end{Bmatrix}\right] \tag{4.58}$$

where $T^{ij} = T_{ij}/h_i h_j$ is the contravariant form of the tensor T_{ij}. The expression $\begin{Bmatrix} j \\ i \; k \end{Bmatrix}$ is a Christoffel symbol with the following properties:

$$\begin{Bmatrix} i \\ i \; i \end{Bmatrix} = \frac{1}{h_i} \frac{\partial h_i}{\partial x_i} \; ; \quad \begin{Bmatrix} i \\ i \; j \end{Bmatrix} = \begin{Bmatrix} i \\ j \; i \end{Bmatrix} = \frac{1}{h_i} \frac{\partial h_i}{\partial x_j} \; ;$$

$$\begin{Bmatrix} j \\ i \; i \end{Bmatrix} = \frac{-h_i}{(h_j)^2} \frac{\partial h_i}{\partial x_j} \; ; \quad \begin{Bmatrix} i \\ j \; k \end{Bmatrix} = 0 \quad \text{for } i, j, k \text{ all different.}$$

This notation, for the Christoffel symbols of the second kind, represents the change in direction of the unit vectors as one moves in space. For completeness, the first component of $\vec{\nabla} \cdot \hat{T}$ expands into the equation

$$(\vec{\nabla}\cdot\hat{T})_1 = \frac{1}{h_1 h_2 h_3} \left[\frac{\partial}{\partial x_1}(h_2 h_3 T_{11}) + \frac{\partial}{\partial x_2}(h_2 h_3 T_{21}) + \frac{\partial}{\partial x_3}(h_1 h_2 T_{31}) \right.$$
$$\left. + h_3 T_{12} \frac{\partial h_1}{\partial x_2} + h_2 T_{13} \frac{\partial h_1}{\partial x_3} - \left(h_3 T_{22} \frac{\partial h_2}{\partial x_1} + h_2 T_{33} \frac{\partial h_3}{\partial x_1} \right) \right] . \tag{4.59}$$

This equation contains terms which look like the normal vector divergence, plus four extra Coriolis terms that arise due to the change in the direction of the unit vectors with changes in position.

The final relation required for the compressible MGD equations, is an expression for the gradient of a vector. As developed by [4.9], the resulting dyadic is given by

$$\overleftrightarrow{\nabla v} = \begin{cases} A_{nm} = \dfrac{1}{h_n}\dfrac{\partial v_n}{\partial x_n} - \dfrac{v_n}{h_n h_m}\cdot\dfrac{\partial v_n}{\partial x_m} \quad \text{for } m \neq n \ . \\[2ex] A_{mm} = \dfrac{\partial}{\partial x_m}\left(\dfrac{v_m}{h_m}\right) + \dfrac{1}{h_m}\sum\limits_n \dfrac{v_n}{h_n}\cdot\dfrac{\partial h_m}{\partial x_n} \ . \end{cases} \tag{4.60}$$

With these definitions it is now possible to write out the compressible MGD equations in component form. First, the generalized form of the conservation of mass, Eqn. 4.2, becomes

$$\frac{\partial \rho}{\partial t} + \frac{1}{h_1 h_2 h_3}\left\{\frac{\partial}{\partial x_1}(h_2 h_3 \rho v_1) + \frac{\partial}{\partial x_2}(h_1 h_3 \rho v_2) + \frac{\partial}{\partial x_3}(h_1 h_2 \rho v_3)\right\} = 0 \ . \tag{4.61a}$$

Next, the generalized form of the conservation of momentum, Eqn. 4.12 is given as

$$\begin{aligned} &\frac{\partial}{\partial t}(\rho v_1) + \frac{1}{h_1 h_2 h_3}\left\{\frac{\partial}{\partial x_1}(h_2 h_3 \rho v_1^2) + \frac{\partial}{\partial x_2}(h_1 h_3 \rho v_1 v_2) + \frac{\partial}{\partial x_3}(h_1 h_2 \rho v_1 v_3)\right. \\ &\quad \left. + h_3 \rho v_1 v_2 \frac{\partial h_1}{\partial x_2} + h_2 \rho v_1 v_3 \frac{\partial h_1}{\partial x_3} - \left[h_3 \rho v_2^2 \frac{\partial h_2}{\partial x_1} + h_2 \rho v_3^2 \frac{\partial h_3}{\partial x_1}\right]\right\} + \frac{kT_n}{m_n}\cdot\frac{1}{h_1}\frac{\partial \rho}{\partial x_1} \\ &\quad - \frac{\mu}{h_1 h_2 h_3}\left\{\frac{\partial}{\partial x_1}(h_2 h_3 A_{11}) + \frac{\partial}{\partial x_2}(h_1 h_3 A_{21}) + \frac{\partial}{\partial x_3}(h_1 h_2 A_{31})\right. \\ &\quad \left. + h_3 \frac{\partial h_1}{\partial x_2} A_{12} + h_2 \frac{\partial h_1}{\partial x_3} A_{13} - \left[h_3 \frac{\partial h_2}{\partial x_1} A_{22} + h_2 \frac{\partial h_3}{\partial x_1} A_{33}\right]\right\} \\ &\quad - \left(\zeta + \frac{1}{3}\mu\right)\frac{1}{h_1}\frac{\partial}{\partial x_1}\left\{\frac{1}{h_1 h_2 h_3}\left[\frac{\partial}{\partial x_1}(h_2 h_3 v_1) + \frac{\partial}{\partial x_2}(h_1 h_3 v_2) + \frac{\partial}{\partial x_3}(h_1 h_2 v_3)\right]\right\} \\ &\quad - (J_2 B_3 - J_3 B_2) = 0 \ . \end{aligned} \tag{4.61b}$$

The dyadic terms A_{ij} are described by Eqn. 4.60. The two other components of the momentum equation can be obtained by interchanging all subscripts 1 to 2 or 3.

CHAPTER 5

COMPUTATIONAL TECHNIQUES

5.1 INTRODUCTION

The understanding of complex gas discharge systems has, thus far, been limited to very specialized applications. Although gas discharges can be analytically described, these studies generally represent an oversimplified view of the actual situation. Moreover, detailed realistic theoretical studies of the behavior of a gas discharge with electromagnetic fields (both static and time-varying) are indeed rare. The reasons for this lack of understanding is due to the extremely complex nature of such systems. A typical gas discharge may consist of electrons, fully and partially ionized ions, and neutrals all rapidly varying with time. Consequently, only computer simulation techniques are adequately suited to handle the complexity involved in these types of problems.

A computer code has been developed to solve the nonlinear time-varying, two-dimensional coupled set of compressible MGD equations describing a partially ionized gas discharge. The complete description of such a plasma is impractical due to the enormous number of particles, their complex trajectories, and the resulting induced electromagnetic fields. This problem can be circumvented by the application of statistical mechanics to describe the plasma in terms of distribution functions. These averaged plasma properties are then used to compose a fluid description of the plasma. In this manner, a macroscopic view of a rotating gas discharge under the influence of a nonlinear magnetic field can be developed.

5.2 BASIC NUMERICAL CONCEPTS

In the numerical solution of a system of differential equations, the continuous space-time domain is replaced by a discrete space-time mesh. In addition, the differential equations are approximated, at each mesh point, by an algebraic finite difference equation which relates the dependent variables at time t^{n+1} to the known variables at time t^n. If the finite difference equations are uncoupled in these unknowns between time levels, then the equations are classified as explicit. Therefore, in order to solve a set of m difference equations valid over a two-dimensional lattice containing $N \times M$ points, a set of $m \times N \times M$ algebraic equations must be solved for $m \times N \times M$ unknowns.

Should the finite difference equations be coupled with respect to the unknown variables at the time level t^n, the resulting $m \times N \times M$ implicit equations must be solved simultaneously. As stated in [5.1], the number of multiplications involved in solving N simultaneous linear algebraic equations is approximately $\frac{2}{3} N^3$. Therefore, the computing time per time step in a two-dimensional fully implicit calculation can be quite excessive. Thus, for multi-dimensional problems, this type of calculation is rarely used.

In order to avoid this limitation, an alternating direction implicit (ADI) method may be employed. As derived by Peaceman and Rachford [5.2], this algorithm breaks the time advancement of the equations into two steps. In the first half step, variables are advanced implicitly in one dimension and explicitly in the other dimension. During the second half step, the procedure is reversed. Consequently, in the ADI technique, there are alternately M uncoupled sets of $m \times N$ coupled simultaneous equations combined with N uncoupled sets of $m \times M$ coupled simultaneous equations to be solved. This technique drastically reduces the computational costs in contrast to the fully implicit method. The mesh points involved in each of the explicit, fully implicit, and ADI techniques for second order operations in two dimensions are depicted in Fig. 5.1.

The numerical solution of the multi-dimensional compressible Navier-Stokes equation requires a considerable amount of computer time, and consequently, efficient computational methods are necessary. A number of prior methods for solving this problem have been based upon explicit finite difference schemes. However, this procedure is subject to stability restrictions on the time step sizes as dictated by the Courant-Friedrichs-Lewy (CFL) condition. This condition states that the difference solution, which can propagate information across the mesh at a maximum rate of one space step Δx during each time step Δt, must exceed all propagation speeds of the physical system. This includes such diverse effects as waves, fluid motion and diffusion [5.3].

Within a general viscous gas discharge, influenced by time-varying magnetic fields, an explicit difference scheme will encounter instabilities unless

$$\left\{ |v| + \frac{\mu}{\rho \Delta x} + \left(c_s^2 + v_A^2 \right)^{\frac{1}{2}} \right\} \frac{\Delta t}{\Delta x} \leq 1. \tag{5.1}$$

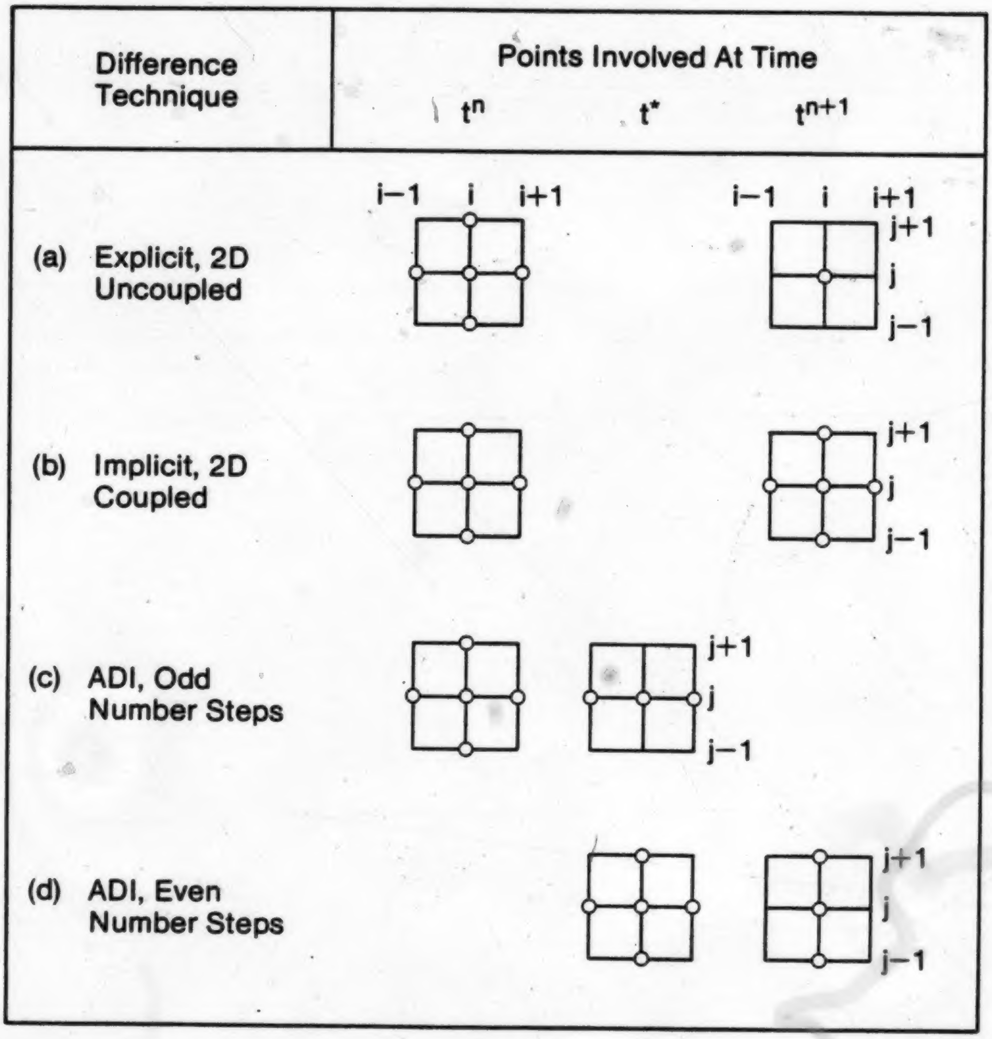
Difference Technique
Points Involved At Time
t^n
t^*
t^{n+1}
i−1
i
i+1
j+1
j
j−1
(a) Explicit, 2D Uncoupled
(b) Implicit, 2D Coupled
(c) ADI, Odd Number Steps
(d) ADI, Even Number Steps

Fig. 5.1 Two-Dimensional Mesh Point Orientation for Several Finite Difference Techniques.

Through this relation, the CFL condition then ensures that any physical velocity, within the system, will be less than the lattice speed, $\Delta x/\Delta t$. In Eqn. 5.1, v is the advective velocity, μ is the viscosity coefficient, and c_s is the adiabatic sound speed given by

$$c_s^2 = \frac{\gamma P}{\rho} . \tag{5.2}$$

The term v_A is designated as the Alfvén speed

$$v_A^2 = \frac{B^2}{\mu_0 \rho} . \tag{5.3}$$

In general, discharge regions penetrated by a high magnetic flux tend to have low densities as a result of a balance between kinetic and magnetic pressures [5.4]. This effect can create very high Alfvén velocities which severely restrict the allowable explicit time step. Therefore, the significance of this stability restriction is that computational efficiency is lowered by imposing a smaller time step than would otherwise be desirable.

In contrast to explicit schemes, the implicit finite difference technique is stable regardless of the time step size for linear differential equations with constant coefficients. In this case, the values $\vec{u}^{n+1}$ are fully coupled to the values $\vec{u}^{n}$ at the old time level. Thus, a disturbance at any grid point can propagate to any other point on the mesh during one time step. As a result, the lattice speed or velocity of information transmittal on the mesh is infinite and the CFL limitation is always satisfied.

For the implicit case under consideration where the differential equations are nonlinear, stability theory suggests that the time step restriction is relaxed from the CFL condition [5.5]. This enhanced numerical stability should create a substantial increase in computational efficiency since fewer time steps are required.

The magnetic Reynolds number R_m is a measure of the ease with which the magnetic field can slip through a fluid. More precisely, this fluid interaction number is the ratio of fluid flux to magnetic diffusivity or

$$R_m = \frac{vL}{1/\mu_0\sigma} = \frac{\tau_{\text{diffusion}}}{\tau_{\text{problem}}} . \tag{5.4}$$

Here, v is the advective velocity, L is the scale length or mesh increment, μ_0 is the free space permeability, and σ is the fluid electrical conductivity. Within the slightly ionized gas discharge under investigation, $R_m \approx 2\pi \times 10^{-7}$ and even moderate size currents will only produce very slight perturbations in the applied field. Therefore, the magnetic field equation can be neglected in the analysis of the flow pattern. With the absence of this equation, the critical velocity used in the CFL condition becomes the acoustic velocity.

For an operational pressure of 30 torr and a neutral gas density of 0.0256 kg/m^3, the acoustic speed, $c_s \approx 480$ m/s. This translates to a maximum explicit Courant time step of approximately 10 μs. As a result of this small time step size, it is hoped that the relaxed time step limitation of the ADI method will substantially reduce computational cost.

The choice of an implicit scheme has also been found to be beneficial for situations involving high Mach number flows. Briley and McDonald [5.6] have found that in these cases, the CFL condition becomes increasingly restrictive when a small lattice spacing is desired. The subsequent use of an implicit technique reduces computation time while providing the necessary spatial resolution.

5.3 COMPUTATIONAL MESH

Since the mathematics dealt with in a computer is both discrete and finite, the values of a continuous function must be defined as discrete points in space over a finite mesh. This discretization technique also arises in many areas of physics and EM theory where the equations of force and motion are applied to small finite elements. In the limit, these discrete elements become vanishingly small, thereby producing a differential equation.

To represent a continuous function over the domain (X_1, X_2), it is first necessary to divide the domain into a set of $N - 1$ elements of width Δx_i . A vector set $\{x_i\}$ may then be constructed by defining the continuous variable x only at the points i. Thus, the space lattice points are

$$x_i = X_1 + \sum_{\nu=1}^{i} \Delta x_\nu$$

where $\Delta x_i = x_i - x_{i-1}$. The dependent function $f(x)$ will now be approximated by its corresponding vector set $\{f_i\}$ defined on the independent variable mesh $\{x_i\}$ such that $f_i = f(x_i)$. The nature of this approximation must be such that the scale length Δx_i be small in comparison to any wavelength of the rapidly varying function f. Thus, the mesh element Δx_i essentially defines a cutoff wavelength, below which no phenomena can be described.

For a general initial value problem, the time dimension is also divided into small finite intervals which separates discrete levels or moments in time. This process can be represented by

$$t^n = t^0 + \sum_{\nu=1}^{n} \Delta t^\nu$$

where t^0 is some initial time and $\Delta t^n = t^n - t^{n-1}$. Here again, Δt^n must be sufficiently small in order that significant time dependent information not be lost.

The continuous function $\vec{u}(\vec{x},t)$ can now be expressed as the discrete function $\vec{u}_i^n = \vec{u}(x_i,t^n)$ defined over a temporal and spatial mesh. The computational mesh designated for the program MAGIC is classified as Eulerian since it has no velocity with respect to a stationary observer in the laboratory reference frame.

The values of the discrete function $\vec{u}(x_i,t^n)$ are specified to be cell-centered quantities. In this description, the value of $\vec{u}_{i,j}$ is the average value of $\vec{u}$ in the two-dimensional cell centered at (x_{1_i},x_{2_j}). The two-dimensional mesh is illustrated by Fig. 5.2 where the dots represent the points at which the values of the state vector $\vec{u}$ are stored. Similarly, the crosses represent the interface points at which the fluxes and forces are to be evaluated.

To adequately describe the computational mesh, the mesh elements $\Delta_{1\pm}$ and $\Delta_{2\pm}$ are defined as the distance between points x_{n_i} and $x_{n_{i\pm1}}$ where $x_n = \{x_1,x_2\}$ are members of the orthogonal curvilinear coordinates. That is,

$$\begin{aligned} \Delta_{1\pm} &= x_{1_{i\pm1}} - x_{1_i} \\ \Delta_{2\pm} &= x_{2_{j\pm1}} - x_{2_j} \,. \end{aligned} \tag{5.5}$$

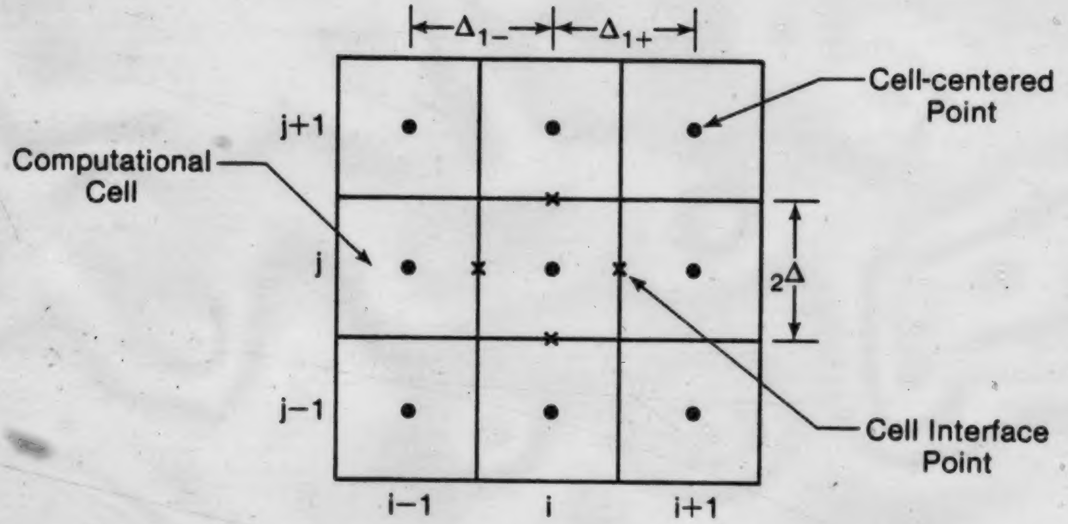
Δ_{1-}
Δ_{1+}
Cell-centered Point
Computational Cell
j+1
j
j−1
2Δ
Cell Interface Point
i−1
i
i+1

Fig. 5.2 Schematic of the Finite Difference Computational Mesh.

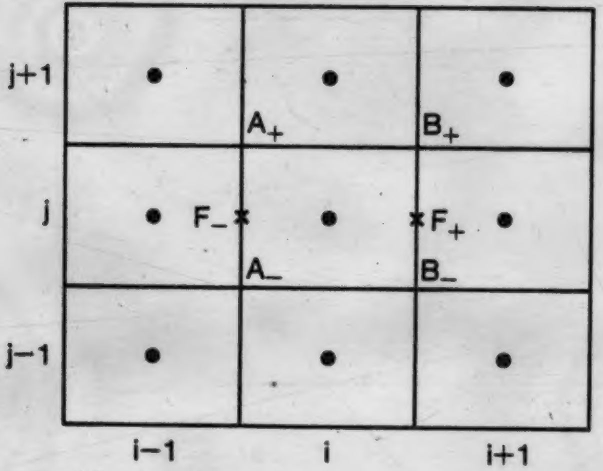
j+1
j
j−1
A_+
B_+
F_-
F_+
A_-
B_-
i−1
i
i+1

Fig. 5.3 Illustration of the Mesh Points Involved in a Mixed Derivative Calculation.

These variable mesh elements allow the specification of a nonuniform mesh. Therefore, the distance between cell interfaces, denoted by ${}_{n}\Delta$, is given by

$$\begin{aligned} {}_{1}\Delta &= \frac{1}{2}(\Delta_{1+} + \Delta_{1-}) \\ {}_{2}\Delta &= \frac{1}{2}(\Delta_{2+} + \Delta_{2-}) \ . \end{aligned} \tag{5.6}$$

The value of any variable at the cell interface is simply the average of two adjacent cells. For example,

$$\begin{aligned} F_{1\pm} &= \frac{1}{2}(F_{i\pm 1} + F_{i}) \\ F_{2\pm} &= \frac{1}{2}(F_{j\pm 1} + F_{j}) \ . \end{aligned} \tag{5.7}$$

Finally, to determine the flux or force difference across an interface, the δ operator produces the terms

$$\begin{aligned} \delta_{1+}(F) &= \frac{1}{\Delta_{1+}}(F_{i+1} - F_{i}) \\ \delta_{1-}(F) &= \frac{1}{\Delta_{1-}}(F_{i} - F_{i-1}) \ . \end{aligned} \tag{5.8a}$$

These operators represent the forwards and backwards differencing scheme along the x_1 direction, which are evaluated at the cell interface. Similarly, for the x_2 direction

$$\begin{aligned} \delta_{2+}(F) &= \frac{1}{\Delta_{2+}}(F_{j+1} - F_{j}) \\ \delta_{2-}(F) &= \frac{1}{\Delta_{2-}}(F_{j} - F_{j-1}) \ . \end{aligned} \tag{5.8b}$$

5.4 SPATIAL FINITE DIFFERENCING

The conservative MGD equations (4.61) are composed of two basic types of terms. The first type arises from the divergence of flux transport terms as a result of advection and viscous processes. From the expanded MGD equations, all flux terms have the form $\frac{\partial}{\partial x_1}(\alpha F)$ where α is normally a transport coefficient and F is any general factor including differential terms. The second type of term found in these equations have the form $\beta\frac{\partial F}{\partial x_1}$ where β is some function of the state vector $\vec{u}$. These force terms originate from $\vec{J} \times \vec{B}$ and pressure gradient forces. The resulting flux and force terms are now used to denote the type of finite differencing that will be applied throughout the MGD equations.

The application of a spatial finite difference technique to a set of differential equations, forms a system of algebraic equations which depict variations to the cell-centered variables. These changes are due to the transport of flux through each individual cell as a result of applied driving forces. Hence, flux and force terms are calculated at the cell interfaces.

Since flux terms measure the flow through a computational cell, the finite difference form evaluated at the cell boundaries, is written as

$$\frac{\partial}{\partial x_1}(\alpha F) \rightarrow \frac{\alpha_+ F_+ - \alpha_- F_-}{{}_1\Delta} \qquad (5.9)$$

where $\alpha_\pm$ and $F_\pm$ are simply the average of two adjacent cells as defined by Eqn. 5.7. If the variable F represents a derivative term, the finite difference form becomes

$$\frac{\partial}{\partial x_1}\left(\alpha\frac{\partial G}{\partial x_1}\right) \rightarrow \frac{\alpha_+\delta_{1+}(G)-\alpha_-\delta_{1-}(G)}{{}_1\Delta} \tag{5.10}$$

where the δ operator is the difference across a cell interface.

For the frequently occurring case of mixed derivatives, $F = \frac{\partial G}{\partial x_2}$, it is first necessary to take the derivative in the x_2 direction at the points B_+,B_- and average them to arrive at a value F_+ at the cell interface. The procedure is repeated at the points A_+,A_- to determine F_-. The differential with respect to x_1 is then performed to give the expression

$$\frac{\partial}{\partial x_1}\left(\alpha\frac{\partial G}{\partial x_2}\right) \rightarrow \frac{\alpha_+F_+-\alpha_-F_-}{{}_1\Delta} = \frac{\alpha_+\left(\frac{\partial G}{\partial x_2}\right)_+ -\alpha_-\left(\frac{\partial G}{\partial x_2}\right)_-}{{}_1\Delta} \tag{5.11}$$

where

$$\begin{aligned}\left(\frac{\partial G}{\partial x_2}\right)_+ = \frac{1}{2}\{[\tfrac{1}{2}(G_{i+1,j+1}+G_{i,j+1}) - \tfrac{1}{2}(G_{i+1,j}+G_{i,j})]/\Delta_{2+} \\ + \tfrac{1}{2}(G_{i+1,j}+G_{i,j}) - \tfrac{1}{2}(G_{i+1,j-1}+G_{i,j-1})]/\Delta_{2-}\} .\end{aligned} \tag{5.12}$$

The points involved in this derivation are shown in Fig. 5.3.

The force terms measure the overall effect that applied forces have on the edges of a computational cell. In this case, it is necessary to define these terms as the average of the forces applied on each cell face, that is,

$$\beta\frac{\partial F}{\partial x_1} \rightarrow \frac{1}{2}\{\beta_+\delta_{1+}(F)+\beta_-\delta_{1-}(F)\} . \tag{5.13}$$

5.5 TEMPORAL FINITE DIFFERENCING

The system of equations derived in the previous chapter can be represented by the vector equation

$$\frac{\partial \vec{T}}{\partial t}(\vec{u}) + \vec{F}(\vec{u}) + \vec{G}(\vec{u}) + \vec{H}(\vec{u}) - \vec{J} \times \vec{B} = 0 \qquad (5.14)$$

where $\vec{u} = \{v_1, v_2, v_3, \rho\}$ is the state vector of the system, and $\vec{T}(\vec{u}) = \{\rho\vec{v}, \rho\}$ are the quantities advanced with time. The function $\vec{F}(\vec{u})$ contains all terms in Eqn. 4.61 that have leading derivatives with respect to x_1. Several of the possible forms that these leading derivatives can take include: $a\frac{\partial\phi}{\partial x_1}$, $\frac{\partial}{\partial x_1}(a\phi)$ and $\frac{\partial}{\partial x_1}(a\frac{\partial\phi}{\partial x_j})$ for all j. In a similar manner, the functions $\vec{G}(\vec{u})$ and $\vec{H}(\vec{u})$ contain all terms with leading derivatives with respect to x_2 and x_3 respectively. However, due to the type of applied driving force, the rotating plasma is assumed to have θ symmetry. As a result, all partial derivatives with respect to θ are zero for the case under consideration. Therefore, the function $\vec{G}(\vec{u}) = 0$.

The ADI finite difference method, discussed by Peaceman and Rachford [5.2] allows for the solution of large matrix problems using a straightforward algorithm. This technique employs two finite difference equations which are used in turn over successive time steps each of duration $\Delta t/2$. Each part is treated implicitly on alternate time steps while the other part is treated explicitly. Thus, if $\vec{u}^*$ is an intermediate value at the end of the first time step, then this time-centering ADI technique yields a two-step approach:

$$\frac{\vec{T}(\vec{u}^{\star})-\vec{T}(\vec{u}^{n})}{\Delta t/2} + \vec{F}(\vec{u}^{\star},\vec{u}^{n}) + \vec{H}(\vec{u}^{n}) - \vec{J} \times \vec{B} = 0 \qquad (5.15a)$$

and

$$\frac{\vec{T}(\vec{u}^{n+1})-\vec{T}(\vec{u}^{\star})}{\Delta t/2} + \vec{F}(\vec{u}^{\star}) + \vec{H}(\vec{u}^{n+1},\vec{u}^{\star}) - \vec{J} \times \vec{B} = 0 \ . \qquad (5.15b)$$

These two equations describe the time advancement scheme employed in MAGIC. Initially, Eqn. 5.15a is used to solve for the intermediate values $\vec{u}^{\star}$, which are then applied in Eqn. 5.15b to determine the solution $\vec{u}^{n+1}$ at the end of the time step Δt. It can be shown that these equations are each accurate only to first order in Δt, but when the two equations are combined, a second order accurate equation is produced. Consequently, the overall ADI procedure is second order accurate.

The forms of the functions $\vec{F}(\vec{u})$ and $\vec{H}(\vec{u})$ are well defined except for mixed and product derivative terms. The application of finite difference techniques to these terms requires advanced time values for rows not yet computed by the tridiagonal ADI method. In order to accommodate these terms, banded matrix techniques are normally used. To avoid these complicated banded techniques and still use a tridiagonal ADI finite difference scheme, it becomes necessary to treat the mixed derivatives in a special way. Finan [5.5] suggests several involved methods, but advocates treating the mixed derivative terms in an explicit manner. This procedure lowers the accuracy for these terms to order Δt and introduces a Courant time limit on the time step size. However, it was felt that the simplicity of this mixed derivative treatment would outweigh the occurrence of any slight inaccuracies. The problem of product derivatives could be treated in a similar manner. These terms are normally found in the energy conservation equation.

5.6 LINEARIZATION OF THE FINITE DIFFERENCE EQUATIONS

Applying the temporal finite difference techniques to the MGD equations, yields a set of nonlinear algebraic equations of the form

$$\vec{T}(\vec{u}^{*}) - T(\vec{u}^{n}) + \frac{\Delta t}{2}\ \{\vec{F}(\vec{u}^{*},\vec{u}^{n}) + \vec{H}(\vec{u}^{n})\} - \frac{\Delta t}{2}(\vec{J}\times\vec{B}) = 0 \qquad (5.16)$$

where $\vec{u} = \{\vec{v},\rho\}$ and $\vec{T}(\vec{u}) = \{\rho\vec{v},\rho\}$. The term $\rho\vec{v}$ in the vector $\vec{T}$ is an example of a nonlinear term. Since Eqn. 5.16 is nonlinear, terms such as ρv are present when both ρ and v are being sought for at the next time step. Consequently, a straightforward solution of this system of equations is not possible. Instead, an iterative technique will be developed to solve for the nonlinearly coupled unknowns in Eqn. 5.16 at the new time step.

The nonlinear set of vector equations given by Eqn. 5.16 can be written in the form

$$\vec{W}(\vec{u}^{n},\vec{u}^{*}) = \vec{W}_{e}(\vec{u}^{n}) + \vec{W}_{i}(\vec{u}^{n},\vec{u}^{*}) = 0\ , \qquad (5.17)$$

since $\vec{W}(\vec{u}^{n},\vec{u}^{*})$ can be considered to have an explicit part $\vec{W}_{e}(\vec{u}^{n})$ which only depends on $\vec{u}^{n}$; and an implicit part $\vec{W}_{i}(\vec{u}^{n},\vec{u}^{*})$ which depends on $\vec{u}^{*}$ and $\vec{u}^{n}$.

In order to linearize this set of equations, the function $\vec{W}(\vec{u}^{n},\vec{u}^{*})$ must be continuous and differentiable so that it may be expanded in a Taylor series. In this manner, the function $\vec{W}({}^{\ell+1}\vec{u})$ be expressed in terms of the function and its derivatives at ${}^{\ell}\vec{u}$

as follows:

$$ {}^{\ell+1}\vec{W} = {}^{\ell}\vec{W} + \left(\frac{\partial\vec{W}}{\partial\vec{u}^{*}}\right)^{\ell} \cdot \left(\frac{\partial\vec{u}^{*}}{\partial t}\right)^{\ell} \Delta t + O(\Delta t)^2 \ , \qquad (5.18) $$

where ${}^{\ell+1}\vec{W} = \vec{W}({}^{\ell+1}\vec{u})$ and ℓ is the iteration index. The linearization is performed by a two-step process of expansion about the known time level t^n and subsequent approximation of the quantity $\left(\frac{\partial\vec{u}^{*}}{\partial t}\right)\Delta t$ by $({}^{\ell+1}\vec{u} - {}^{\ell}\vec{u})$. This term arises from chain rule differentiation. If the vector ${}^{\ell+1}\vec{u}$ is close to the actual root of Eqn. 5.18, then ${}^{\ell+1}\vec{W} \simeq 0$. In addition, if ${}^{\ell}\vec{u}$ is very close to ${}^{\ell+1}\vec{u}$, then all terms of second order or higher may be neglected, that is $({}^{\ell+1}\vec{u} - {}^{\ell}\vec{u})^2 \simeq 0$. Applying these results, the Taylor series expansion simplifies to

$$ 0 \simeq {}^{\ell}\vec{W} + \left(\frac{\partial\vec{W}}{\partial\vec{u}^{*}}\right)^{\ell} \cdot ({}^{\ell+1}\vec{u} - {}^{\ell}\vec{u}) + O(\Delta t)^2 \ . \qquad (5.19) $$

The matrix $(\partial\vec{W}/\partial\vec{u}^{*})$ is a standard Jacobian whose elements are defined as

$$ \hat{J} = \left(\frac{\partial\vec{W}}{\partial\vec{u}^{*}}\right) = \frac{\partial(W_1,W_2,W_3,W_4)}{\partial(v_1^{*},v_2^{*},v_3^{*},\rho^{*})} \ . $$

Since the Jacobian $\hat{J}$ only measures the $\vec{u}^{*}$ dependence, only the implicit portion of $\vec{W}(\vec{u}^{n},\vec{u}^{*})$ need be differentiated.

The expression in Eqn. 5.19 describes a generalized Newton-Raphson iteration method which provides second order convergence. Rearranging this equation reveals a simple iteration formula, namely,

$$ {}^{\ell}\hat{J} \cdot {}^{\ell+1}\vec{u} = {}^{\ell}\hat{J} \cdot {}^{\ell}\vec{u} - {}^{\ell}\vec{W} \ , \qquad (5.20) $$

where the first iteration ${}^{1}\vec{u}$ takes on the value of $\vec{u}^{n}$ at the old level t^n. As derived by Finan [5.5], this equation is representative of the actual expression to be solved. The solution of the finite difference expression (Eqn. 5.16), at the grid point i, will involve state vector values at three lattice points, namely $i + 1$, i, and $i - 1$. As a result of the Newton-Raphson iterative procedure, a Jacobian must also be determined with respect to each of these lattice points. Thus, for an implicit expression in the ith direction, the finite difference scheme produces a formulation similar to Eqn. 5.20, that is,

$$
\begin{aligned}
&{}^{\ell}\hat{J}_{i+1,j} \cdot {}^{\ell+1}\vec{u}_{i+1,j} + {}^{\ell}\hat{J}_{i,j} \cdot {}^{\ell+1}\vec{u}_{i,j} + {}^{\ell}\hat{J}_{i-1,j} \cdot {}^{\ell+1}\vec{u}_{i-1,j} \\
&\quad = {}^{\ell}\hat{J}_{i+1,j} \cdot {}^{\ell}\vec{u}_{i+1,j} + {}^{\ell}\hat{J}_{i,j} \cdot {}^{\ell}\vec{u}_{i,j} + {}^{\ell}\hat{J}_{i-1,j} \cdot {}^{\ell}\vec{u}_{i-1,j} - {}^{\ell}W \,. \qquad (5.21)
\end{aligned}
$$

The function ${}^{\ell}W$ also includes the explicit mixed derivative terms.

The solution matrix can now be rearranged into the standard ADI form, namely

$$
- \hat{A}_{i,j} \cdot {}^{\ell+1}\vec{u}_{i+1,j} + \hat{B}_{i,j} \cdot {}^{\ell+1}\vec{u}_{i,j} - \hat{C}_{i,j} \cdot {}^{\ell+1}\vec{u}_{i-1,j} = \vec{D}_{i,j} \qquad (5.22)
$$

where $\hat{A}$, $\hat{B}$, and $\hat{C}$ are the Jacobians differentiated with respect to the vector $\vec{u}$ on the lattice points $(i+1,j)$, (i,j), and $(i-1,j)$ respectively. The vector $\vec{D}$ contains all the explicit terms and satisfies the equation

$$
\vec{D}_{i,j} = -\hat{A}_{i,j} \cdot {}^{\ell}\vec{u}_{i+1,j} + \hat{B}_{i,j} \cdot {}^{\ell}\vec{u}_{i,j} - \hat{C}_{i,j} \cdot {}^{\ell}\vec{u}_{i-1,j} - {}^{\ell}W \,. \qquad (5.23)
$$

Since the ADI vector equations (5.22, 5.23) are uncoupled with respect to j, the two-dimensional problem can be expressed as two problems in which only one dimension is advanced implicitly per half time step. More simply, Eqn. 5.22 takes on a block tridiagonal matrix structure where each block is an $m \times m$ submatrix. Here, m represents the number of state variables to be solved, that is, three velocity components and the mass density. The resulting tridiagonal matrix can then be written in the form

$$\begin{bmatrix} \hat{B}_1 & -\hat{C}_1 & & & & & 0 \\ -\hat{A}_2 & \hat{B}_2 & -\hat{C}_2 & & & & \\ & -\hat{A}_3 & \hat{B}_3 & -\hat{C}_3 & & & \\ & & \cdots\cdots & & & & \\ & & -\hat{A}_i & \hat{B}_i & -\hat{C}_i & & \\ & & & \cdots\cdots & & & \\ 0 & & & -\hat{A}_{N-1} & \hat{B}_{N-1} & -\hat{C}_{N-1} \\ & & & & -\hat{A}_N & \hat{B}_N \end{bmatrix} \cdot \begin{bmatrix} \vec{u}_1 \\ \vec{u}_2 \\ \vec{u}_3 \\ \vdots \\ \vec{u}_i \\ \vdots \\ \vec{u}_{N-1} \\ \vec{u}_N \end{bmatrix} = \begin{bmatrix} \vec{D}_1 \\ \vec{D}_2 \\ \vec{D}_3 \\ \vdots \\ \vec{D}_i \\ \vdots \\ \vec{D}_{N-1} \\ \vec{D}_N \end{bmatrix} . \quad (5.24)$$

In this representation, the block elements are depicted by the Jacobian matrices $\hat{A}$, $\hat{B}$, and $\hat{C}$. This convenient form is then readily solved by a Gaussian elimination method.

5.7 SOLUTION OF THE DIFFERENCE EQUATIONS

The problem of solving the set of two-dimensional partial differential equations has now been reduced to solving sets of simultaneous linear algebraic equations. The resulting difference equations, after the first half time step, have the form

$$-\hat{A}^{n}_{i,j} \cdot \vec{u}^{\star}_{i+1,j} + \hat{B}^{n}_{i,j} \cdot \vec{u}^{\star}_{i,j} - \hat{C}^{n}_{i,j} \cdot \vec{u}^{\star}_{i-1,j} = \vec{D}^{n}_{i,j} \tag{5.25a}$$

and on the following half time step

$$-\hat{A}^{\star}_{i,j} \cdot \vec{u}^{n+1}_{i,j+1} + \hat{B}^{\star}_{i,j} \cdot \vec{u}^{n+1}_{i,j} - \hat{C}^{\star}_{i,j} \cdot \vec{u}^{n+1}_{i,j-1} = \vec{D}^{\star}_{i,j} \ . \tag{5.25b}$$

For a set of m partial differential equations, $\hat{A}$, $\hat{B}$, and $\hat{C}$ represent $m \times m$ matrices while $\vec{u}$ and $\vec{D}$ represent m component vectors defined at the mesh point i,j. Equations 5.25 are valid over the interior mesh points for which $i = 2,3,\ldots,N-1$ and $j = 2,3,\ldots M-1$. However, they do not form a complete set. The remaining equations are provided by the boundary conditions at i equal to 1 and N for all j; and for j equal to 1 and M for all i.

The ADI finite difference scheme requires boundary conditions, on the first half time step, to have the form

$$\hat{G}^{n}_{1,j} \cdot \vec{u}^{\star}_{1,j} = \hat{H}^{n}_{1,j} \cdot \vec{u}^{\star}_{2,j} + \vec{J}^{n}_{1,j} \ , \tag{5.26a}$$

and

$$\hat{G}^{n}_{N,j} \cdot \vec{u}^{\star}_{N,j} = \hat{H}^{n}_{N,j} \cdot \vec{u}^{\star}_{N-1,j} + \vec{J}^{n}_{N,j} \tag{5.26b}$$

for $1 < j < M$, while

$$\hat{G}^{n}_{i,1} \cdot \vec{u}^{\star}_{i,1} = \hat{H}^{n}_{i,1} \cdot \vec{u}^{\star}_{i,2} + \vec{J}^{n}_{i,1} \tag{5.27a}$$

and

$$\hat{G}^{n}_{i,M} \cdot \vec{u}^{*}_{i,M} = \hat{H}^{n}_{i,M} \cdot \vec{u}^{*}_{i,M-1} + \vec{J}^{n}_{i,M} \qquad (5.27b)$$

for $1 < i < N$. In the above equations, $\hat{G}$ and $\hat{H}$ are $m \times m$ matrices and $\vec{J}$ represents an m component vector. Each of these four boundary conditions satisfies one side of the two-dimensional mesh. On the second half time step, the boundary conditions will have the same form as Eqns. 5.26 and 5.27 but with the superscripts n and $*$ replaced by $*$ and $n + 1$, respectively.

The procedure for solving this system of equations, is a generalization of the method developed by Richtmyer and Morton [5.7] for a two-dimensional case. In this situation, their scalar equation becomes a vector equation with matrix coefficients. Since Eqns. 5.25a and 5.26 are uncoupled with respect to j, the state vector $\vec{u}$, along lines of constant j, can be determined independent of $\vec{u}$ along other lines of constant j. This attractive feature of the ADI technique leads to the recursion relationship between the $\vec{u}$ values at adjacent mesh points, that is,

$$\vec{u}^{*}_{i,j} = \hat{E}^{n}_{i,j} \cdot \vec{u}^{*}_{i+1,j} + \vec{F}^{n}_{i,j} \qquad (5.28)$$

for $i = 1,2,\ldots,N-1$.

The values for the matrix $\hat{E}_{1,j}$ and vector $\vec{F}_{1,j}$ at $i = 1$ can be calculated by first rearranging the boundary condition (Eqn. 5.26a) into the form

$$\vec{u}^{*}_{1,j} = (\hat{G}^{n}_{1,j})^{-1} \; \hat{H}^{n}_{1,j} \cdot \vec{u}^{*}_{2,j} + (\hat{G}^{n}_{1,j})^{-1} \cdot \vec{J}^{n}_{1,j} \; .$$

Comparing this result with Eqn. 5.28 yields

$$\hat{E}^n_{i,j} = (\hat{G}^n_{1,j})^{-1}\cdot\hat{H}^n_{1,j} \tag{5.29a}$$

and

$$\vec{F}^n_{1,j} = (\hat{G}^n_{1,j})^{-1}\cdot\vec{J}^n_{1,j}\ . \tag{5.29b}$$

To obtain the recurrence relation for $\hat{E}^n_{i,j}$ and $\vec{F}^n_{i,j}$ for $1 < i < N$, it is necessary to substitute Eqn. 5.28 for $i - 1$ into Eqn. 5.25a. This produces the expression

$$-\hat{A}^n_{i,j}\cdot\vec{u}^{\,*}_{i+1,j} + (\hat{B}^n_{i,j}-\hat{C}^n_{i,j}\ \hat{E}^n_{i-1,j})\cdot\vec{u}^{\,*}_{i,j} = \vec{D}^n_{i,j} + \hat{C}^n_{i,j}\cdot\vec{F}^n_{i-1,j}\ .$$

Now solving for the $\vec{u}^{\,*}_{i,j}$ gives

$$\begin{aligned}\vec{u}^{\,*}_{i,j} &= (\hat{B}^n_{i,j}-\hat{C}^n_{i,j}\ \hat{E}^n_{i-1,j})^{-1}\ \hat{A}^n_{i,j}\cdot\vec{u}^{\,*}_{i+1,j}\\ &\quad+ (\hat{B}^n_{i,j}-\hat{C}^n_{i,j}\ \hat{E}^n_{i-1,j})^{-1}\cdot(\vec{D}^n_{i,j}+\hat{C}^n_{i,j}\cdot\vec{F}_{i-1,j})\ .\end{aligned} \tag{5.30}$$

Comparison of Eqn. 5.30 with 5.28 shows that

$$\hat{E}^n_{i,j} = (\hat{B}^n_{i,j}-\hat{C}^n_{i,j}\ \hat{E}^n_{i-1,j})^{-1}\ \hat{A}^n_{i,j} \tag{5.31a}$$

and

$$\vec{F}^n_{i,j} = (\hat{B}^n_{i,j}-\hat{C}^n_{i,j}\ \hat{E}^n_{i-1,j})^{-1}\cdot(\vec{D}^n_{i,j}+\hat{C}^n_{i,j}\cdot\vec{F}^n_{i-1,j}) \tag{5.31b}$$

valid for $i = 2,3,\ldots,N-1$.

Lastly, the recursion relation of Eqn. 5.28 with $i = N - 1$, can be substituted into the boundary condition (Eqn. 5.26b) to solve for $\vec{u}^{\,*}_N$. That is,

$$\hat{G}^n_{N,j}\cdot\vec{u}^{\,*}_{N,j} = \hat{H}^n_{N,j}\cdot(\hat{E}^n_{N-1,j}\cdot\vec{u}^{\,*}_{N,j}+\vec{F}_{N-1,j}) + \vec{J}^n_{N,j}\ .$$

Rearranging this expression yields

$$\vec{u}^{\,*}_{N,j} = (\hat{G}^{n}_{N,j} - \hat{H}^{n}_{N,j}\,\hat{E}^{n}_{N-1,j})^{-1}\cdot(\hat{H}^{n}_{N,j}\cdot\vec{F}^{n}_{N-1,j} + \vec{J}^{n}_{N,j}) \ . \qquad (5.32)$$

The solution algorithm is now almost complete. During calculation, the recurrence matrix $\hat{E}$ and vector $\vec{F}$ are first calculated by making a forward sweep from i equal to 1 to $N - 1$ using Eqns. 5.29 and 5.31. Next $\vec{u}^{\,*}_{N,j}$ is determined through Eqn. 5.32. Finally, the remaining state vectors $\vec{u}^{\,*}_{i,j}$ are computed by backsubstitution using Eqn. 5.28.

The method presented, thus far, enables the calculation of all $\vec{u}^{\,*}$ values for all i when $1 < j < M$. The remaining values along $j = 1$ and $j = M$ for $1 < i < N$ can be calculated by rearranging the boundary condition (Eqn. 5.27) using previously determined values. Now, only the $\vec{u}^{\,*}$ values located at the four corner points (1,1), (1,M), (N,1), and (N,M) remain to be calculated. Any symmetry condition along either boundary can be used to estimate these points. If no symmetry condition exists, then the values at the corner points can be determined by passing a polynomial through the adjacent mesh points, for which the $\vec{u}^{\,*}$ values have already been calculated [5.8]. A second order accurate polynomial for the corner point (1,1) produces

$$\vec{u}^{\,*}_{1,1} = \vec{u}^{\,*}_{1,2} + \vec{u}^{\,*}_{2,1} - \vec{u}^{\,*}_{2,2} \ . \qquad (5.33)$$

The remaining corner points are estimated in the same manner.

On the second half time step, the difference equations are solved along rows of constant i, using the equation

$$\vec{u}^{\,n+1}_{i,j} = \hat{E}^{*}_{i,j}\cdot\vec{u}^{\,n+1}_{i,j+1} + \vec{F}^{*}_{i,j} \ . \qquad (5.34)$$

The procedure followed when the ith component becomes the implicit variable is identical to the previous half time step, but with the subscript indices i and j interchanged.

For a general set of $m \times M \times N$ simultaneous equations, an $m \times M \times N$ matrix must be inverted. However, the method presented takes advantage of the block tridiagonal nature of the ADI finite difference technique. As a result, this procedure only involves the inversion of M $m \times m$ matrices along one dimension and N $m \times m$ matrices along the other. The substantial reduction in the number of floating point operations in the ADI scheme greatly enhances computational efficiency and reduces roundoff error.

5.8 BOUNDARY CONDITIONS

To ensure a proper solution over the entire mesh, the boundary conditions must be accurately specified. In addition, the boundary conditions must be compatible with the block tridiagonal form of the ADI solution technique. Examination of the matrix expression in Eqn. 5.24, reveals that the boundary conditions are represented by the rows $i = 1$ and $i = N$ for the case when i is implicit. These rows have the general form

$$\hat{G} \cdot \vec{u}_{BP} = \hat{H} \cdot \vec{u}_{INT} + \vec{J} \qquad (5.35)$$

where $\vec{u}_{BP}$ is the boundary point and $\vec{u}_{INT}$ is the next interior point. All forms of Dirichlet, Neumann, and mixed boundary conditions can be depicted by the equation

$$\hat{\alpha} \cdot \frac{\partial \vec{u}}{\partial n} + \beta \cdot \vec{u} = \vec{\gamma} \qquad (5.36)$$

where $\frac{\partial}{\partial n}$ is the derivative normal to the boundary. Applying the finite difference technique to Eqn. 5.36 transforms it into the standard form of Eqn. 5.35. Consequently, all classifications of boundary conditions can be employed in the ADI scheme.

In order to preserve second order finite difference accuracy throughout the program, ghost point boundary conditions were selected. In this method, the boundary walls are chosen to lie halfway between the first two mesh row points and the last two rows. Through this procedure, the derivatives along the boundary are second order accurate approximations.

The simulation mesh covers the domain $0 \leq r \leq R_0$ and $0 \leq z \leq d$. Due to azimuthal symmetry, the solution is valid for all values of θ. The anode and cathode can be assumed to be perfectly conducting walls which lie along the rows $j = 1 + 1/2$ and $j = M - 1/2$. Thus, the ghost or exterior mesh points lie along the rows $j = 1$ and $j = M$. This particular arrangement of boundaries is illustrated by Fig. 5.4. Since the electrodes can be considered a solid wall,

$$\vec{n} \cdot \vec{v}_w = 0$$

where $\vec{n}$ is the unit normal vector outward from the wall, and $\vec{v}_w$ is the velocity at the wall. Since $\vec{v}_w$ is parallel to $\vec{n}$, this Dirichlet boundary condition can only be satisfied if $v_w = 0$. Therefore, at the electrode walls

$$v_z(r,0) = v_z(r,d) = 0 \ . \tag{5.37}$$

The boundary conditions must also consider that the ionized gas cannot

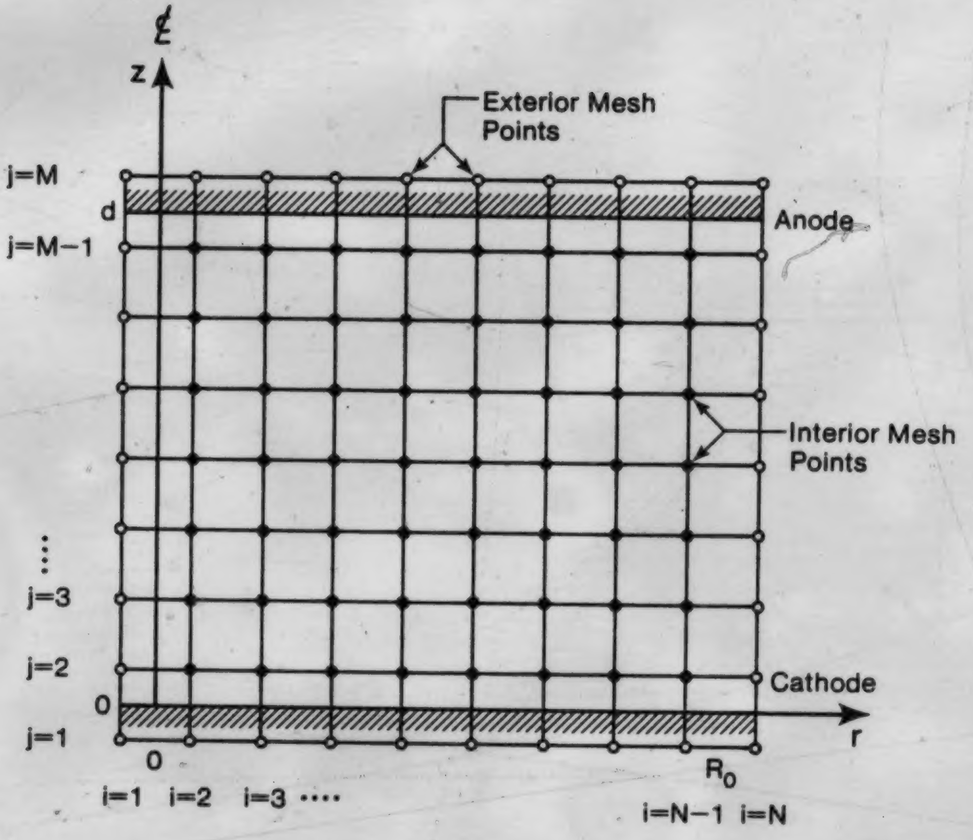
℄
z
Exterior Mesh Points
j=M
d
Anode
j=M−1
Interior Mesh Points
j=3
j=2
Cathode
0
j=1
r
0
R0
i=1 i=2 i=3 ····
i=N−1 i=N

Fig. 5.4 Arrangement of Ghost Point Boundaries on the Finite Difference Mesh.

slip along these walls. Consequently, the tangential velocity $\vec{v}_t$ is fixed at the wall by the relation

$$\vec{v}_t = 0 \ .$$

With this Dirichlet condition,

$$\begin{aligned} &v_r(r,0) = v_r(r,d) = 0 \\ \text{and} \qquad & \qquad\qquad\qquad\qquad\qquad\qquad (5.38) \\ &v_\theta(r,0) = v_\theta(r,d) = 0 \ . \end{aligned}$$

In order for the solution to remain finite, an axis of symmetry exists along $r = 0$. Furthermore, the following Dirichlet conditions must hold:

$$v_r(0,z) = v_\theta(0,z) = v_z(0,z) = 0 \ . \tag{5.39}$$

Along the outside radial boundary, viscous drag from the walls will start to reduce the azimuthal velocity. However, even though the driving force terms are now reduced to zero, strong viscous coupling of the fluid will keep v_θ high. Consequently, at $r = R_0$, the azimuthal velocity is subject to a Neumann boundary condition of the form

$$\frac{\partial}{\partial r}(h_2 v_\theta(R_0,z)) = 0 \ . \tag{5.40}$$

The boundaries, for the secondary flow velocities, are sufficiently removed so that the solution should approach zero. Therefore, they satisfy the Dirichlet condition

$$v_r(R_0,z) = v_z(R_0,z) = 0 \ . \tag{5.41}$$

Outside the domain of interest, the neutral mass density is assumed to be constant. Therefore, to satisfy this condition, the boundary condition

$$\frac{\partial \rho}{\partial n} = 0 \tag{5.42}$$

is applied along all boundaries.

Applying the finite difference operations of Section 5.4, to Eqns. 5.37-5.41, produces a set of equations which will represent the boundary conditions. Combining these difference equations into the matrix Eqn. 5.35, creates the submatrix elements used in the block tridiagonal form. Along the $j = 1$, and $j = M$ boundaries

$$\hat{G}_U = \hat{G}_D = \begin{bmatrix} 1 & 0 & 0 & 0 \\ 0 & 1 & 0 & 0 \\ 0 & 0 & 1 & 0 \\ 0 & 0 & 0 & 1 \end{bmatrix} \tag{5.43a}$$

and

$$\hat{H}_U = \hat{H}_D = \begin{bmatrix} -1 & 0 & 0 & 0 \\ 0 & -1 & 0 & 0 \\ 0 & 0 & -1 & 0 \\ 0 & 0 & 0 & 1 \end{bmatrix} \tag{5.43b}$$

and

$$\vec{J}_U = \vec{J}_D = 0 \tag{5.43c}$$

where the subscripts U and D refer to the 'up' and 'down' boundary walls.

Similarly, for the $i = 1$, and $i = N$ boundaries

$$\hat{G}_L = \begin{bmatrix} 1 & 0 & 0 & 0 \\ 0 & 1 & 0 & 0 \\ & & & \\ 0 & 0 & 1 & 0 \\ 0 & 0 & 0 & 1 \end{bmatrix} , \quad \hat{G}_R = \begin{bmatrix} 1 & 0 & 0 & 0 \\ 0 & h_{2_{N-1}} & 0 & 0 \\ & & & \\ 0 & 0 & 1 & 0 \\ 0 & 0 & 0 & 1 \end{bmatrix} \tag{5.44a}$$

and

$$\hat{H}_L = \begin{bmatrix} -1 & 0 & 0 & 0 \\ 0 & -1 & 0 & 0 \\ & & & \\ 0 & 0 & -1 & 0 \\ 0 & 0 & 0 & 1 \end{bmatrix} , \quad \hat{H}_R = \begin{bmatrix} -1 & 0 & 0 & 0 \\ 0 & h_{2_N} & 0 & 0 \\ & & & \\ 0 & 0 & -1 & 0 \\ 0 & 0 & 0 & 1 \end{bmatrix} \tag{5.44b}$$

and

$$\vec{\mathcal{J}}_L = \vec{\mathcal{J}}_R = 0 \tag{5.44c}$$

where the subscripts L and R refer to the 'left' and 'right' boundary sides.

5.9 ITERATIONS AND DYNAMIC TIME STEP CONTROLS

The derived set of nonlinear finite difference equations employs a Newton-Raphson iterative procedure in order to accurately invert the block tridiagonal matrix. Since the ADI technique decouples the rows of the mesh, it becomes possible to vary the number of iterations per row depending upon the degree of change in a state variable along that row. Thus, rows with large changes will iterate many times while rows that have little or no change will only iterate a few times. Each row is tested for convergence by comparing the maximum variation of the state vector between iterations versus the average value of the iterations. Specifically, the convergence criterion ε is given by

$$\varepsilon = \max \left| 2({}^{\ell+1}\vec{u}_{i,j} - {}^{\ell}\vec{u}_{i,j})/({}^{\ell+1}\vec{u}_{i,j} + {}^{\ell}\vec{u}_{i,j}) \right| . \tag{5.45}$$

This condition is subject to the constraint that should ${}^{\ell}\vec{u}_{i,j}$ be less than a preset floor value, then the floor value is used for ${}^{\ell+1}\vec{u}_{i,j}$ in the denominator of Eqn. 5.45. The maximum value of ε along a row is then compared with an allowable convergence criterion $\varepsilon_{\max}$. If $\varepsilon < \varepsilon_{\max}$, the row is declared converged; otherwise the iteration procedure is continued. The value of the convergence criterion depends upon the accuracy desired; typically $\varepsilon_{\max} < 10^{-5}$ for most operational runs.

In order to minimize computational costs, a dynamic time stepping routine was also implemented. This algorithm permitted the program to operate over a range of allowable time steps. The extent over which the time step could operate was determined by monitoring the maximum change in the state vector between time steps. Should the state vector values be below a floor condition, no check was performed. Furthermore, by constantly revising the floor condition to 5 percent of the maximum mesh velocity, the program time step will not be limited by small variations on the mesh.

The maximum variation over the mesh can be expressed as

$$V_{\max} = \max \left| (\vec{u}^{\,n+1}_{i,j} - \vec{u}^{\,n}_{i,j})/\vec{u}^{\,n}_{i,j} \right| . \tag{5.46}$$

To implement this dynamic time stepping procedure, the maximum variation $V_{\max}$ is compared with a prescribed maximum allowable change c. For a typical computer run, the maximum fractional change, in any state variable, has been kept to less than 60 percent per time step, that is, $c = 0.6$. If $V_{\text{max}} < 0.8c$, then the time step is increased by 10 percent. For the case $V_{\text{max}} > 1.5c$, a recycle is performed; otherwise if $0.8c \le V_{\text{max}} \le 1.5c$, the time step is decreased by the relation

$$\Delta t = 0.8\Delta t(c/V_{\text{max}}) \ . \tag{5.47}$$

This technique is very flexible in that it allows the program to check the variation of any variable; including velocity, momentum, or energy. As a result of these time step controls, the optimal efficiency of MAGIC, with respect to computational running costs, is maintained.

CHAPTER 6

EXPERIMENTAL RESULTS AND DISCHARGE OBSERVATIONS

6.1 NUMERICAL RESULTS OF THE TRANSVERSE GEOMETRY

6.1.1 Velocity Profile

As described in the previous chapter, a computer code was developed to model the time dependent behavior of a gas discharge. Its primary objective was to determine the three-dimensional gas flow pattern created by the spatially dependent $\vec{J} \times \vec{B}$ Lorentz force. In order to accurately simulate this behavior it became necessary to include secondary flow terms in the MGD equations. Such terms are often assumed to be small and are neglected in order to simplify the analysis in gas discharge systems [1.17-1.21]. However, as will be subsequently described, this assumption can be an extreme oversimplification to a complex gas discharge problem.

An analysis of the steady-state magnetically stabilized gas discharge was initially performed by neglecting secondary axial and radial mass flows [4.5]. The rotational gas discharge velocity obtained from the one-fluid Navier-Stokes equation is illustrated in Fig. 6.1. This plot indicates that a strongly sheared velocity profile exists across the discharge. Furthermore, a peak rotational velocity of 250 m/s can be noted. Subsequent experiments with the transverse geometry have revealed a much smaller rotational velocity in addition to the observance of a radial afterglow. This large

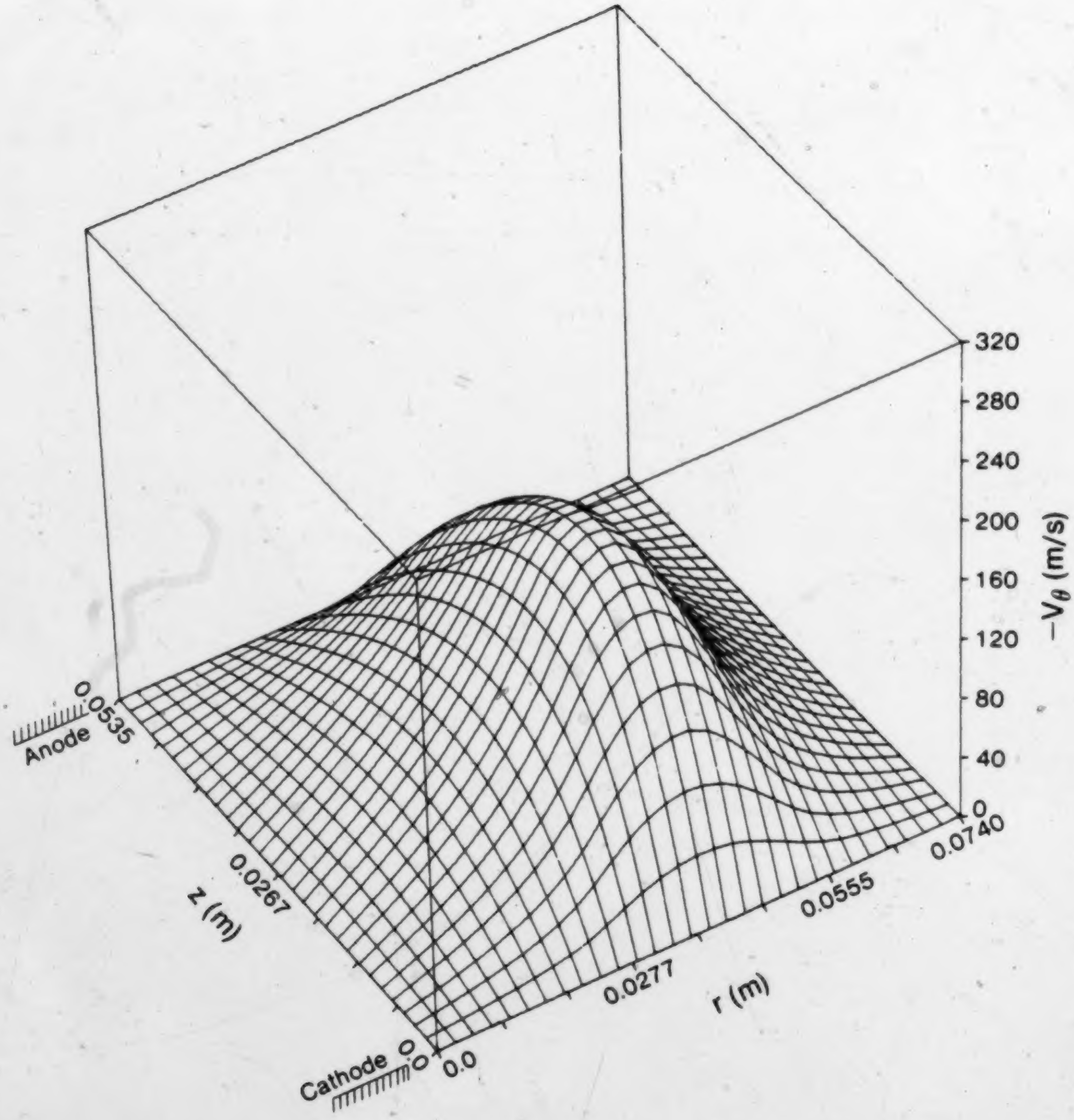

Fig. 6.1 Rotational Velocity Distribution for the Transverse Geometry Neglecting Secondary Flow. Discharge parameters include: $J = 22$ mA/cm^2, $\mu = 6.6 \times 10^{-6}$ kg/(m·s).

discrepancy between the initial theoretical model and the experimental studies can only be explained by the neglect of the secondary flow terms.

In a gas discharge system, designed for a high power laser, it is preferable to excite the gas molecules into the upper vibrational and rotational levels rather than produce ionization. As a result, the applied E/n values are kept relatively low so that the degree of ionization is maintained in the range 10^{-6} to 10^{-7}. Since the number of energetic ions is orders of magnitude less than that used in highly ionized gas centrifuge devices, substantially less momentum will be transferred to the predominantly neutral gas via inelastic collisions. As a consequence, greatly reduced gas flow velocities are expected in a laser gas discharge.

Upon application of a magnetic field, the charged particles are subjected to a Lorentz force which alters their normal collisional behavior. The derivation in Chapter 7 will show that the usual direction of the charged particle drift velocity will be changed such that the electrons and ions will have a longer inter-electrode transit time. During this transit period, the charged particles undergo additional inelastic collisions with the neutral particles. This process allows more momentum to be transferred to the neutral particles than would otherwise be possible. The additional momentum transferred to the neutral gas molecules is preferentially applied in the direction of the driving force, that is, the azimuthal direction. However, due to the existence of pressure gradient forces, ion momentum can be transferred to other directions as well. This process is responsible for the creation of secondary flows. Within spatially dependent magnetic fields, additional Lorentz forces are produced which can further stimulate these flows.

In this section, the results of the ADI program MAGIC will be presented along with an evaluation of its performance. As stated earlier, the rotational velocity produced by an applied Lorentz force is expected to be significantly reduced due to the presence of secondary flows in this highly viscous, partially ionized gas. The plot in Fig. 6.2 is a representation of the azimuthal velocity v_θ, 4.0 ms after the Lorentz force has been applied. The parameters used in this calculation include a 2:2:16 torr gas mixture of $CO_2/N_2/He$ with a neutral gas temperature of 425°K. In addition, the total discharge current was 5 A and the viscosity coefficient, μ was set to 6.6×10^{-6} kg/m·s. With these discharge parameters, the maximum rotational velocity was 35 m/s. This value is substantially below that predicted by the original model which neglected secondary flows. The peak rotational velocity occurs near the cathode surface since the driving forces are largest in this region. It is also evident that the rotational flow is strongly sheared throughout the discharge volume as a result of the spatially dependent Lorentz forces. The conservation of momentum equation (Eqn. 4.12) indicates that the rotational velocity will be proportional to the Lorentz force and hence to the discharge current. Thus, it appears feasible that larger flow velocities can be produced through the use of higher current densities.

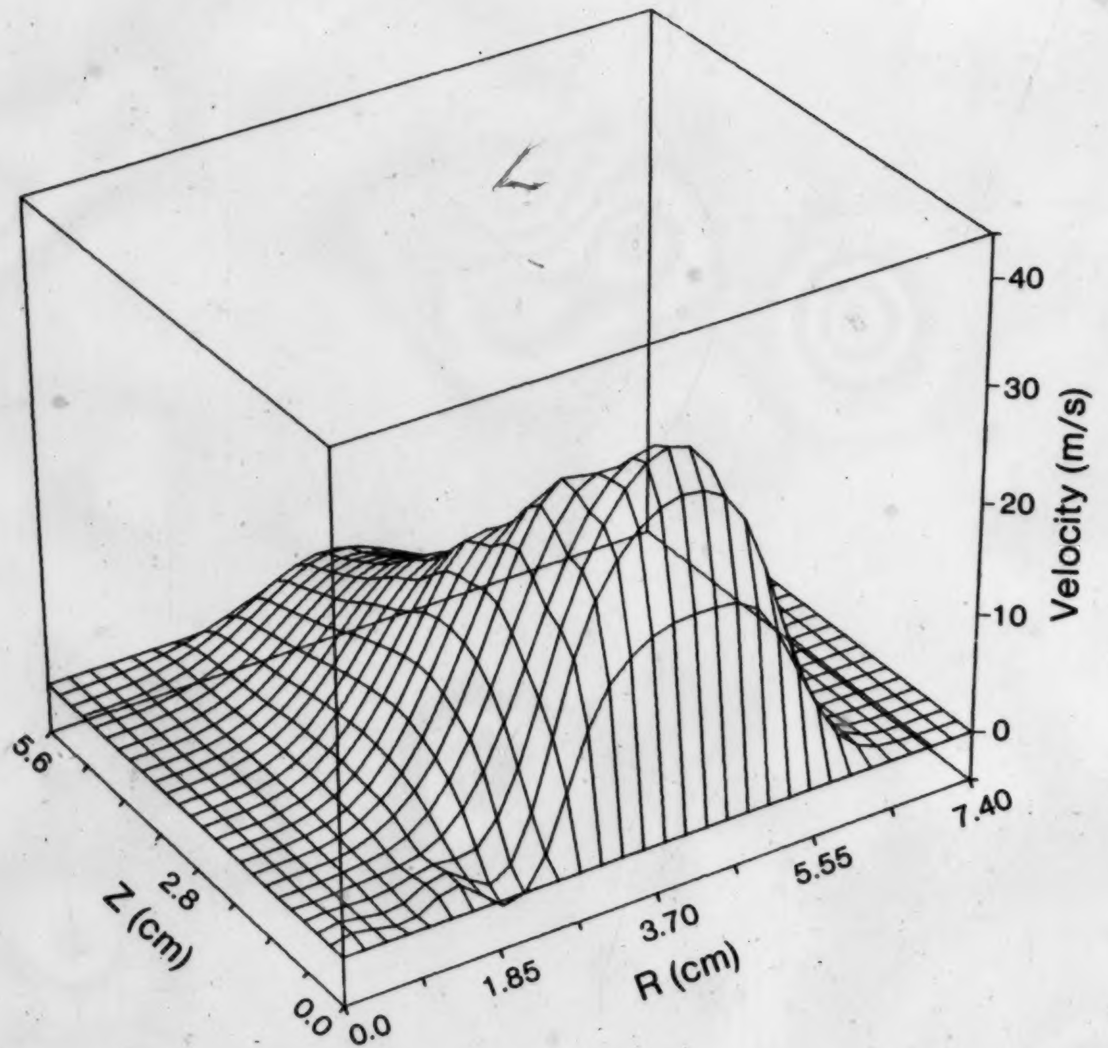

Fig. 6.2 Rotational Velocity Distribution for the Transverse Geometry Including Secondary Flow. Discharge parameters include: $J = 22\ \mathrm{mA/cm^2}$, $\mu = 6.6 \times 10^{-6}\ \mathrm{kg/(m \cdot s)}$.

Figure 6.3 is a computer plot of the secondary flow pattern generated by the MGD model employed in MAGIC. The arrows show the direction and magnitude of the secondary flow at a time, 6.0 ms after the driving force has been applied. The longest arrows in this diagram represent velocities of approximately 32 m/s. This figure clearly shows the existence of a convective cell where the secondary flow is forced to recirculate upon itself. In order to save computational costs, the outer radial finite difference mesh boundary was moved closer to the discharge. The actual outer boundary wall is somewhat further away, however, little change in the recirulating flow pattern is expected.

In this MGD system, the normally neglected secondary flows have been found to be approximately equal in magnitude to the principle rotational flow v_θ . The existence of such large axial and radial gas flows must therefore be highly significant in determining the overall behavior of the gas discharge. It is obvious that such characteristics play an important role in the exceptionally effective stabilization mechanism found in this system. It is suspected that any localized nonuniformities in density, temperature, or current are rapidly distributed over the entire discharge volume in a time very much less than the normal instability formation time.

It may also be possible to exploit the large radial gas flows in order to cool the hot gas produced within the plasma. It is anticipated that with further adjustments, a large recirculating convective cell may be established. This would allow the hot neutral gas to be transported radially outwards towards a heat exchanger where

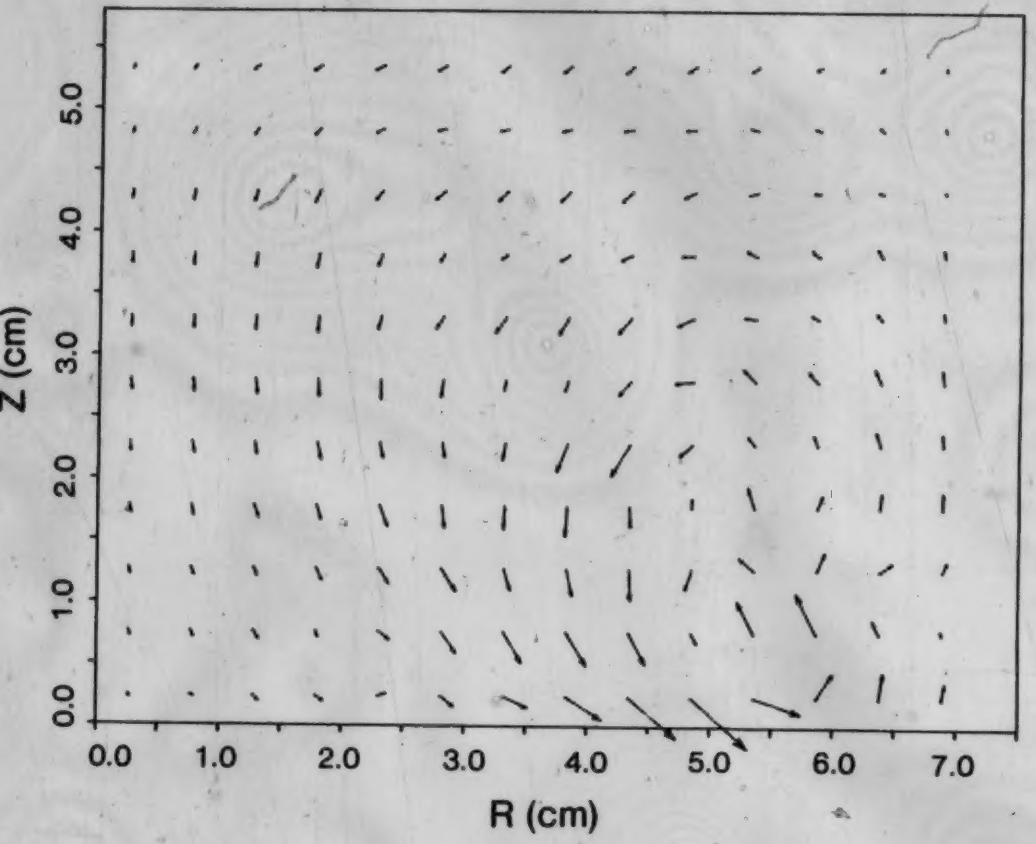

Fig. 6.3 Secondary Flow Pattern for the Transverse Geometry.

it can then be cooled and returned back to the discharge. In this radial flow system, the hot gas need only travel across one-half the electrode length to escape the excitation processes. Consequently, such a system will only have one-half the normal gas residence time found in conventional transverse devices.

It must be noted that the calculated flow velocity values represent the mass averaged flow of the gas discharge system as determined by a one-fluid MGD model. Since the degree of ionization is only 2.6×10^{-7}, the plotted values are essentially those of the viscous neutral gas and do not represent the flow pattern of the charged species. This additional information can only be attained through the use of a two-fluid model which could account for the motion of charged and neutral particles and their interaction through collisions.

To ensure that the computer code was functioning properly, an elaborate series of checks were performed as outlined in Section 5.9. An additional accuracy test was also implemented whereby the state vector solution was backsubstituted into the original set of momentum conservation equations. Through this process it was determined that each equation was satisfied to within a relative error normally less than 3%. A detailed analysis of the program has shown that this iterative ADI code can normally be operated at twice the CFL time step limit without creating any significant errors. This result makes the ADI scheme very attractive since most explicit codes of this complexity can only run at a fraction of the Courant limit (usually 20%) just to ensure stability. The net result is a substantial savings in computational costs. Further improvements in the accuracy and time step size are currently under investigation.

It has been found that ADI direction splitting methods can lead to difficulties when large magnetic fields and low electrical conductivities are involved. Craxton and McCrory [6.1] have found that the direction splitting technique produced smooth solution profiles in the last implicit direction scanned, but noisy profiles in the other direction scanned explicitly. This noise was also observed in MAGIC but could be eliminated by reducing the time step.

At present the isothermal model cannot predict the expansion of the ionized gas due to a temperature rise. In the next phase of this project, MAGIC will be expanded to incorporate the conservation of energy equation. The inclusion of this equation will be especially useful for modelling the heat transfer effect established by the rapidly recirculating flow. This will then complete the MGD model and should produce an accurate representation of a magnetically stablized gas discharge.

6.1.2 Radial Pressure Profile

A thorough analysis of the rotating gas discharge system must consider the density distribution of the charged and neutral gas molecules. In order to determine these pressure profiles, a two-fluid model must now be employed.

The momentum conservation equations for the charged and neutral fluids may be written as

$$\rho_c \frac{d\vec{v}_c}{dt} = \vec{J}\times\vec{B} - \vec{\nabla}p_c - \rho_c\nu(\vec{v}_c-\vec{v}_n) + \mu_i\vec{\nabla}^2\vec{v}_c \tag{6.1}$$

$$\rho_n \frac{d\vec{v}_n}{dt} = -\vec{\nabla}p_n - \rho_c\nu(\vec{v}_n-\vec{v}_c) + \mu_n\vec{\nabla}^2\vec{v}_n \tag{6.2}$$

where d/dt is the convective derivative for each species, $\vec{v}_c$ is the charged fluid velocity, $\vec{v}_n$ the neutral fluid velocity, $p_c = p_e + p_i$ is the sum of the electron and ion partial pressure, p_n the neutral gas pressure, and μ_i and μ_n are the viscosity coefficients for the charged and neutral fluids. The parameter ν is the collision frequency for the transfer of momentum between the charged and the neutral fluids.

The degree of coupling between the two fluids can be obtained by considering the steady-state θ-component of Eqn. 6.2, which yields

$$v_{n\theta} \simeq \frac{v_{c\theta}}{1+\mu_n/(\delta^2\rho_c\nu)} \; . \tag{6.3}$$

The Laplacian in Eqn. 6.3 has been approximated as $-1/\delta^2$. An estimated value for δ may be obtained from a second-order difference approximation for the Laplacian evaluated at the midpoint of the discharge. This result is given by $\delta \simeq L/4$ where L is the anode to cathode distance ($L = 0.0535$ m). For the discharge under examination, $\mu_n = 6.6\times10^{-6}$, $\rho_c = 2.07\times10^{-9}$, and the ion-neutral collision frequency is $\nu = 1.285\times10^{8}$. The expected neutral velocity $v_{n\theta}$ is therefore approximately 0.88 $v_{c\theta}$, which indicates a very strong coupling between the two fluids. It must be noted that the coupling that does exist is primarily between ions and neutrals since the heavy ions dominate the charged particle fluid equation.

A pressure profile for the neutral fluid can be determined by examining the steady-state r component of Eqn. 6.2 with $v_{nr} \simeq v_{cr}$. An ordering of terms will show that the viscous drag term is small. Thus, a neutral gas pressure profile will exist through a balance between centrifugal and radial pressure terms, that is,

$$-\frac{\rho_n v_{n\theta}^2}{r} + \frac{\partial p_n}{\partial r} \simeq 0 \ . \qquad (6.4)$$

This simple expression indicates that a strong centrifugal force term will transport neutral particles radially out of the discharge region. This result has indeed been confirmed by visual and experimental observations.

Results from the computer simulations show only slight variations in neutral mass density; although a small accumulation of mass was noticed near the axis of symmetry of the glow discharge. This effect can be explained by the small azimuthal velocity term found in the region near $r = 0$. Since the overall variation over the discharge volume is small, the neutral gas can be assumed incompressible.

The pressure profile for the charged particles is more complex because of Lorentz forces tending to force the plasma into an annular region. A detailed analysis of these forces will be given in Section 7.2. Since the neutral gas body is strongly coupled to the motion of the charged particles, $v_{n\theta} \simeq v_{c\theta}$. The radial component of the charged particle fluid equation, in steady-state, can now be approximated by the expression

$$\frac{\partial p_c}{\partial r} \simeq \frac{\rho_c v_{c\theta}^2}{r} + J_\theta B_z \qquad (6.5)$$

where the largest convective term has been included. Through an ordering of terms, all remaining terms have been found to be small.

The term $J_\theta B_z$ may be evaluated through the use of Ohm's law (Eqn. 4.22). The conductivity tensor $\hat{\sigma}$, has been expressed as a matrix given by Eqn. 4.23. From these equations, the current density in the azimuthal direction can be written as

$$J_\theta = -\sigma_{12} v_\theta B_z + \sigma_{22}(v_z B_r - v_r B_z) + \sigma_{23}(E_z - v_\theta B_r) \tag{6.6}$$

where σ_{ij} refers to the ijth matrix element in the conductivity tensor. This equation may be simplified by neglecting terms of order $\frac{vB}{E_z} \simeq 10^{-3}$. Therefore, to a good approximation

$$J_\theta \simeq \sigma_{23} E_z \; . \tag{6.7}$$

Upon substitution of Eqn. 6.7 into Eqn. 6.5, the charged particle pressure distribution becomes

$$\frac{\partial p_c}{\partial r} \simeq \frac{\rho_c v_{c\theta}^2}{r} + \sigma_T \cos(\phi) \cdot E_z B_z \tag{6.8}$$

where ϕ is the angle between the magnetic field lines and the general coordinate system.

The plot of $\left|\frac{\partial p_c}{\partial r}\right|$ in Fig. 6.4 was obtained by using the magnetic field profile for the re-entrant electromagnet shown in Fig. 3.7 and the predicted velocity profile obtained from Fig. 6.2. This figure illustrates the creation of a radial pressure well since B_z changes direction and therefore sign. The pressure well depth varies directly with the magnetic field strength and is therefore greatest near the cathode surface.

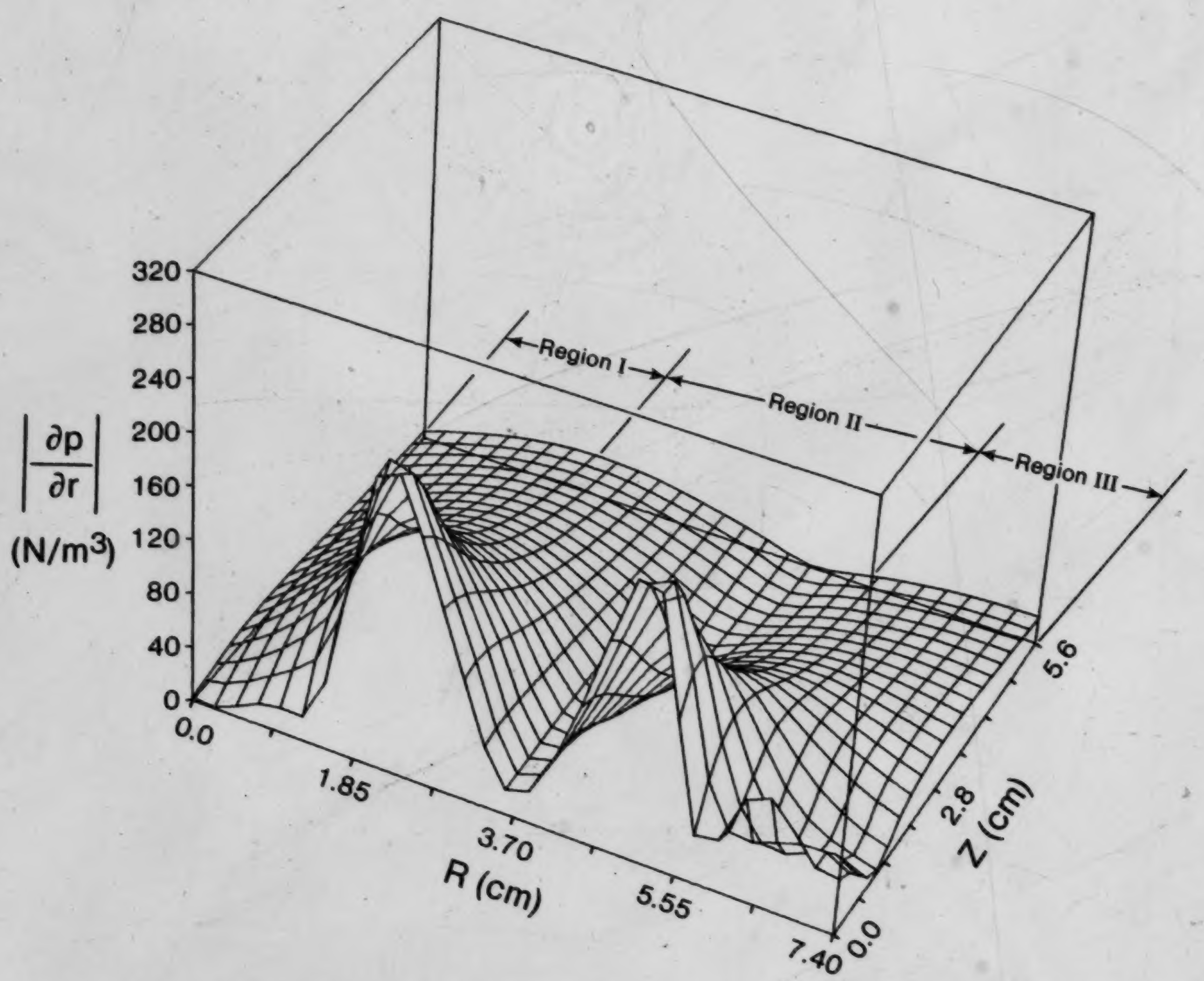

Fig. 6.4 Absolute Value of the Radial Pressure Gradient Distribution for the Charged Particle Fluid.

The profile of the radial pressure gradient in Fig. 6.4 reveals that the Lorentz force is responsible for confining the gas discharge in one of two possible locations. For very low discharge current values, the gas discharge is located in the central portion of the pressure well, that is, region I. In this mode, the discharge formation resembles a typical plasma column. As the current is increased further, the plasma cannot be contained within the inner well because of rising centrifugal forces and consequently jumps into region II. In this second mode, a rapidly rotating annular discharge is formed which is centered in the pressure well. Since this region contains a much larger volume, the plasma is capable of supporting a greater current density.

In the tubular anode geometry, it was observed that if the current density was too high, or the magnet field too low, the centrifugal force $\left(\frac{\rho_c v_{c\theta}^2}{r}\right)$ could exceed the magnetic radial confinement force $(\vec{J}_\theta \times \vec{B}_z)$. At this point, the discharge could not be contained in region II and would subsequently blow out into region III, forming a glow-to-arc transition along some point on the electrode extremity. This process could be controlled by increasing the magnetic field strength thereby creating a deeper pressure well. Unfortunately this procedure caused the discharge to narrow. An alternative method for confining the discharge is to redesign the magnetic geometry to create a "saucer" shaped pressure profile which would maximize the discharge volume. However, when the anode was redesigned into the fluid ballasted geometry, this problem was essentially eliminated since the ballasted anode was very effective in distributing the plasma over the discharge volume.

A comparison of Fig. 6.4 with the photographs shown in the next few sections reveals that the theoretical predictions for the radial position of the discharge is in good agreement with the experimental results.

6.2 ANALYTICAL MODEL AND RESULTS OF THE COAXIAL GEOMETRY

The behavior of a glow discharge in a coaxial geometry can also be determined by a MGD analysis. In the structure shown in Fig. 3.4, the axial magnetic field B_z in combination with the radial current J_r , provides a Lorentz force which causes a rotation of the ionized particles in the negative θ direction. The motion of the charged and neutral particles is coupled through collisions and results in a bulk gas rotation in the same direction. The radial magnetic field B_r in combination with the Hall current J_θ produces an axial Lorentz force which serves to confine the discharge to the central region of the electrode.

The Hartmann number given by the expression

$$H_a = BL\left(\frac{\sigma}{\mu_n}\right)^{\frac{1}{2}}$$

gives the ratio of magnetic forces to viscous forces. For the experimental parameters appropriate to the magnetically stabilized gas discharge, $H_a \leq 1$. This implies that $|v_\theta| << E_r/B_z$ and consequently, the Lorentz forces in the azimuthal and radial directions can be approximated as

$$F_\theta \simeq -\sigma_\perp E_r B_z \qquad (6.9)$$

$$F_z \simeq -\sigma_T \cos(\phi) \cdot E_r B_r \; .$$

The force F_z is negative for $z > 0$ and positive for $z < 0$ and therefore serves to confine the plasma about $z = 0$ as indicated by Fig. 6.5.

To simplify the analysis of this problem, Fig. 6.5 is employed to model the current emission from the rotating disk shaped plasma. Here it is assumed that $|J_z| << J_r$ so that uniform cathode emission occurs over the region $-D/2 \le z \le D/2$, and zero elsewhere. The current density may then be approximated in the following manner.

$$J_r = \begin{cases} \dfrac{I_T}{2\pi r D} \, , & \text{for } -D/2 \le z \le D/2 \\ 0 \, , & \text{otherwise} \end{cases} \qquad (6.10)$$

$$J_z \simeq 0$$

where I_T is the total discharge current, and D is the width of the discharge, usually 2.0 cm.

The solution for this coaxial electrode geometry was initially carried out for a single fluid model as described in [6.2]. In that analysis, a steady-state solution, neglecting secondary flows, was obtained by considering the θ component of the momentum conservation equation, that is,

$$J_r B_z + \mu_n (\vec{\nabla}^2 \vec{v})_\theta \simeq 0 \; . \qquad (6.11)$$

By using the approximation for the current density (Eqn. 6.10) and assuming that the azimuthal velocity was independent of z, Eqn. 6.11

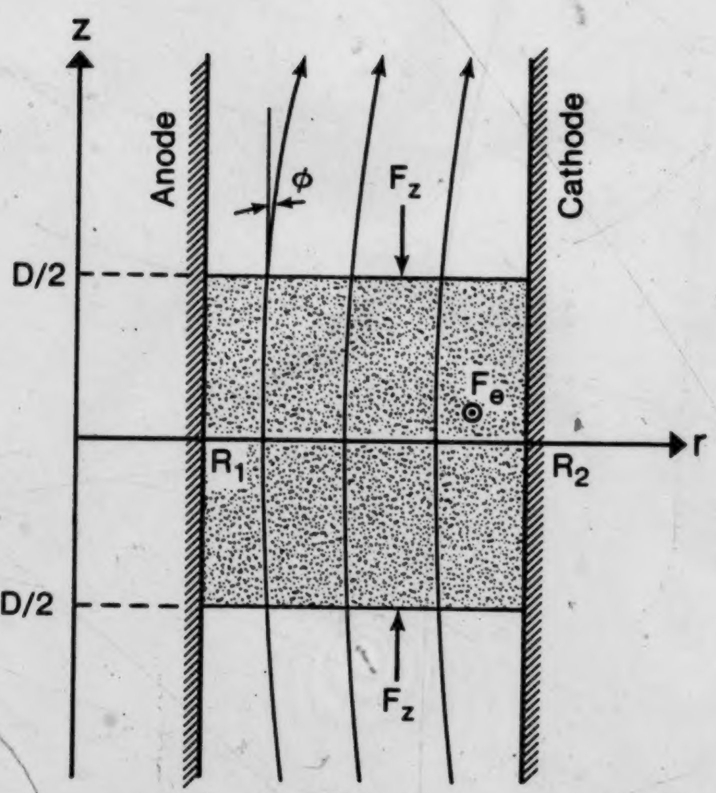
z
Anode
ϕ
F_z
Cathode
D/2
F_θ
R_1
R_2
r
−D/2
F_z

Fig. 6.5 Current Density Distribution Model for the Coaxial Geometry.

could be written as

$$\frac{\partial^2 v_\theta}{\partial r} + \frac{1}{r}\frac{\partial v_\theta}{\partial r} - \frac{v_\theta}{r^2} = \frac{I_T B_z}{2\pi r D \mu_n} . \tag{6.12}$$

The one dimensional analytic solution to the partial differential equation in Eqn. 6.12 was then expressed as

$$v_\theta(r) = F_d\left[c_1 r + \frac{c_2}{r} + r\ ln(r)\right] \tag{6.13}$$

where

$$F_d = \frac{I_T B_z}{4\pi\mu_n D}$$

and

$$c_1 = \frac{R_1^2}{(R_2^2 - R_1^2)}\left\{ln\ R_1 - \left(\frac{R_2}{R_1}\right)^2 ln\ R_2\right\}$$

$$c_2 = \frac{R_1^2 R_2^2}{(R_2^2 - R_1^2)}\ ln\left(\frac{R_2}{R_1}\right) .$$

The parameters R_1 and R_2 are the inner and outer radial boundaries of the discharge.

A two-dimensional steady-state solution, which neglected secondary flows has also been carried out by numerical methods in [6.3]. Figure 6.6 illustrates the computed rotational velocity profile for a 4:16:20 torr gas mixture containing CO_2/N_2/He with a total discharge curent of 7 A and a viscosity of 1.43×10^{-5} kg/(m·s). A comparison of the peak rotational velocities determined from the one- and two-dimensional models is displayed in Fig. 6.7. It is clearly seen that both velocity profiles are similar, although the velocities obtained for the two-dimensional model is 40% less. This result can

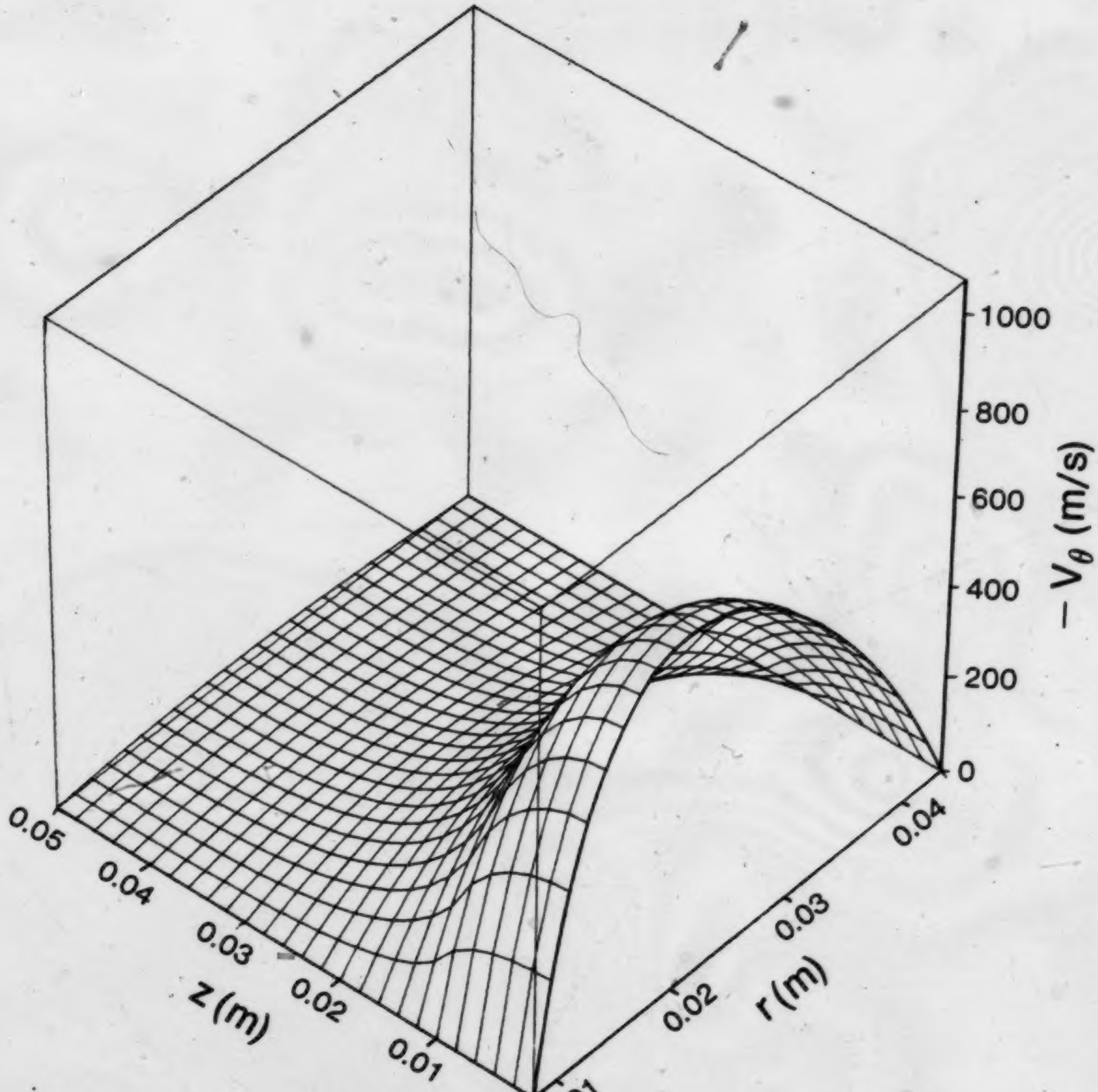

Fig. 6.6 Rotational Velocity Distribution for the Coaxial Geometry Neglecting Secondary Flow. Discharge parameters include: J = 155 mA/cm^2, μ = 1.43 × 10^{-5} kg/(m·s).

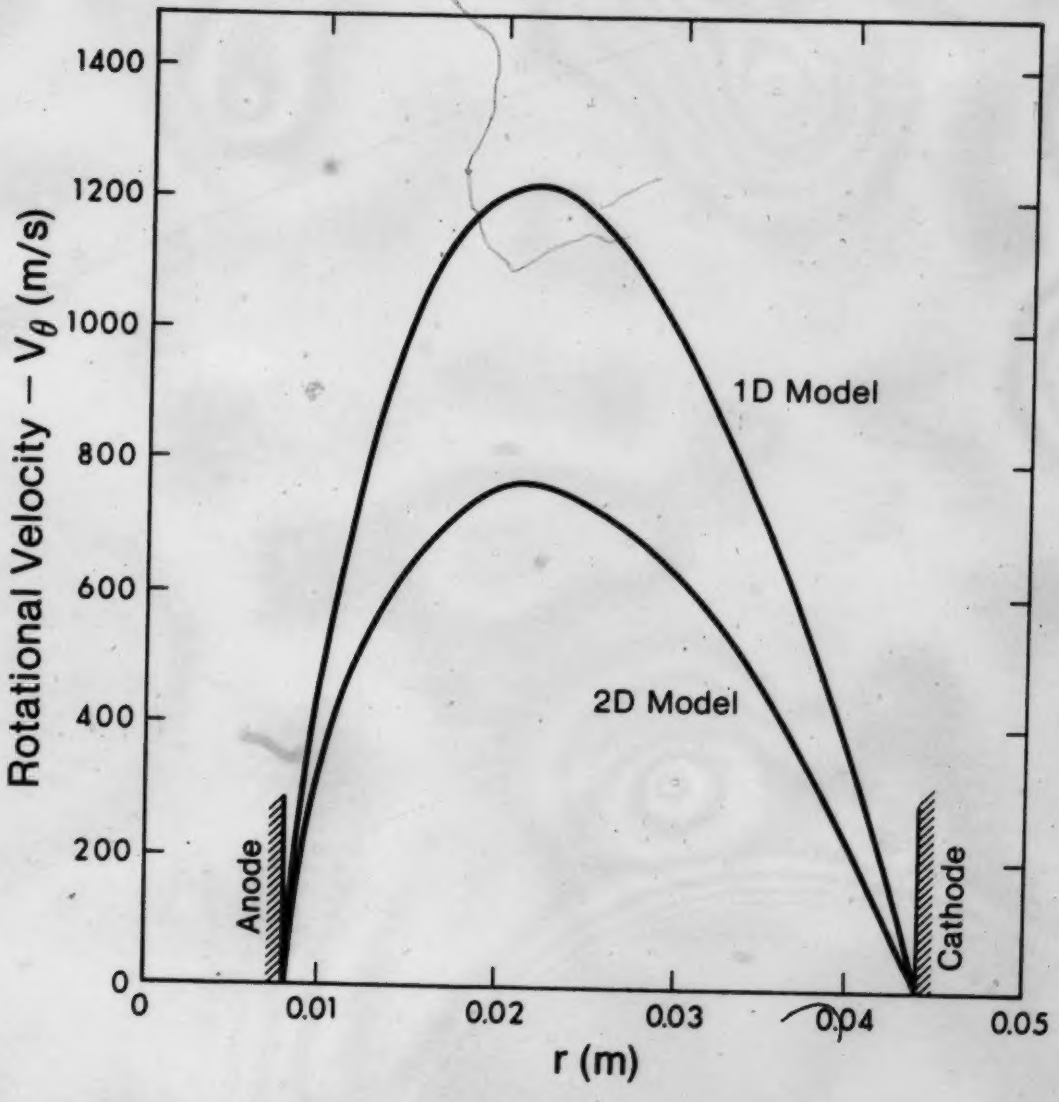

Fig. 6.7 Comparison of the Peak Rotational Velocity Profile Between a 1D and 2D Model, Neglecting Secondary Flow.

be attributed to the presence of a larger active discharge volume with correspondingly larger viscous drag associated with the regions outside the uniform plasma emission.

These initial models reveal that extremely large amplitude, highly sheared flow velocities can be expected to exist in the coaxial electrode structure. In the near future, the computer code MAGIC will be modified to determine the secondary flows generated by this geometry. Again, it is expected that the actual rotational velocities will be much lower than suggested by the initial models.

In both electrode geometries, secondary flows are created as a result of pressure gradient forces which convect momentum into regions of high viscosity and low azimuthal velocity. The radial and axial secondary flows are eventually restricted by boundary walls where momentum is continually lost. The flows are then forced to return to the discharge thereby forming a small convective cell. In the process of returning, the secondary flows intercept the region of high speed rotational flow causing the azimuthal velocity to be loaded down. Thus, the Lorentz driving force must perform additional work in order to maintain the azimuthal momentum. It is this dynamic process which is responsible for lowering the overall rotational velocity. From these results it is obvious that a modified convective cell is needed to create a less restrictive flow pattern which would substantially increase the rotational flow velocity.

6.3 OBSERVED PHYSICAL PHENOMENA

6.3.1 Preliminary Observations

During the initial phase of this project the effects of a magnetic field on the behavior of a self-sustained and a pulser sustained glow discharge was studied. It was observed that in the absence of a magnetic field, the gas discharge would undergo a glow-to-arc transition at an electrode edge, when the applied voltage approached the gas breakdown voltage. To prevent this sudden transition, a uniform preionization was established by means of a high voltage thyratron pulser. Now, as the gas breakdown voltage was approached, a pulser sustained, normal glow discharge column began to form between the electrodes. With a further increase in discharge current, the gas discharge entered the abnormal glow regime and eventually deteriorated into a glow-to-arc transiton. This problem in conventional laser systems is normally solved by employing high speed blowers to spread the constricting plasma column and to provide convective cooling. However, it was proposed that magnetic fields could accomplish the same task but with improved performance and increased power loading.

The general behavior of a magnetized glow discharge was determined for three different electrode geometries, through the use of high speed photography. The resulting photographs revealed the kinematics of motion present when a glow discharge is subject to a Lorentz force. In addition, an estimate of the rotational discharge velocity was obtained for both a transverse and coaxial electrode design.

A. Tubular Anode Geometry

The first electrode geometry examined was a transverse design with a flow through tubular anode (Fig. 3.3). It was observed that the behavior of the glow discharge column was radically changed with the application of a magnetic field. Under the influence of a small magnetic field, the plasma column began to slowly move over the tubular anode in a circular motion. The direction of this motion was in accordance with the resulting Lorentz force. As the discharge current or magnetic field current was increased, the plasma column began to spread as it rotated with increasing speed. At this stage, the glow discharge resembled a uniformly distributed annular ring and gave little indication that it was actually rotating.

The cathode glow layer was also observed to be annular in shape. This particular characteristic shape is the result of radial Lorentz forces ($\vec{J}_\theta \times \vec{B}_z$) interacting with the charged fluid. This process can create a radial pressure gradient for the charged fluid as previously explained in Section 6.12. A detailed explanation of the physical mechanism for this discharge shape will be discussed in Section 7.2.

The photograph in Plate 1.a, taken at 1/60 of a second, reveals some of the internal structure in the rotating discharge. However, it can be clearly seen that the discharge is still occupying its full annular region. At this point, it was still unknown whether the discharge was simply a single plasma column rotating at a very high speed or whether the discharge was actually spread out over the entire electrode surface. Consequently, higher speed photographs were needed in order to resolve this dilemma. The photograph in Plate 1.b, taken

1. High Speed Photographs of a Tubular Anode Geometry.

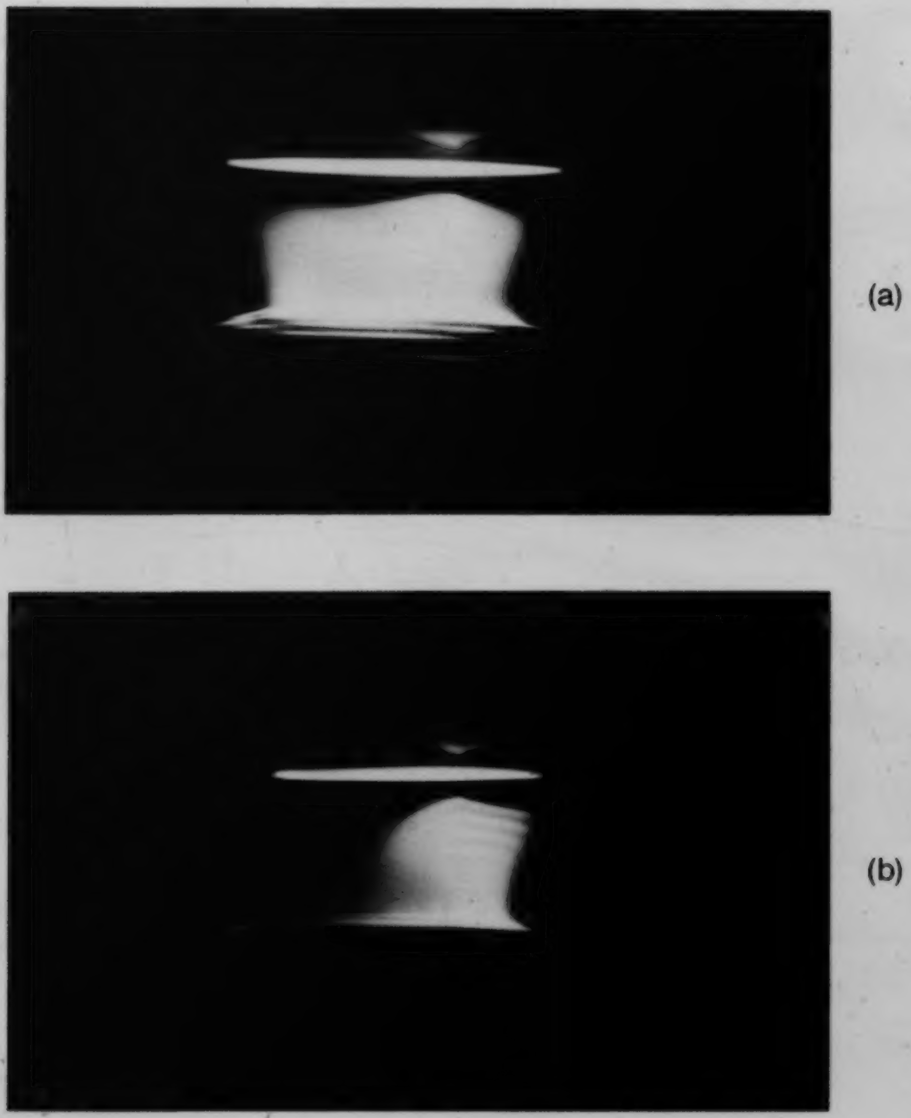

Plate 1. Gas discharge parameters include: $CO_2/N_2/He$ laser gas mixture at 1:7:12 torr, V_{DC} = 640 V, I_{DC} = 1.6 A, $B_{av} \approx 250$ G. Photographs are of (a) 16.7 ms and (b) 1.0 ms duration.

COLOURED PICTURES
Images en couleur

at 1/1000 of a second, still shows definite rotational structure. However, the glow discharge is now incomplete and appears to be just a smeared plasma column. This premise was corroborated by other photographs showing an ionization trail as the plasma column rotated.

It is well known that the plasma column is a region of intense current density and subsequently high conductivity. It is suspected that the uniform electric field profile that exists between the electrodes becomes distorted in the vicinity of the plasma column. As the gas discharge rotates, the distortion in the electric field follows the motion of the column. As shown in Fig. 6.8, the ions emitted from the anode surface are now subject to a θ-component in the electric field and are forced to follow the distorted field lines. The collective motion of numerous charged particles produces the corresponding ionization trail.

While examining the behavior of arc discharges, it was observed that the application of a strong magnetic field was sufficient to extinguish an arc and form an annular shaped glow discharge. During this process, the arc looked as if it was slowly being pulled into the center of the electrode by the magnetic field. It is reasonable to speculate that the magnetic field slowly draws charged particles from the arc into the radial pressure well. This procedure would reduce the overall current density since charged particles would now be free to rotate in a large discharge volume under the governing influence of the Lorentz forces. The process of extinguishing the arc was most noticeable at the cathode surface where the magnetic field is strongest. It is therefore suspected that if the magnetic

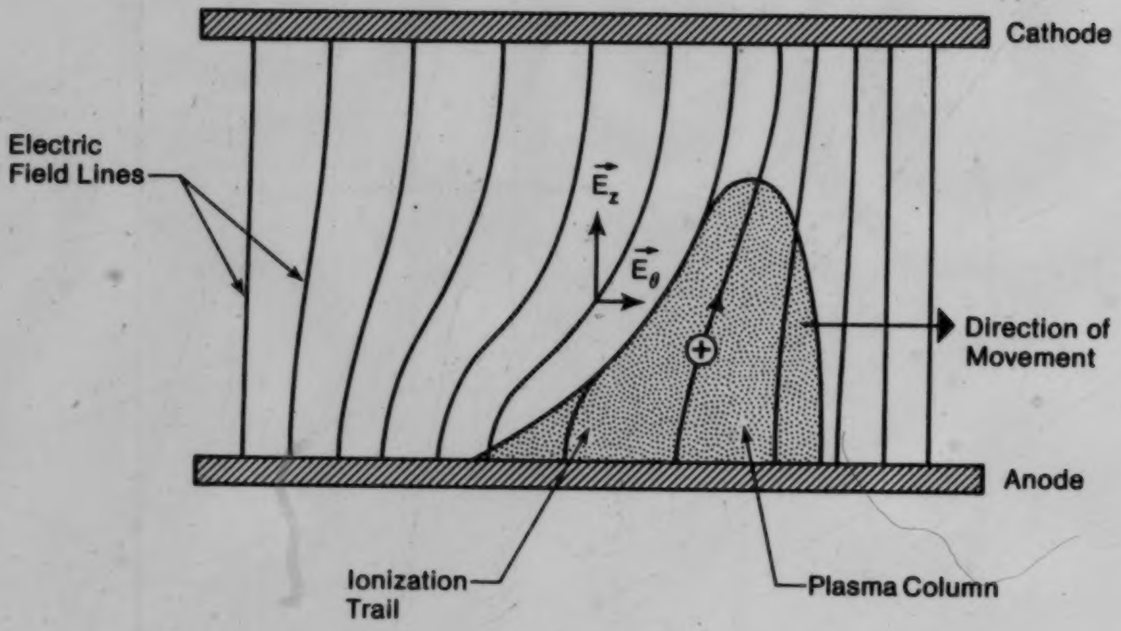
Cathode
Electric Field Lines
$\vec{E}_z$
$\vec{E}_\theta$
⊕
Direction of Movement
Anode
Ionization Trail
Plasma Column

Fig. 6.8 Distortion of the Electric Field by a Rotating Discharge Column.

field can stabilize the cathode glow layer, the remaining arc discharge must also follow suit.

B. Coaxial Electrode Geometry

The second electrode geometry examined, consisted of a coaxial design operating in a magnetic field produced by a solenoid. In this arrangement, a radial electric field combines with an axial magnetic field to produce a Lorentz force in the θ direction as shown in Fig. 3.4. As in the previous geometry, a pulser was employed to provide a uniform preionization over the discharge volume. The high voltage pulser created numerous streamers which radiated from the anode and formed small 1 cm diameter spots on the cathode surface. As the DC voltage increased, the spots became brighter and larger. Eventually these spots coalesced into a uniform cathode glow layer approximately 5 cm wide.

As the gas breakdown voltage was exceeded, a discharge column was formed. With the application of a magnetic field, the radial discharge column began to rotate about the anode and rapidly accelerated into a thin rotating disk. As the discharge current was increased further, the width of the rotating plasma body expanded longitudinally into the inter-electrode volume. The Hall current J_θ coupled with the radial component of the magnetic field, B_r produces a Lorentz force which confines the discharge axially to the central portion of the electrode structure. This magnetic containment feature is especially useful, since it becomes unnecessary to profile the strong fringing electric fields created by the coaxial electrodes.

The photographs in Plate 2 were each taken at 1/1000 of a second with a gas composition of He and N_2 (10:10 torr) and 20 torr of CO_2 , respectively. Both photographs indicate that the disk is rotating at very high speeds since no internal structure could be detected. Thus, for the 7 cm diameter coaxial electrode, the estimated minimum rotational velocity is 200 m/s. This very high velocity is due to a large driving force acting upon a small active discharge volume. In addition, both coaxial electrodes are smooth and continuous and consequently do not subject the rotating discharge to excess turbulence.

A wide variety of gases and mixtures were tested in the coaxial structure including Ar, He, N_2 , and CO_2 . All gas combinations produced excellent results for pressures exceeding 100 torr. Stable high power discharges were also obtained in electronegative gases such as O_2 and SF_6 . The electric discharge containing 5 torr of SF_6 was particularly interesting since observations revealed an absence of a Faraday dark space. This effect was due to the extremely high electron affinity that exists for this electronegative gas. Consequently, this rapid recombination process to form negative ions, prevents the formation of any large concentrations of electrons.

These tests have demonstrated that the magnetic stabilization technique is largely insensitive to gas composition and pressure. Furthermore, in order to uniformly distribute the rotating disk discharge over a larger active volume, it may be necessary to construct a fluid ballasted electrode.

2. High Speed Rotating Coaxial Discharge.

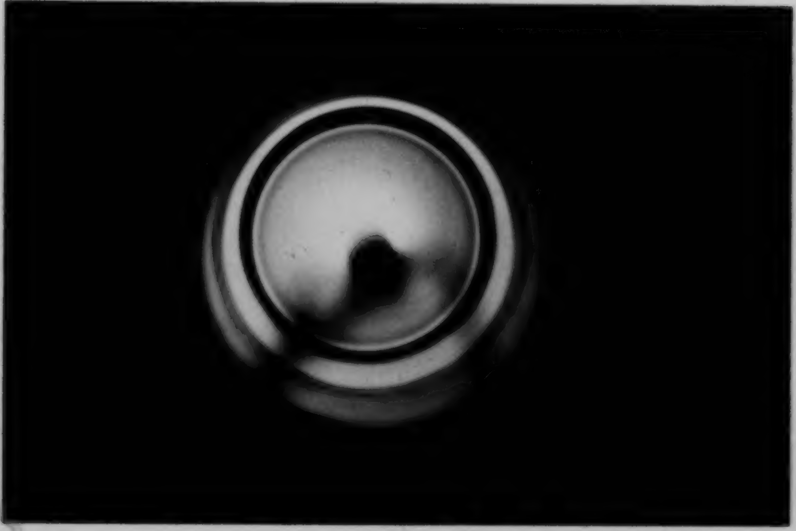

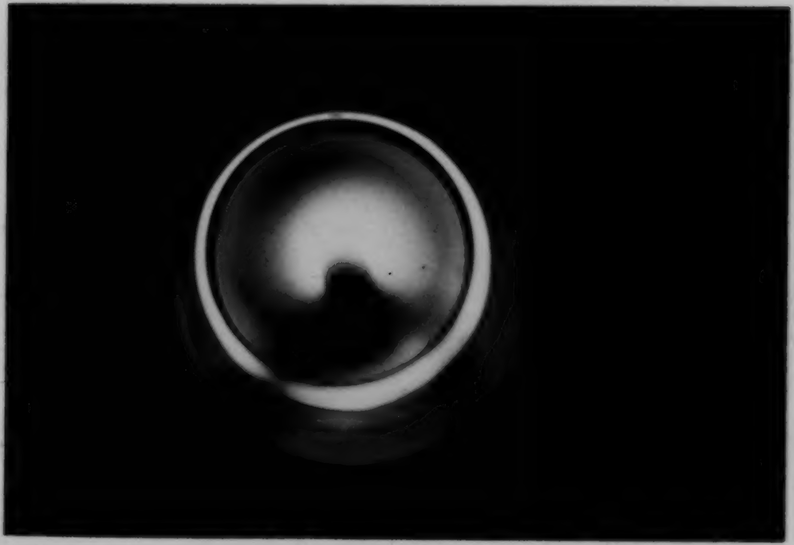

Plate 2. (a) Gas discharge consists of a N_2/He mixture at 10:10 torr; V_{DC} = 480 V, I_{DC} = 3.2 A, $B_{av} \simeq$ 400 G. (b) Gas discharge consists of 20 torr CO_2; V_{DC} = 700 V, I_{DC} = 4.0 A, $B_{av} \simeq$ 400 G. Both photographs are of 1.0 ms duration.

COLOURED PICTURES
Images en couleur

C. Multi-Pin Ballasted Anode Geometry

The previous experiments with the transverse tubular anode geometry indicated that the gas discharge operated as a localized plasma column. The resulting small active discharge volume made very inefficient use of the potential volume between the electrodes. In an attempt to solve this problem, a multi-pin ballasted anode (Fig. 3.5) was constructed to replace the tubular device. The ballasted anode was designed to create a uniformly distributed plasma through an array of sub-electrode pins. Since the other components of the transverse structure remained unchanged, a thorough comparison of the two electrodes could be performed.

To initiate the glow discharge, a high voltage pulser was first applied to the anode. Due to the performance of the individually ballasted sub-electrode pins, a homogeneous preionized discharge volume was established. Upon initiation of the gas breakdown voltage, a widely dispersed glow discharge began to form in the center of the electrodes. With the application of a magnetic field, the glow discharge rapidly accelerated into a uniformly distributed plasma, covering the entire electrode surface. The resulting gas discharge was only slightly annular in shape, being dispersed by the individually ballasted sub-electrode pins. Thus, it can be surmised that the radial Lorentz forces are still playing a factor in determining the gas discharge characteristics.

The photographs in Plate 3, taken at 1/250 and 1/1000 of a second, revealed an evenly distributed plasma with little internal structure. As a result, the rotational discharge velocity could not

3. High Speed Photographs of a Discharge in a Multi-Pin Ballasted Anode Geometry.

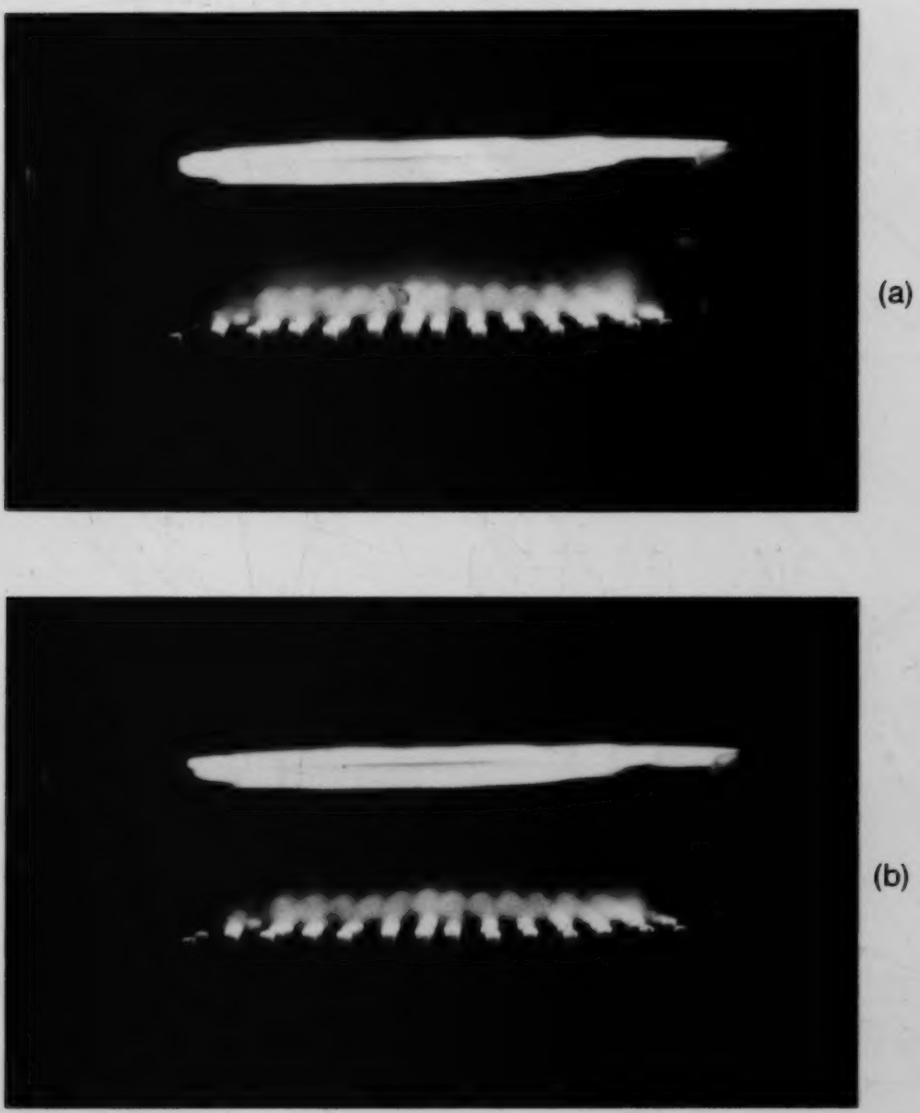

Plate 3. Gas discharge parameters include: $CO_2/N_2/He$ laser gas mixture at 4:16:20 torr, V_{DC} = 750 V, I_{DC} = 9.0 A, B_{av} = 400 G. Photographs are of (a) 4.0 ms and, (b) 1.0 ms duration.

COLOURED PICTURES
Images en couleur

be accurately inferred from these photographs. Subsequent determination of the parameter will require more sophisticated diagnostic techniques.

Since the entire discharge volume was now more effectively utilized, the local discharge current density and luminosity was significantly reduced compared with the tubular anode device. This uniform distribution of current density enabled the electrode to handle a large increase in overall discharge current. Typically, the maximum value of current density achieved was 50 mA/cm^2. Through a variety of experiments, it was also determined that the electrode system was capable of stable operation at pressures exceeding 60 torr. These results were repeated numerous times with an assortment of gas mixtures. Once again the magnetic stabilization approach has proved highly successful and thus far, has only been limited by power supply restrictions.

6.3.2 High Speed Photographic Interpretation

The electric discharges produced by the different electrode geometries were all initially analyzed, under various conditions, with a 35 mm single lens reflex camera. The resulting high speed color photographs revealed that a uniform glow discharge had been established in the coaxial and ballasted anode geometries. However, it was observed that the supposedly uniform glow discharge found in the tubular anode geometry was actually a plasma column rotating at high speeds between the electrodes. In order to study this phenomenon further, a high speed framing camera was employed. The gas discharges were examined with a 16 mm DBM-54 Milliken motion picture camera capable of frame rates in excess of 400 frames per second. The shutter used in this special camera consisted of a rapidly rotating plate with a small adjustable slot. By varying the slot width, a shutter speed as low as 1/4000 of a second could be achieved.

Previous experiments have indicated that the cathode glow layer was also rotating under the influence of the Lorentz force. High speed photographs revealed that the cathode glow layer only existed as a half-moon shaped region on the cathode surface. As stated by Nasser [3.2], a proper glow discharge cannot function without a cathode glow layer. Now, since the plasma column is strongly influenced by the magnetic field, the positive column must move in unison with the cathode glow layer. This effect was observed by viewing the film taken by the high speed framing camera. The sequence of photographs shown in Plate 4 show the cathode glow layer rotating in conjunction with the positive column. Furthermore, each frame in this series confirms that the rotating discharge is actually a single column rotating between the electrodes.

From the film sequence, the positive column was estimated to be 2-3 cm in diameter. Also observed was the emergence of a radial afterglow from the top of the positive column near the cathode. Due to the loss of these particles, this region became diffuse and less luminous than the bulk of the positive column. By examining the film, frame by frame, the rotating discharge column was observed to jump along the tubes of the anode as it made its way around the electrode. It is believed that this process reduced the velocity of the rotating plasma

4. High Speed Rotating Discharge Sequence in a Tubular Anode Geometry.

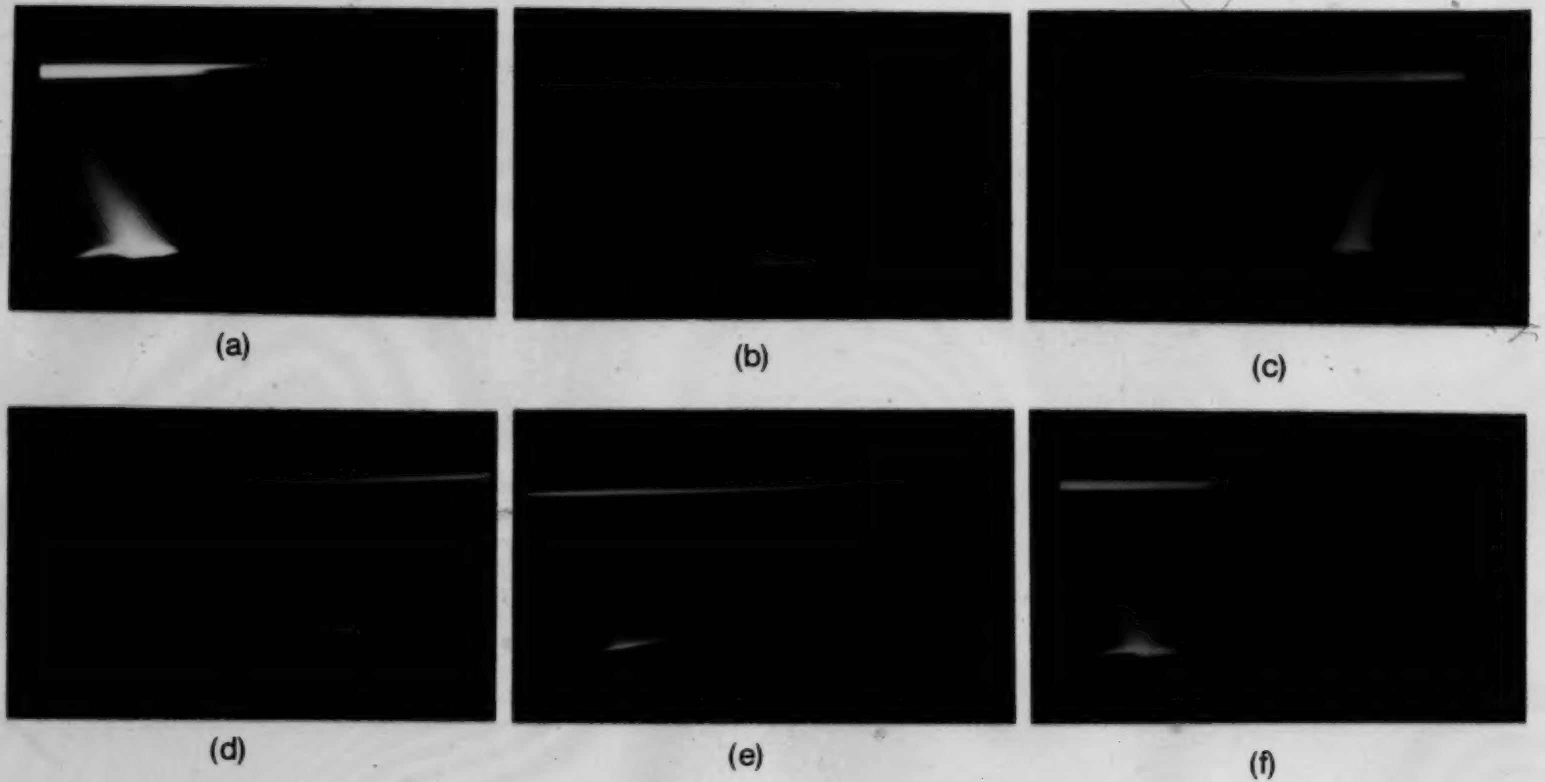

Plate 4. Gas discharge parameters include: $CO_2/N_2/He$ laser gas mixture at 2:8:10 torr, V_{DC} = 520 V, I_{DC} = 4.5 A, B_{av} ≈ 450 G. Each photograph represents a duration of 1.11 ms taken at 2.5 ms intervals.

column since a new ionization channel had to be established with the cathode glow layer.

The cathode glow layer was estimated to cover an area of 50 cm^2 on the cathode surface. Since this discharge region is more extensive than the positive column, it was hoped that further increases in the applied driving force would be sufficient to enlarge the cathode glow layer and thus extend the positive column. Unfortunately, the magnetic field intensity was limited by saturation effects. In addition, the power supply was unable to provide the required amount of current to test this speculation.

By examining the film sequence in Plate 4 it becomes possible to estimate the velocity of the rotating column. This can be accomplished by simply counting the number of frames that the discharge takes to complete one revolution around the anode. Since the framing speed of the motion picture camera was 400 frames/s, each photograph was taken at 2.5 ms intervals. Viewing this 16 mm film on a film editing machine, indicates that for the conditions specified, there are 5 frames per revolution. Subsequently, the rotational velocity of the plasma column is given by

$$v = \frac{\pi d \cdot \text{framing speed}}{\text{\# of frames/rev.}}$$

where d is the diameter of the dishcarge. This formula indicates a rotational velocity of $v = 27.6$ m/s which confirms the results of the photodiode experiment discussed in Section 6.4.1.

6.3.3 Afterglow Effect

As the plasma rapidly accelerates to a steady-state value, an increasing radial pressure profile begins to develop across the discharge. The resulting centrifugal force will in turn drive secondary flows. Since the applied driving forces are stronger near the cathode, larger rotational velocities are created in this region. Consequently, the outward flow of gases will also be predominantly emanating from the cathode. In the transverse geometry, this flow will be radially outward along the cathode surface. To complete the convective cell, the inward flow is expected to return upwards through the tubular or multi-pin flow through anode. In the coaxial geometry, the outward flow will be driven axially along the outer electrode and return axially along the inner electrode.

This outward flow of gas was visually confirmed in all electrode geometries, by the light emitted from metastable particles. The light in the form of an afterglow could be seen spewing outwards from the Faraday dark space and cathode regions. Further examination by the high speed film sequence, indicated that the radial afterglow actually originated from the top-half of the positive column as it rotated over the tubular anode surface.

The metastable particles are normally the result of a recombination process involving the capture of an electron by a positive ion according to the reaction

$$X^{+} + e \rightarrow X^{*} + h\nu \ .$$

From this reaction, a metastable particle is produced and a photon is emitted. These metastable particles can only be created when the captured electron cannot return to a lower energy level without violating certain selection rules. These long-lived metastables can only be restored back to their ground state through an energy absorbing process. This will allow the electron to move to a higher energy level from which it can then return to its ground state. The energy absorbing process is usually the result of inelastic collisions.

The afterglows were visually observed as a result of the photons emitted during the metastable production process. A bright orange afterglow was observed for large concentrations of N_2 (> 20 torr) while a light green afterglow was produced in a CO_2 gas discharge. Since the electric discharge dissociates CO_2 into CO and O_2 , it is believed that the CO_2 afterglow is associated with the presence of O_2 .

The afterglow emanating from the rotating ionized gas is known to result from collisional processes occurring within the discharge. Since the metastables are uncharged, they are not bound to the charged particle pressure well. Consequently, these uncharged particles are convected radially outwards, in the transverse geometry, by the centrifugal pumping action of the rotating gas discharge. In the coaxial geometry, this flow was generated axially. The afterglow velocity was experimentally determined by the Pitot tube measurements discussed in Section 6.4.2. These results indicate that the afterglow velocity was proportional to the magnetic field and the current density, that is, to the applied driving force. The significant outward flow generated by these forces can be particularly important in the design of a laser system since the effects can be exploited to recirculate and cool the gas.

6.3.4 Standing Wave Striations

One of the more prominent characteristics exhibited by the rotating gas discharge concerns the occurrence of fluctuations in light intensity. In the transverse geometry, these fluctuations appeared as horizontal bands in the plasma column. These fluctuations were visually observed upon careful inspection of the gas discharge. Through the use of high speed photography, these bands were clearly evident since the amount of light entering the camera had been reduced (Plate 1). The luminous bands were also recorded by a high speed framing camera. An examination of a sequence of frames revealed that the light intensity fluctuations were stationary even as the plasma column rotated. It therefore became evident that these stationary luminous bands were the result of standing wave striations in the positive column.

A detailed study of the coaxial electrode geometry again revealed the occurrence of fluctuations in light intensity in the form of concentric rings. These luminous rings, located in the rotating positive column were visually observed and photographed. The pictures displayed in Plate 5, were taken of gas discharges containing 10:10 torr of He/N_2 and 20 torr of CO_2 respectively. The number of rings varied according to the discharge current density and applied magnetic field, that is, to the $\vec{J} \times \vec{B}$ driving force. As the Lorentz force increased the number of rings grew until they merged and became indistinguishable. This effect can be illustrated by Plate 2 where only one ring remains. This finding is consistent with those of

5. Standing Wave Striations Observed in a Coaxial Geometry.

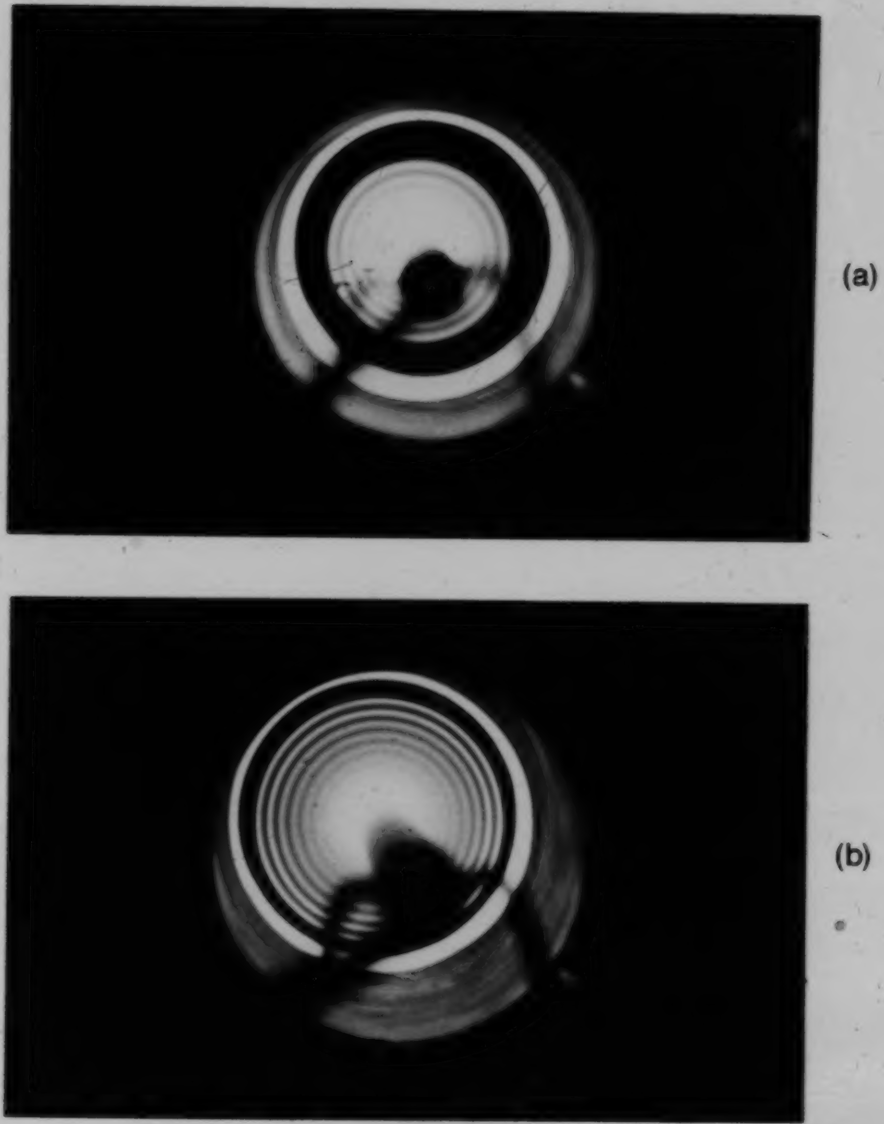

Plate 5. (a) Gas discharge consists of a N_2/He mixture at 10:10 torr; V_{DC} = 425 V, I_{DC} = 2.7 A, B_{av} = 300 G. Photograph is of 8 ms duration. (b) Gas discharge consists of 20 torr CO_2; V_{DC} = 660 V, I_{DC} = 3.6 A, B_{av} = 300 G. Photograph is of 16.7 ms duration.

COLOURED PICTURES
Images en couleur

Crandall and Cooper [6.4] who observed a single standing striation usually located near the cathode.

Since the gas discharges under examination are highly collisional and only partially ionized ($n_e/n_n \approx 2 \times 10^{-7}$), it is highly probable that the standing wave striations are due to acoustic waves propagating in the positive column. Within an ionized gas, an acoustic wave can be generated as a result of an external disturbance. If this disturbance is due to a local change in the electric field, an increase in the dissociation of particles may result. The ensuing local pressure increase can then initiate an acoustic wave propagating in the neutral gas at the wavespeed

$$c_s = \sqrt{\frac{\gamma P}{\rho}}\ .$$

The passage of the acoustic disturbance is recognized by a local increase in light intensity due to a rarefraction wave, and a local decrease in luminosity for a compression wave [6.4]. The light intensity decrease with compression is attributed to a decrease in the electron temperature resulting from an increased collision frequency. The less energetic electrons are now unable to fully excite the neutral particles to produce spontaneous emission of light.

The analysis of Pekarek and Krejci [6.5] has shown that the formation of a striation is caused by a disturbance in the local electric field. The resulting perturbation in the electric field causes a rise in the rate of production of ion pairs, which in turn, produces a positive space-charge. The electrons are easily separated from the ions, due to their large diffusion coefficient, and eventually create a separation of charge carriers. As the positive ion density accumulates, an electric field produced by the space-charge begins to oppose the original perturbed field. Consequently, the perturbed electric field is reduced and the positive ion density begins to decrease in this discharge region. Further along the discharge axis, the perturbed field now combines with the space-charge field and a new striation is formed. The analytic solution of the resulting perturbed electric field and positive ion density, after an initial aperiodic disturbance, can be described by an oscillating Bessel function. Thus, it can be shown that moving striations will result from the superposition of many repeated disturbances in the electric field [6.5].

It is suspected that the initial disturbance in the electric field is created by the periodic application of the high voltage pulser. Unfortunately this recently known cause was not verified at the time of the experiment. It is also believed that the occurrence of standing waves rather than moving striations can be attributed to the use of parallel electrodes in both the tubular anode and the coaxial systems. This was especially true in the coaxial geometry with its smooth concentric electrodes. These solid electrode walls were perfectly reflecting and thus ideal for the production of acoustic standing waves. While operating the multi-pin ballasted anode system, no standing wave striations were observed, since the pin anode is a poor reflecting surface for acoustic waves.

6.3.5 Dark Space Width

Another interesting feature exhibited by the magnetized glow discharge pertains to the dark space width and its dependence upon the applied magnetic field. It was observed that for the three electrode geometries, the physical width of the cathode dark space could be easily varied by an order of magnitude upon adjustment of the magnetic field. For very large field values, the dark space could be reduced to within 2 mm of the cathode surface.

The variation in dark space width is attributed to the effective reduction of the ratio E/n due to the presence of a magnetic field. As reported earlier in Section 4.5, E/n was reduced by over 65% in the cathode fall region compared to its non-magnetized state. This substantial change in electric field will significantly reduce the electron temperature and correspondingly its energy as it accelerates through the cathode fall. The maximum energy attained by these accelerating electrons occurs at the end of the cathode dark space. Here, they participate in inelastic collisions with the negative glow. Normally, since the electron energies are too high, their inelastic collision cross sections are small. Consequently, the excitation and ionization rates only increases after the electrons have been slowed down. However, with the reduction in cathode fall voltage, due to E/n, the less energetic electrons are able to produce inelastic collisions sooner. This effect has been substantiated by Brewer and Westhaver [6.6] who have correlated the width of the negative glow with the electrons which have gained energy in the Crookes dark space.

Their results show that as the electron energy is reduced, there is a corresponding decrease in the width of the negative glow.

From the analysis presented, a reduction in E/n leads to an enhanced electron collision frequency. Therefore, the addition of a magnetic field is equivalent to an increase in pressure. Under these conditions, the negative glow and the two dark spaces that surround it, will shrink towards the cathode, and the positive column will extend to fill the void. Subsequently, the positive column is established closer to the cathode and more of the active discharge volume can participate in laser excitation processes. A more theoretical approach to describe this change in gas discharge behavior is described in Chapter 7.

6.4 GAS DISCHARGE DIAGNOSTIC TECHNIQUES

6.4.1 Photodiode Measurements

The results of the high speed photographs revealed that the rotating gas discharge was not continuous, but merely a single plasma column moving rapidly over the tubular anode surface. Though high speed motion pictures gave a good indication of the azimuthal velocity, a more convenient and accurate approach was needed.

It was proposed that a sensitive photodiode could be used to detect the light emission from the plasma column. As the column rotated, the resulting periodic signal would be used to determine the discharge velocity. The experimental photodiode apparatus is illustrated in Fig. 6.9. In this schematic, two shielded photodiodes were

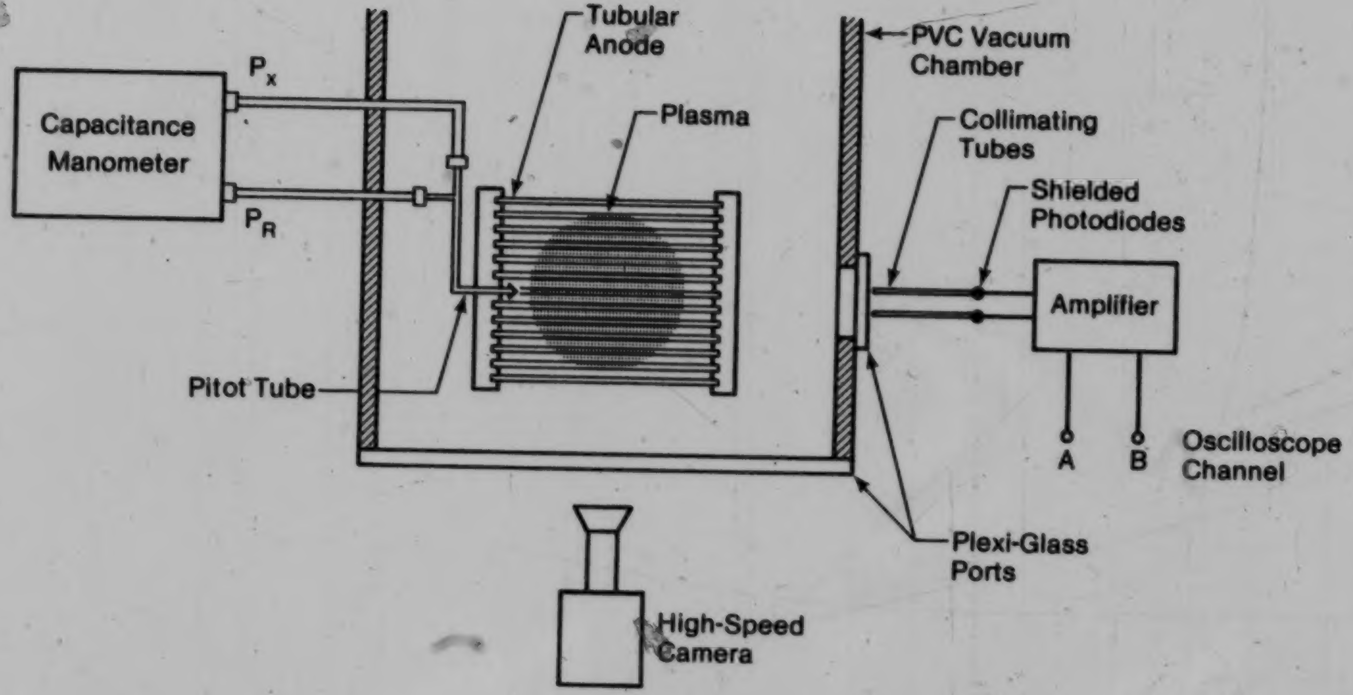
Capacitance Manometer
P_x
P_R
Tubular Anode
Plasma
Pitot Tube
PVC Vacuum Chamber
Collimating Tubes
Shielded Photodiodes
Amplifier
A
B
Oscilloscope Channel
Plexi-Glass Ports
High-Speed Camera

Fig. 6.9 Gas Discharge Diagnostic Apparatus.

employed to detect the passage of the plasma column as it rotated around the tubular anode surface. The initial deployment of two photodiodes were used to ensure that the rotational velocity was indeed constant. Each photodiode was mounted against a 3 mm diameter, 15 cm long brass collimating tube. The long narrow tubes were necessary in order to collect the incident light and prevent stray light from reaching the photodiodes. The tubes were mounted in parallel 6 mm apart so as not to overlap the incoming spectral signal.

During operation of the discharge, a pulsed beam of light was received by the photodiode with each revolution of the plasma column. This signal was then amplified by an emitter follower circuit. The resulting voltage peaks were viewed on an oscilloscope and recorded. A typical voltage trace can be seen in Fig. 6.10. Note the occurrence of a primary and secondary voltage pulse. As the plasma column passes point A, it is detected by the first photodiode. A short time later, $\Delta\tau$, the second photodiode observes the passage of the column past point B. As the plasma column continues around the electrode it passes point C where it is seen by detector 2 and detector 1, as it passes point D, $\Delta\tau$ seconds later. Note that the detected amplitude of the discharge column light intensity, as it passes the far side, is much smaller and broader. This effect is due to the increase in the depth of field seen by the photodiode. This experiment was repeated, but with the magnetic field polarity reversed. This action changed the orientation of the Lorentz force and accordingly reversed the direction of discharge rotation.

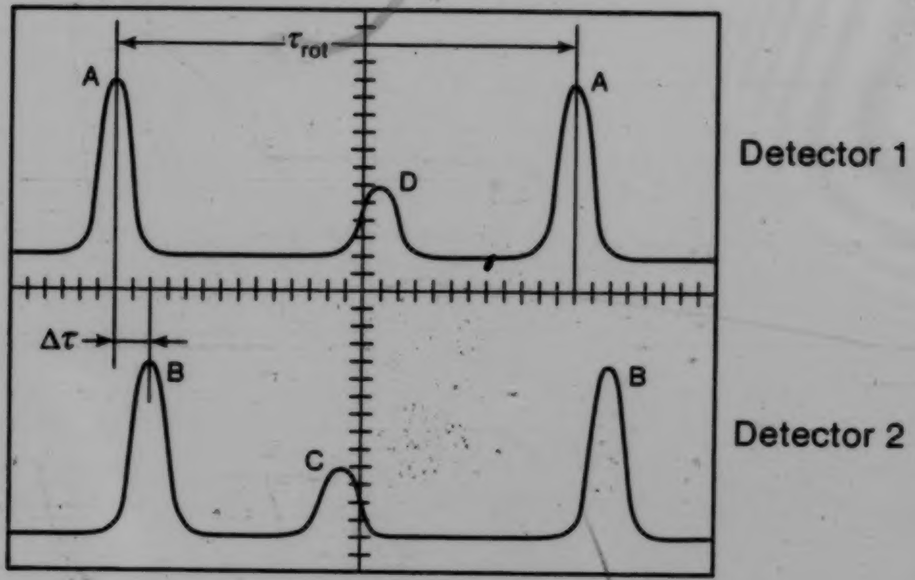

τ_{rot}
A
A
D
Detector 1
$\Delta\tau$
B
B
C
Detector 2

Fig. 6.10 Oscilloscope Recording of Photodiode Voltage Measurements.

The rotational velocity of the plasma column was initially calculated by measuring the time delay, $\Delta\tau$, between detected pulses using both photodiodes. These initial measurements provided conclusive evidence that the rotational speed was constant. Since the detected light pulses were also periodic, only one photodiode was now required. The rotational discharge speed could now be calculated by the formula

$$v_\theta = \frac{\pi d}{\tau_{rot}}$$

where πd is the peripheral path taken by the discharge, and τ_{rot} is the period of revolution determined by the oscilloscope time base.

As shown in Fig. 6.11, an increase in magnetic field and/or applied current is accompanied by a rise in rotational speed. The dotted lines indicate the expected initial velocity relationship. After a proper plasma column has been established, it is clearly seen that this relationship becomes linear. These expected results correspond to a linear increase in the applied $\vec{J} \times \vec{B}$ driving force. However, as indicated in Fig. 6.11, the magnetic flux density becomes slightly nonlinear as the magnetic field current is increased. This effect is due to saturation of the magnet core. Since the magnetic flux density is of nonuniform strength throughout the discharge volume, it was decided that the applied magnetic field current is best suited to represent magnetic field effects. This parameter is easily measured and is strictly linear with respect to the magnetic field; neglecting iron core saturation effects. However, as a rough guide, each ampere of magnetic field current corresponds to an average magnetic flux density of approximately 200 Gauss.

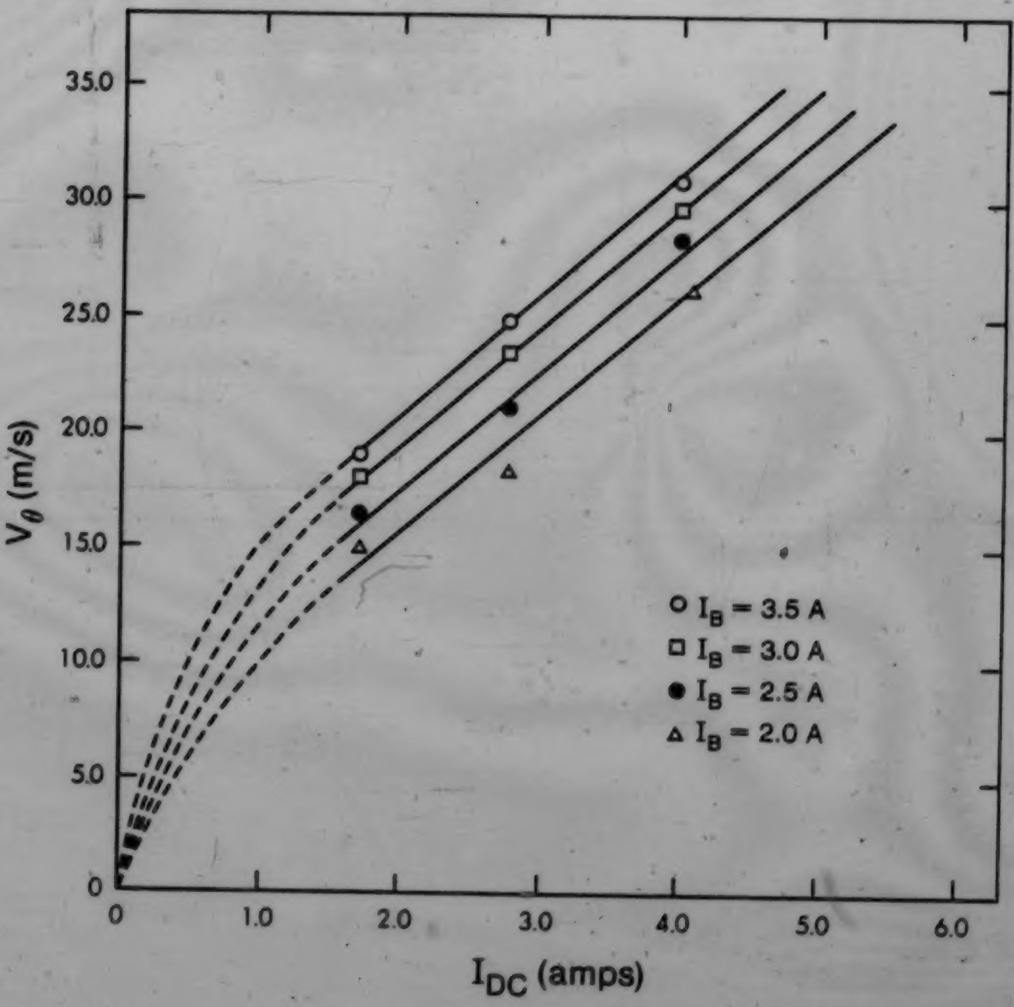

Fig. 6.11 Dependence of Plasma Column Rotational Velocity on Applied Discharge Current. Gas discharge contains a 2:8:10 torr mixture of $CO_2/N_2/He$.

The width of the plasma column was estimated by measuring the half maximum width τ_w , of the light intensity pulse received by the photodiode. Since the rotational period is known, the discharge column width d_w , is calculated through the ratio

$$d_w = \frac{\pi d}{\tau_{rot}} \cdot \tau_w \quad .$$

As Fig. 6.12 indicates, for a given magnetic flux density, the plasma column expands in response to the applied discharge current. This expansion is the outgrowth of two possible competing effects. First, it is probable that the increased current density stimulates further ionization which contributes to the expansion of the plasma column. Secondly, an increase in the Lorentz driving force would spread the discharge column due to acceleration of the rotating charged particles in the v_θ direction.

It was also noted that the discharge column width decreases with applied magnetic field. It is apparent that the constricting plasma column is caused by the charged particle pressure well which narrows in response to an increase in magnetic field. The largest diameter of the plasma column occurred in the absence of a magnetic field, however, this was an unstable situation and a glow-to-arc transition could easily develop. At higher pressures, the plasma column simply constricted to the center of the electrode. At this point, the radial magnetic field component, responsible for creating the rotational driving force, was quite small and consequently no rotation was observed.

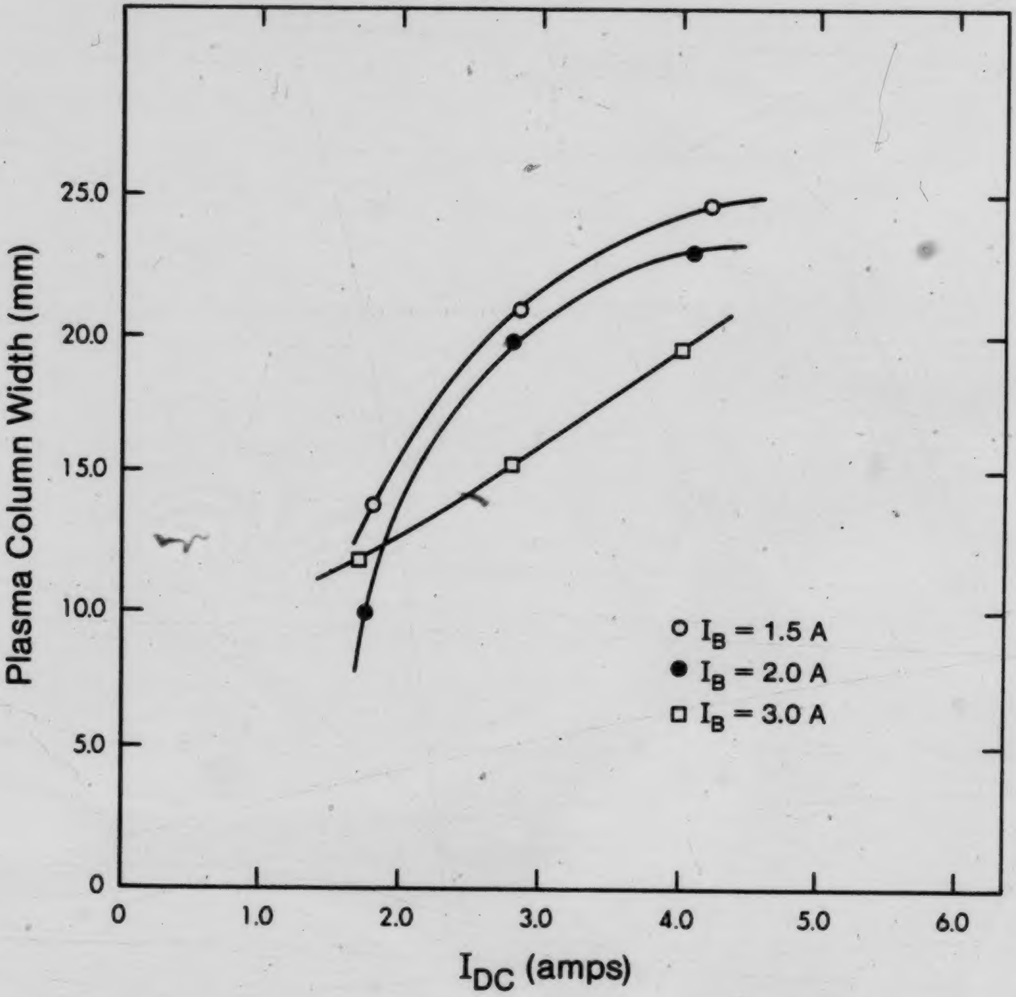

Fig. 6.12 Variation in Plasma Column Width.

One further observation noted in this experiment, concerns the intensity variation of the plasma column. It was ascertained that the discharge luminosity fell off rapidly as the photodiode axially scanned from the anode to the cathode. This investigation confirmed results from the high speed photographs which revealed a substantial expansion of the positive column near the cathode. This observed effect is attributed to the presence of a stronger Lorentz force, near the cathode, which assists in spreading the discharge column.

The photodiode apparatus was not implemented to determine the discharge velocity achieved by the coaxial electrode design. It was felt that since both the transverse and coaxial rotating plasma experiments were based upon the same principles, concentration on both projects would deviate from the central theme of this thesis. Nevertheless, the coaxial discharge geometry proved interesting and worthy of continued study.

As a result of the undesirable qualities manifested by the tubular anode, a fluid ballasted multi-pin electrode was constructed to provide a uniformly distributed glow discharge. Since the new anode evenly spreads the glow discharge over the entire electrode surface, the rotating plasma column phenomena was no longer apparent. The photodiode apparatus was used to confirm this assumption. The resulting investigation only revealed a uniform background light intensity level present along any horizontal plane. The light intensity level did become more diffuse and eventually disappeared as the detector scanned the positive glow and the Faraday dark space, as in the previous case with the tubular anode. These observed facts suggests that under the influence of a magnetic field, the new electrode design produced a uniformly rotating plasma with no discernible structure.

6.4.2 Pitot Tube Measurements

The rotating gas discharge was suspected of also producing a radial gas flow that might originate due to the presence of powerful centrifugal forces. This suspicion was confirmed through the observation of a radial afterglow being ejected out of the gas discharge. An experiment was then devised to measure this flow and determine its characteristics. As illustrated in Fig. 6.9, a Pitot tube was mounted to measure the static and stagnation pressures. A capacitance manometer was then employed to sense the difference in these pressures and produce an electronic output signal. From these results, a radial flow velocity can be determined.

From any standard gas dynamic text, the ratio of static to stagnation pressure is given by the expression

$$\frac{P_s}{P_0} = \left[1 - \left(\frac{\gamma-1}{2}\right)M^2\right]^{\frac{\gamma}{\gamma-1}} \tag{6.14}$$

where $\gamma = c_P/c_V$ is the ratio of specific heat capacities, and M is the Mach number. Rearranging this equation yields

$$M^2 = \left(\frac{2}{\gamma-1}\right)\left[1 - \left(\frac{P_s}{P_0}\right)^{\frac{\gamma-1}{\gamma}}\right] \tag{6.15}$$

where $M = v/c_s$, $c_s = \sqrt{\gamma R T_0}$ is the sonic speed and R is the universal gas constant. With these substitutions Eqn. 6.15 becomes

$$v = \left\{\frac{2\gamma RT_0}{\gamma-1}\left[1-\left(\frac{P_s}{P_0}\right)^{\frac{\gamma-1}{\gamma}}\right]\right\}^{\frac{1}{2}} . \qquad (6.16)$$

It is also known that $\frac{\gamma}{\gamma-1} = \frac{c_P}{R}$ so

$$v = \left\{2c_PT_0\left[1-\left(\frac{P_s}{P_0}\right)^{\frac{\gamma-1}{\gamma}}\right]\right\}^{\frac{1}{2}} . \qquad (6.17)$$

Now, letting the parameter f define the quantity

$$f = \frac{P_0-P_s}{P_0} = \frac{\Delta P}{P_0} ,$$

it then becomes convenient to simplify Eqn. 6.4 through the use of the binomial theorem, that is,

$$1-\left(\frac{P_s}{P_0}\right)^{\frac{\gamma-1}{\gamma}} \simeq f\left(1-\frac{1}{\gamma}\right)\left(1+\frac{f}{2\gamma}\right) . \qquad (6.18)$$

For a laser gas mixture, the overall specific heat capacity per unit mass, at a constant pressure, is given by [6.7]

$$c_P = \frac{k\sum_i\left(\frac{N_i+2}{2}\right)f_i}{\sum_i m_if_i} = \frac{kN_A\left\{\frac{7}{2}\left(f_{N_2}+f_{CO_2}\right)+\frac{5}{2}f_{He}\right\}}{\frac{1}{1000}\left(4f_{He}+28f_{N_2}+44f_{CO_2}\right)} . \qquad (6.19)$$

In this expression, k is Boltzmann's constant, N_A is Avogadro's number, f_i is the fractional concentration of the ith gas species, and N_i is the number of degrees of freedom for the ith species.

The expression for the radial gas flow velocity can now be written as

$$v \simeq \left\{2c_P T_0 f\left(1 - \frac{1}{\gamma}\right)\left(1 + \frac{f}{2\gamma}\right)\right\}^{\frac{1}{2}} . \qquad (6.20)$$

where $\gamma = \frac{c_P}{c_P - R}$, and c_P is defined from Eqn. 6.19.

The differential pressure, as determined by the capacitance manometer, was correlated with the appropriate gas mixture to yield the velocity curves displayed in Figs. 6.13-6.14. These results were obtained using a 1:7:12 torr gas mixture consisting of $CO_2/N_2/He$. The curves of Fig. 6.13 show the change in radial gas flow as the Pitot tube detected pressure changes just outside the active discharge volume. As expected, from visual observation of the afterglow, the radial gas velocity measured near the cathode region, was substantially higher than the measured values at the center or near the anode. These measurements indicate that the centrifugal forces are definitely higher near the cathode. An analysis of the magnetic field profile within the discharge volume, confirms this conjecture. It was found that the magnetic flux density was significantly larger in this region and thereby contributed to a larger Lorentz driving force.

In the absence of a magnetic field, the Pitot tube apparatus detected no pressure differential. With the initiation of a magnetic field, the plasma column began to rotate. However, no radial gas flow was detected until the rotating gas discharge was fully established and an afterglow observed. This effect is speculated by the dashed lines in Fig. 6.14. In addition, it was noticed that a stronger magnetic field was needed to fully establish a rotating discharge for

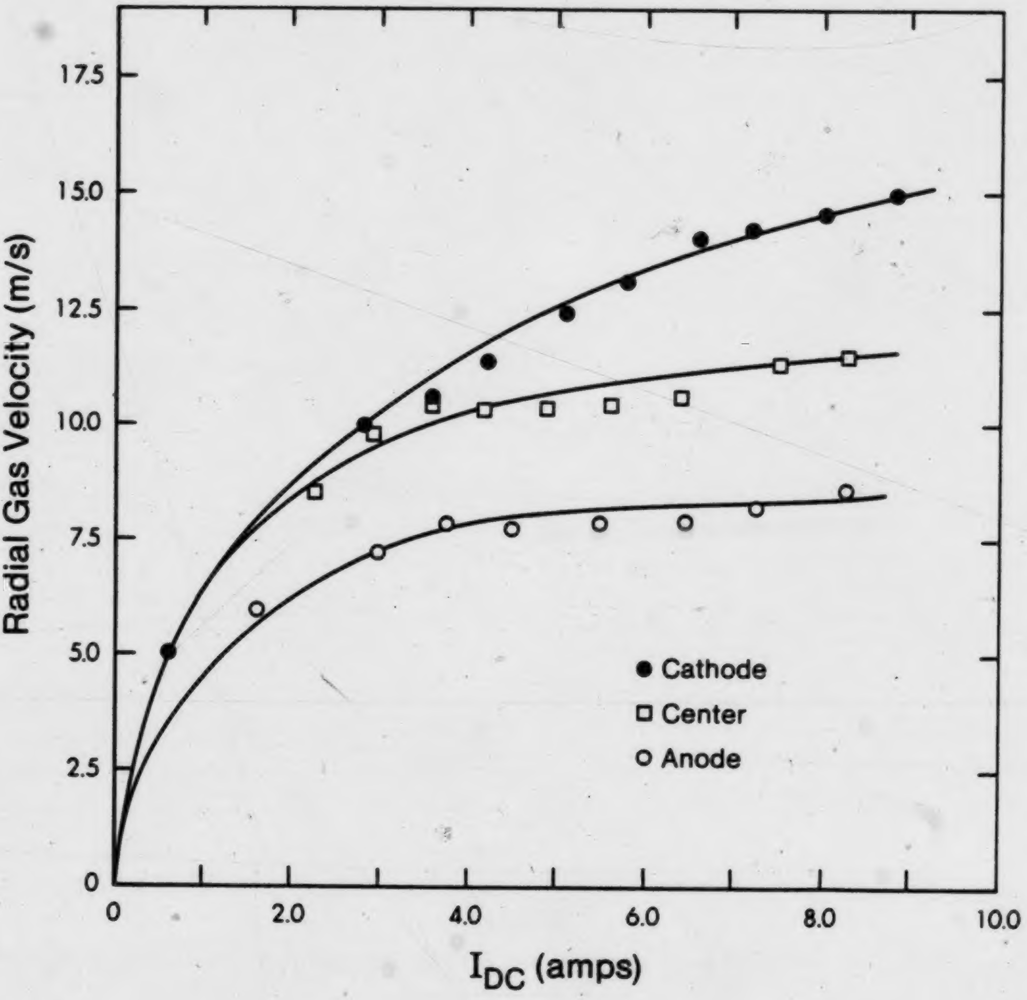

Fig. 6.13 Effect of Applied Discharge Current on the Radial Gas Velocity Profile. Gas discharge contains a 1:7:12 torr mixture of $CO_2/N_2/He$ with $B_{av} \simeq 400$ G.

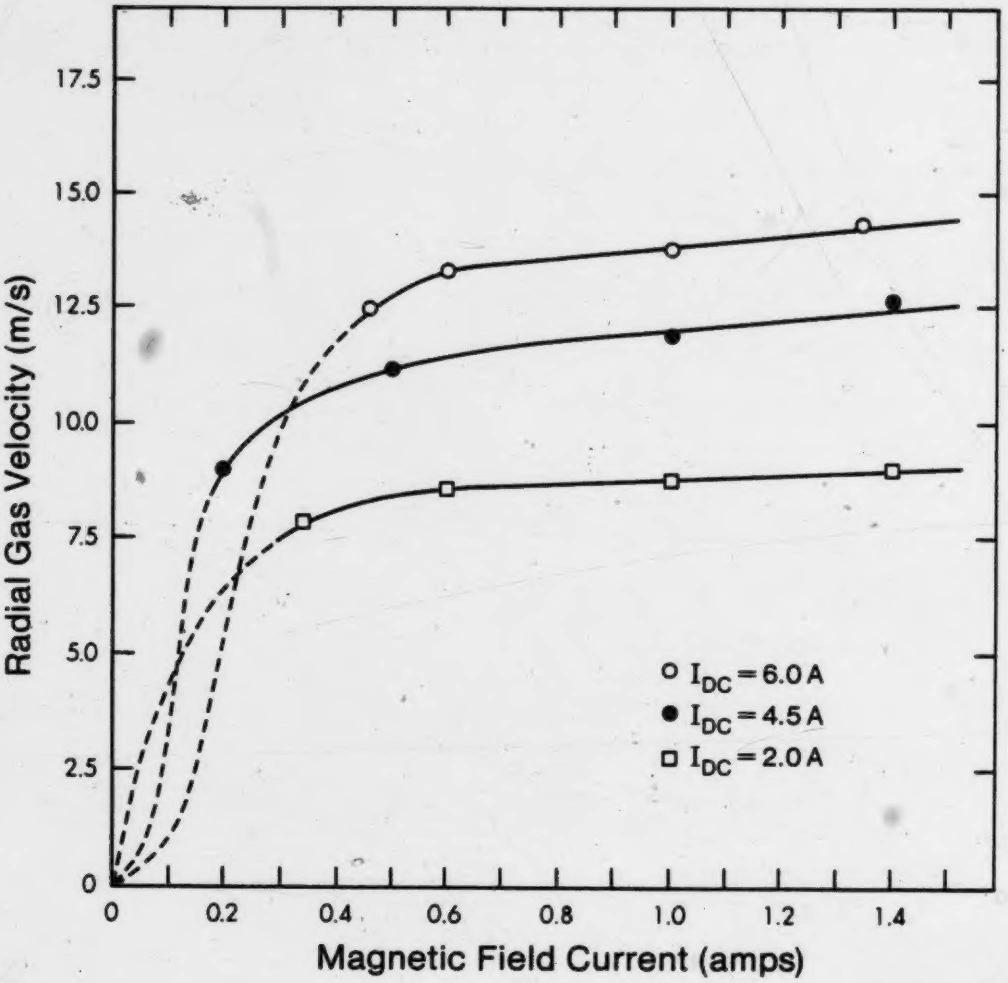

Fig. 6.14 Dependence of Radial Gas Velocity on Magnetic Field. Gas discharge contains 1:7:12 torr mixture of $CO_2/N_2/He$.

larger values of applied current. It is believed that this effect is due to a stronger Lorentz force required to overcome the high probability of a glow-to-arc transition for discharges with large current densities.

With further increase in magnetic field strength, the afterglow noticeably changed its shape by expanding radially. Reducing the magnetic flux density, immediately caused the afterglow to shrink in size and lose some of its luminosity. By maintaining a constant discharge current, an increase in magnetic field produced a linear rise in the detected radial gas flow. Figure 6.14 illustrates this dependence for several values of discharge current.

For a constant magnetic field, Fig. 6.13 also reveals that the radial gas velocity is an increasing function with respect to the applied discharge current. This result was also expected since the driving force is proportional to the current density. Thus, for large values of $\vec{J} \times \vec{B}$, a strong centrifugal force is created. The effect of this force, on the rotating plasma column, would tend to throw off neutral particles since they are strongly coupled to the motion of the charged particles by viscosity. However, the neutral particles are not bound by the applied electric and magnetic fields as are the charged particles. Therefore, they are free to establish a convective cell in which momentum can be transported out of the discharge volume. The resulting centrifugal pumping action is thus able to quickly remove hot spots from the discharge and replace it with fresh, cool gas.

6.5 VI CHARACTERISTICS OF A MAGNETIZED GLOW DISCHARGE

6.5.1 Glow-To-Arc Transition

It has long been known that most high power CW laser gas discharges operate in the abnormal glow region [1.2]. This region is characterized by a rapidly increasing plasma impedance as shown by the lower curve in Fig. 6.15. To maintain the gas discharge in the abnormal glow region it is necessary to continually increase the external ballast resistance. This procedure will shift the load line to a more stable point on the VI characteristic curve, at the expense of system efficiency. Failure to follow this guideline, will ultimately lead to a glow-to-arc transition, as speculated by the dashed curve in Fig. 6.15.

Under the influence of a magnetic field, the same gas discharge now has the characteristics of a normal glow, as illustrated by the upper curve in Fig. 6.15. In order to understand this marked difference in gas discharge behavior, it is instructive to follow the transition from a normal glow to an arc discharge. While operating in the normal glow regime, the discharge only partially covers the cathode surface. As the discharge current is increased, the current density and voltage remain constant. Consequently, the area of the discharge must increase proportionately. At the termination of the normal glow region, the cathode is completely covered by the glow, and its entire surface serves as an electron emitter. In order to further intensify the discharge current, it becomes necessary to increase the number of electrons created by ionization in the cathode fall. This

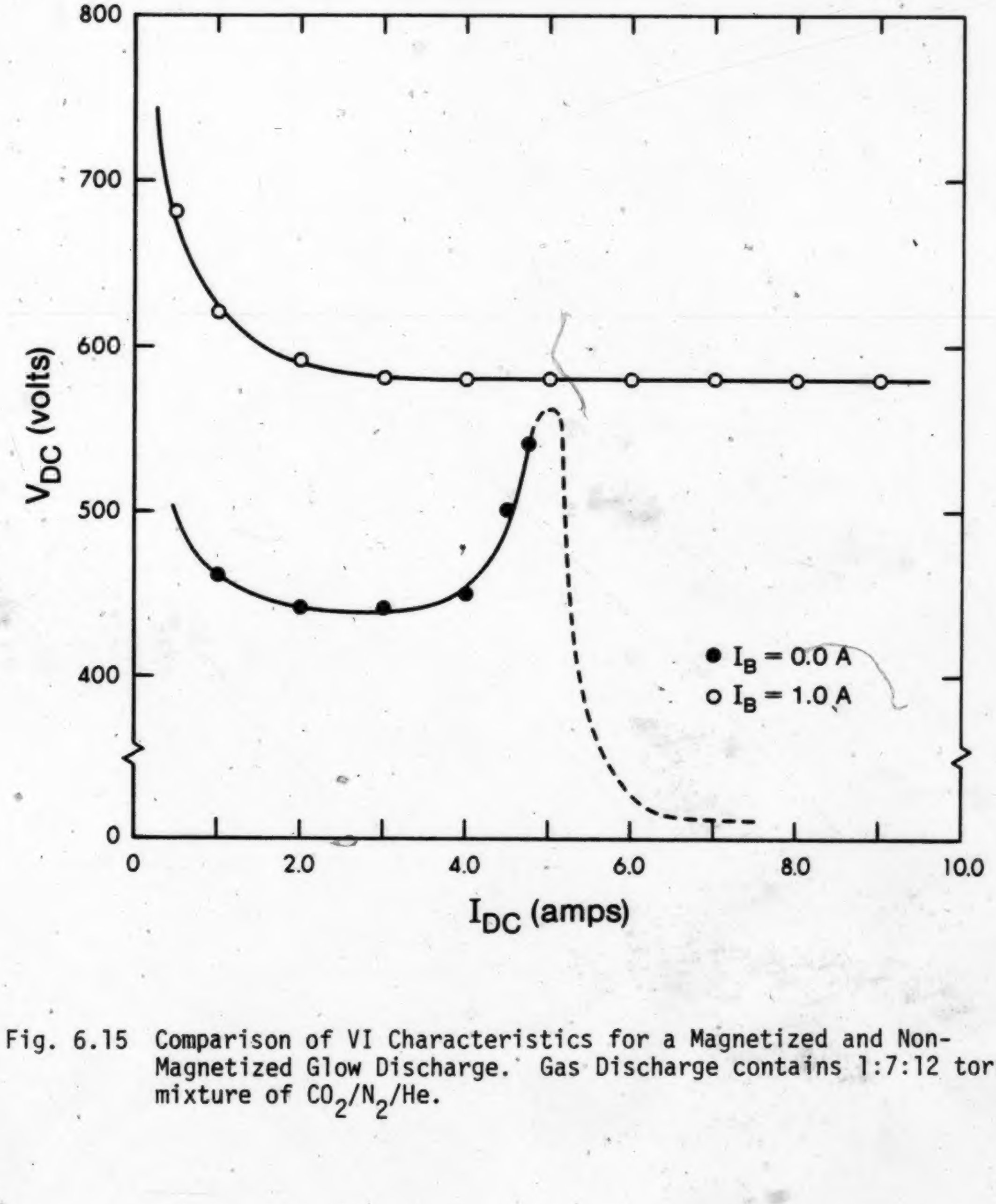

Fig. 6.15 Comparison of VI Characteristics for a Magnetized and Non-Magnetized Glow Discharge. Gas Discharge contains 1:7:12 torr mixture of $CO_2/N_2/He$.

process can be accomplished by increasing the voltage, and hence the electric field, in order to stimulate the rate of ionization by electron impact. The characteristic rise in voltage signals the onset of the abnormal glow. Since the cathode now receives a larger number of positive ions, each with a higher energy, its temperature rises. This process continues until the thermionic emission from the cathode surface becomes comparable to the electron emission by positive-ion bombardment. Since the thermionic emission current is a strongly increasing function of temperature, an additional rise in discharge current leads to greatly increased electron emission. The excess electrons increase the discharge conductivity by initiating an inter-electrode ionization channel or streamer. Upon further influx of energy, the streamer builds in intensity to form an arc discharge, characterized by a high current and a low voltage.

6.5.2 Behavior as a Normal Glow

A comparison of the two VI curves in Fig. 6.15 reveals that the magnetized glow discharge has an extended normal glow region. It is suspected that as the cathode glow layer expands to cover the cathode surface, an abnormal glow will eventually develop. Thus far, this transition has been far beyond the range of the existing power supplies. It is therefore believed that the magnetic field is creating an effect which prevents or delays the occurrence of an abnormal glow and subsequently a glow-to-arc transition. This section will explain the physical mechanisms involved in maintaining an otherwise unstable gas discharge as a normal glow.

As reported in Section 6.1.2, the annular shaped discharge is confined to a radial pressure well as a result of the radial Lorentz pressure $\vec{J}_\theta \times \vec{B}_z$. In addition, this force interacts with the space-charge sheaths, creating an annular shaped glow layer which only partially covers the cathode. Consequently, it would appear that the Lorentz forces can inhibit the expansion of the electron space-charge sheath and the positive column, thereby preventing the transition to an abnormal glow.

It has been determined from the theoretical analysis in Section 6.1.2, that the discharge can only rotate in regions where the forces created by electric and magnetic fields are balanced with radial pressure forces. Furthermore, the magnetic field profile controls and continuously adjusts the emitting cathode area to supply the desired discharge current. Therefore, the cathode becomes a more efficient emitter of electrons by producing more current through the cathode glow layer. At present, there are two known effects which can account for this process; involving the use of electrons and/or positive ions.

In the presence of a magnetic field, electrons and ions are required to gyrate about magnetic lines of force. It has been speculated that near the cathode, some electrons will acquire a sufficiently small Larmor radius such that they will be forced to return to the cathode, causing further secondary emission. This process is possible provided the electrons have not undergone any collisions. This can be expressed mathematically as

$$2\pi r_L < \lambda_m \tag{6.21}$$

where λ_m is the mean free path, and r_L is the Larmor radius defined by $r_L = \langle c_e \rangle / \omega_{ce}$. Equation 6.21 can be rearranged to yield an expression for the required magnetic field necessary for electron back-diffusion, that is,

$$B > \frac{2}{e\lambda_m}\left(8\pi m_e kT_e\right)^{\frac{1}{2}} = \frac{2.303 \times 10^{-7}\sqrt{T_e}}{\lambda_m} . \qquad (6.22)$$

This equation indicates that for typical gas discharge conditions, the electrons emitted from the cathode will be too energetic to be affected by the moderate strength of the magnetic field. Only electrons with energies less than 1 eV will have a chance of returning to the cathode. However, these electrons have insufficient energy to cause secondary emission and will thus be simply recaptured by the cathode.

Ion kinetic behavior can also be strongly influenced by a magnetic field. In particular, the applied Lorentz force creates a significant azimuthal velocity component. However, due to the nonlinear nature of the magnetic field, the rotational driving forces are strongly spatially dependent. Thus, the highly effective rotational shear will cause the ions to bombard the cathode surface at angles far from normal incidence. It has been well documented that the secondary electron emission yield can be effectively increased by over 100% for ionic angles of incidence greater than 45° [6.8]. The reason for this increased emission yield is due to secondary electrons being produced closer to the cathode surface for angles of oblique incidence. Thus, these newly liberated electrons have a higher probability of reaching the surface with correspondingly higher energy.

There is some experimental evidence to support this latter hypothesis. In particular, after running the gas discharge for an extended period, the cathode surface, upon examination, revealed a surface texture resembling a myriad of fine, closely spaced, hairline scratches. These scratches, up to 1 cm in length, were all parallel and uniformly distributed in the directon of discharge rotation. This effect was particularly noticeable for an aluminum cathode. The resulting scratches are believed to be due to sputtering action of the cathode's thin oxide coating by bombarding ions near grazing incidence [6.9].

6.5.3 Voltage-Current Curves

As shown in the previous section, the VI characteristics of a magnetically stabilized discharge, indicate that the plasma operates at a near constant E/n within the normal glow regime. Since the gas discharge was extremely stable, even for large current densities, only a small amount of external ballast was required for operation, typically about 15%. Further analysis was necessary to determine whether these beneficial characteristics could be affected by other parameters. This section will examine the operating conditions of the gas discharge and its dependence upon geometry, gas mixture, and pressure.

Through numerous experiments, the MGD stabilization approach was found to work effectively with each geometry considered. In each case, a stabilized gas discharge was observed to operate as a normal glow. However, it was quickly determined that the magnetic field was not of sufficient strength or configuration to establish a uniform plasma throughout the discharge volume. During operation of the tubular anode geometry, the plasma preferred to remain as a discharge column which rotated between the electrodes. In addition, the high speed rotating plasma, found in the coaxial geometry, preferred to exist as a thin disk. Thus, it can be surmised that the primary configuration of an electrical discharge is one that will occupy the least amount of volume in order to remain self-sustained.

Continued study of the gas discharge systems, revealed that an externally applied force has no ability to create additional current sources on the electrode surface. It can only distribute the existing current source in the direction of the applied force. As a consequence, the establishment of a uniform glow discharge is only partially promoted.

This problem was overcome through construction of a fluid ballasted, multi-pin anode. In this geometry, each pin electrode creates a small uniform glow discharge between it and the cathode. The resulting array of pins establishes a uniform glow discharge which fills the entire active volume. Now, the application of a magnetic field can impart convective motion to each individual discharge column, thereby forming a uniformly distributed rotating glow discharge.

Further testing revealed that the magnetic stabilization technique was relatively insensitive to the type and mixture of gases utilized. All were found to behave as a normal glow in the presence of a magnetic field. This included the electronegative gases O_2 and SF_6 , which could be stabilized when subjected to large magnetic fields. Accordingly, the magnetic stabilization technique may find numerous applications for a variety of laser gas mixtures.

These tests were repeated to test the effectiveness of this technique on varying gas pressures and magnetic fields. Figure 6.16 illustrates the VI characteristics of the magnetically stabilized coaxial discharge for a 2:8:10 torr mixture of $CO_2/N_2/He$. It is clearly seen that the magnetic field can appreciably change the operating discharge voltage. This variation in voltage is approximately linear with the applied magnetic field. However, as stated previously, saturation of the electromagnet core tends to reduce the field strength for larger values of field current. In Fig. 6.17, the partial pressures of each gas have now been doubled. The resulting curves are similar in shape to the previous case, but show higher operating voltages. This expected result is due to the larger breakdown voltages required for gases at higher pressures. By comparing Figs. 6.16 and 6.17, it can be stated that the influence of a magnetic field is equivalent to an increase in pressure of the gas discharge system.

It was also noticed that as the magnetic field or pressure increased, the gas discharge requires more current to establish a normal glow (constant voltage region). This effect can be explained through the use of Townsend's equation, that is,

$$\frac{\alpha}{p} = Ae^{-Bp/E} \quad . \tag{6.23}$$

His equation indicates that α, the number of electrons produced per unit length in the field direction, is reduced upon an increase in pressure. If a constant electric field is maintained, an increase in pressure will result in a larger number of low energy collisions,

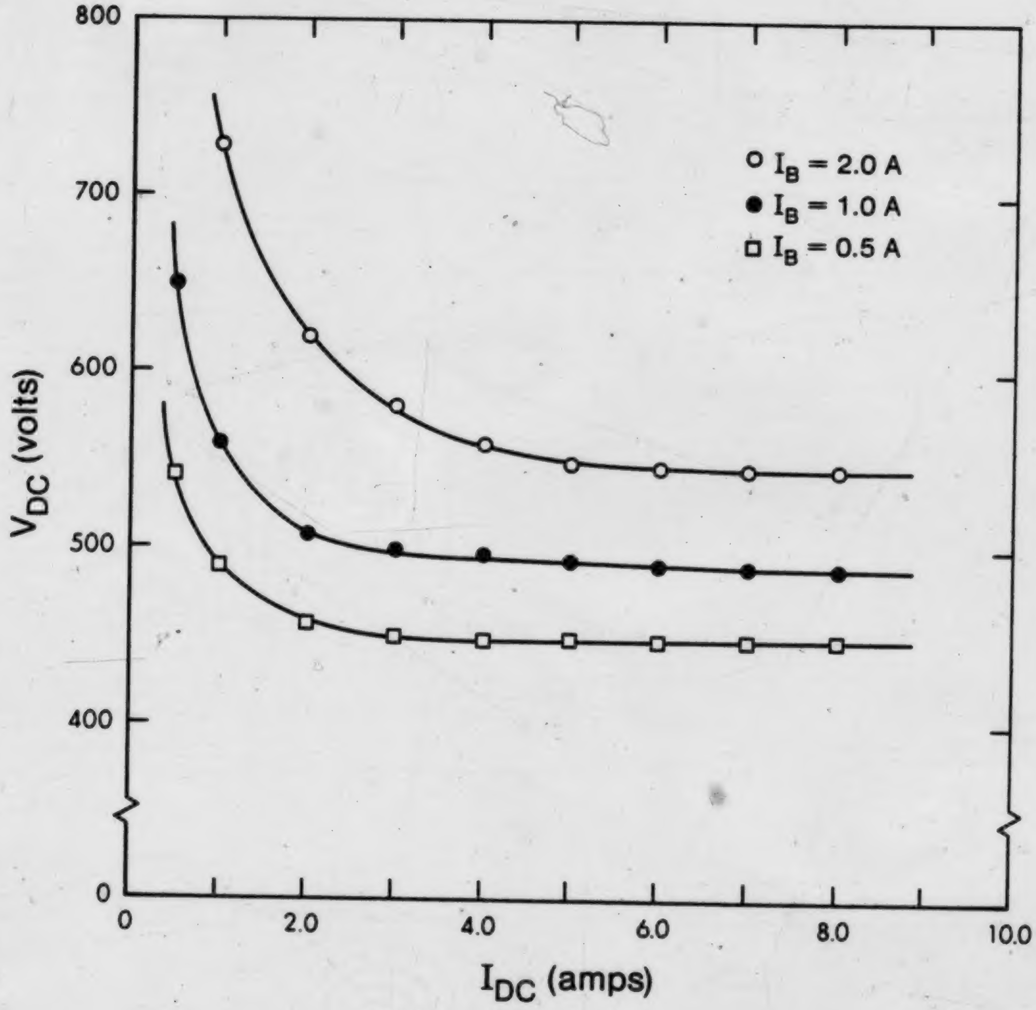

Fig. 6.16 VI Characteristics of a Magnetically Stabilized Coaxial Discharge. Gas discharge contains 2:8:10 torr mixture of $CO_2/N_2/He$.

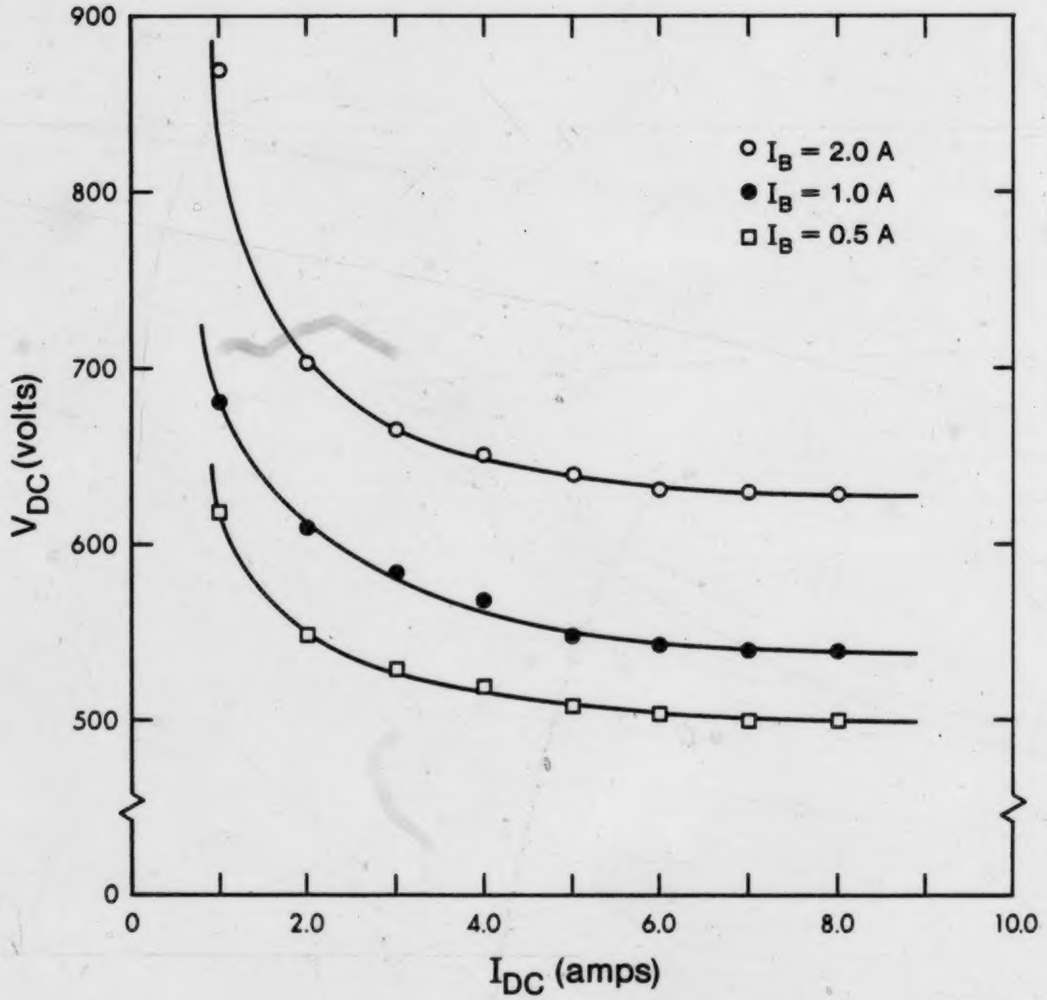

Fig. 6.17 VI Characteristics of a Magnetically Stabilized Coaxial Discharge. Gas discharge contains 4:16:20 torr mixture of $CO_2/N_2/He$.

thereby reducing the number of collisions involving ionization. The presence of a magnetic field also promotes less ionizing collisions since the charged particles must now gyrate about the magnetic field lines. During this process, the electrons and ions suffer periods of deceleration as they travel against the electric field. Thus, with less kinetic energy, the existing charged particles are less proficient in stimulating additional ionization. The resulting loss of electrons changes the VI characteristics by reducing the current density. Consequently, more applied discharge current is required to maintain a normal glow behavior.

This behavioral pattern was repeated for all gas mixtures analyzed including the 30:30:30 torr mixture of $CO_2/N_2/He$ shown in Fig. 6.18. Since the supply voltage was limited, the anode to cathode distance was reduced in order to achieve a breakdown voltage. Even at these very high gas concentrations, the magnetic field is highly effective in producing a normal glow discharge from an inherently unstable one.

Similar VI curves were made for the fluid ballasted, multi-pin anode structure and are displayed in Fig. 6.19. Examination of these curves also show a voltage variation with magnetic field. In addition, the VI characteristics of this electrode design show a glow-to-arc transition when the magnetic field is absent. This brief transition is speculated by the dashed curve. From these curves, it is also quite apparent that the constant voltage discharge is operating in the normal glow regime. This behavior is consistent with the small annular shaped cathode glow layer. Additional data were taken from

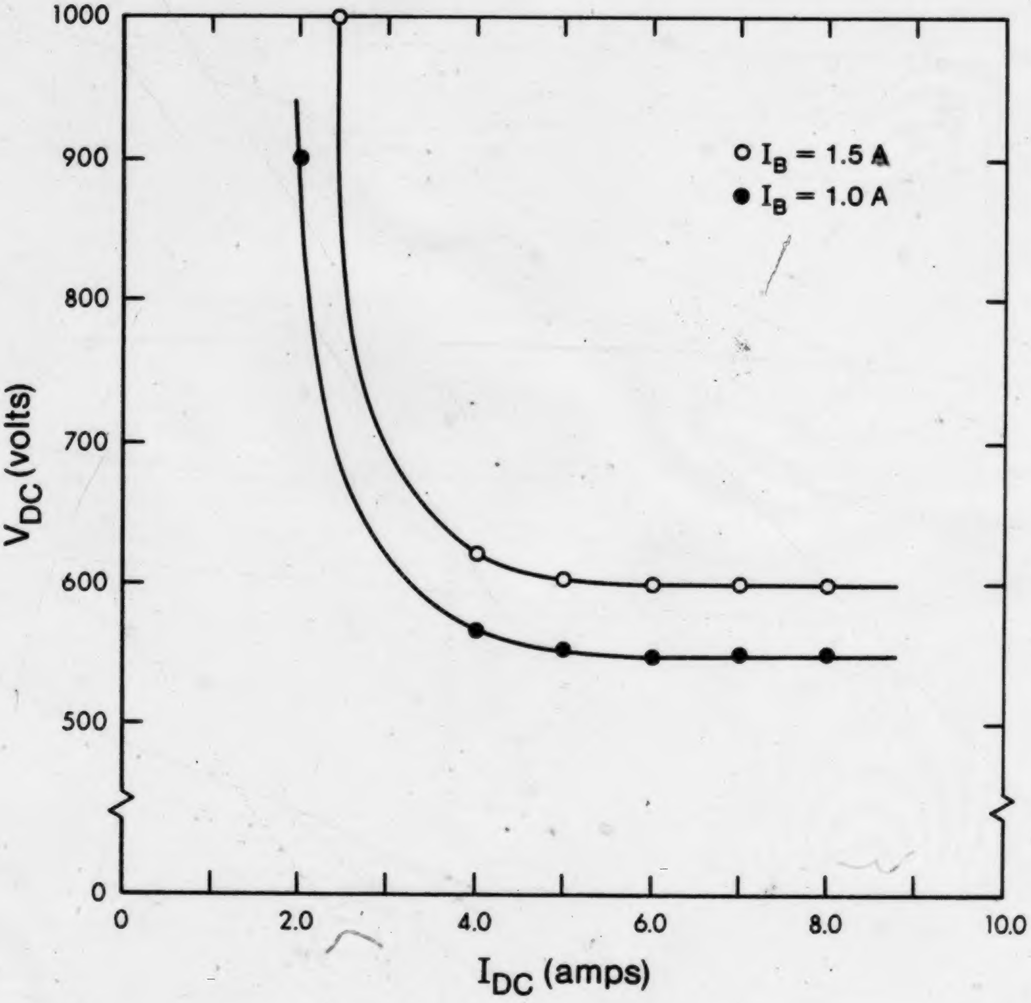

Fig. 6.18 VI Characteristics of a Magnetically Stabilized Coaxial Discharge. Gas discharge contains 30:30:30 torr mixture of $CO_2/N_2/He$.

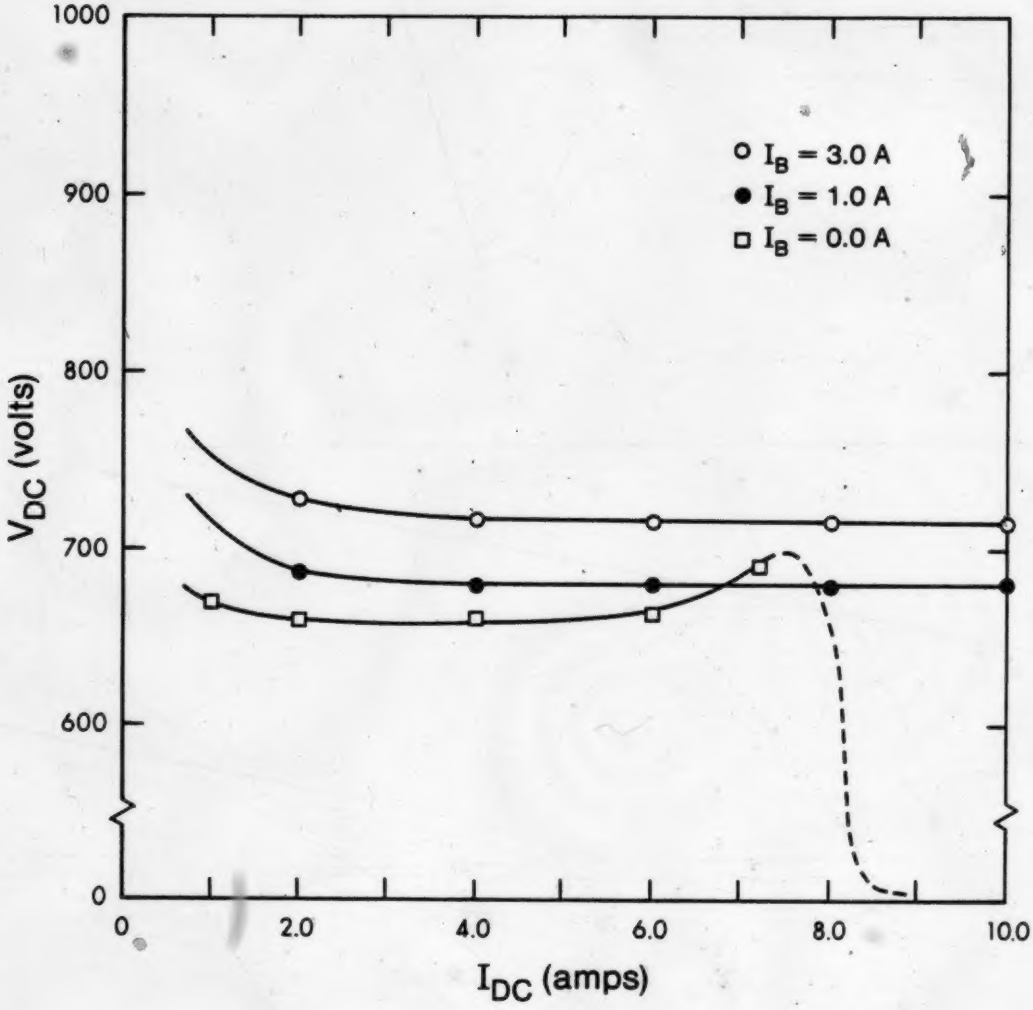

Fig. 6.19 VI Characteristics of a Magnetically Stabilized Fluid Ballasted Discharge. Gas discharge contains a 2:8:10 torr mixture of $CO_2/N_2/He$.

a similar gas composition but with a total pressure of 40 torr. Similar results were obtained but at a higher operating voltage.

The upper experimental points in these figures represent a specific discharge power loading of about 10 kW/l. This value is particularly encouraging in that it is substantially more than that which could be achieved under comparable conditions with a conventionally ballasted electrode structure. To date, an upper instability threshold has still not yet been observed, suggesting that even higher power loading is possible.

6.5.4 Variation of the VI Characteristics with Magnetic Field

It is well known that numerous changes in a gas discharge's characteristics can occur when it has been subjected to a magnetic field. Some of these effects have already been observed in the form of a discharge rotation due to Lorentz forces, oblique angle bombardment of the cathode surface and a variation of the length of the cathode dark space. As demonstrated throughout this thesis, the applied Lorentz force has usually been found to be responsible for the plasma's distinct behavior. This section will now investigate the variation of the discharge current and voltage in the presence of a magnetic field.

It has been previously determined that the normal glow behavior exhibited by the magnetically stabilized discharge, was due to the creation of a more efficient cathode emitter. Furthermore, the motion of charged particles is directly influenced by the combination of electric and magnetic fields. Thus, under the action of a magnetic field that is transverse to the applied electric field, a significant number of electrons and ions will be deflected away from the discharge axis. In the transverse geometry, the radial magnetic field forces particles to travel in the radial and azimuthal directions. Similarly, in the coaxial geometry, an axial magnetic field forced the particles to flow radially and azimuthally.

Through the use of Boltzmann's transport equation, it can be shown that the magnetic field does not affect the component of charged particle drift velocity parallel to $\vec{B}$. However, the drift velocity in the direction of $\vec{E}$, perpendicular to $\vec{B}$, decreases and a velocity component perpendicular to both $\vec{E}$ and $\vec{B}$ appears. The newly created drift velocity components are thus responsible for the dramatic change in gas discharge behavior. A more detailed analysis will be presented in Chapter 7.

It is well known that a particle's drift velocity is related to its mobility. Thus, it becomes possible to associate the effect of a transverse magnetic field with the transport properties of the gas. In this respect, the mobility becomes a tensor and may be written in the form

$$u_{ij} = \frac{e}{m_e} \Omega_{ij} \tag{6.24}$$

where Ω_{ij} is the collision frequency tensor defined by Eqn. 4.39. Examination of the mobility component perpendicular to $\vec{B}$, indicates that charged particle transport is now reduced in this direction since

$$u_{\perp} = \frac{e}{m_e \nu_{es}} \left(\frac{\nu_{es}^2}{\omega_{ce}^2 + \nu_{es}^2} \right) < u_{\parallel} \ .$$

In other words, the transverse magnetic field reduces the mobility of the charged particles in the direction of the applied electric field. Thus, the effective electric field normal to the electrodes, is decreased. This result confirms that the ratio E/p is reduced upon application of a magnetic field.

Due to the transverse magnetic field, deflected charged particles can undergo several revolutions of the discharge active volume during an inter-electrode transit. Thus as a result of this process, a new electric field perpendicular to the original field will be created. The total effective electric field will then take the form

$$E_{eff}^2 = E_{11}^2 + E_{\perp}^2 \left(\frac{\nu_{es}^2}{\omega_{ce}^2 + \nu_{es}^2} \right) \qquad (6.25)$$

as derived by Golant [6.10]. In this expression, E_{11} is the new component of electric field parallel to B and the second term is the reduced electric field normal to the electrodes. The effective increase in the overall electric field could then be detected as a rise in the measured discharge voltage.

The VI characteristic curves in Figs. 6.16-6.18 illustrate that a significant variation in discharge voltage does accompany a change in magnetic field. This association is depicted in Fig. 6.20 where the initial operating voltage is observed to rise linearly with applied magnetic field. As expected, Fig. 6.20 also shows that the discharge voltage is dependent upon pressure.

Additional investigation has revealed that since the current density is a function of the electron drift velocity, it too will

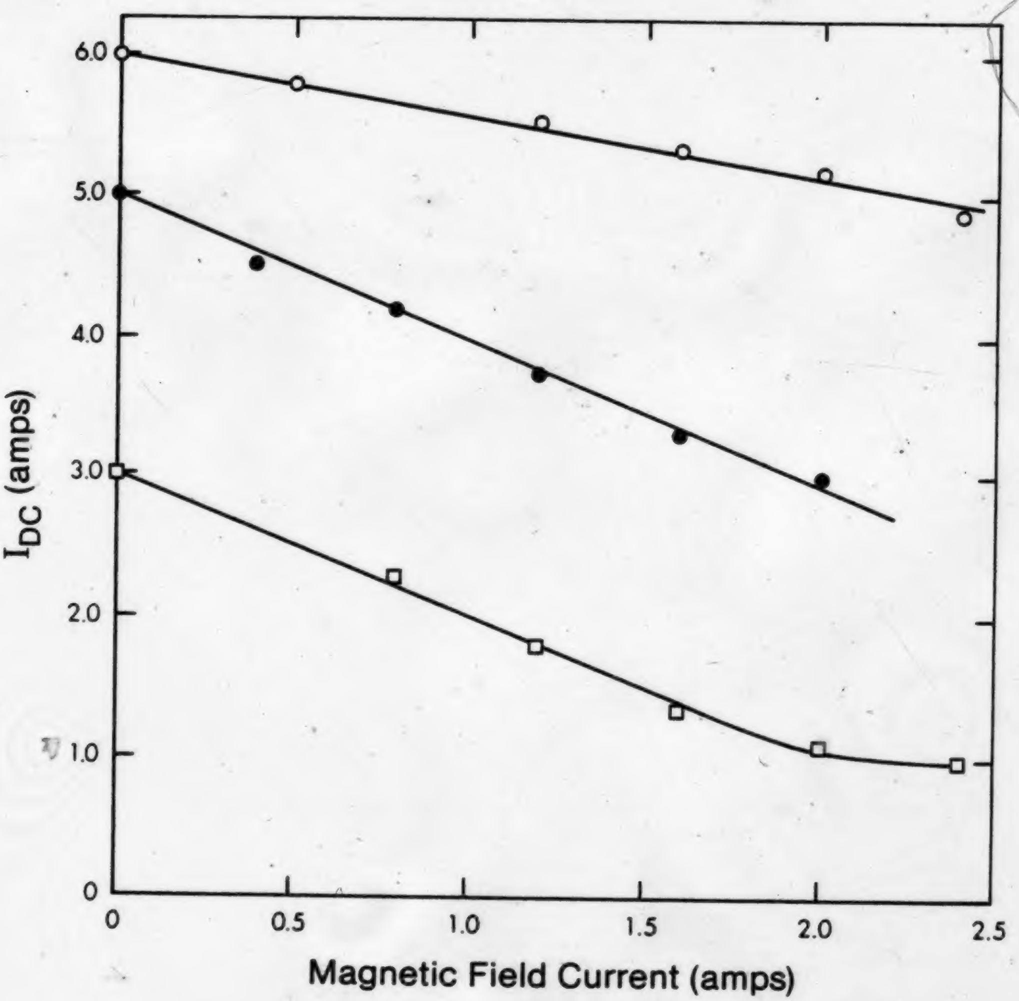

Fig. 6.20 Variation of Discharge Voltage with Magnetic Field.

decline with applied magnetic field. This relationship has been confirmed by Fig. 6.21 which shows the variation of discharge current for different values of $\vec{B}$ with different initial discharge currents. Over the region of interest, this dependence appears to be linear. However, due to saturation effects of the magnet core, the magnetic field values at high field currents tend to be slightly inaccurate. The plot in Fig. 6.21 is typical of those measured for each discharge geometry. In addition, the linear variation of discharge current was observed to be independent of gas species and mixture.

Similar results were obtained for a small gas discharge tube by Sen and Gupta [6.11] where variations in discharge current were observed with respect to changes in pressure. However, their pressure-current relationship decreased as the pressure exceeded 150 mtorr. Consequently, this second variation was not observed in the present investigation since operating pressures normally exceeded 10 torr.

One further parameter of interest concerns the dependence of the plasma impedance, R_p , on the magnetic field strength. This relationship is displayed in Fig. 6.22, and is found to be initially linear for low magnetic field values. Overall, the graph indicates that the plasma impedance rises as the applied magnetic field increases. An examination of the conductivity tensor reveals that the perpendicular component $\sigma_\perp$ is a decreasing function of magnetic field strength. Thus, current flow is reduced in this direction as previously seen. Consequently, this process will not favour the formation of highly conductive ionization channels or arc-like streamers along the discharge axis.

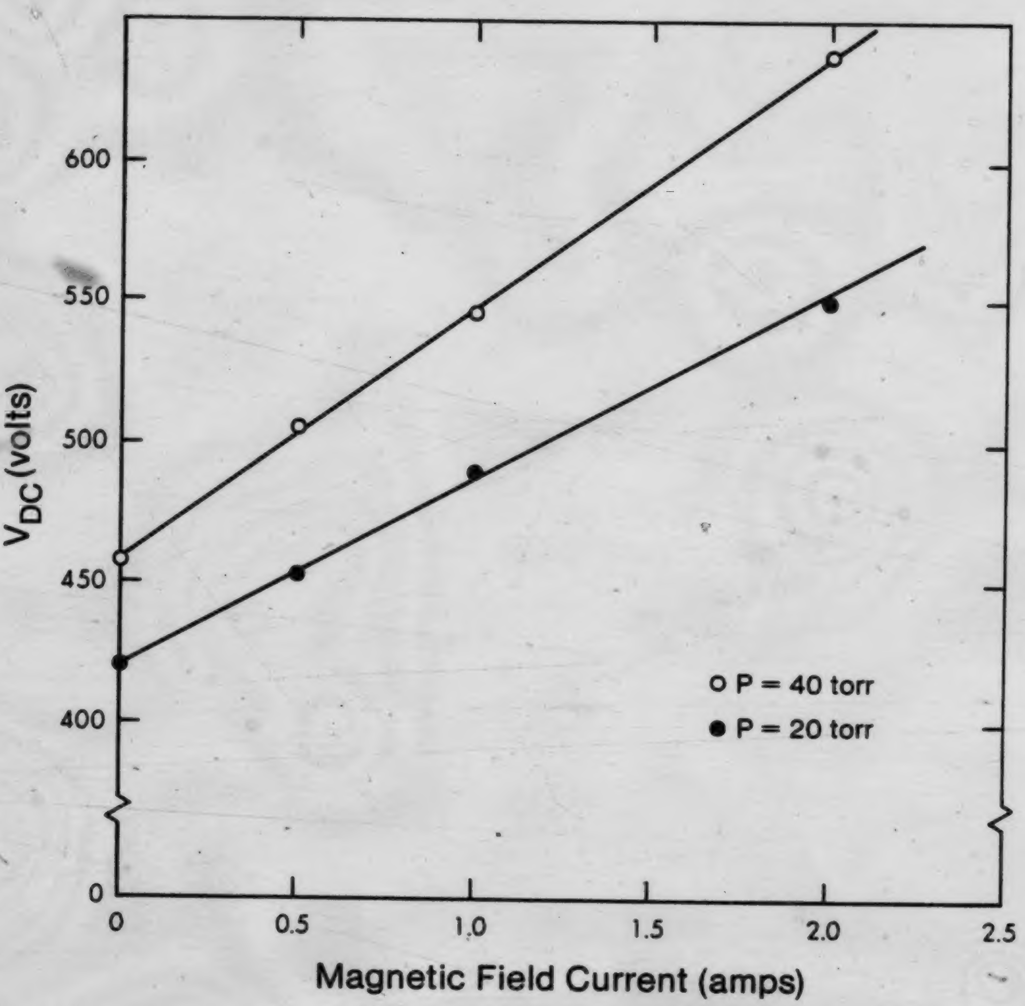

Fig. 6.21 Variation of Discharge Current with Magnetic Field.

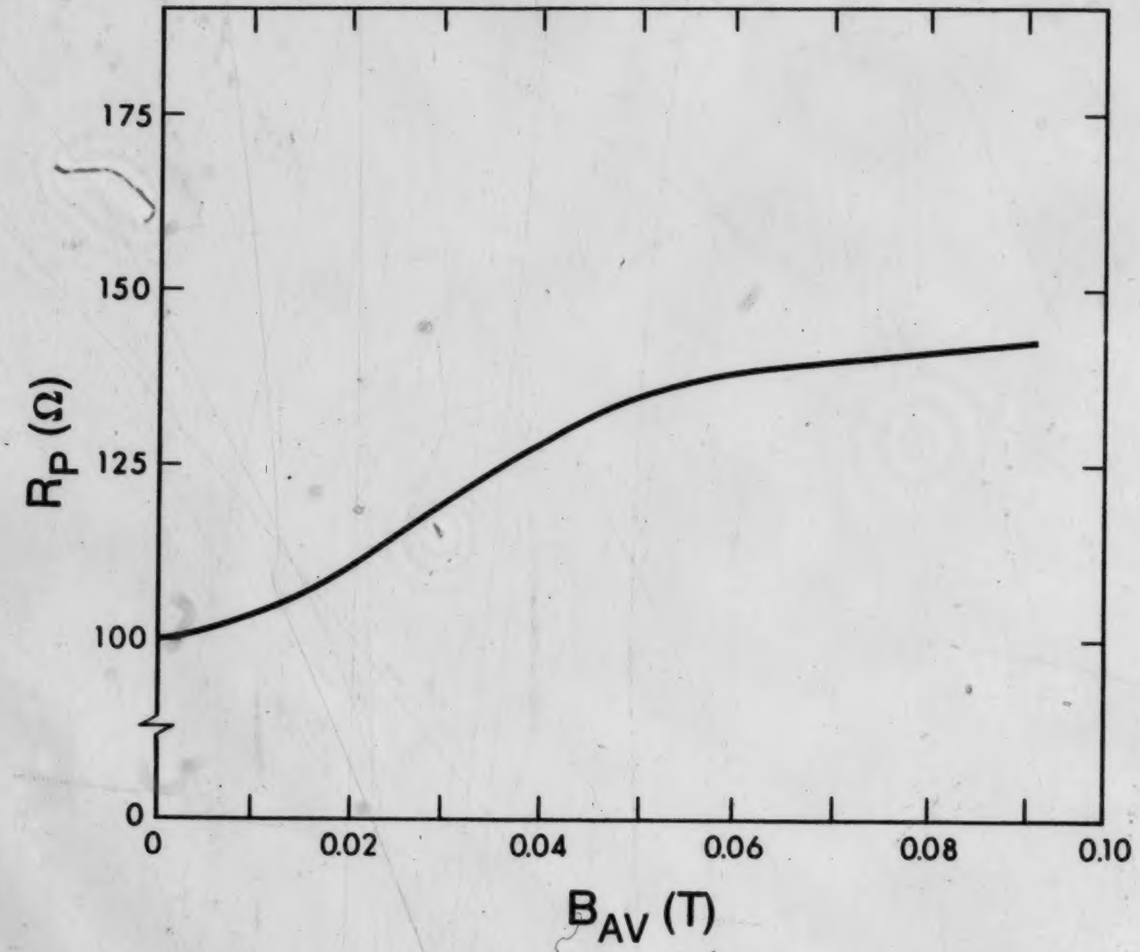

Fig. 6.22 Variation of Plasma Impedance with Magnetic Field.

CHAPTER 7

DYNAMICS OF A MAGNETIZED GAS DISCHARGE

7.1 INTRODUCTION

Throughout this thesis, the influence of a magnetic field has been shown to have a substantial effect on the behavior of an ionized gas discharge. It has already been determined that the magnetic field can alter discharge characteristics through variations in the charged particle drift velocity, and collision frequency. Further analysis will show that the magnetic field is capable of modifying the expressions for the Townsend coefficients as well. All of the effects may be derived from an analysis of the electron distribution function.

It is well known that a stabilized gas discharge is the first requirement for the construction of a high power laser. Thus far, it has been observed that the magnetic field is extremely effective in maintaining a stable, normal glow discharge. This chapter will elaborate upon the MGD stabilization scheme in both the space-charge sheaths and the plasma bulk regions. Furthermore, it will be explained how the reduction in the effective value of E/p leads to a less self-sustained discharge.

The magnetic field has been found to be responsible for increasing the total number of inelastic electron-neutral collisions. This effect has the potential of increasing the excitation rate for vibrational pumping and thereby improving laser excitation efficiency. Verification of this theory will be revealed through a detailed gain analysis.

7.2 DISCHARGE STABILIZATION MECHANISM

The initial study and preliminary analysis performance on the magnetic discharge structure of Fig. 3.2, suggested that the mechanism responsible for the stabilization of the glow discharge involved a highly sheared rotational velocity. The resulting velocity, driven by spatially dependent Lorentz forces, developed an effective mixing of the ionized gas within the space-charge region near the cathode surface and in the positive column.

It is well known that within a glow discharge, the largest electric field strengths are found within the cathode fall region. Here, field strengths can be several orders of magnitude larger than in the plasma bulk. This implies that the largest rotational mixing processes will occur in the space-charge sheaths directly below the cathode surface. Since the electric field strength within the cathode fall region drops linearly with distance from the electrode surface [7.1], a strong rotational velocity shear will be developed in this region. This particular aspect has already been speculated by the oblique angle bombardment of positive ions upon the cathode surface.

The analysis of the stabilization mechanism can be accomplished by examining the Lorentz forces acting upon the glow discharge. As indicated by Fig. 7.1, the discharge can be approximated as consisting of three radial and three axial regions. The radial regions are defined as zones of different magnetic field strengths and direction, that is, region I ($B_z > 0$, $|B_z| > B_r$), region II ($|B_z| < B_r$), and region III ($B_z < 0$, $|B_z| > B_r$). Similarly, the three axial regions

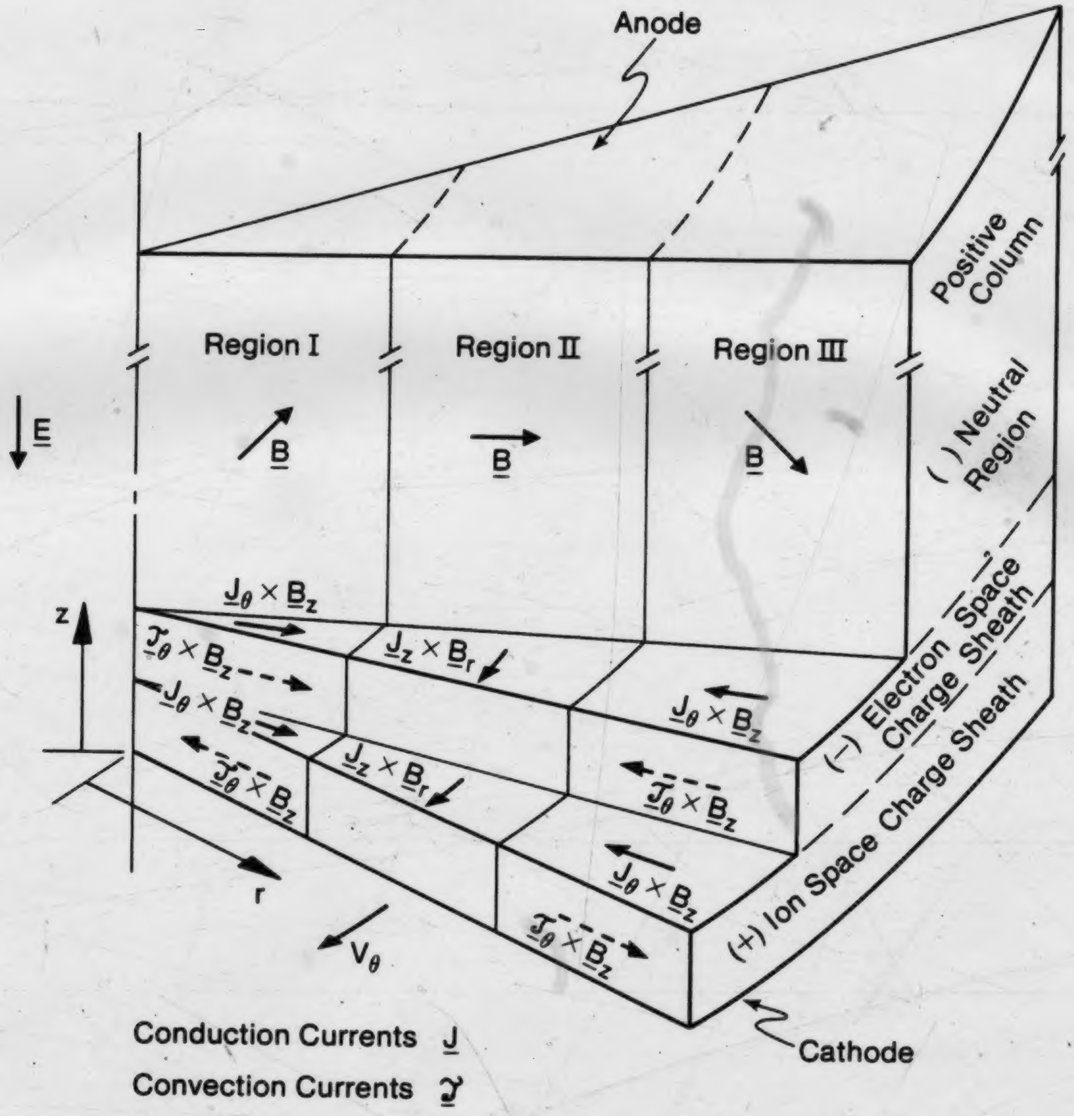
Anode
Positive Column
Region I
Region II
Region III
E
B
B
B
( ) Neutral Region
(−) Electron Space Charge Sheath
(+) Ion Space Charge Sheath
$J_\theta \times B_z$
$\mathcal{J}_\theta \times B_z$
$J_z \times B_r$
$J_\theta \times B_z$
$\mathcal{J}_\theta \times B_z$
$J_z \times B_r$
$J_\theta \times B_z$
$\mathcal{J}_\theta \times B_z$
$J_\theta \times B_z$
$\mathcal{J}_\theta \times B_z$
z
r
V_θ
Cathode
Conduction Currents J
Convection Currents $\mathcal{J}$

Fig. 7.1 Lorentz Forces Acting Upon a Glow Discharge in a Transverse Electrode Geometry.

are defined by (1) an ion space-charge sheath found in the cathode dark space and negative glow, (2) an electron space-charge sheath located in the Faraday dark space, and (3) the neutral plasma bulk found in the positive column.

The total current in the positive and negative sheath layers must include a conduction current $\vec{J}$ and a convection current $\vec{J}$, resulting from the azimuthal rotation of the space-charge layer. An examination of force terms in the θ direction reveals that the $\vec{J}_z \times \vec{B}_r$ force will cause a rotation of both the charged and the neutral fluids in the negative θ direction. It is assumed that both fluids are strongly coupled together within this highly collisional gas discharge. The radial forces $(\vec{J}_\theta \times \vec{B}_z)$ acting on the charged fluid in regions I and III will tend to force the discharge current into an annulus (region II). This process has been confirmed by experimental observations.

The convection current J_θ in the ion space-charge sheath, will create an outward radial force $(\vec{J}_\theta \times \vec{B}_z)$ which will tend to spread the ion sheath along the cathode surface. It is expected that this force will be minimal since the ion sheath velocity is low due to viscous drag. The actual location of the discharge within region II will be dependent upon a balance between centrifugal, radial pressure, and Lorentz force terms as illustrated by Eqn. 6.5.

The strong spatial variation in the discharge current and the direction and magnitude of the imposed magentic field, implies that the rotational driving force $(\vec{J}_z \times \vec{B}_r)$ will also exhibit a strong spatial dependence. This result confirms that the rotational velocity within the charged sheath regions and in the positive column will be highly sheared. As previously discussed, the sheared flow profile, within the ion and electron sheaths, creates a uniform and controlled secondary emission from the cathode. The plasma bulk is therefore uniformly supplied with charge carriers from this electron emitting region. The strongly sheared flow within the remainder of the discharge volume will rapidly distribute any local nonuniformities in density, temperature, or current throughout the active volume. It is this convective process that is instrumental in preventing the development of self-regenerative electrothermal bulk instabilities which would normally lead to the formation of a constricted arc discharge [2.6].

7.3 ELECTRON DISTRIBUTION FUNCTION IN A MAGNETIC FIELD

In order to thoroughly explain the variation of gas discharge parameters in the presence of a magnetic field, an analysis of the electron distribution function is necessary. The technique employed to solve the kinetic or Boltzmann transport equation given by

$$\frac{\partial}{\partial t}(nf) + \vec{v}\cdot\vec{\nabla}(nf) + \frac{e}{m_e}(\vec{E}+\vec{v}\times\vec{B})\cdot\vec{\nabla}_v(nf) = \frac{\delta}{\delta t}(nf) \ , \tag{7.1}$$

is based upon the assumed low anisotropy of the electron distribution function in a uniform electric field [6.10]. When the electric field strength is not excessive, the electron velocity distribution function depends only upon the velocity $\vec{v}$ and the angle θ between the directions of velocity $\vec{v}$ and the field $\vec{E}$. This assumption is quite valid for values of $\vec{E}$ normally utilized in gas laser discharges. The dependence of the angle θ, which is due to the anisotropy of the distribution function, must also be small. In this limit, the distribution function can be expanded in orthogonal Legendre polynomials, that is,

$$f(\vec{v}) = \sum_{n=0}^{\infty} f_n(v) P_n(\cos\,\theta)$$

where the distribution function $f_n(v)$ only depends upon the velocity. If the perturbation in the distribution function is small, it is possible to restrict the expansion of $f(\vec{v})$ in terms of spherical harmonics to the first two terms in the series. Consequently

$$f(\vec{v}) = f_0(v) + \cos(\theta) f_1(v) \tag{7.3}$$

where the function $f_0(v)$ is the isotropic Maxwellian distribution and $f_1(v)$ is the directed component of the distribution function.

In the presence of electric and magnetic fields, the solution for the electron distribution function is sought in the general form

$$\begin{aligned} f(\vec{v}) &= f_0(v) + \frac{v_x f_{1_x}(v)}{v} + \frac{v_y f_{1_y}(v)}{v} + \frac{v_z f_{1_z}(v)}{v} \qquad (7.4) \\ &= f_0(v) + \frac{\vec{v}\cdot\vec{f}_1(v)}{v} \end{aligned}$$

which depends upon all velocity components. Substituting the representation for the altered distribution function, Eqn. 7.4, into the kinetic equation will produce a set of equations for the functions f_0 , f_{1_x} , f_{1_y} , and f_{1_z} . The first equation is obtained by averaging the kinetic equation over all the velocity directions by integrating over the solid angle $d\omega$. The equations for the directed components are obtained by averaging after multiplying by the direction cosines of the angles between the velocity vector and the coordinate axes [7.1]. This produces the equation

$$\frac{\partial}{\partial t}(n_e f_0) + \frac{v}{3}\vec{\nabla}\cdot(n_e\vec{f}_1) - \frac{en_e}{3m_e v^2}\frac{d}{dv}(v^2\vec{E}\cdot\vec{f}_1) = S_0 \tag{7.5}$$

and

$$\frac{\partial}{\partial t}(n_e\vec{f}_1) + v\vec{\nabla}(n_e f_0) - \frac{en_e}{m_e}\vec{E}\,\frac{df_0}{dv} - \frac{en_e}{m_e}(\vec{B}\times\vec{f}_1) = \vec{S}_1\ . \tag{7.6}$$

The collision terms S_0 and $\vec{S}_1$ are given by the terms

$$S_0 = \frac{1}{4\pi}\int_\omega \frac{\delta(n_e f)}{\delta t}\,d\omega \tag{7.7}$$

and

$$S_{1_k} = \frac{3}{4\pi}\int_\omega \frac{\delta(n_e f)}{\delta t}\cos\,\theta_k d\omega \tag{7.8}$$

where $d\omega = \sin\,\theta d\theta d\phi$ and θ_k is the angle between the k axis and the velocity vector.

If the distribution function is independent of time and coordinates, Eqns. 7.5 and 7.6 may be simplified to

$$\frac{-n_e e}{3m_e v^2}\frac{d}{dv}(v^2\vec{E}\cdot\vec{f}_1) = S_0 \tag{7.9}$$

and

$$\frac{n_e e\vec{E}}{m_e}\frac{df_0}{dv} + \frac{n_e e}{m_e}(\vec{B}\times\vec{f}_1) = -\vec{S}_1\ . \tag{7.10}$$

The collision integral $\vec{S}_1$ can be obtained by substituting the elastic and inelastic collision integrals for the term $\left(\frac{\delta f}{\delta t}\right)$. The electron-neutral momentum transfer collision frequency is large compared with the electron-electron and electron-ion collision frequencies and thus $\vec{S}_1$ may be resolved into the form [6.10]

$$\vec{S}_0 = -n_e \nu_{es} \vec{f}_1 \ . \tag{7.11}$$

Substituting this expression into Eqn. 7.10 produces the equation

$$\frac{e\vec{E}}{m_e}\frac{df_0}{dv} + \frac{e}{m_e}(\vec{B} \times \vec{f}_1) - \nu_{es} f_1 = 0 \ . \tag{7.12}$$

If the magnetic field is directed along the z-axis, the projections of Eqn. 7.12 on the coordinate axes take the form

$$\frac{eE_x}{m_e}\frac{df_0}{dv} - \frac{eBf_{1_y}}{m_e} - \nu f_{1_x} = 0$$

$$\frac{eE_y}{m_e}\frac{df_0}{dv} - \frac{eBf_{1_x}}{m_e} - \nu f_{1_y} = 0$$

$$\frac{eE_z}{m_e}\frac{df_0}{dv} - v f_{1_z} = 0 \ .$$

Rearranging and solving this system of equations yields

$$\vec{f}_1 = \frac{e\hat{\Omega}}{m_e} \cdot \vec{E}\,\frac{df_0}{dv} \tag{7.13}$$

where $\hat{\Omega}$ is the collision frequency tensor described by Eqn. 4.39. These results indicate that the magnetic field can introduce anisotropy throughout the ionized gas in the form of a perturbation to the electron distribution function. In the absence of a magnetic field, the collision frequency tensor becomes the unit tensor and Eqn. 7.13 simply indicates the perturbation of the distribution function due to the imposed electric field, that is,

$$\vec{f}_1 = \frac{e}{m_e \nu_{es}} \vec{E} \frac{df_0}{dv} \quad \text{for} \quad B = 0 \; .$$

Equation 7.9 can be conveniently expressed in the form of the divergence of a spherically symmetric flux in velocity space, that is,

$$S_0 = \vec{\nabla}_v \cdot \Gamma_E = \frac{1}{v^2} \frac{d}{dv}(v^2 \Gamma_E)$$

where

$$\Gamma_E = \frac{-n_e e}{3m_e} \vec{E} \cdot \vec{f}_1 = \frac{-n_e e^2}{3m_e^2} \vec{E} \cdot (\hat{\Omega} \cdot \vec{E}) \frac{df_0}{dv} \; .$$

The term $\vec{E} \cdot (\hat{\Omega} \cdot \vec{E})$ can be simplified by introducing an effective electric field, defined as

$$E_{eff}^2 = \vec{E} \cdot (\hat{\Omega} \cdot \vec{E}) \nu_{es} \; . \tag{7.14}$$

If no electric field component exists in the y direction, then Eqn. 7.14 simplifies to

$$E_{eff}^2 = E_z^2 + E_x^2 \left(\frac{\nu_{es}^2}{\omega_{ce}^2 + \nu_{es}^2} \right)$$

as derived by Golant et. al. [6.10]. By defining an effective electric field in this manner, Eqn. 7.9 can be written in a form common for both the presence and absence of a magnetic field. The dependence of f_0 on B appears only in terms of E_{eff} . Therefore, to determine the effect of a magnetic field on the distribution function, it is only required to replace E by E_{eff} .

7.4 DRIFT VELOCITY IN A MAGNETIC FIELD

As was earlier surmised, the magnetic field can dramatically change the drift velocity pattern for charged particles. This section will closely examine their altered behavior and derive an expression for the electron drift velocity in the presence of a magnetic field.

The average electron drift velocity can be obtained by applying Eqn. 4.36 which states

$$<v_k> = \frac{1}{n_e} \int v_k f(\vec{v}) d\vec{v} \ .$$

By substituting the approximation given by Eqn. 7.4 for $f(\vec{v})$ into the above integral, the following result is obtained for the drift velocity

$$V_{e_k} = \frac{1}{n_e} \int_V \left(v_k f_0(v) + \sum_\ell \frac{v_k v_\ell}{v} f_{1_\ell}(v) \right) v^2 dv \sin\theta d\theta d\phi \ . \qquad (7.15)$$

By inserting the direction cosines and integrating over the angles, the kth component of the drift velocity becomes

$$V_{e_k} = \frac{4\pi}{3n_e} \int_0^\infty v^3 f_{1_k}(v) dv \qquad (7.16)$$

since all remaining terms contain odd functions which vanish upon integration. The substitution of Eqn. 7.13 into Eqn. 7.16 yields

$$V_{ek} = \frac{4\pi e}{3n_e m_e} \ E_k \int_0^\infty v^3 \Omega_{jk} \frac{df_0}{dv} dv \ .$$

Provided the electron collision frequency, ν_{es} is a constant, the integration can be done by parts to give

$$V_{e_k} = \frac{4\pi e}{3n_e m_e} \Omega_{jk} E_k \left\{ v^3 f_0(v) \Big|_0^\infty - 3\int_0^\infty v^2 f_0(v) dv \right\}$$

where the first term approaches zero at both limits when the Maxwellian distribution function is used for f_0 . Integration of the second term produces the result,

$$V_{e_k} = -\frac{e}{m_e} \Omega_{jk} E_k \ . \tag{7.17}$$

Equation 7.17 indicates that the electron drift velocity is also a function of the collision frequency tensor and accordingly the magnetic field.

This result shows that the velocity component parallel to the magnetic field is unaffected. In addition the effect of the magnetic field on the perpendicular velocity components is substantial when $\omega_{ce} > \nu_{es}$. In this limit the electrons are able to make numerous gyrations during an inter-collisional time. As the electrons gyrate, they undergo an $\vec{E} \times \vec{B}$ drift which increases the inter-electrode transit time and correspondingly the distance traveled. This process also increases the number of inelastic collisions, and as indicated by Eqn. 7.17, reduces the electron drift velocity in the $E_\perp$ direction. Consequently, the rate of energy acquired by the electrons from the $E_\perp$ field component, is significantly decreased.

A similar analysis for the ions can be performed using the perturbed ion distribution function in electric and magnetic fields.

The results will be identical in form, however, the collision frequency tensor will now contain the ion cyclotron and ion-neutral collision frequencies respectively.

7.5 IONIZATION AND COLLISIONAL RATE COEFFICIENTS IN A MAGNETIC FIELD

As previously seen, the application of a transverse magnetic field, complicates the analysis of an ionized gas. This complication extends to the determination of the ionization and collisional rate coefficients. In this section, the effect of a magnetic field on these coefficients will be examined to account for the noticeable change in gas discharge behavior.

It was first theoretically determined by Wehrli [7.2], that the presence of a magnetic field was equivalent to an increase in the pressure of the gas discharge. It was later established by Blevin and Haydon [7.3], that the discharge reacted as though the pressure had increased by a factor $\{1+(\omega_{ce}\tau_{es})^2\}^{\frac{1}{2}}$, when a magnetic field was present. This meant that the charged particles behaved as though only an electric field was present and the pressure was increased from p to p', that is,

$$p' = p\{1+(\omega_{ce}\tau_{es})^2\}^{\frac{1}{2}} . \tag{7.18}$$

Here τ_{es} is the mean free time between electron and gas molecule collisions.

The expression in Eqn. 7.18 has been experimentally verified over the range $20 \leq E/p \leq 150$ by Bernstein [7.4]. His work indicates that this formula is also applicable over a wide range of

Hall parameters, that is $0 \leq \omega_{ce}\tau_{es} \leq 25$. Further extensions to these limits may be possible once reliable collision cross sections are obtained. Nevertheless, these values indicate that the increased pressure concept is a valid approach to the study of most types of laser gas discharges under the influence of a magnetic field.

In Section 7.3 it was shown that the presence of a magnetic field could be accounted for by defining an effective electric field. The expression for the new electric field includes the collision frequency tensor $\hat{\Omega}$. The incorporation of this term is equivalent to an increase in the electron collision frequency in all directions perpendicular to the magnetic field. Hence, the corresponding increase in the number of electron-neutral collisions constitutes an effective rise in gas pressure. The results of this derivation are in agreement with the results of Blevin and Haydon [7.3].

The expression for the first Townsend ionization coefficient, α must now be modified to include this effective pressure increase. Therefore, the expression

$$\frac{\alpha(x)}{p'} = Ae^{-\left(\frac{Bp'}{E(x)}\right)}$$

becomes

$$\frac{\alpha(x)}{p} = A\{1 + (\omega_{ce}\tau_{es})^2\}^{\frac{1}{2}} \exp - \left(\frac{Bp}{E(x)}\{1 + (\omega_{ce}\tau_{es})^2\}^{\frac{1}{2}}\right) \qquad (7.19)$$

where A and B are ionization constants. From the above equation, it can be shown that in the presence of a magnetic field, $\alpha(x)$ is reduced. This effect can be explained by considering the electron kinetics as they leave the cathode surface. Under the action of crossed electric and magnetic fields, a force is exerted on the electrons which diverts their path from the anode. Thus, the electrons spend more time between the electrodes. During the long inter-electrode transit time, electrons undergo more elastic and inelastic collisions. If the applied Lorentz force is in the proper direction, the electrons will gain less energy from the electric field and thus cause fewer ionizations per unit distance in the electric field direction. The reduction of $\alpha(x)/p$ with increasing magnetic field has been experimentally verified by Bernstein [7.4].

In the experiments undertaken, the crossed electric and magnetic fields create an azimuthal velocity, v_θ . As the magnetic field is increased, more force is applied to the electrons and ions. This produces more rotation and the charged particles are able to spend more time between the electrodes. Furthermore, each electron or ion is involved in more collisions which transfer excitation energy to the neutral particles. Consequently, the charged particle temperatures T_e and T_i must also be lowered. This process is effective in reducing the charged particle temperature dependence on the production of instability modes.

In the previous section, it was shown that the form of the electron distribution is altered in the presence of electric and magnetic fields. Through this variation, it was determined that the electric field component and the electron drift velocity were reduced in the direction perpendicular to $\vec{B}$. Consequently, the magnetic field is also able to reduce the average electron energy, $<\xi>$ and thereby its temperature, since

$$\langle\xi\rangle = \frac{2}{3}\int_0^\infty \xi^{3/2} f(\xi,E/n)\,d\xi \; . \qquad (7.20)$$

From the previous discussions, the electron velocity is known to be dependent upon the electron energy and the ratio E/n. Therefore, the electron distribution function can be written as a function of these variables. In this expression, the ratio E/n is shown to be uniquely related to the average electron energy through the electron distribution function. In addition, it has been shown by Nighan [2.2], that the electron distribution function can be extremely sensitive to variations in the parameter E/n.

From the arguments presented, the ratio E/p will be decreased by the ratio

$$\frac{E}{p'} = \frac{E}{p}\,\frac{1}{\{1+(\omega_{ce}\tau_{es})^2\}^{1/2}} \qquad (7.21)$$

for a gas discharge under the influence of a magnetic field. Should this change occur, Fig. 2.1 indicates that the gas discharge will become less self-sustained. Furthermore, as E/n is lowered, the rate coefficients k_j are also reduced as shown in Fig. 2.1. This result can be mathematically derived since the collisional rate coefficients, responsible for instability growth, were functions of the ratio E/n through the relation

$$k_j = \frac{\nu_{ij}}{n_j} = \left(\frac{2e}{m_e}\right)^{1/2} \int_0^\infty \xi f(\xi,E/n)\cdot Q_{ej}(\xi)\,d\xi \; .$$

where the electron energy distribution function now takes on the form

$$f(\xi) = f_0(\xi) + \frac{\vec{v}}{v} \cdot \left(\frac{e\hat{\Omega}}{m_e} \cdot \vec{E}\right) \frac{df_0(\xi)}{d\xi} . \tag{7.22}$$

Consequently, the presence of a magnetic field helps to reduce the ability of the rate processes to initiate a micro-instability.

7.6 GAIN CHARACTERISTICS OF A MAGNETIZED GAS DISCHARGE

7.6.1 Temperature and Absorption Effects

The values of vibrational population density and their distribution over the rotational levels are important quantities basic to the understanding of the mechanism responsible for the production of a population inversion in molecular gas lasers. In a $CO_2/N_2/He$ gas system, the population inversion density and the vibrational temperatures can be obtained by analyzing the distribution in gain over the (00°1) → (10°0) vibrational transition which is known to exhibit stimulated emission. In this investigation, it is also important to determine the effect of a magnetic field upon these parameters and accordingly examine this behavior in terms of laser gain.

Gain measurements were attempted with the oscillation-amplifier arrangement shown in Fig. 7.2. The oscillator consisted of a water cooled CO_2 laser with a 50 cm active discharge length. The amplifying media was provided by the magnetically stabilized glow discharge. To increase the detectable signal, the effective gain length was tripled by folding the path of the probe laser beam through the gain media. This was accomplished by placing two gold coated mirrors within the vacuum chamber. The resulting gain length path was thereby increased

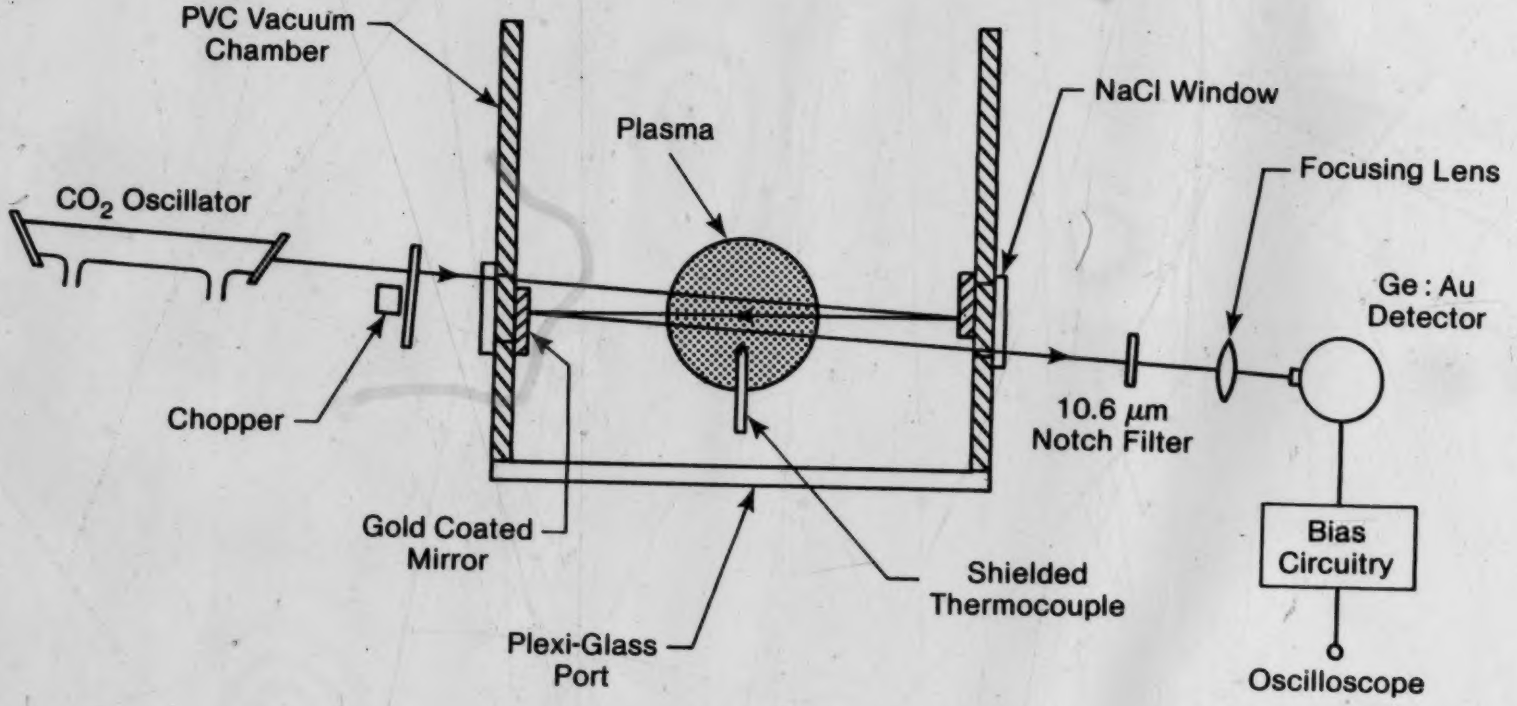
PVC Vacuum Chamber
NaCl Window
Plasma
Focusing Lens
CO$_2$ Oscillator
Ge : Au Detector
Chopper
10.6 μm Notch Filter
Gold Coated Mirror
Bias Circuitry
Shielded Thermocouple
Plexi-Glass Port
Oscilloscope

Fig. 7.2 Absorption Measurement Apparatus.

to 60 cm. Salt windows were used to allow optical access into the chamber.

The optical signal output was detected by a gold doped germanium crystal mounted in a vacuum vessel. In order to increase signal sensitivity, the chamber was evacuated and cryogenically cooled with liquid N_2 . This procedure increased the Ge crystal impedance to approximately 1 MΩ and with the proper bias circuitry, a voltage proportional to the detected optical signal could then be viewed on an oscilloscope. To avoid detection of the wide optical spectrum emitted by the glow discharge, a notch filter centered at 10.6 μm was placed in front of the detector. This ensured that only stimulated emission would be detected. An increase in the signal to noise ratio was achieved by focusing the emitted radiation onto the detector with an anti-reflection coated Ge lens.

The power gain was measured as the ratio of the detector output power with the discharge on, to that with the discharge off. However, in all cases, the output signal was dramatically reduced upon operation of the gas discharge. It can therefore be concluded that the CO_2 laser beam is undergoing absorption as it passes through the ionized gas.

The absorption coefficient α, can be estimated from Beer's law which states

$$I = I_0 e^{-\alpha \ell} \tag{7.23}$$

where I_0 is the initial laser intensity and ℓ is the gain path length. Under normal operating conditions, the measured absorption coefficient was $\alpha = 0.023 \text{ cm}^{-1}$, for a discharge current of 4.0 A and a voltage of

660 V. The fact that only absorption was noted is attributed to the presence of a hot CO_2 gas. The value obtained for the absorption coefficient compares favorably with those of Strilchuk and Offenberger [7.5], who measured similar values at an elevated gas temperature of 875 K.

In order to determine the neutral gas temperature, an iron-constantan thermocouple was inserted into the glow discharge. The thermocouple was contained in a thermally conductive but electrically insulating ceramic tube in order to shield it from electrical and chemical reactions caused by the plasma. Figure 7.3 depicts the radial gas temperature profile of the fluid ballasted design operating at a current of 4.0 A. Examination of Fig. 7.3, reveals the significant effect created by the application of a magnetic field. For low values of magnetic field, the hot plasma was essentially confined to the center of the electrode. Near the electrode edge, the gas discharge was minimal and the temperature began to drop off rapidly. As the magnetic field increased, the recorded temperature at the electrode edge began to rise while the temperature in the central region dramatically decreased. This effect can be explained by considering that as $\vec{B}$ increases, the discharge moves radially outward from the center to form an annular shaped glow discharge.

The results of Fig. 7.4 reveal the effect of the magnetic field upon three points located at the center (r = 0 cm), middle (r = 4.0 cm), and outside edge (r = 8.0 cm) of the glow discharge. The dramatic temperature change in the center of the discharge illustrates the rapid transition to an annular shaped discharge. The initially hot

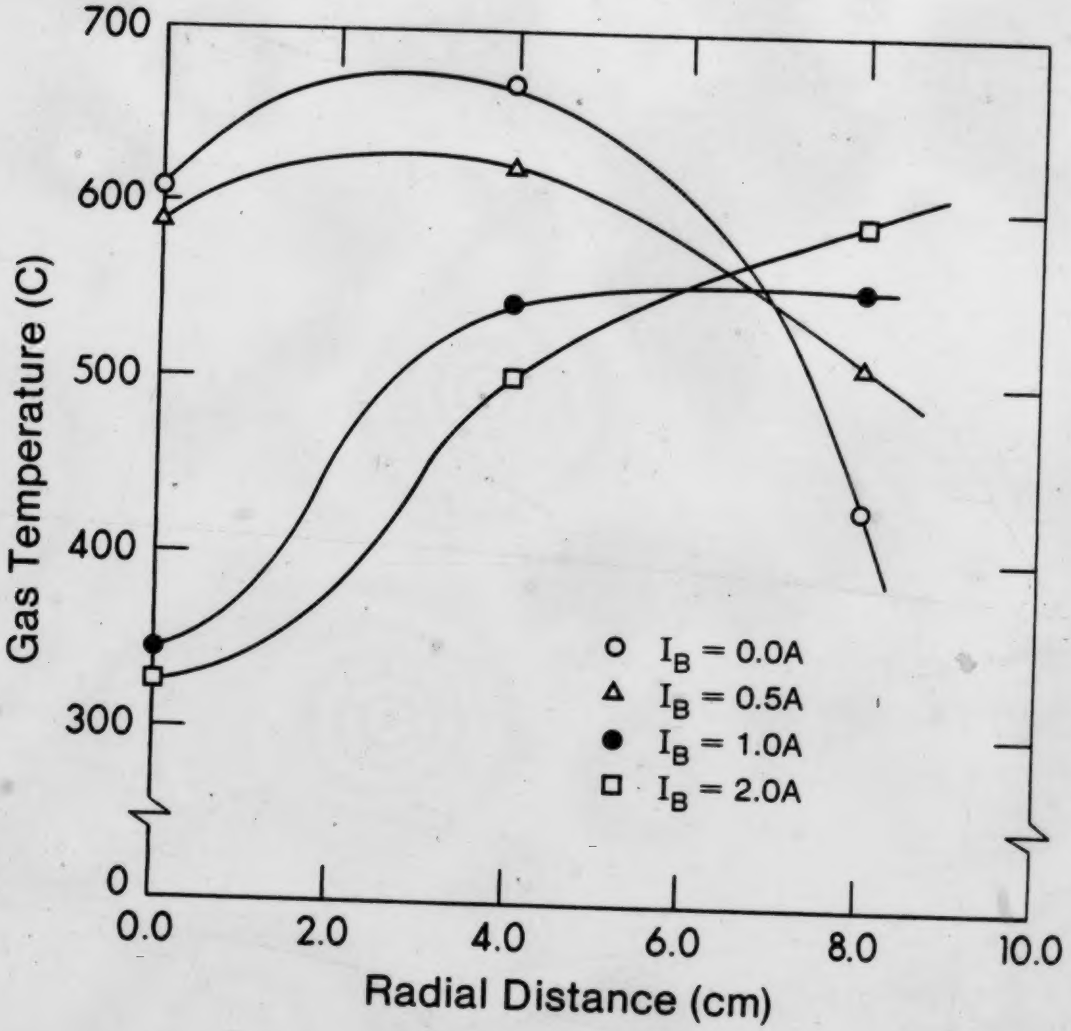

Fig. 7.3 Radial Gas Temperature Profile. Discharge parameters include: J = 18 mA/cm^2, 2:8:10 torr gas mixture of $CO_2/N_2/He$.

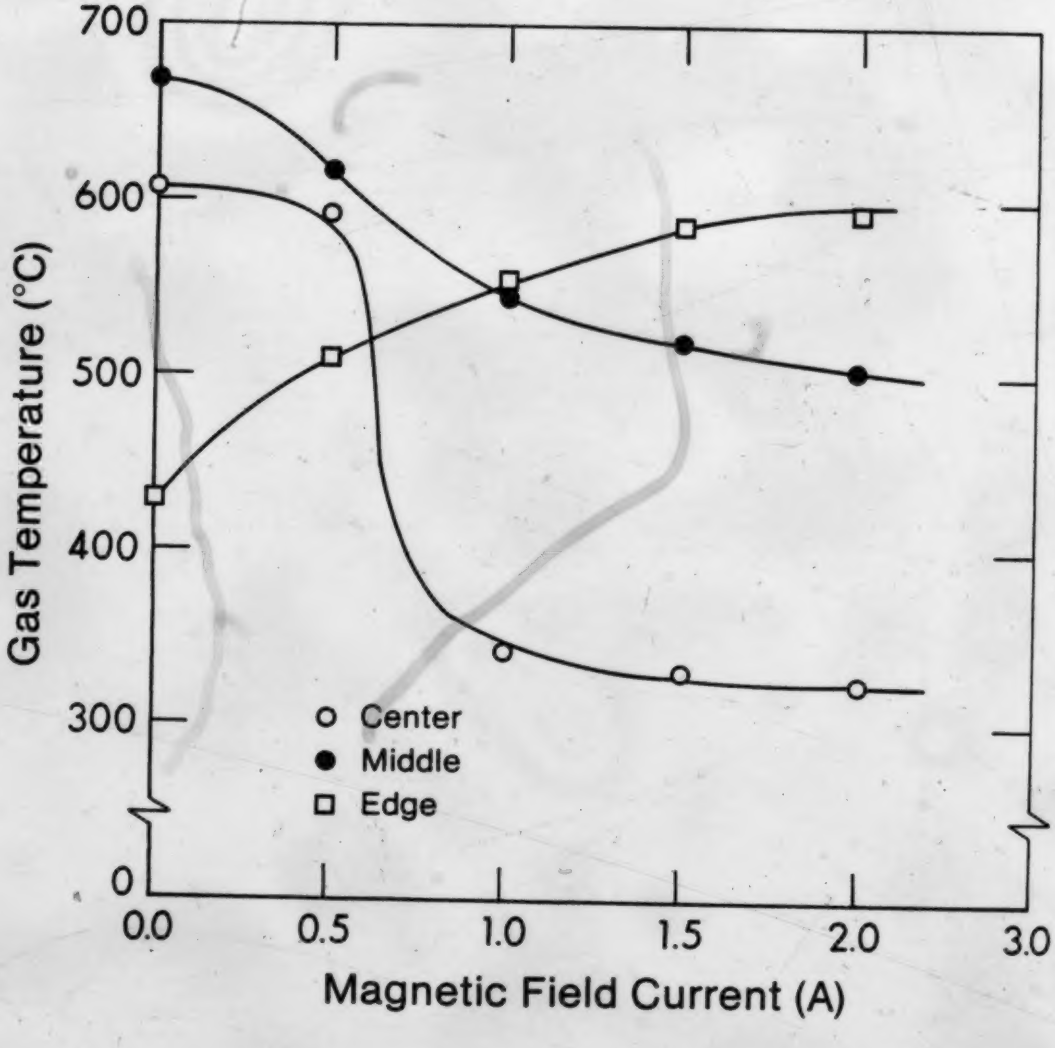

Fig. 7.4 Variation of Discharge Temperature with Magnetic Field.

gas in the middle of discharge is also observed to cool upon application of the magnetic field. Furthermore, the substantial rise in gas temperature along the electrode edge can be attributed to the convective radial gas flow produced by the Lorentz force. From these results, it is obvious that the magnetic field is reducing the temperature of the ionized gas by convective motion. Through this technique, the ability of the discharge to generate local hot spots and thermal instabilities is being curtailed.

Attempts were made to cool the gas temperature through the use of a heat exchanger and small electric fan. However the high power loading permitted by the magnetically stabilized glow discharge, overwhelmed the 500 W capacity of the existing heat exchanger. Since the input power loading of the gas discharge could easily exceed several kilowatts, the gas temperature continued to rise until an equilibrium was achieved. At steady-state, the average gas temperature, as determined from Fig. 7.2, was approximately 550-600 C. Furthermore, it was not possible to install additional heat exchangers due to the small size of the vacuum chamber. In order to maintain a low gas temperature, the discharge current was limited to less than 1 A. At this low current value, the discharge could not be uniformly excited nor the current density evenly distributed.

It was initially believed that the natural radial flow of the gas discharge formed a closed loop convective cell and thus did not permit efficient use of the heat exchanger. This hypothesis was later confirmed by the computer simulation of the secondary flows as displayed in Fig. 6.3. In the next phase of this investigation, an improved design will be constructed to allow the hot gas to recirculate through a larger heat exchanger and up past the transparent anode with the assistance of a pair of tangential blowers. This new design is illustrated by Fig. 7.5.

7.6.2 Excitation Processes in a Magnetic Field

In order to ensure that the MGD stabilization technique is suitable for CO_2 laser applications, it is necessary to examine the effect of a magnetic field upon the gain of an excited media. However, due to the problems encountered with the removal of excess heat, no definite conclusions could be made. As an alternative, this section will speculate upon the possible beneficial aspects created by the presence of a magnetic field.

The optical gain coefficient for the P and R branch rotational transitions between vibrational levels J and $J \pm 1$ in a CO_2 gas discharge, can be written as

$$\gamma(\nu) = \frac{\lambda^2 g(\nu)}{n^2 t_{\text{spont}}} \left(N_{00^\circ 1} - \frac{g_J}{g_{J\pm 1}} N_{10^\circ 0} \right) . \qquad (7.24)$$

In this expression, $g(\nu)$ is the lineshaping function dependent on the dominant broadening process, and n is the index of refraction of the plasma. Upon examination of Eqn. 7.24, it is clearly seen that $\gamma(\nu)$ is primarily a function of t_{spont} and the population densities. It has already been shown that the magnetic field is responsible for lowering the temperature of the gas discharge through rapid convection motion. It is hoped that this process will prevent the growth

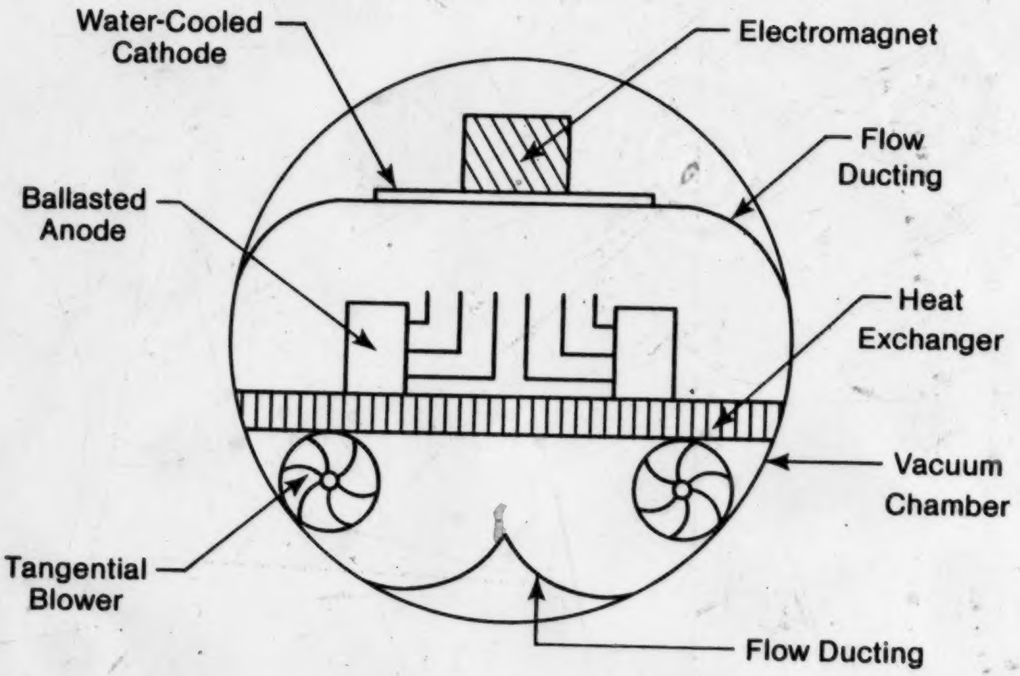
Water-Cooled
Cathode
Electromagnet
Flow
Ducting
Ballasted
Anode
Heat
Exchanger
Vacuum
Chamber
Tangential
Blower
Flow Ducting

Fig. 7.5 Improved Convective Flow Design for a Magnetically Stabilized Gas Discharge.

of the lower laser level population density, thereby ensuring a large population inversion. This efficient technique of rapid gas convection is widely established in the high power laser industry. However, their methods have relied upon the deployment of large high speed blowers to cool the gas. In this MGD technique, large velocities can be created by the Lorentz force which provide a non-mechanical means of cooling the gas discharge and hopefully improving the gain characteristics.

The lifetime of the upper laser level t_2 is determine by molecular collisions and is inversely proportional to the pressure [7.6]. Thus, as t_2 decreases with a rise in pressure, the pumping power per molecule will increase since it can be recycled more rapidly. It has been previously stated that the influence of a magnetic field on a gas discharge is equivalent to a rise in pressure due to the increased number of molecular collisions. In this manner, the magnetic field can effectively reduce the lifetime of the upper laser level and correspondingly increase the saturation intensity.

The analysis of Nighan [2.2] has determined that for an average electron energy of less than 1 eV, the electron-CO_2 molecule energy exchange is clearly dominated by vibrational excitation, while above 2 eV, electronic excitation dominates. More specifically, Boness and Schulz [7.7] have determined that the maximum excitation of the (00°1) asymmetric vibration mode occurs for an electron energy of 0.9 eV. At this point, the collision cross sections of the (10°0) symmetric and (01°0) bending modes are an order of magnitude lower, and are thereby negligible. Thus, the population inversion by electron impact and therefore stimulated emission at 10.6 μm is enhanced for this low energy region. For electron energies greater than 3 eV, laser action is likely to be suppressed since the population inversion will be reduced by the diminished cross section of the (00°1) level, and by the enhanced cross section for the lower laser level (10°0). Consequently, by choosing the proper E/p ratio, corresponding to an electron energy of approximately 1 eV, it is possible to optimize the lasing process.

Throughout this chapter it has been shown that the presence of a magnetic field can alter the electron distribution function, the electron energy, and consequently the ratio E/p. Thus, by proper adjustment of the magnetic field strength, E/p can be sufficiently lowered such that the energy transferred to the upper laser level can be maximized. With the construction of a larger vacuum chamber, a complete verification of the anticipated effects of introducing a magnetic field will be investigated.

CHAPTER 8

CONCLUDING REMARKS

8.1 SUMMARY OF DISCHARGE STABILIZATION PROCESSES

The presence of a transverse magnetic field has dramatically demonstrated its stabilizing influence on a glow discharge. It has been experimentally and theoretically shown that a magnetic field can effectively suppress both plasma micro-instabilities and bulk thermal instabilities. This highly effective stabilization technique has, thus far, achieved a specific power loading of over 10 kW/l without experiencing a glow-to-arc transition and without the benefit of external gas cooling. These results are especially encouraging since an upper instability threshold has not yet been observed, suggesting that even higher power loading is possible.

One of the reasons for this exceptional degree of stability can be attributed to the trapping of charged particles into Larmor orbits. As a result of this orbital motion, the charged particles spend more time travelling between the electrodes, and are therefore involved in more inelastic collisions. The increase in the electron-neutral and ion-neutral collision frequencies essentially acts as though an increase in gas discharge pressure had occurred. Through this mechanism, the application of a magnetic field lowers the parameter E/p such that the glow discharge becomes less self-sustained. Since E/p is a measure of the average energy gained between collisions, the charged particle's drift velocity and its energy are correspondingly reduced. As a result of a decrease in electron temperature or E/p, the magnitudes of the dominating ionization and attachment rate coefficients are also reduced. Since the rate of these collisional processes is decreased in the presence of a magnetic field, the probability of an attachment induced ionization instability is dramatically lowered. Consequently, charge production and loss in the plasma are effectively decoupled from the applied electric field.

It has been determined that the Lorentz forces, acting upon the space-charge sheaths, are responsible for maintaining the gas discharge as a normal glow. Furthermore, the magnetic field is suspected of controlling the electron emission from the cathode by increasing secondary emission yield through oblique ion bombardment of the cathode. Together, these processes dynamically inhibit the growth of electrode induced instabilities.

The Lorentz forces are also responsible for stabilizing the bulk thermal instabilities through a rapid rotation of the charged and neutral fluids. The high rotational velocity exhibited by the glow discharge can rapidly convect nonuniformities in electron density, temperature, or current and distribute them throughout the discharge volume in a time less than the normal instability formation time. Since the applied magnetic fields are spatially dependent, large shear forces exist which are able to break up streamers and arc-like filaments.

Due to the imposed magnetic field, pressure gradient forces are also created which drive secondary radial and axial flows. A one-fluid MGD computer model has predicted the existence of a convective cell formed by these secondary flows. The discovery and prediction of large secondary flows is an important advance in resolving the behavior of a glow discharge subject to a transverse magnetic field. Furthermore, the secondary flows play an important role in the stabilization process by allowing the convection of hot gas out of the active discharge volume. This radial flow system is highly efficient since the hot neutral gas has only one-half the discharge residence time of conventional transverse flow designs.

8.2 SUMMARY OF COMPUTATIONAL WORK

The development of the computer program MAGIC has produced a detailed simulation of a time dependent, partially ionized gas discharge with an imposed magnetic field. Through the use of a one-fluid MGD model, this program can accurately predict the magnitude of the highly sheared rotational flow and the existence of strong secondary flows. These rapid flows provide an efficient non-mechanical means of reducing the gas residence time, thereby convecting electrothermal instabilities from the active discharge volume.

The use of a large time step, iterative ADI finite difference technique has enabled MAGIC to operate with time steps larger than the CFL limit. Such a technique can be regarded as state of the art in terms of advanced computer codes. The utilization of variable time step size controls has proven to be an excellent method of maintaining maximum computational efficiency while avoiding the limitation in time step size that is imposed by explicit techniques. This effort, though indeed a major one, must be considered an initial one, suggesting many new ideas and areas for future consideration. Thus far, MAGIC has proven to be a valuable research tool and hopefully upon further refinement, a variety of discharge devices and structures may be entirely designed and simulated using this powerful computational aid.

8.3 FUTURE CONSIDERATIONS

In the near future, the computer code will be extended to include the conservation of energy equation. This additional feature will allow simulation of heat transport throughout the gas discharge. A more ambitious project is currently planned which will include the development of a two-fluid MGD model designed to determine the complex interactions formed between the charged and the neutral fluids.

It is also planned to extend MAGIC's capabilities to handle a variety of discharge configurations. This would initially include the coaxial discharge geometry discussed earlier and a new axial discharge device. In this geometry, the Lorentz driving force is supplied by an axial electric field and a rapidly rotating radial magnetic field. The time dependent nature of the code will also be utilized to ascertain if the magnetic stabilization technique can be adapted to pulsed TEA laser systems where the duration of the discharge is very brief.

To further substantiate the observed and numerical results, additional diagnostic measurements will be undertaken. Of primary importance is the determination of the electron density. This could be accomplished by the deployment of an electrostatic probe at various locations within the plasma. Alternatively, an externally generated microwave source can be used as a non-perturbing probe. In this case, the electron density is simply determined by varying the signal source frequency until the phenomenon of cutoff is reached. The rotational velocity of the ions and neutrals can be determined by measuring the Doppler shift of the spectral lines emitted by the plasma particles. The ion and neutral gas temperatures can be calculated from the Doppler width of the emitted spectral lines.

Due to the broad scope of the investigations described in this thesis, a thorough study of all aspects of this project was difficult to accomplish. However, a significant amount of data and understanding now exists which confirm some basic theories. It has now been confirmed that magnetic fields can shape, confine, and stabilize glow discharges suitable for use in high power gas lasers. With the promising results shown thus far, the MGD stabilization technique should have a major impact on the design of future gas lasers. It is anticipated that such a laser will be built and tested in the near future.

REFERENCES

CHAPTER 1

1.1 W.J. Wittermann, "High Output and Long Lifetimes of Sealed-Off CO_2 Lasers", Appl. Phys. Lett., Vol. 11, No. 11, p. 337, 1967.

1.2 A.J. Demaria, "Review of CW High-Power CO_2 Lasers", Proc. IEEE, Vol. 61, No. 6, p. 731, 1973.

1.3 W.L. Nighan, "Progress in High Pressure Electric Lasers", presented at the 11th International Conference on Phenomena in Ionized Gases, Prague, Czechoslovakia, Sept. 1971.

1.4 A.C. Eckbreth and J.W. Davis, "RF Augmentation in CO_2 Closed-Cycle DC Electric Discharge Convection Lasers", Appl. Phys. Lett., Vol. 21, No. 1, p. 25, 1972.

1.5 C.A. Fenstremacher, M.J. Nutter, W.T. Leyland, and K. Boyer, "Electron-Beam Controlled Electric Discharges as a Method of Pumping Large Volumes of CO_2 Laser Media at High Pressure", Appl. Phys. Lett., Vol. 20, No. 2, p. 56, 1972.

1.6 H.J.J. Seguin, J. Tulip, "Photoinitiated and Photosustained Laser", Appl. Phys. Lett. Vol. 21, No. 9, p. 414, 1972.

1.7 A. Jowan and J.S. Levine, "The Feasibility of Producing Laser Plasmas Via Photoionization", IEEE J. of Quantum Electronics, Vol. QE-8, No. 11, p. 827, 1972.

1.8 O.P. Judd, "An Efficient Electrical CO_2 Laser Using Preionization by Ultraviolet Radiation", Appl. Phys. Lett., Vol. 22, No. 3, p. 95, 1973.

1.9 O.P. Judd and J.Y. Wada, "Investigations of a UV Preionized Electric Discharge and CO_2 Laser", IEEE J. Quantum Electronics, Vol. QE-10, No. 1, p. 12, 1974.

1.10 A.E. Hill, "Uniform Electrical Excitation of Large Volume High-Pressure Near Sonic CO_2-N_2-He Flowstream", Appl. Phys. Lett. Vol. 18, No. 5, p. 194, 1971.

1.11 G.A. Garosi, G. Bekefi, M. Schulz, "Response of a Weakly Ionized Plasma to Turbulent Gas Flow", Phys. of Fluids, Vol. 13, No. 11, p. 2795, 1970.

1.12 W.C. Roman and T.W. Myers, "Experimental Investigations of an Electric Arc in Transverse Aerodynamic and Magnetic Fields", AIAA Journal, Vol. 5, No. 11, p. 2011, 1967.

1.13 Y.Y. Winograd and J.F. Klein, "Electric Arc Stabilization in Crossed Convective and Magnetic Fields", AIAA Journal, Vol. 7, No. 9, p. 1699, 1969.

1.14 C.J. Buczek, R.J. Freiberg, P.P. Chenausky, and R.J. Wayne, "Magnetic Stabilization of the Plasma Column in Flowing Molecular Lasers", Proc. IEEE, Vol. 59, No. 4, p. 659, 1971.

1.15 B.A. Tozer, "Rotating Plasma", Proc. IEE, Vol. 112, No. 1, p. 218, 1965.

1.16 B. Lehnert, "Rotating Plasmas", Nuclear Fusion, Vol. 11, p. 485, 1971.

1.17 B.W. James and S.W. Simpson, "Isotope Separation in the Plasma Centrifuge", Plasma Physics, Vol. 18, p. 289, 1976.

1.18 B.W. James and S.W. Simpson, "The Viscous Dynamics of a Rotating Plasma", Plasma Physics, Vol. 20, p. 759, 1978.

1.19 H.E. Wilhelm and S.H. Hong, "Plasma Rotation by Electric and Magnetic Fields in a Discharge Cylinder", J. Appl. Phys., Vol. 48, No. 2, p. 561, 1977.

1.20 S.H. Hong and H.E. Wilhelm, "Boundary Value Problem for a Counter-rotating Electrical Discharge in an Axial Magnetic Field", J. Appl. Phys., Vol. 49, No. 1, p. 146, 1978.

1.21 M.M.B. Wijnakker, E.H.A. Granneman, and J. Kistemaker, "A Study of a Weakly Ionized Rotating Plasma", Z. Naturforsch, Vol. 34a, p. 672, 1979.

CHAPTER 2

2.1 R.A. Haas, "Plasma Stability of Electric Discharges in Molecular Gases", Phys. Review A, Vol. 8, No. 2, p. 1017, 1973.

2.2 W.L. Nighan, "Electron Energy Distributions and Collision Rates in Electrically Excited N_2, CO, and CO_2", Phys. Review A, Vol. 2, No. 5, p. 1989, 1970.

2.3 W.J. Wiegand and W.L. Nighan, "Plasma Chemistry of CO_2-N_2-He Discharges", Appl. Phys. Lett., Vol. 22, No. 11, p. 583, 1973.

2.4 W.L. Nighan and W.J. Wiegand, "Influence of Negative-Ion Processes on Steady-State Properties and Striations in Molecular Gas Discharges", Phys. Review A, Vol. 10, No. 3, p. 922, 1974.

2.5 W.L. Nighan, W.J. Wiegand, R.A. Haas, "Ionization Instability in CO_2 Laser Discharges", Appl. Phys. Lett., Vol. 22, No. 11, p. 579, 1973.

2.6 W.L. Nighan and W.J. Wiegand, "Causes of Arcing in CW CO_2 Convection Laser Discharges", Appl. Phys. Lett., Vol. 25, No. 11, p. 633, 1974.

CHAPTER 3

3.1 L. Holland, W. Steckelmacher, and J. Yarwood, "Vacuum Manual", Spon Ltd., 1974.

3.2 E. Nasser, "Fundamentals of Gaseous Ionization and Plasma Electronics", Wiley, New York, 1971.

3.3 K.H. Nam, Ph.D. Thesis, University of Alberta, Dept. of Electrical Engineering, 1978.

3.4 C.L. Thomas, "Software for Numerical Mathematics", Loughborough Leic. Eng., Academic Press, p. 315, 1974.

3.5 F.B.A. Frungel, "High Speed Pulse Technology", Vol. 1, Academic Press, New York, 1965.

3.6 G.N. Glasoe and J.V. Lebacqz, "Pulse Generators", McGraw-Hill, New York, 1948.

CHAPTER 4

4.1 B.S. Tanenbaum, "Plasma Physics", McGraw-Hill, New York, 1967.

4.2 G.W. Sutton and A. Sherman, "Engineering Magnetohydrodynamics", McGraw-Hill, New York, 1965.

4.3 L.D. Landau and E.M. Lifshitz, "Fluid Mechanics", Pergamon Press, London, 1959.

4.4 N.A. Krall and A.W. Trivelpiece, "Principles of Plasma Physics", McGraw-Hill, New York, 1973.

4.5 C.E. Capjack, D.M. Antoniuk, and H.J.J. Seguin, "Dynamics of Magnetically Stabilized Laser Discharge", J. Appl. Phys., Vol. 52, No. 7, p. 4517, 1981.

4.6 S. Chapman and T.G. Cowling, "Mathematical Theory of Non-Uniform Gases", Cambridge University Press, London, 1970, 3rd edition.

4.7 J.O. Hirschfelder, C.F. Curtis, and R.B. Bird, "Molecular Theory of Gases and Liquids", Wiley, New York, 1954.

4.8 C.J. Elliot, O.P. Judd, A.M. Lockett, and S.D. Rockwood, "Electron Transport Coefficients and Vibrational Excitation Rates for Electrically Excited CO_2 Gas Lasers", Report #LA-5562-MS, Los Alamos Scientific Laboratory, 1974.

4.9 P.M. Morse and H. Feshback, "Methods of Theoretical Physics", McGraw-Hill, New York, 1953.

CHAPTER 5

5.1 R.H. Pennington, "Introductory Computer Methods and Numerical Analysis", Macmillan, New York, 1965.

5.2 D.W. Peaceman and H.H. Rachford Jr., "The Numerical Solution of Parabolic and Elliptic Differential Equations", J. Soc. Indust. Appl. Math., Vol. 3, p. 28, 1955.

5.3 D. Potter, "Computational Physics", Wiley, New York, 1973.

5.4 F.F. Chen, "Introduction to Plasma Physics", Plenum Press, New York, 1974.

5.5 C.H. Finan, Ph.D. Thesis; University of California, Davis, Department of Applied Science, 1980.

5.6 W.R. Briley and H. McDonald, "Solution of the Multidimensional Compressible Navier-Stokes Equations by a Generalized Implicit Method", J. of Comp. Phys. Vol. 24, p. 372, 1977.

5.7 R.D. Richtmyer and K.W. Morton, "Difference Methods for Initial Value Problems", Interscience, New York, 1967, 2nd edition.

5.8 I.R. Lindemuth, Ph.D.Thesis, University of California, Davis, Department of Applied Science, 1971.

CHAPTER 6

6.1 R.S. Craxton and R.L. McCrory,"Two-Dimensional Calculations of Non-Spherical Laser Fusion Implosion", Report #99, Laboratory for Laser Energetics, University of Rochester, 1980.

6.2 H.J.J. Seguin, C.E. Capjack, D.M. Antoniuk, V.A. Seguin, "A Magnetically Stabilized Radial Discharge for a High-Powered Laser", Appl. Phys. Lett., Vol. 39, No. 3, p. 203, 1981.

6.3 C.E. Capjack, H.J.J. Seguin, D.M. Antoniuk, V.A. Seguin, "A Magnetically Stabilized Coaxial Laser Discharge", Appl. Phys. B., Vol. 26, p. 161, 1981.

6.4 J.L. Crandall and A.W. Cooper, "Acoustic Generation of Moving Striations in Neon", Proceedings of the 8th International Conference of the Phenomena of Ionized Gases, Springer, Vienna, p. 133, 1967.

6.5 L. Pekarek and V. Krejci, "The Physical Nature of the Production of Moving Striations in a DC Discharge Plasma", Czech. J. Phys. B., Vol. 11, p. 729, 1961.

6.6 A.K. Brewer and J.W. Westhaver, "The Cathode Region in the Glow Discharge", J. Appl. Phys., Vol. 8, p. 779, 1937.

6.7 M. Cloutier, "Computed Physical and Thermodynamic Properties of Various He/CO_2/N_2 Mixtures", DREV Technical Notes, Quebec, Canada, 1970.

6.8 M.L.E. Oliphant, "Liberation of Electrons from Metal Surfaces by Positive Ions", Proc. Royal Soc., A-127, p. 373, 1930.

6.9 O. Almen and G. Bruce, "Collection and Sputtering Experiments with Noble Gas Ions", Nucl. Instr. and Methods, Vol. 11, p. 257, 1961.

6.10 V.E. Golant, A.P. Zhilinsky, I.E. Sakharov, "Fundamentals of Plasma Physics", Wiley, New York, 1977.

6.11 S.N. Sen and R.N. Gupta, "Variations of Discharge Current in a Transverse Magnetic Field in a Glow Discharge", J. Appl. Phys. D, Vol. 4, p. 510, 1971.

CHAPTER 7

7.1 T.N. An, E. Marode, P.C. Johnson, "Monte Carlo Simulation of Electrons within the Cathode Fall of a Glow Discharge in Helium", J. Phys. D, Vol. 10, p. 2317, 1977.

7.2 M. Wehrli, "Funkenpotentiale im Transversalen Magnetfelde", Ann. der Physik, Vol. 69, Ser. 4, p. 285, 1922.

7.3 H.A. Blevin and S.C. Haydon, "The Townsend Ionization Coefficients in Crossed Electric and Magnetic Fields", Aust. J. Phys., Vol. 11, No. 18, p. 18, 1958.

7.4 M.J. Bernstein, "Townsend Ionization Coefficient for Hydrogen in a Transverse Strong Magnetic Field", Phys. Rev., Vol. 127, p. 342, 1962.

7.5 A.R. Strilchuk and A.A. Offenberger, "High Temperature Absorption in CO_2 at 10.6 μm", Appl. Optics, Vol. 13, No. 11, p. 2643, 1974.

7.6 A. Yariv, "Quantum Electronics", Wiley, New York, 1977, 2nd edition.

7.7 M.J.W. Boness and G.J. Schulz, "Vibrational Excitation of CO_2 by Electron Impact", Phys. Rev. Letters, Vol. 21, p. 1031, 1968.

APPENDIX A

In order to utilize the conductivity tensor $\hat{\sigma}$ in a cylindrical coordinate system, it is necessary to perform a similarity transformation. This new conductivity tensor would then be valid for any orientation of the nonlinear magnetic field depicted in Fig. 3.7. The first step in this coordinate transformation requires a change in basis vector from local magnetic field (Cartesian) coordinates to local cylindrical coordinates. This can be represented by

$$\vec{x} = \hat{R}\vec{x}' \tag{A.1}$$

where $\vec{x} = \sum_i x_i e_i$ is a vector representing cylindrical coordinates and $\vec{x}' = \sum_i x_i' e_i'$ is a vector representing the local Cartesian coordinates along the magnetic field. The matrix $\hat{R}$ is an orthogonal transformation matrix formed by the change of basis vectors from Cartesian to cylindrical coordinates. From Fig. A.1 the new cylindrical basis vectors are written as

$$\begin{aligned} \vec{e}_r &= -\sin\phi\vec{e}_{x'} + \cos\phi\vec{e}_{z'} \\ \vec{e}_\theta &= -\vec{e}_{y'} \\ \vec{e}_z &= \cos\phi\vec{e}_{x'} + \sin\phi\vec{e}_{z'} \ . \end{aligned} \tag{A.2}$$

By using Eqns. A.1 and A.2, the transformation matrix becomes

$$\hat{R} = \begin{bmatrix} -\sin\phi & 0 & \cos\phi \\ 0 & -1 & 0 \\ \cos\phi & 0 & \sin\phi \end{bmatrix} \tag{A.3}$$

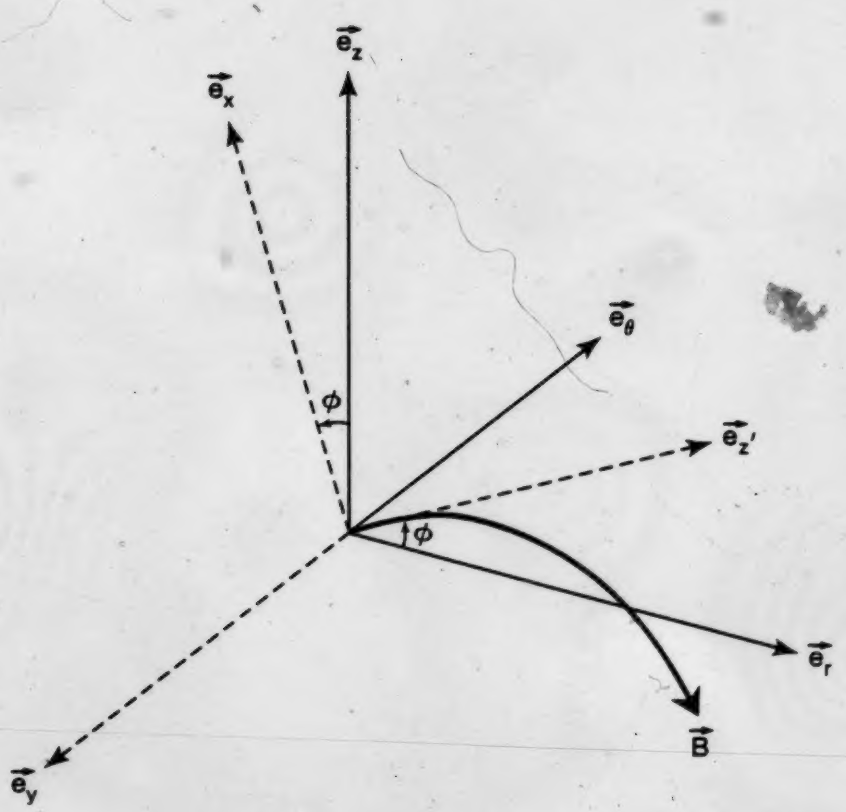
$\vec{e}_z$
$\vec{e}_x$
$\vec{e}_\theta$
ϕ
$\vec{e}_{z'}$
ϕ
$\vec{e}_r$
$\vec{B}$
$\vec{e}_y$

Fig. A.1 Transformation of Coordinate System Basis Vectors.

where $\hat{R}$ is an orthogonal matrix such that $\hat{R}^{-1} = \hat{R}^{T} = \hat{R}$.

In local Cartesian coordinates, Ohm's law may be written as

$$\vec{J}' = \hat{\sigma}' \cdot \vec{E}' \ . \qquad \text{(A.4)}$$

Now, using the transformation Eqn. A.1 for both the current density and electric field vectors yields

$$\hat{R}^{-1} \cdot \vec{J} = \hat{\sigma}' \hat{R}^{-1} \cdot \vec{E}$$

or

$$\vec{J} = (\hat{R}\hat{\sigma}'\hat{R}^{-1}) \cdot \vec{E} = \hat{\sigma} \cdot \vec{E} \qquad \text{(A.5)}$$

where $\hat{\sigma} = \hat{R}\hat{\sigma}'\hat{R}^{-1}$ is the similarity transformation.

The Cartesian conductivity tensor $\hat{\sigma}'$ is normally aligned with the *z* component of the magnetic field. Written in matrix form, $\hat{\sigma}'$ becomes

$$\hat{\sigma}' = \begin{bmatrix} \sigma_{\perp} & \sigma_{T} & 0 \\ \sigma_{T} & \sigma_{\perp} & 0 \\ 0 & 0 & \sigma_{11} \end{bmatrix} \qquad \text{(A.6)}$$

Performing the necessary matrix multiplications as indicated by Eqn. A.5, the similarity transformation produces the new cylindircal conductivity tensor

$$\hat{\sigma} = \begin{bmatrix} \sigma_{\perp}\sin^2\phi + \sigma_{11}\cos^2\phi & -\sigma_{T}\sin\phi & (\sigma_{11}-\sigma_{\perp})\sin\phi\cos\phi \\ \sigma_{T}\sin\phi & \sigma_{\perp} & -\sigma_{T}\cos\phi \\ (\sigma_{11}-\sigma_{\perp})\sin\phi\cos\phi & \sigma_{T}\cos\phi & \sigma_{\perp}\cos^2\phi + \sigma_{11}\sin^2\phi \end{bmatrix} . \qquad \text{(A.7)}$$

VITA

NAME: David Michael Antoniuk

PLACE OF BIRTH: Edmonton, Alberta

YEAR OF BIRTH: 1955

POST-SECONDARY EDUCATION AND DEGREES

University of Alberta
Edmonton, Alberta

1973-78 B.Sc. Electrical Engineering
1978-83 Ph.D. Electrical Engineering

HONOURS AND AWARDS:

Board of Governor's Prize 1973

Province of Alberta Undergraduate Scholarship 1973-74

NSERC Postgraduate Scholarship 1980-82

NSERC Postdoctoral Fellowship 1983-84

RELATED WORK EXPERIENCE:

Technician
Tri-Universities Meson Facility (TRIUMF)
Summer of 1977

Teaching Assistant
University of Alberta
1977-82

Sessional Instructor
University of Alberta
1983

PUBLICATIONS

1. H.J.J. Seguin, C.E. Capjack, D.M. Antoniuk, K.A. Nam, "High Power Laser Discharge Stabilization with Magnetic Fields", Appl. Phys. Lett., Vol. 37, No. 2, p. 130, 1980.

2. C.E. Capjack, D.M. Antoniuk, H.J.J. Seguin, "Dynamics of Magnetically Stabilized Laser Discharge", J. Appl. Phys., Vol. 52, No. 7, p. 4517, 1981.

3. H.J.J. Seguin, C.E. Capjack, D.M. Antoniuk, V.A. Seguin, "A Magnetically Stabilized Radial Discharge for a High-Powered Laser", Appl. Phys. Lett., Vol. 39, No. 3, p. 203, 1981.

4. C.E. Capjack, H.J.J. Seguin, D.M. Antoniuk, V.A. Seguin, "A Magnetically Stabilized Coaxial Laser Discharge", Appl. Phys. B, Vol. 26, p. 161, 1981.